I. R. IRAN

ISSN: 2423-7167
e-ISSN: 1735-9244

International Journal of Engineering

Journal Homepage: www.ije.ir

MERC

TRANSACTIONS C: Aspects

Volume 33, Number 09, September 2020

Materials and Energy Research Center

In the Name of God

INTERNATIONAL JOURNAL OF ENGINEERING
Transactions C: Aspects

DISCLAIMER
The publication of papers in International Journal of Engineering does not imply that the editorial board, reviewers or publisher accept, approve or endorse the data and conclusions of authors.

International **J**ournal of **E**ngineering *Transactions A: Basics* (ISSN 1728-1431) (EISSN 1735-9244)
International **J**ournal of **E**ngineering *Transactions B: Applications* (ISSN 1728-144X) (EISSN 1735-9244)
International **J**ournal of **E**ngineering *Transactions C: Aspects* (ISSN 2423-7167) (EISSN 1735-9244)
Web Sites: www.ije.ir & www.ijeir.info E-mails: ije.editor8@gmail.com, Tel: (+9821) 88771578, Fax: (+9821) 88773352
Materials and Energy Research Center (MERC)

ISSN: 2423-7167, e-ISSN: 1735-9244

International Journal of Engineering, Volume 33, Number 9, September 2020

CONTENTS:

ISSN: 2423-7167, e-ISSN: 1735-9244

International Journal of Engineering, Volume 33, Number 9, September 2020

IJE TRANSACTIONS C: Aspects Vol. 33, No. 9, (September 2020) 1696-1702

International Journal of Engineering

Journal Homepage: www.ije.ir

Determination of Riboflavin by Nanocomposite Modified Carbon Paste Electrode in Biological Fluids Using Fast Fourier Transform Square Wave Voltammetry

M. Asgharian Marzabad[a], B. Jafari[b], P. Norouzi*[b,c]

[a] *CEITEC—Central European Institute of Technology and Department of Chemistry, Faculty of Science, Masaryk University, Kamenice 5, Czechia*
[b] *Center of Excellence in Electrochemistry, School of Chemistry, College of Science, University of Tehran, Tehran, Iran*
[c] *Biosensor Research Center, Endocrinology & Metabolism Molecular-Cellular Sciences Institute, Tehran University of Medical Sciences, Tehran, Iran*

P A P E R I N F O

Paper history:
Received 13 March 2020
Received in revised form 04 April 2020
Accepted 12 June 2020

Keywords:
Fast Fourier Transforms Square Wave Voltammetry
Riboflavin
Reduced Graphene Oxide
Samarium Oxide

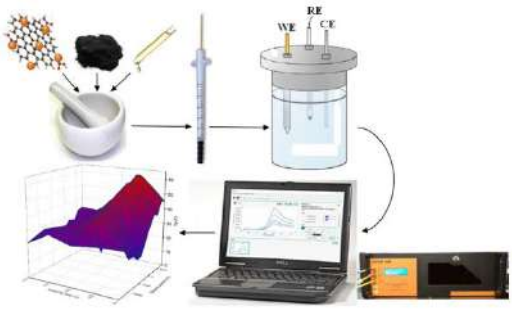

A B S T R A C T

Herein, fast Fourier transformation square-wave voltammetry (FFT-SWV) as a novel electrochemical determination technique was used to investigate the electrochemical behavior and determination of Riboflavin at the surface of a nanocomposite modified carbon paste electrode. The carbon paste electrode was modified by nanocomposite containing Samarium oxide (Sm_2O_3)/reduced graphene oxide (RGO) (2:1) to improve detection sensitivity of Riboflavin under optimal experimental conditions. Furthermore, the signal-to-noise ratio was significantly increased by application of discrete fast Fourier transformation analysis, background subtraction and two-dimensional integration of the electrode response over the selected potential range and the time window. Obtained cyclic voltammograms demonstrated a diffusion-controlled reversible electron transfer reaction for Riboflavin in phosphate buffer solution (pH=7.2). The peak potential values were pH-dependent, involving the same numbers of protons and electrons. To obtain the maximum sensitivity, some effective parameters such as scan rate (10 mV/s), accumulation time (0.2 s) and potential (+400 mV), frequency (1420 Hz) and amplitude (20 mV) were optimized. As a result, determination of Riboflavin using FFT-SWV showed a linear range of response from 10 to 400 nM (R^2=0.9993), with limit of detection of 0.86 nM. An acceptable recovery percent was also obtained for Riboflavin in human plasma samples as criteria of measurement applicability of the proposed modified electrode.

***doi**: 10.5829/ije.2020.33.09c.01*

1. INTRODUCTION

Vitamin B2 or Riboflavin is a renowned water-soluble vitamin from Vitamin B group with a chemical structure shown as Scheme 1. Riboflavin could be found in natural foods, like milk and dairy products; meat, eggs, cereals, and fresh vegetables [1]. As this vitamin would not be stored in human body, regular daily consumption would be so critical. In order to ensure the daily recommendations of riboflavin intake, accurate and fast method for determination of Riboflavin in pharmaceutical and serum samples is crucially important.

Riboflavin comprises two coenzymes, flavin adenine dinucleotide (FAD) and flavin mononucleotide (FMN). In general, FAD and FMN [2] can easily loss or gain one or two electrons or hydrogen atoms through bonding to specific enzymes, thus Riboflavin participates in redox reactions [3]. Several techniques have been used for determination of Riboflavin such as chemiluminescence [4], high-performance

*Corresponding Author Institutional Email: *norouzi@khayam.ut.ac.ir* (P. Norouzi)

Please cite this article as: M. Asgharian Marzabad, B. Jafari, P. Norouzi, Determination of Riboflavin by Nanocomposite Modified Carbon Paste Electrode in Biological Fluids Using Fast Fourier Transform Square Wave Voltammetry, International Journal of Engineering (IJE), IJE TRANSACTIONS C: Aspects Vol. 33, No. 9, (September 2020) 1696-1702

chromatography (HPLC) [5] coupled with fluorometric [6] or ultraviolet, voltammetry, surface plasmon resonance (SPR), fluorescence, and spectrophotometry [1]. Although, these methods having their own advantages, they mostly are time-consuming, exclusive instruments, and include intricate sample preparation and procedures. Today, modern electrochemical determination techniques are more striking due to their unique properties like being low-cost, having high sensitivity, long-term reliability and reproducibility [7]. In addition, it is proved that combining classic electrochemical techniques such as SWV with fast Fourier transform (FFT) could successfully lead to gain higher sensitivity compared with using the conventional technique. Based on literature [8], the electro-reduction of Riboflavin is a reversible process including two electrons and two protons (Figure 1).

In electrochemical systems, the working electrode has known to have special place since it has a highly determinative role in the result outcome both from sensitivity and accuracy aspect. One of the most important criteria is being able to be chemically modified by vast range of nanomaterial types. Among all carbon based nanomaterials, graphene, graphene oxide and reduced graphene oxide (RGO) due to their mechanical, chemical and electronic approaches are the center of focus nowadays [9-11]. However, aggregating and stacking of the layers of RGO is known as one of disadvantages [12]. Due to this reason, the presence of oxide state of nanomaterials like samarium oxide could prevent this phenomenon[۱۳] by moving the layer sheets apart for specific period of time [14].

This work presents the quantitative determination of Riboflavin by a nanocomposite modified carbon paste electrode using fast Fourier transform square wave voltammetry (FFTSWV) under effective experimental optimal conditions. The obtained calibration curve was achieved and then Riboflavin was determined in some biological fluids as the real sample.

2. EXPERIMENTAL

2. 1. Chemicals and Apparatus Graphite powder with a 1–2 µm particle size (Merck) and paraffin oil (Aldrich) with high purity was used for the preparation of the carbon paste electrodes. Phosphate buffer solutions 0.1 M were prepared using potassium phosphate and D-potassium phosphate salts purchased from Merck. Moreover, for adjusting the pH value of the electrolyte solution NaOH and HCl were used that were also purchased from Merck. The Sm_2O_3 and RGO nanomaterials, which were employed as modifiers were prepared and used through the previous work [15]. A concentrated solution of Riboflavin (10^{-3} M) was obtained by dissolving the appropriate stoichiometric value into double distilled water, other solutions with less concentration values were prepared by diluting the stock solution. Due to the sensitivity of the drug and its lifetime, all solutions of the drug were stored in dark and cold place and prepared freshly every day.

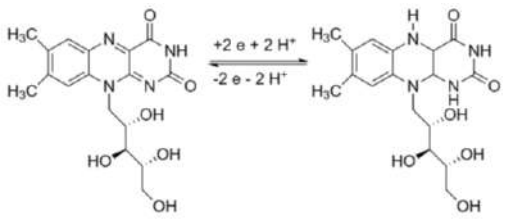

Figure 1. Chemical structure and redox reaction of Riboflavin

For the real sample analysis, human blood plasma samples were collected from a local blood products organization and stored at -20°C. After slow melting, nitric acid was added to the plasma to precipitate the proteins. Then, the mixture was stirred for 30 min and centrifuged for 10 min at 5600 rpm. The riboflavin also was purchased from a local company.

All electrochemical experiments were carried out using a homemade ultra-voltammetry system designed in center of excellence electrochemistry at University of Tehran. The setup comprised of a PC PIV Pentium 900 MHz microcomputer, equipped with a data acquisition board (PCL-818HG, Advantech. Co.), and a custom-made potentiostat connected to a PC, was assembled with an analog to digital (A/D) board. All data acquisition and data processing programs were developed in Delphi 6® program software environment [16]. Also, the employed electrochemical system contained an Ag/AgCl as the reference electrode, a pencil graphite as the counter electrode and modified carbon paste electrodes as the working electrode.

2. 2.Carbon Paste Electrode Preparation The bare carbon paste electrode was prepared by mixing a certain amount of graphite powder and the paraffin oil (7:3 w/w) and the modified one was reached through mixing the graphite powder, 300 µL of modifier with the same amount of the oil. In the case of making the modified electrode, the paste materials were sonicated for 15 minutes to spread the materials more appropriately. Besides, in order to have a uniform paste it was then mixed thoroughly with the certain amount of oil for 10 minutes. The paste was then packed into a plastic syringe. The electrical contact was made by copper wire inserted into the opposite end. The surface of all CPEs was polished on a soft clean paper and rinsed with double distilled water prior to each measurement.

3. RESULT AND DISCUSSION

3. 1. Electrochemical Behavior Study of Riboflavin To perform electrochemical measurements of Riboflavin, selecting the best composition of the electrode material is very important. Figure 2 shows the current changes in terms of different percentages of modifiers in Riboflavin 1.0×10^{-4} M in PBS 0.1M at pH=7.2 using cyclic voltammetry. Therefore, the Sm_2O_3/RGO (2:1) modified CPE had higher sensitivity for the electrochemical determination of Riboflavin and this composition was selected for further steps.

3. 2. Electrode Surface Characterization Field emission scanning electron microscopy (FESEM) was used for investigation of the surface of bare and nanocomposite modified carbon paste electrodes. FESEM images of bare (a) RGO (b) and Sm_2O_3/RGO (2:1) (c) modified electrodes are shown in Figure 3. As shown in this figure, nanoparticles could fill the holes in the bare electrode surface and distributed uniformly through the whole of electrode surface. Samarium oxide nanoparticles also could fill the empty space between graphene single layers and prevent the restacking of the RGO sheets. Hence, using these nanocomposite has effecitvely increased the electrode surface. The scattering pattern of carbon, oxygen, and samarium were shown in Figure 4. These images clearly indicate presence of samarium oxide in the electrode. Also, Table 1 shows the EDX analysis resulted in from the related SEM image for the nanocomposite modified CPE.

3. 3. Effective Parameters

3. 3. 1. Effect of pH Due to the dependence of the redox reaction mechanism of Riboflavin to pH value of the reaction solution, the pH effect was studied in the value range of 3.2 to 8.2. As shown in Figure 5, by increasing the pH of the solution from 3.2 to 7.2, the potential of the cathodic and anodic peaks were shifted to more negative ones, and the current response of the cathodic and anodic peaks increased as well. In the case

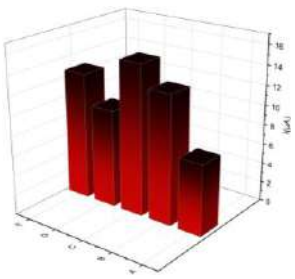

Figure 2. Current changes of different type of CPEs A: Bare CPEs, B: RGO, C: Sm_2O_3/RGO (2:1), D: Sm_2O_3/RGO (1:1) and E: Sm_2O_3/RGO modified CPEs (1:2) in Riboflavin solution 1×10^{-4} M in PBS at pH=7.2 at scan rate of 10 mV/s

TABLE 1. EDX Analysis obtained from the nanocomposite modified CPE SEM image

Element	W%	A%
C	84.07	91.47
O	9.79	8.00
Sm	6.14	0.53
	100.00	100.00

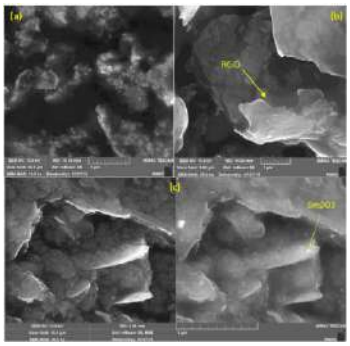

Figure 3. SEM images of bare CPE (a), the RGO modified CPE (b) and Sm_2O_3/RGO (2:1) modified CPE (c)

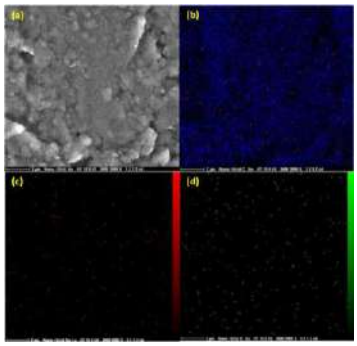

Figure 4. (a) SEM image of the nanocomposite modified CPE used for map analysis, disperse pattern of carbon (b), samarium (c), oxygen (d)

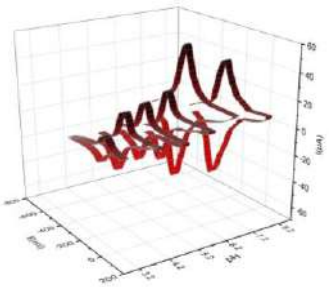

Figure 5. Effect of pH on the redox reaction of Riboflavin solution 1×10^{-4}M

of alkaline solutions, Riboflavin structure could have been destroyed and absorption would be increased due to the protonation process ehnacement [17]. Also, the anodic and cathodic peaks shifted toward positive potentials, and the current intensity decreased and it totally disappeared in more alkaline solutions. Regarding the current intensity in these voltammograms at various pH values, PBS with pH=7.2 was selected as optimum pH value.

The potential of electrochemical reaction of Riboflavin observes the following equation

$$E'_{ox} = E_{ox} - (2.303mRT/2F)pH \quad (1)$$

In which, m, R, T, F and E_{ox} are number of electrons involved in the reaction, universal gas constant, temperature, Faraday constant and potential of oxidation at pH=0, respectively. Hence we expected E'_{ox} to be changed linearity as a function of pH. The linear relationship for the reduction process was also observed.

Oxidation-reduction of Riboflavin in different pH values shows that by increasing the pH, the redox peaks shifted to more negative potential values. The obtained experimental results are in agreement with the theorical principles of redox reactions, which suggested that both of the half-electrochemical reactions followed the same mechanism of proton transfer [18, 19].

3. 3. 2. Scan Rate Effect In order to investigate the scan rate effect on the experimental system, the response of the nanocomposite modified CPE in 1.0×10^{-4}M Riboflavin in PBS (pH=7.2) was exposed to the various scan rates in the range of 1–12mV/s. As shown in Figure 6(a) the current intensity of the cathodic and anodic peak was increased by enhancing the scan rate from 6.2 to 14.3 and 6.0 to 16.4, respectively. The nanocomposite modified CPE showed the maximum current value at scan rate of 10 mV/s. In addition, as Figure 6(b) presents, linear relationship between I_{pa}, I_{pc} *vs.* square root of scan rate. This linear relationship could be the indication of diffusion-controlled behavior of Riboflavin electrochemical, which is essential for the quantitative measurements.

3. 4. FFTSWV Measurements In this step, the measurement applicability of the nanocomposite modified CPE was studied. Prior to the step, in order to reach the maximum efficiency, the electrochemical technique parameters such as frequency and amplitude were investigated and optimized.

3. 4. 1. Frequency And Number of Cycles Effect Since every redox reaction at the electrode surface has kinetic limitation, the rate of applied potential can be considered as a key factor for the method sensitivity. The applied potential rate is highly dependent on the frequency range of the amplitude [20]. On this approach, frequency was changed in the range of 88-1420Hz and the result is shown in Figure 7(a). Although the sensitivity could be increased at higher frequencies, but it was also limited by some parameters such as solution resistance and electrode diameter as well. On the other hand, the capacitance could be increased in the same manor. The frequency in square wave voltammetry has the same role as the sweep rate in cyclic voltammetry so, as expected as it increased, the scanning time and current enhanced, but in frequencies higher than 1420 Hz, due to the electrode capacitance, the peak was broaden. Therefore, frequency of 1420 Hz was selected for quantitative measurement of Riboflavin.

One of the advantages of the FFTSWV method is the ability to apply multiple cycles in each step of the potential. By changing the number of cycles, it would be possible to average the obtained data and record the result. Averaging the obtained data could successfully increase the signal-to-noise ratio. As shown in Figure 7(b), by enhancing the number of cycles from 2, the electrode response decreased due to the occurrence of the very fast redox reaction of Riboflavin at the electrode surface. Besides, the decrease in response could be allotted to the surface saturation and reduced active sites.

3. 4. 2. Effect of Accumulation Time and Potential From another point of view, the sensitivity of electrochemical systems depends on the

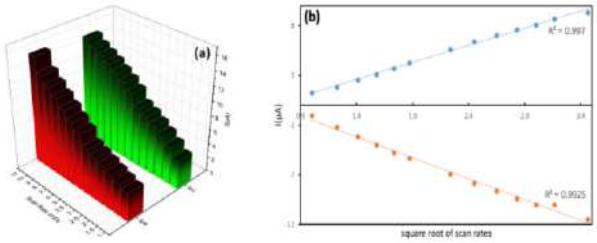

Figure 6. (a) The electrode response for cathodic and anodic peaks based on different scan rates and (b) anodic and cathodic currents *vs.* square root of scan rate for Riboflavin solution 1×10^{-4} M in PBS pH=7.2

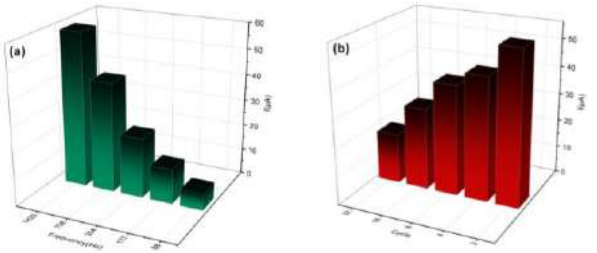

Figure 7. Effect of frequency (a) and number of cycles (b) on redox reaction of Riboflavin solution 1×10^{-4} M at pH=7.2

preconcentration of the analyte through physical, chemical, and electrochemical adsorption. On this basis, if the optimum time is not given to the analyte to be accumulated at the electrode surface, the outcome response would be decreased and if accumulation time is considered much more than the optimum value, the electrode response would also decrease due to the saturation of the species at the electrode surface.

To investigate the effect of these parameters, the accumulation potential and time were changed from -1400 to +800 mV in the range of 0.1 to 0.5 s, respectively for Riboflavin 1.0×10^{-4} M of in PBS at pH=7.2. As shown in Figure 8, the accumulation time of 0.2s and potential of +400mV were selected as the optimum values (Figure 8).

3. 4. 4. Effect of Amplitude In FFT measurements, factor of amplitude, as well as frequency, is one of the effective parameters in the electrode response, background noise and voltammogram peak width [21]. To investigate the effect of amplitude, it was changed in the range of 10-40mV. The results showed that the electrode response was increased by increasing the amplitude value up to 20mV and after that, in more amplitude values, the electrode response decreased, so the 20mV was selected as the optimized amplitude for the next steps.

3. 5. The Calibration Curve In order to evaluate the measurement applicability of the nanocomposite modified CPE in Riboflavin determination, the concentration series of Riboflavin in the range of 0.06 to 100000 nM was prepared in PBS pH = 7.2 and the electrode was exposed to them and the related signal was recorded. As shown in Figure 9, there were two linear regions of response, the first region was related to high concentrations, so had less sensitivity and was not been considered, and the second region was associated with low concentrations of Riboflavin. One of the other important criterias in determination is the relative standard deviation (RSD) percentage that was 1.2% for5 times determination and was calculated through the following equation:

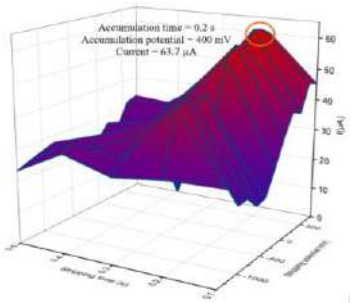

Figure 8. Effect of accumulation time and potential for Riboflavin solution 1×10^{-4} M in PBS 0.1 M at pH=7.2

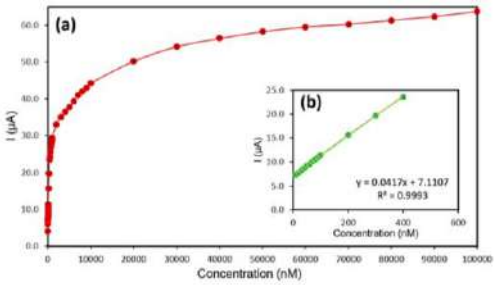

Figure 9. Calibration curve of Riboflavin in PBS 0.1 M at pH=7.2, frequency 1420 Hz, accumulation time 0.2 s, accumulation potential +400 mV, cycles 2 and amplitude 20 mV

$$\%\mathrm{RSD} = {}^{s}/_{\bar{x}} \times 100 \quad (2)$$

Where s is standard deviation and $\bar{x}$ is the mean of the data.

Also, the detection limit of 0.86nM was calculated for 10-400 nM linear range (R^2 =0.9993) using the equation below:

$$\mathrm{LOD} = 3\,S_b/m \quad (3)$$

where S_b is the standard deviation obtained from the PBS without Riboflavin and m is the slope of the calibration curve.

Furthermore, Table 2 shows the limit of detection of some recent methods employed for Riboflavin determination. As it can be seen, the proposed electrode and the used electrochmeical method in this study has provided acceptable detection limit compared with the other methods besides, the obtained linear range was wide in low concentration values and the proposed method procedure was much more simple.

3. 6. The Real Sample Analysis The purpose of this step is to demonstrate the feasibility of the proposed method for measuring Riboflavin in some biological environments. Real sample analysis and the experiment was done using standard addition method. Based on the

TABLE 2. Riboflavin determination results in comparison with some recent applied methods

Method	Detection Limit	Linear Range	Ref.
CV[a]-with modified CPE	7.1 µM	1.7-34 µM	[22]
DPV[b]with modified GCE[c]	0.027µM	2.0-110 µM	[23]
SWAdSV[d]-with BiFE[e]	0.1 µM	1.0-9.0 µM	[24]
SWV-with SMDE[f]	0.1 µM	-------	[25]
FFT-SWV	0.86 nM	10-400 nM	This work

[a]: Cyclic voltammetry, [b]: differential pulse voltammetry, [c]: glassy carbon electrode, [d]: square wave adsorptive stripping voltammetry, [e]: bismuth film electrode, [f]: static drop mercury electrode

method, the first sample contained no added volume of standard solution of Riboflavin. Then, for other samples, constant values of Riboflavin in the biological sample were considered and the fianl concentration for each sample was reached by adding various volumes of standard solution of Riboflavin. Finally, each solution response was recorded as mentioned in previous sections. As shown in Table 3, the added and found values besides the relative standard deviation and the recovery percents are available. Appropriate results indicated that the proposed electrode had high selectivity to determine Riboflavin in complex biological matrices.

TABLE 3. Results of drug measurement in plasma

No.	Added (nM)	Founded (nM)	Number of runs	Recovery (%)	RSD (%)
1	0	20.2	3	-	-
2	80	92.5	3	115.6 %	3.1 %
3	200	215.2	3	107.6 %	3.9 %
4	300	319.7	3	106.5 %	2.9 %

4. CONCOLUSION

In the present study Riboflavin was determined by Sm_2O_3/RGO nanocomposite modified carbon paste electrode under optimized experimental conditions using FFTSWV. The nanocomposite proved to have uniformed structure and successfully catalyzed Riboflavin redox reaction at the electrode surface. Furthermore, based on the obtained results, a wide linear range of response in low concentrations were obtained and also the detection limit of 0.863 nM was achieved. The proposed electrode in combination with the developed electrochemical determination technique was shown to have simplicity of procedure, non-toxic besides having appropriate sensitivity and accuracy, while having adequate performance ability in Riboflavin determination specifically in some biological complex matrices.

5. REFERENCES

1. Khaloo, S.S., Mozaffari, S., Alimohammadi, P., Kargar, H. and Ordookhanian, J., "Sensitive and selective determination of riboflavin in food and pharmaceutical samples using manganese (iii) tetraphenylporphyrin modified carbon paste electrode", ***International Journal of Food Properties***, Vol. 19, No. 10, (2016), 2272-2283. https://doi.org/10.1080/10942912.2015.1130054.
2. Karimian, F., Rounaghi, G. and Mohadeszadeh, M., "Electrochemical determination of riboflavin using a synthesized ethyl [(methythio) carbonothioyl] glycinate monolayer modified gold electrode", ***Journal of Analytical Chemistry***, Vol. 71, No. 10, (2016), 1057-1062. https://doi.org/10.1134/S1061934816080062.
3. Ensafi, A.A., Heydari-Bafrooei, E. and Amini, M., "DNA-functionalized biosensor for riboflavin based electrochemical interaction on pretreated pencil graphite electrode", ***Biosensors and Bioelectronics***, Vol. 31, No. 1, (2012), 376-381. https://doi.org/10.1016/j.bios.2011.10.050.
4. Wang, M., Zhao, L., Liu, M. and Lin, J.-M., "Determination of riboflavin by enhancing the chemiluminescence intensity of peroxomonosulfate–cobalt (ii) system", ***Spectrochimica Acta Part A: Molecular and Biomolecular Spectroscopy***, Vol. 66, No. 4-5, (2007), 1222-1227. https://doi.org/10.1016/j.saa.2006.06.010.
5. Petteys, B.J. and Frank, E.L., "Rapid determination of vitamin b2 (riboflavin) in plasma by hplc", ***Clinica Chimica Acta***, Vol. 412, No. 1-2, (2011), 38-43. https://doi.org/10.1016/j.cca.2010.08.037.
6. Hodson, A. and Norris, L., "A fluorometric method for determining the riboflavin content of foodstuffs", ***Journal of Biological Chemistry***, Vol. 131, (1939), 621-630.
7. Yu, Y.-Y., Wang, J.-X., Si, R.-W., Yang, Y., Zhang, C.-L. and Yong, Y.-C., "Sensitive amperometric detection of riboflavin with a whole-cell electrochemical sensor", ***Analytica Chimica Acta***, Vol. 985, (2017), 148-154. https://doi.org/10.1016/j.aca.2017.06.053.
8. Gu, H.-Y., Yu, A.-M. and Chen, H.-Y., "Electrochemical behavior and simultaneous determination of vitamin b2, b6, and c at electrochemically pretreated glassy carbon electrode", ***Analytical Letters***, Vol. 34, No. 13, (2001), 2361-2374. https://doi.org/10.1081/AL-100107301.
9. Resmi, P., Palaniayappan, A., Ramachandran, T. and Babu, T.S., "Electrochemical synthesis of graphene and its application in electrochemical sensing of glucose", ***Materials Today: Proceedings***, Vol. 5, No. 8, (2018), 16487-16493. https://doi.org/10.1016/j.matpr.2018.06.001.
10. Rao, C., Biswas, K., Subrahmanyam, K. and Govindaraj, A., "Graphene, the new nanocarbon", ***Journal of Materials Chemistry***, Vol. 19, No. 17, (2009), 2457-2469. https://doi.org/10.1039/B815239J.
11. Zaidi, S.A., "Graphene: A comprehensive review on its utilization in carbon paste electrodes for improved sensor performances", ***International Journal of Electrochemical Science,*** Vol. 8, (2013), 11337-11355.
12. Lv, H., Shen, X., Ji, Z., Chen, K. and Zhu, G., "One-pot synthesis of prpo 4 nanorods–reduced graphene oxide composites and their photocatalytic properties", ***New Journal of Chemistry***, Vol. 38, No. 6, (2014), 2305-2311. https://doi.org/10.1039/C3NJ01261A
13. Ling, Q., Yang, M., Rao, R., Yang, H., Zhang, Q., Liu, H. and Zhang, A., "Simple synthesis of layered CeO_2–graphene hybrid and their superior catalytic performance in dehydrogenation of ethylbenzene", ***Applied Surface Science***, Vol. 274, (2013), 131-137. https://doi.org/10.1016/j.apsusc.2013.02.129.
14. Adachi, G.-y. and Imanaka, N., "The binary rare earth oxides", ***Chemical Reviews***, Vol. 98, No. 4, (1998), 1479-1514. https://doi.org/10.1021/cr940055h.
15. Dezfuli, A.S., Ganjali, M.R., Jafari, H. and Faridbod, F., "Samaria/reduced graphene oxide nanocomposites; sonochemical synthesis and electrochemical evaluation", ***Journal of Materials Science: Materials in Electronics***, Vol. 28, No. 8, (2017), 6176-6185. https://doi.org/10.1007/s10854-016-6296-1.
16. Marzabad, M.A., Norouzi, P. and Ebrahimi, M., "Electrochemical determination and recovery of copper ion in water samples by supported liquid membrane using 2-amino-n-

(2-pyridylmethyl)-benzamide as carrier", ***Analytical Bioanalytical Electrochemistry***, Vol. 11, No. 2, 2019, 137-149.

17. Berchmans, S. and Vijayavalli, R., "Surface modification of glassy carbon by riboflavin", ***Langmuir***, Vol. 11, No. 1, (1995), 286-290. https://doi.org/10.1021/la00001a048.
18. Jabbar, M.A., Salahuddin, S., Mahmood, A.J. and Mannan, R.J., "Voltammetric evidences for the interaction of riboflavin with cadmium in aqueous media", ***Journal of Saudi Chemical Society***, Vol. 20, No. 2, (2016), 158-164. https://doi.org/10.1016/j.jscs.2012.06.005.
19. Bandžuchová, L., Šelešovská, R., Navrátil, T., Chýlková, J. and Novotný, L., "Voltammetric monitoring of electrochemical reduction of riboflavin using silver solid amalgam electrodes", ***Electrochimica Acta***, Vol. 75, (2012), 316-324. https://doi.org/10.1016/j.electacta.2012.05.009.
20. Bonazzola, C. and Gordillo, G., "Advanced analysis for electrode kinetic studies of surface reactions by applying square-wave voltammetry", ***Electrochimica Acta***, Vol. 213, (2016), 613-619. https://doi.org/10.1016/j.electacta.2016.07.137.
21. Kounaves, S.P. and Young, J.B., "Carbon fiber electrode cell for square wave voltammetric detection of biogenic amines in high-performance liquid chromatography", ***Analytical Chemistry***, Vol. 61, No. 13, (1989), 1469-1472. https://doi.org/10.1021/ac00188a035.
22. Nezamzadeh-Ejhieh, A. and Pouladsaz, P., "Voltammetric determination of riboflavin based on electrocatalytic oxidation at zeolite-modified carbon paste electrodes", ***Journal of Industrial and Engineering Chemistry***, Vol. 20, No. 4, (2014), 2146-2152.
23. Huang, D.-Q., Wu, H., Song, C., Zhu, Q., Zhang, H., Sheng, L.-Q., Xu, H.-J. and Liu, Z.-D., "The determination of riboflavin (vitamin b-2) using manganese dioxide modified glassy carbon electrode by differential pulse voltammetry", ***International Journal of Electrochemical Science***, Vol. 13, No. 9, (2018), 8303-8312. https://doi.org/10.20964/2018.09.02.
24. Sá, É.S., da Silva, P.S., Jost, C.L. and Spinelli, A., "Electrochemical sensor based on bismuth-film electrode for voltammetric studies on vitamin b2 (riboflavin)", ***Sensors and Actuators B: Chemical***, Vol. 209, (2015), 423-430. https://doi.org/10.1016/j.snb.2014.11.136.
25. Çakir, S., Atayman, İ. and Çakir, O., "Simultaneous square-wave voltammetric determination of riboflavin and folic acid in pharmaceutical preparations", ***Microchimica Acta***, Vol. 126, No. 3-4, (1997), 237-240. https://doi.org/10.1007/BF01242327.

Persian Abstract

چکیده

برای بررسی رفتار الکتروشیمیایی و اندازه‌گیری ریبوفلاوین در سطح الکترود خمیر کربن اصلاح شده از روش ولتامتری عاری‌سازی موج مربعی با تبدیل فوریه استفاده شد. برای بهبود حد تشخیص، الکترود خمیر کربنی با نانوکامپوزیت ساماریم اکساید/گرافن اکساید کاهش یافته با نسبت ۲ به ۱ اصلاح گردید. مطالعات ولتامتری چرخه‌ای نشان داد ویتامین $B2$ در بافر فسفاتی در یک فرآیند انتقال الکترون برگشت پذیر تحت کنترل نفوذ شرکت می‌کند و پتانسیل اکسایش-کاهش به pH محیط بستگی دارد. برای بهبود حد تشخیص و افزایش حساسیت اندازه‌گیری به بهینه‌سازی پارامترهای موثر در اندازه‌گیری پرداخته شد. شرایط بهینه اندازه‌گیری در فرکانس موج مربعی ۱٤۲۰ هرتز، زمان تجمع ۲/. ثانیه، پتانسیل تجمع ٤۰۰ میلی ولت و دامنه موج مربعی ۲۰ میلی ولت بدست آمد. ناحیه خطی برای ریبوفلاوین ٤۰۰-۱۰ نانومولار با حد تشخیص ۸٦/. نانو مولار می‌باشد.

International Journal of Engineering

Journal Homepage: www.ije.ir

Experiments on Coupled Technique for Adjacent Similar Buildings

U. Ramakrishna*, S. C. Mohan

Department of Civil Engineering, BITS Pilani Hyderabad Campus, Hyderabad, Telangana, India

P A P E R I N F O

Paper history:
Received 09 April 2020
Received in revised form 29 June 2020
Accepted 04 August 2020

Keywords:
Similar Building
Structural Coupling
Bracing
Viscoelastic Damper
Shake Table

A B S T R A C T

Increasing the population, urbanization has led to rapid construction of buildings. Due to space constraints and an increase in land cost, these buildings are built too close to each other and can cause damage under dynamic actions such as earthquakes. A new technique, known as structural coupling, has been developed recently, has found very effective in dissipating the dispersive vibrations. So far using coupling technique, adjacent dissimilar buildings are connected through a coupling device, such that it can reduce the dynamic response of the structure. The application of the structural coupling technique becomes challenging for similar buildings due to their in-phase behavior under dynamic loads. In the current research, the seismic performance of similar buildings with the coupling technique is experimentally tested on a shake table. A three storey model has been simulated using a unidirectional shake table with the scaled ground motion. Similar building construction uncertainties are accounted for in the study with slight variations in their dynamic properties. The connection devices used are bracings and passive viscoelastic dampers. The results obtained confirm the effectiveness of structural coupling technique with various configurations of dampers for similar buildings over seismic protection individual buildings.

***doi**: 10.5829/ije.2020.33.09c.02*

1. INTRODUCTION

Earthquakes are highly unpredictable in their frequency place and time of occurrence. The main reason for the failure of buildings during an earthquake is due to inadequate design to resist seismic forces. All buildings in seismic zones should be constructed by following the design codes, so that, the damage could be minimized and catastrophic failure can be avoided during the aseismic event. Thence, the behavior of buildings during an earthquake needs to be studied in advance to formulate such design. The seismic performance of a building is defined as the measure of recorded or expected ability of the structure to sustain due functions (safety and serviceability) during and after the earthquake. The damage and other parameters of the building during the earthquake depends on a number of factors. One of the main factors is the response of the building to the ground motion. The response involves the following parameters, deformation, velocity, and acceleration demands of structural components of the building. The parameters which can be considered for estimation of seismic performance of buildings are residual storey drift ratio, peak floor velocity, floor acceleration, and peak story drift ratio at every floor in the corresponding direction [1]. Usually, a set of buildings that serve the same facilities, such as educational institutes, residential quarters, etc., are often have identical structural designs and are built adjacent to each other, which makes them dynamically similar to each other. Seismic protection provided individually to each building is uneconomical. Rather, structural coupling technique can effectively reduce the seismic response of buildings simultaneously proves to be economical. From the past earthquake case studies [2], it can be clearly seen that the dynamically similar buildings also undergo damage during an earthquake. Hence, it is very important to study the possibility of improving the seismic behavior of dynamically similar buildings economically.

Pounding behavior in buildings which are adjacent to each other during the earthquakes causes serious damage and ultimate fatality. To prevent these, researchers have

*Corresponding Author Institutional Email: *p20170409@hyderabad.bits-pilani.ac.in* (U. Ramakrishna)

Please cite this article as: U. Ramakrishna, S. C. Mohan, Experiments on Coupled Technique for Adjacent Similar Buildings, International Journal of Engineering (IJE), IJE TRANSACTIONS C: Aspects Vol. 33, No. 9, (September 2020) 1703-1709

proposed to connect the adjacent structures using a connected control technique known as structural coupling technique. It has found to be very efficient in minimizing seismic response between two adjacent structures. The seismic behaviour of adjacent structures with similar and dissimilar dynamic characteristics, subjected to five different seismic excitations [3]. The study concluded that the effect of pounding from adjacent buildings on the seismic behavior of a structure is more pronounced for the end structures in a row. The effect of collision of adjacent buildings in series is numerically studied for different separation distances. Three alignment configurations under nine ground motions, the obtained responses are compared with the no pounding case [4]. The seismic interaction between adjacent buildings that are a part and non-symmetric in the plan may pound each other because of significant torsional oscillations [5]. In order to overcome the pounding effect on dissimilar buildings, many studies are carried out with connected control techniques. The connected control technique with the rigid links helps to avoid the pounding effect between two dissimilar buildings [6]. A fluid damper connected to the adjacent buildings has been simulated under ground excitation and has concluded that it is the best way for protection of flexible building structures [7]. Another study compared the efficiency of active and passive coupled building control for flexible adjacent dissimilar buildings [8]. But all the above research was limited to dynamically dissimilar buildings. A straight damper connection between dynamically similar buildings is thought to be inefficient as the motion of both the structures will be in the same direction. Few studies have found where behavior has been studied with the combination of coupling technique and other isolation techniques. The behavior of the two similar coupled building was studied with one building base-isolated, and others coupled with viscoelastic dampers. Three cases (both the buildings were fixed at the base, one fixed at the base, and other base-isolated, both the buildings isolated) were studied [9]. It was concluded that the system would be most effective when one building is base-isolated and the other is fixed. Also, this hybrid method was found to be effective in controlling the response under a long duration earthquake as well as a near-fault earthquake. The same hybrid method was adopted to study the seismic performance of podium structures and two similar moment-resisting frames that are isolated at the base [10, 11].

Further, the buildings are connected through passive dampers. This approach enabled the simultaneous optimization of the control performance and the control cost [12]. Few studies were conducted on the modeling of magnetorheological (MR) damper in control studies of adjacent buildings [13, 14]. These studies show the effective use of such damper in this application of coupled technique. All the above research focuses on making one of the similar buildings dissimilar by providing base isolation or bracing and then connecting those using straight dampers. This hybrid technique is uneconomical as one of the buildings has to be made dissimilar, and then dampers need to be connected. However, coupling techniques can also be adapted to dynamically similar structures with different damper configurations without putting an extra cost on making one of the buildings dissimilar.

The most commonly used passive control damper, which increases the structural damping and dissipating the vibration, is the viscoelastic damper [15]. Most of the research carried out in the past two decades focused on characterizing the VE material properties using a series of harmonic tests at different strain amplitudes, frequencies, and temperatures [16, 17]. A higher-order fractional derivative model can be used to simulate the mechanical behavior of viscoelastic (VE) dampers. This model describes the effects of environmental temperature and excitation frequency with different VE materials [18]. The study on seismic response of a scaled steel structure with added VE dampers shows that VE dampers are very effective in reducing excessive vibration of the test structure due to seismic excitation [19]. Fatigue analyses of buildings with viscoelastic dampers were carried out to reduce the dynamic response of the structure effectively [20, 21]. The analytical and experimental studies were carried out for plan asymmetric structures with viscoelastic dampers [22]. It demonstrated that VE dampers could control the response of asymmetric structures. A steel frame was simulated experimentally with a viscoelastic damper [23]. It was observed that the response of the model reduced as per the design standard. Similarly, another type of viscoelastic damper was used in a structural application to improve seismic performance [24]. Few studies were carried out to verify the coupling technique of adjacent buildings. The seismic performance of VE damper connected coupled buildings was experimentally studied on two adjacent two-degree freedom buildings models [25]. In order to understand the vibration control effect, the earthquake response of connected single-degree-of-freedom (SDOF) building models using hysteresis dampers was studied analytically and experimentally [26]. The study of the coupled buildings was concluded that the dynamic properties and the connector properties influence the behavior of the coupling technique [27]. Also the seismic performance of structure with various connecting devices were studid to reduse the dynamic response [28-33].

The above experimental works are limited to dissimilar building models and SDOF similar buildings models. The numerical and experimental studies have demonstrated the feasibility of these strategies. From the reviews mentioned above, it can be seen that the mechanical and geometrical properties of the buildings and the connectors influence the efficiency of the

coupling technique. In the present study, the potential of the coupling technique has been evaluated for similar adjacent structures when subjected to earthquake motion. Bracings and viscoelastic dampers are used as a connecting element between two adjacent structures. The efficiency of the coupled control method for similar structures entirely depends on the orientation and configuration of connecting elements. Hence, the present study focuses on the effect of connecting elements configuration on seismic control of dynamically similar buildings using the coupled technique.

2. METHODOLOGY

Initially, a numerical analysis has been carried out to finalize the geometrical and mechanical properties of the model. For the fabrication and for validation of the numerical model, the model updating technique was used to correlate the natural frequencies and vibrational modes. This is to ensure that physical behavior is obtained in terms of numerical models. This correlation can be used to obtain the different geometrical and mechanical properties of the model as well as the connector. This analysis was carried out in Sap2000. Then, the uncoupled models were simulated on the shake table subjected to scaled ground motion, and the acceleration data were obtained with accelerometers. Subsequently, the models were coupled using a brace and viscoelastic damper between first and second floors in the structure and subjected to scaled earthquake excitation. Finally, these results were analyzed to verify the effectiveness of the coupling technique to reduce the seismic response of similar structures.

3. STRUCTURAL MODELING

A scaled model of a multi-storied frame structure is fabricated as steel frames and mounted on the shake table. Accelerometers are placed at different levels to record the dynamic response under earthquake loading. Through experimental testing, the natural frequency of the fabricated test models is obtained. Also, the test structure is modeled through the numerical tool, and the numerical model is being updated to match the experimental results.

3. 1. 3D Frames Models Two framed buildings models of each three-story are fabricated using steel sections and combined with brace/damper, as shown in Figure 1. Each model has plan dimensions of 0.8m × 0.6m. The height of each floor is 0.6m and has three floors. The beams and columns are chosen from mild steel tubular square section with 20mm × 20mm × 1.8mm. Each floor is fabricated with a steel plate of 6mm thick welded to the floor beams. As per the above model dimensions, the mass and stiffness properties of the experimental model is considered for dynamic analysis. Both building models are fixed on a solid shake table mount, and hence the assumption of no soil-structure interaction is valid. Though the same geometric and material properties for both the buildings are considered at the design stage, their dynamic properties may slightly vary due to practical uncertainty in the construction stage. The allowance for such slight variations is accounted for in scaled building models during fabrication by procuring materials from different sources.

3. 2. Shake Table and Data Acquisition System In order to simulate the base movement for the small-scale building models, the unidirectional shake table is used. The shake table with actuator specifications are given in Table 1.

A compact data acquisition (DAQ) system, NI 9234 module with a four-channel dynamic signal acquisition, is used for recording high-precision acceleration measurements. The specifications of the DAQ system are given in Table 2. This DAQ module is compatible with a single-module USB carrier and has compact hardware, ideal for field measurements.

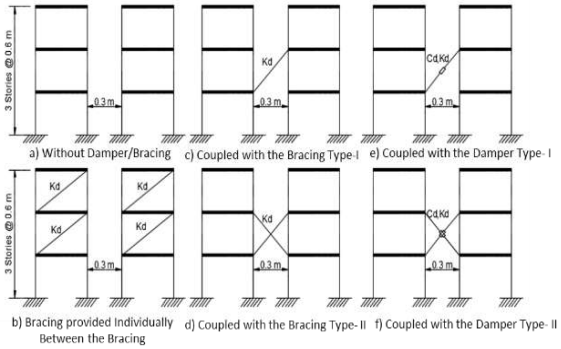

Figure 1. Different configuration coupled system

TABLE 1. Specification of the shake table system

Uni-Axial Shake Table: Size 2 m x 3 m	
Payload	12 Ton
Table maximum displacement	± 75 mm
Maximum Velocity	1 m/s
Maximum Acceleration	3g
Frequency	0 to 100 Hz
Actuator	
Make	MTS, USA
Capacity	250 kN
Stroke	± 75 mm

TABLE 2. Data acquisition system

Product Name	NI 9234
Signal Ranges	±5 V
Channels	4
Sample Rate	51.2 kS/s/ch
Input Configurations	IEPE with AC Coupling, AC Coupling, DC Coupling
Noise at Maximum Sample Rate	50 μVrms
Connectivity	BNC

LabVIEW software[2] interface is used for processing the recorded signals. High sensitivity accelerometers for seismic applications are used for recording the acceleration response of building models, and their specifications are given in Table 3.

3. 3. Passive Control Device–Brace and Viscoelastic Damper As a connecting element, a brace and viscoelastic dampers are used as passive control devices. The bracing element is chosen from mild steel solid square section with 10mm × 10mm and length as per between connecting joints. The locally available viscoelastic dampers (Figure 2) are used as a connecting element. The dimensions of the viscoelastic damper are also shown in Figure 2 with length as per between connecting joints. The viscoelastic material is made up of natural rubber with hardness 45-55 as per the vendor's specification[3]. These connecting elements are installed within individual structures, between two structures, and their performance under seismic excitation is studied. In numerical modelling, the mass of these link elements is ignored.

TABLE 3. Specification of Uni-Axial accelerometer

Model	PCB-393B04
Measuring range	5 g
Sensitivity	1,000 mV / g,
Frequency range	0.06 - 450 Hz
Frequency	Up to 100 Hz

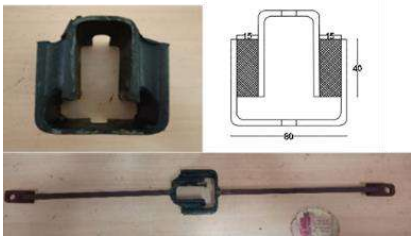

Figure 2. Viscoelastic dampers

[2] https://www.ni.com/en-in/innovations.html

4. RESULTS AND DISCUSSIONS

4. 1. Dynamic Properties of 3D Frame Models The fabricated building models are fixed on the shake table, tested using impact hammer, and the response at the top floor is measured using accelerometers. The time history response signal is post-processed in the frequency domain to obtain the dynamic properties of building models. The obtained first three natural frequencies and corresponding damping ratios are given in Table 4. The tests were repeated to rule out the possible errors during acquisition, and at most care was taken to make sure that the errors related to boundary conditions (fixity of the base) are negligible. Then, the numerical model of the building frame is updated [34] using the model updating technique to match the experimental frequencies. The initial material properties and the updated material properties of the steel used for the fabrication of building models are shown in Table 5. After updating the numerical model, the natural frequencies were compared with that of the experimental building model, as summarized in Table 4. The slight variation in natural frequencies of left and right building models were observed due to fabrication uncertainties. After the update of the model the dynamic behaviour of the numerical model is expected to replicate the real building model. The measured damping ratios of the both building frames were close to each other and very less indicating the need for external damping or bracing to control the vibration.

4. 2. Dynamic Properties of 3D Frame Models The shake table testing of building frames subjected to scaled EL-Centro (1940) ground motion is carried out. At first, the building frames without any connecting devices (Figure 4a) are tested for their seismic responses. Then each building with bracings provided individually between the floors (Figure 3b) is tested. Further, both the buildings coupled with bracings connection Type-I (Figure 3c) and bracings connection Type-II (Figure 3d) were examined. Finally, both buildings coupled with viscoelastic damper connection Type - I (Figure 3e) and viscoelastic damper connection Type-II (Figure 3f) were tested.

TABLE 4. Dynamic property of building models

Modes	Experimental frequency (Hz)		Sap2000 frequency (Hz)	Damping Ratio
	Left model	Right model		
1	5.86	5.5	5.645	0.007
2	17.93	16.813	17.372	0.005
3	31.26	28.188	28.358	0.004

[3] http://www.rsarora.com

TABLE 5. Material properties of numerical model in SAP

Model	Young's modulus (Gpa)	Density (kg/m^3)
Original	200	7850
Updated	193	7820

In all the above cases, the acceleration records at the top floor of both building models are recorded. Acceleration response data gives an indication of the effectiveness of each coupling technique in reducing seismic responses. The comparisons of the seismic response in terms of acceleration time history for all the building model cases with and without connecting links are shown in Figure 4. The seismic response of left and right building frames without any connecting devices are different due to slight variation in their dynamic properties. This behaviour was expected as the uncertainties are considered during their fabrication. The maximum acceleration response of each building cases (shown in Figure 3) has been tabulated in Table 6 along with percentage reduction with connecting links. In case of buildings provided with individual bracings, the maximum percentage of reduction in seismic response is observed compared to other cases. This is because the bracing links used in both building frames are eight in total number, whereas, in other cases only two number of link elements in total are used to for their coupling. Hence, providing bracing for individual building may be effective but becomes uneconomical. Therefore, further investigations and comparisons are done by coupling building models with two link elements. Among all the coupled building models, the maximum seismic response reduction is observed for buildings coupled with viscoelastic damper connection type-II. In this case left building response is reduced by 47% while the right building response is reduced by 25%. The considerable variation among the response of left and right building mainly attributes to unsymmetrical damper connection along with slight variation in their dynamic properties. The coupling technique is able to effectively reduce the accelerations of the two structures in the order of 20-50%

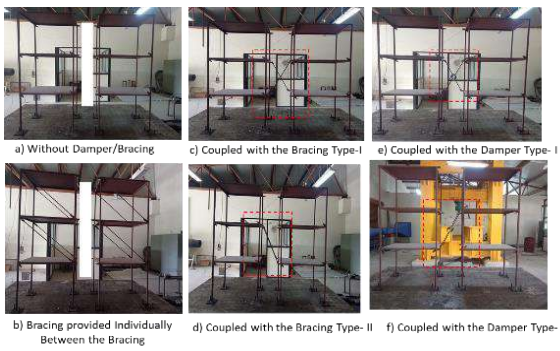

Figure 3. Relative displacement and Drift ratio plots for El-Centro ground motion

TABLE 6. The maximum acceleration response in each

ConnectionType as shown in Figure 4	Maximum Acceleration (g)		Percentage reduction (%)	
	Left building	Right building	Light building	Right building
Figure 4a	0.155	0.199	-	-
Figure 4b	0.06	0.09	61.29	54.77
Figure 4c	0.114	0.145	26.45	27.14
Figure 4d	0.091	0.155	41.29	22.11
Figure 4e	0.099	0.162	36.13	18.59
Figure 4f	0.082	0.149	47.10	25.13

with only two link elements. Further, by increasing the number of coupling link elements, the percentage reduction can be increased.

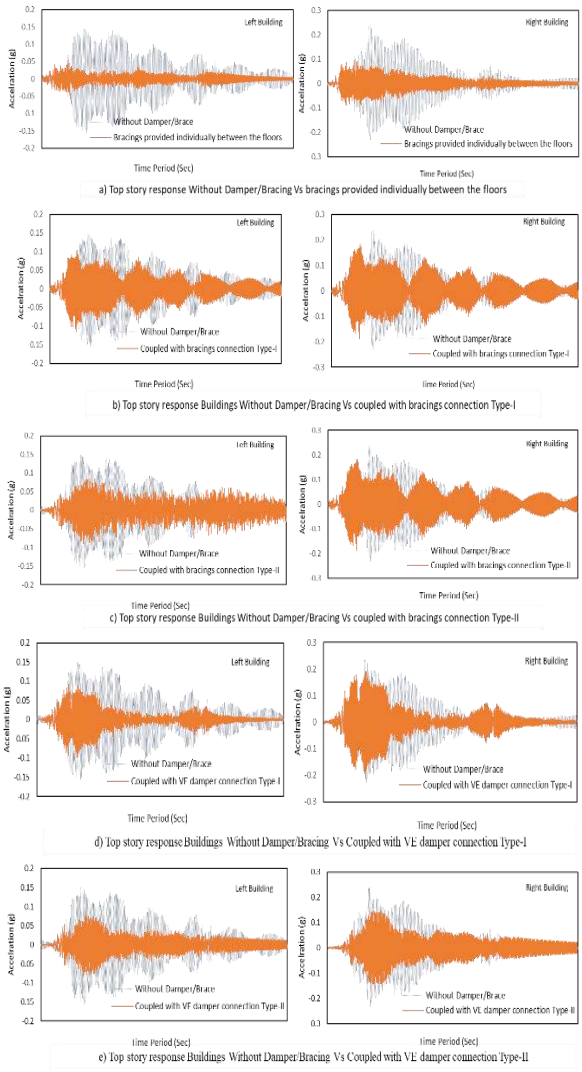

Figure 4. Acceleration record for different configuration of coupled system

5. CONCLUSION

The experiments have demonstrated the possibility of using structural coupling to control the seismic responses of both adjacent similar buildings. The effect of constructional uncertainties on dynamic properties of buildings and its consequence on coupled buildings is studied. The efficiency of the structural coupling technique is evaluated by testing the building frames on shake table excited with scaled seismic ground motions. Studies on the effects of different configurations of link elements in reducing the seismic response of similar buildings has led to interesting results. Providing bracing for both buildings individually can be effective but leads to uneconomical solution. A comparative study with different dumper configurations shows that, the alternative diagonal viscoelastic damper configurations are more effective in seismic response reduction.

By increasing the number of coupling link elements, the percentage reduction can be increased. This structural coupling technique can be extended to high-rise buildings with numerical and experimental studies. Further, study can be carried out using the updated numerical model to find the optimal location of the connecting links between the similar buildings without repeated experimental studies.

6. ACKNOWLEDGMENTS

The research described in this paper was financially supported by the “Department of science and technology (DST)-Science and Engineering Board (SERB), India.”

Also, we acknowledge the facility provided by the “Department of science and technology (DST)- Fund for Improvement of S&T Infrastructure in Higher Educational Institutions (FIST), India.”

7. REFERENCES

1. Fema, P., "58-1 (2012) seismic performance assessment of buildings (volume 1-methodology)", Federal Emergency Management Agency, Washington, Vol. 1, (2012). doi: 10.1139/l01-070.
2. Humar, J.M., Lau, D. and Pierre, J.-R., "Performance of buildings during the 2001 bhuj earthquake", ***Canadian Journal of Civil Engineering***, Vol. 28, No. 6, (2001), 979-991. doi: 10.1139/l01-070.
3. Athanassiadou, C.J., Penelis, G.G. and Kappos, A.J., "Seismic response of adjacent buildings with similar or different dynamic characteristics", ***Earthquake Spectra***, Vol. 10, No. 2, (1994), 293-317. doi: 10.1193/1.1585775
4. Raheem, S.E.A., Fooly, M.Y., Shafy, A.G.A., Taha, A.M., Abbas, Y.A. and Latif, M.M.A., "Numerical simulation of potential seismic pounding among adjacent buildings in series", ***Bulletin of Earthquake Engineering***, Vol. 17, No. 1, (2019), 439-471.
5. Karayannis, C.G. and Naoum, M.C., "Torsional behavior of multistory rc frame structures due to asymmetric seismic interaction", ***Engineering Structures***, Vol. 163, (2018), 93-111. doi: 10.1016/j.engstruct.2018.02.038
6. Passoni, C., Belleri, A., Marini, A. and Riva, P., "Existing structures connected with dampers: State of the art and future developments", in 2ECEES: 2nd European Conference on Earthquake Engineering and Seismology, Istanbul, Turkey, 24-29 August 2014, EAEE (European Association of Earthquake Engineering). (2014), 1-12.
7. Xu, Y., He, Q. and Ko, J., "Dynamic response of damper-connected adjacent buildings under earthquake excitation", ***Engineering Structures***, Vol. 21, No. 2, (1999), 135-148. , doi: 10.1016/S0141-0296(97)00154-5.
8. Christenson, R.E., Spencer Jr, B., Johnson ,E.A. and Seto, K., "Coupled building control considering the effects of building/connector configuration", ***Journal of Structural Engineering***, Vol. 132, No. 6, (2006), 853-863. doi: 10.1061/(asce)0733-9445(2006)132:6(853).
9. Matsagar, V.A. and Jangid, R.S., "Viscoelastic damper connected to adjacent structures involving seismic isolation", ***Journal of Civil Engineering and Management***, Vol. 11, No. 4, (2005), 309-322. doi: 10.1080/13923730.2005.9636362.
10. Kasagi, M., Fujita, K., Tsuji, M. and Takewaki, I., "Automatic generation of smart earthquake-resistant building system: Hybrid system of base-isolation and building-connection", ***Heliyon***, Vol. 2, No. 2, (2016), e00069. doi: 10.1016/j.heliyon.2016.e00069.
11. Fathi, F. and Bahar, O., "Hybrid coupled building control for similar adjacent buildings", ***KSCE Journal of Civil Engineering***, Vol. 21, No. 1, (2017), 265-273. doi: 10.1007/s12205-016-0708-x.
12. Park, K.-S. and Ok, S.-Y., "Hybrid control approach for seismic coupling of two similar adjacent structures", ***Journal of Sound and Vibration***, Vol. 349, (2015), 1-17. doi: 10.1016/j.engstruct.2010.03.015.
13. Bharti, S., Dumne, S. and Shrimali, M., "Seismic response analysis of adjacent buildings connected with mr dampers", ***Engineering Structures***, Vol. 32, No. 8, (2010), 2122-2133.
14. Shrimali, M., Bharti, S. and Dumne, S., "Seismic response analysis of coupled building involving mr damper and elastomeric base isolation", ***Ain Shams Engineering Journal***, Vol. 6, No. 2, (2015), 457-470. doi: 10.1016/j.asej.2014.12.007.
15. Tchamo, J.M. and Zhou, Y., "An alternative practical design method for structures with viscoelastic dampers", ***Earthquake Engineering and Engineering Vibration***, Vol. 17, No. 3, (2018), 459-473. doi: 10.1007/s11803-018-0455-8.
16. Tsai, C., "Temperature effect of viscoelastic dampers during earthquakes", ***Journal of Structural Engineering***, Vol. 120, No. 2, (1994), 394-409.
17. Shen, K., Soong, T., Chang, K. and Lai, M., "Seismic behaviour of reinforced concrete frame with added viscoelastic dampers", ***Engineering Structures***, Vol. 17, No. 5, (1995), 372-380. doi: 10.1016/0141-0296(95)00020-8.
18. Xu, Z.D., Liao, Y.X., Ge, T. and Xu, C., "Experimental and theoretical study of viscoelastic dampers with different matrix rubbers", ***Journal of Engineering Mechanics***, Vol. 142, No. 8, (2016), 04016051. doi: 10.1061/(ASCE)EM.1943-7889.0001101
19. Zhang, R.-H. and Soong, T., "Seismic design of viscoelastic dampers for structural applications", ***Journal of Structural***

Engineering, Vol. 118, No. 5, (1992), 1375-1392. doi: 10.1061/(ASCE)0733-445(1992)118:5(1375).

20. Palmeri, A. and Ricciardelli, F., "Fatigue analyses of buildings with viscoelastic dampers", ***Journal of Wind Engineering and Industrial Aerodynamics***, Vol. 94, No. 5, (2006), 377-395. doi: 10.1016/j.jweia.2006.01.005.
21. Lee, D.-G., Hong, S. and Kim, J., "Efficient siesmic analysis of building structures with added viscoelastic dampers", ***Engineering Structures***, Vol. 24, No. 9, (2002), 1217-1227. doi: 10.1016/S0141-0296(02)00058-5.
22. García, M., Juan, C. and Almazán, J.L., "Torsional balance of plan asymmetric structures with viscoelastic dampers", ***Engineering Structures***, Vol. 29, No. 6, (2007), 914-932. , doi: 10.1016/j.engstruct.2006.06.022.
23. Min, K-.W., Kim, J. and Lee, S.-H., "Vibration tests of 5-storey steel frame with viscoelastic dampers", ***Engineering Structures***, Vol. 26, No. 6, (2004), 831-839. doi: 10.1016/j.engstruct.2004.02.004.
24. Mehrabi, M., Suhatril, M., Ibrahim, Z., Ghodsi, S. and Khatibi, H., "Modeling of a viscoelastic damper and its application in structural control", ***PloS one***, Vol. 12, No. 6, (2017), e0176480.
25. Makita, K., Christenson, R., Seto, K. and Watanabe, T., "Optimal design strategy of connected control method for two dynamically similar structures", ***Journal of Engineering Mechanics***, Vol. 133, No. 12, (2007), 1247-1257. doi: 10.1061/(asce)0733-9399(2007)133:12(1247).
26. Basili, M., De Angelis, M. and Fraraccio, G., "Shaking table experimentation on adjacent structures controlled by passive and semi-active mr dampers", ***Journal of Sound and Vibration*** ,Vol. 332, No. 13, (2013), 3113-3133. doi: 10.1016/j.jsv.2012.12.040.
27. Pérez, L., Avila, S. and Doz, G., "Experimental study of the seismic response of coupled buildings models", ***Procedia Engineering***, Vol. 199, (2017), 1767-1772. doi: 10.1016/j.proeng.2017.09.445.
28. Ramakrishna, U. and Mohan, S., "Performance of low-cost viscoelastic damper for coupling adjacent structures subjected dynamic loads", ***Materials Today: Proceedings***, (2020). doi: 10.1016/j.matpr.2019.12.343.
29. Kamaludin, P.N.C., Kassem, M.M., Farsangi, E.N., Nazri, F.M. and Yamaguchi, E., "Seismic resilience evaluation of rc-mrfs equipped with passive damping devices", ***Earthquakes and Structures***, Vol. 18, No. 3, (2020), 391-405.
30. Bogdanovic, A., Rakicevic, Z. and Noroozinejad Farsangi, E., "Shake table tests and numerical investigation of a resilient damping device for seismic response control of building structures", ***Structural Control and Health Monitoring***, Vol. 26, No. 11, (2019), e2443. doi.org/10.1002/stc.2443
31. Ebanesar, A., Cruze, D., Farsangi, E.N., Seenivasan, V.S.J., Mohammad, A.D., Rashid, D.A. and Gladston, H., "Seismic performance evaluation of a proposed buckling-restrained brace for rc-mrfs", ***Civil and Environmental Engineering Reports***, Vol. 29, No. 3, (2019), 164-173. doi.org/10.2478/ceer-2019-0032.
32. Kassem, M.M., Nazri, F.M. and Farsangi, E.N., "On the quantification of collapse margin of a retrofitted university building in beirut using a probabilistic approach", ***Engineering Science and Technology, an International Journal***, Vol. 23, No. 2, (2020), 373-381.
33. Nazri, F.M., Miari, M.A., Kassem, M.M., Tan, C.-G. and Farsangi, E.N., "Probabilistic evaluation of structural pounding between adjacent buildings subjected to repeated seismic excitations", ***Arabian Journal for Science and Engineering***, Vol. 44, No. 5, (2019), 4931-4945.
34. Ansuman Panda, Ginjala Venkata Ganesh, Shivaraj Kashinath Panigavi, B, C., Ajay Mani Teja, Uppari Ramkrishna, Kalyana Rama J.S. and C, M.S., "Design of experiments for structural model updating of steel structure using dynamic testing", ***International Journal of Recent Technology and Engineering***, Vol. 7, No. 6C2, (2019), 599-604.

Persian Abstract

چکیده

با افزایش جمعیت ، شهرنشینی به ساخت سریع ساختمانها انجامیده است. به دلیل محدودیت های فضا و افزایش هزینه زمین ، این ساختمان ها خیلی نزدیک به یکدیگر ساخته شده اند و در اثر اقدامات پویا مانند زلزله می توانند باعث خسارت شوند. اخیراً روش جدیدی به نام اتصال اتصال ساختاری ایجاد شده است و در از بین بردن لرزشهای پراکنده بسیار مؤثر است. تاکنون با استفاده از تکنیک کوپلینگ ، ساختمانهای مجاور مجزا از طریق دستگاه اتصال به یکدیگر متصل می شوند ، به گونه ای که می تواند پاسخ پویای سازه را کاهش دهد. استفاده از روش اتصال ساختاری به دلیل رفتار درون فاز آنها تحت بارهای پویا برای ساختمانهای مشابه چالش برانگیز می شود. در تحقیق حاضر ، عملکرد لرزه ای ساختمانهای مشابه با تکنیک کوپلینگ به صورت آزمایشی بر روی میز لرزش آزمایش شده است. مدل سه طبقه ای با استفاده از جدول لرزش یک طرفه با حرکت زمین مقیاس شبیه سازی شده است. عدم قطعیت ساخت و سازهای مشابه در ساختمان با تغییرات جزئی در خصوصیات دینامیکی آنها در نظر گرفته شده است. دستگاه های اتصال مورد استفاده بریس ها و میراگرهای ویسکوالاستیک منفعل هستند. نتایج به دست آمده تأثیر تکنیک اتصال جابجایی ساختاری را با تنظیمات مختلفی از میراگرها برای ساختمانهای مشابه بر روی ساختمانهای انفرادی لرزه ای تأیید می کند.

International Journal of Engineering

Journal Homepage: www.ije.ir

Experimental Investigation of Porosity, Installation Angle, Thickness and Second Layer of Permeable Obstacles on Density Current

A. Jahangir[a], K. Esmaili*[a], M. F. Maghrebi[b]

[a] *Department of Water science and Engineering, Ferdowsi University of Mashhad, Mashhad, Iran*
[b] *Department of Civil Engineering, Ferdowsi University of Mashhad, Mashhad, Iran*

PAPER INFO

Paper history:
Received 07 March 2020
Received in revised form 26 April 2020
Accepted 25 July 2020

Keywords:
Density Current
Obstacle Porosity
Obstacle Installation Angle
Obstacle Thickness
Second Layer of Obstacle
Permeable Obstacle

ABSTRACT

This study explored the effect of porosity and installation angle, thickness (dimension) and second layer of permeable obstacles on density current control and trapping in the laboratory. For this purpose, an insoluble suspended polymer and two types of groove and cavity obstacles made from plexiglass sheets were selected. The experiments were conducted with two different concentrations, five different porosities, four different angles, four different thicknesses and two obstacle layers. The results showed that the optimum porosities for cavity and groove obstacles were 22 and 19%, respectively. In all experiments, the cavity trapping rates of 0.13% and 0.14% at 10% and 20% concentrations were higher than those of groove trapping. In addition, by increasing the angle, the rate of trapping decreased and its value was observed in the groove with the correlation coefficients of 0.995 and 0.981 compared to the cavity. The major effect of obstacles was found to be the flow deceleration where the average velocity in the cavity was obtained 3.62% higher than that in the groove. For the increased thickness with 10% porosity and groove type, the passage of materials from the obstacle further increased. By creating the second layer of obstacle, the passage of materials from the obstacle in the both groove and cavity increased, and the optimal distance of the second obstacle was 2.25 m from the first one.

***doi**: 10.5829/ije.2020.33.09c.03*

1. INTRODUCTION

The mechanism of flow sedimentation are among the important and complex issues in hydraulic structures; the issue has been paid attention by many experts [1-4]. Sediments can have significant effect on the behavior of a density current [5]. Density current occurs when a fluid of high density flows into a low density or light fluid [6-8]. One of the effective tools to control flow sediment is the obstacles used in the river course upstream of main structures and dam reservoirs [9, 10]. Permeable obstacles are more common and efficient due to the ability to pass part of the flow and reduce the flow pressure compared to impermeable obstacles [11, 12]. Since the major part of sediments is related to the suspended load of flow, which occurs in the floods and density currents, it is very important to understand and study these types of currents. De Cesare et al. [13] evaluated the passage of density current through different obstacles. Their studies showed that the density current can be effectively designed through the constructive measurements. Asghari Pari et al. [14] presented the velocity curves of flow body and concentration. They concluded that the high height is more effective on the flow control and also at high concentrations, the effect on the velocity and control of flow sediment is also high. Oehy and Schleiss [15] investigated the effect of different obstacles on the control of density current and concluded that the subcritical conditions and not passing over the obstacle are more appropriate. To compare experimentally the effect of porous obstacle and porous stepped obstacle on the control of density current, Kordnaeij et al. [16] used porous obstacle as a permeable ones. The results of the study showed that the porous obstacle outperforms the porous stepped obstacle and further reduces the sediment discharge. Asghari Pari et

*Corresponding Author Institutional Email: *esmaili@um.ac.ir* (K. Esmaili)

Please cite this article as: A. Jahangir, K. Esmaili, M. F. Maghrebi, Experimental Investigation of Porosity, Installation Angle, Thickness and Second Layer of Permeable Obstacles on Density Current, International Journal of Engineering (IJE), IJE TRANSACTIONS C: Aspects Vol. 33, No. 9, (September 2020) 1710-1720

al. [17, 18] numerically investigated the effect of the angle upstream the obstacle and depth of water reservoir on controlling the density current. They stated the high the obstacle height, the low impact of water depth would better control the flow. In addition, the high angle upstream of obstacle would be the greater the flow control by obstacle. Habib Mohammadi et al. [19] studied the effect of height, shape and location of gabion obstacles on the control of sediment density current. They stated that part of the flow passes through or over the obstacle and the high height and close to the inlet, the low velocity resulted in desired performance. Alves and Rossato [20] conducted a series of experiments to investigate the effect of obstacles on density currents. The results showed that the flow velocity decreases with an increase in the obstacle height; while the ratio of different characteristics remains constant in the velocity profile. In a study conducted by Nogueira et al. [21], the dynamic properties of density current on rough bed in experiment approaches were evaluated. The convergence of upstream Froude number showed that the mechanical characteristics of the flow were determined by the means of upstream local variables. Janocko et al. [22] found that the superiority of numerical simulations is the possibility of monitoring all the hydraulic factors in the density current and their reactions to the three-dimensional topography of the walls during the full flow period. In another study, MacArthur et al. [23] experimentally analyzed the density currents using the imaging technique. They concluded that the obstacles with uneven surface reduce the flow velocity, but have a slight effect on the overall flow velocity. Yaghubi et al. [24] experimentally investigated the effect of inlet concentration on the flow behavior in the presence of two consecutive obstacles. The study results showed that an area with an insignificant velocity and significant concentration grows at the top of each obstacle and with the increased inlet concentration, the area becomes larger. Zeinivand et al. [25] investigated the porosity percentage of obstacles and different flow concentrations. The results showed that by increasing the porosity percentage of the obstacles, the absorption rate of flow materials decreased and correspondingly, the efficiency of obstacles in the cont wrol of flow will be lower. Abhari et al. [26] examined the transfer rate of experimentally suspended load. This study showed that in the velocity profile, the obstacle reflects the flow and creates another critical area in addition to the walls in the current, reducing 1% of the average transfer rate of suspended load in downstream the obstacle.

Despite the numerous studies to understand the behavior of density currents [28-30], evaluating the behavior of currents with suspended sediment load colliding with permeable obstacles in their way is a novel issue, There was less report and still needs further investigation. For this purpose, as presented in Figure 1, this paper explores the effect of porosity and installation angle, thickness (dimension) and second layer of permeable obstacles on the density current control and trapping in the laboratory.

2. MATERIALS AND METHODS

2. 1. Laboratory Equipment In this study, a flume with the length of 10 m, width of 30 cm and height of 45 cm was used. Figure 2 shows the overall view of the flume and the related laboratory equipment. The study tests were conducted for duration of 6 months in the hydraulics and sediment laboratory of Water Engineering Department in Agriculture Faculty of Birjand University. Due to constant flow, the velocity recording, collision status and passage of flow over the obstacles were performed using the Pitot tube plate by the imaging technique. The Pitot tube plate was installed in the upstream of the obstacles with measuring capability at distance of 5 cm, and the imaging was performed solely to examine the density current motion along the flume; the physical and mechanical behavior of the collision and passage of flow over the obstacles. The longitudinal slope values were considered zero in the experiments. The plexiglass sheets of 3 mm thick with the width equal to the flume width and the height up to 30 cm were used to build the obstacles. The amount of porosity in the obstacles with different percentages of 10, 15, 20, 25 and 30 in both forms of groove and cavity were created using the equal groove width and diameter of 3 mm (about 3 times the average particle diameter). The obstacles were installed at the distance of 9 m from the inlet of density current injection. The obstacle installation angles were considered at 45, 60, 75 and 90° relative to the direction perpendicular to the bed. Figure 3 shows samples of two types of cavity and groove obstacles.

2. 2. Density Current Characteristics The desired density current was produced by the mixture of

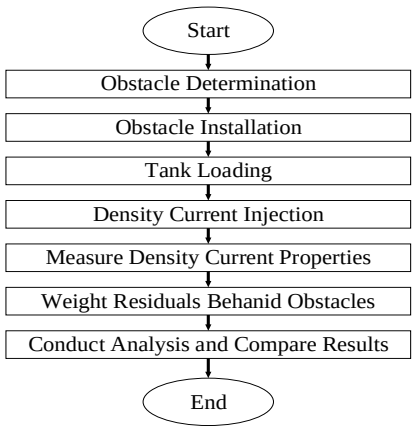

Figure 1. Overall paper flowchart

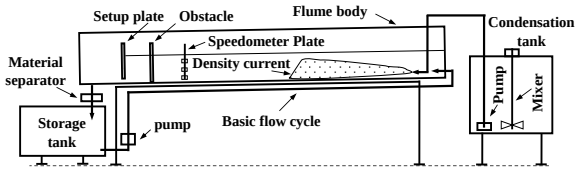

Figure 2. Overall view of flume and laboratory equipment

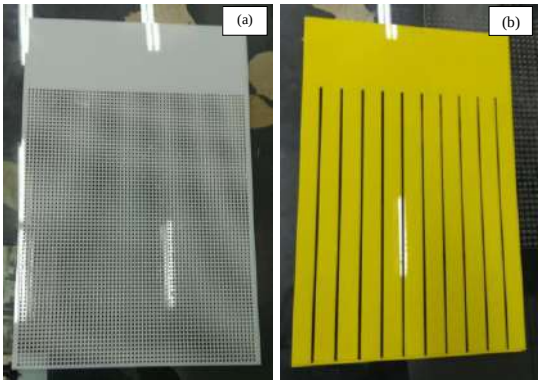

Figure 3. Samples of used obstacles: a) cavity obstacle; b) groove obstacle

water and a type of expanded poly styrene (EPS) with the density of 1135 kg/m^3 and average diameter of 1.15 mm. The current was injected into the main stream at an average discharge of 3.43 L/s at a distance of 7 cm from the bottom of the flume. The density current injection was performed by pump as flood hydrograph. The base water discharge was 5 L/s and the volume of density current was 460 L with a mixer at two different concentrations of 10 and 20%. At the end of the flume, there was a filter and a tank for separating materials from the current for the storage and reuse purposes. Figure 4 shows the tank for the production of density current and the filter for the separation of materials from the current.

According to Figure 4(b), in the test device, a suitable filter with a total flow capacity was placed at the flume outlet against the flow to separate suspended matter passing through the obstacles and to store material-free flow into the storage tanks and continued the flow cycle for the experiments. In addition, the collected materials were the basis for evaluating the performance of the obstacles and used for subsequent tests.

Figure 4. a) Density current production tank; b) material separating filter

2. 3. Test Method To ensure that the material used is suspended, special experiments were carried out based on the proposed theories and the experimental method of mixing and falling speed. Then, the concentration tank was filled with water and the required amount of material for the desired concentration was added and homogenized with the mixer. By installing the control valve and obstacle, the base discharge was set and adjusted to the threshold depth. According to the characteristics of the current and polymer material and considering the limitations of the laboratory flume dimensions according to Schneider method [19], the depth of 25 cm was calculated. Then, as shown in Figure 5, the density current was injected to the stream as flood hydrograph.

As shown in Figure 5, out of the total test time (335.4 seconds), 84 seconds (25%) is dedicated to be the upward trend, 49.8 seconds (15%) to the peak constant discharge, and 201.6 seconds (60%) to the downward trend. The average pumping time is about 133.8 seconds.

To determine the testing time and to validate the test, the control sample was taken as the temporal variations of the suspended sediment load for the desired depth. In this way, the least change of the sediment load was the basis for the time selection, which resulted in the hydrograph, as shown in Figure 4. In all experiments, the flow characteristics including the velocity, body height, injection time, front and tail arrival time of suspended materials to the obstacle, process of collision with and passage over obstacle, situation and location of sedimentation, amount of passed and trapped materials behind the obstacle were measured. The obstacle performance criterion was the amount of trapped materials (fraction of passed materials to total initial material). In this study, 68 independent tests including density currents at two concentrations and five porosities, and obstacles using two different shapes, numbers and thicknesses and four installation angles, were performed.

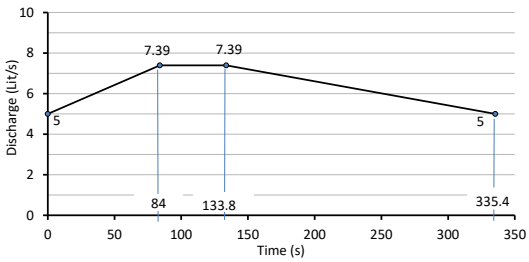

Figure 5. Flood flow hydrograph produced in experiments

3. RESULTS AND DISCUSSION

3. 1. Flow Velocity The flow velocity measurement was performed with a piezometric plate attached to the pitot tubes and also using imaging of the flume sides. The velocity varied by the temporal variations of discharge, relative location of measurement and obstacle at different porosities. An example of the velocity profiles approaching the flow upstream of the obstacle is shown in Figure 6.

The reason for the relative increase in flow velocity in the vicinity of the obstacle can be attributed to the impact of the reduced passage over the obstacle and also the decrease in suspended sediment load along with upstream course. The vertical profiles of velocity and flow concentration at 2 and 5 m upstream of the obstacle are shown in Figure 7.

As can be seen in Figure 7, the density current approaches the obstacle, the average velocity is low and the depth velocity is more widely distributed. In addition, due to the sedimentation in the course to the obstacle, the concentration of materials decreases and the concentration in the deep sections of the stream increases. The depth changes in the vicinity of the upstream obstacles are shown in Figure 8. As can be seen in Figure 8, the high porosity, the low rate of depth decrease as the porosity increases. This trend was observed both for base flow without water level adjustment and for total flow with water level adjustment with depth. The upstream depth of the groove obstacles with an average of 4.14% is always higher than that of the cavity obstacles. The main reason for this difference was the desired distribution of cavities at the surface of cavity obstacle and the easier passage of flow through the cavities.

The studies showed that the velocity profiles differed along with flume depending on the position relative to the obstacle. As such, upstream of the obstacles, the velocities become more balanced with moving away from the obstacles and close to the form of flow without

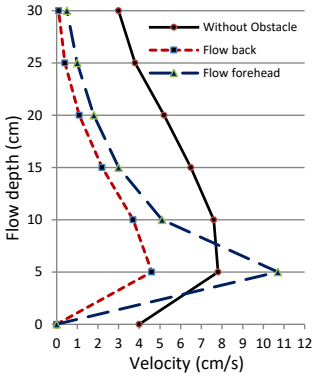

Figure 6. Example of velocity profiles approaching flow upstream of obstacle

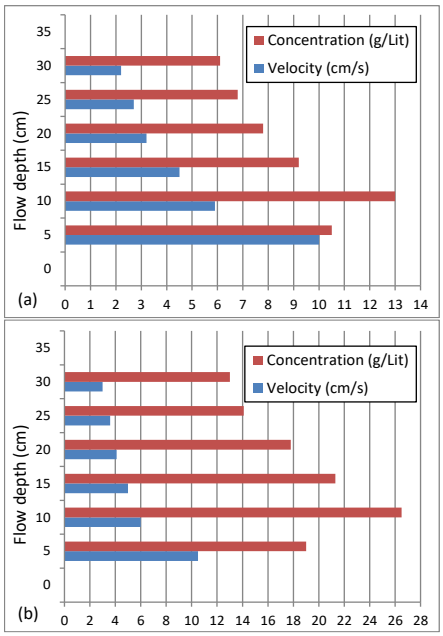

Figure 7. Vertical velocity profile and flow concentration with concentration of 20% in (a) 2m upstream of obstacle; b) 5m upstream of obstacle

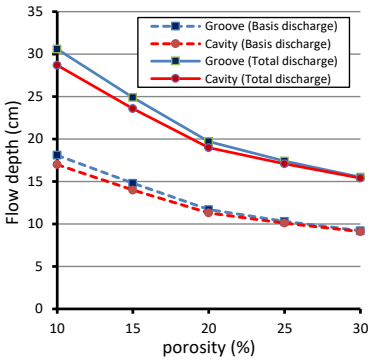

Figure 8. Depth changes in vicinity of obstacles for basis and total discharge

obstacle. In the vicinity of the obstacle, the velocities are more different in depth and higher than the maximum value. The currents with cavity obstacles had a lower upstream depth due to the easier flow while having 3.62% higher velocity. In addition, the mean velocity of the front and tail of density current mass were 10.7 and 4.6 cm/s, which were 37% higher and 30.2% lower than the mean flow velocity, respectively. The differences in velocities can be attributed to the obstacle performance in the flow deceleration and the trapping and sedimentation factors of the density current.

In addition to the velocity profiles and upstream depth, the test time was also evaluated. Figure 9 shows the test time from the beginning of the density current injection to the base flow until the passage of the last particle of suspended load over the obstacle.

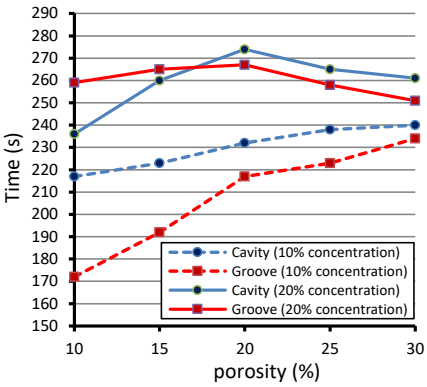

Figure 9. Variations of test time for obstacles with different flow concentrations

As shown in Figure 9, the distribution and temporal variations of the test time at concentration of 10% was greater than that of the 20% concentration. In addition, the variations of test time at the 20% concentration are more balanced compared to those of 10% concentration. The depth and flow velocity data in the vicinity of the upstream obstacles are summarized in Table 2.

The obtained results showed that as part of the flow passes through the obstacle body, the front velocity of the flow occurs with the same pattern as behind the obstacle. However, at high levels, the flow velocity is significantly reduced. It was also observed that the stationary state and even the inverse current of upper and surface parts caused by the collision of flow with obstacles is a factor behind the accumulation of part of the materials on the surface. It should be noted that since this part of the accumulated materials are not part of the suspended flow mass, the floating materials were deducted from the initial materials, which constitute about 11% of the total initial materials. Figure 10 shows how the sediments accumulate upstream of the obstacle.

3. 2. Effect of Obstacle Porosity

To determine the effect of obstacle surface porosity with constant flow conditions, two types of obstacles were tested at two concentrations of 10 and 20% for five porosities of 10, 15, 20, 25 and 30%. Figure 11 shows the amount of

TABLE 2. Depth and flow velocity of upstream obstacles

Porosity (%)	Depth (cm)		Velocity (cm/s)	
	Groove	Cavity	Groove	Cavity
10	9.2	9.8	30.6	28.7
15	11.3	11.9	24.9	23.6
20	14.3	14.8	19.7	19.0
25	16.2	16.5	17.4	17.1
30	18.1	18.3	15.5	15.4

Figure 10. Accumulation of sediments upstream obstacle

materials passing over the obstacles versus the porosity. In addition, the related data are givenin Table 3. By deducting the amount of passed material from the total initial material, the performance of the obstacle in trapping was determined and expressed in percent.

The results showed that in all cases, the trapping performance of the cavity obstacle is better than that of the groove obstacle, so that at concentrations of 10 and 20%, the average trapping of cavity obstacles was reported 0.14% and 0.13% higher than the groove obstacles, respectively. At low concentrations, the performance of the two types of obstacles is relatively similar, but at high concentrations, the cavity-type performance has been found to be more effective in

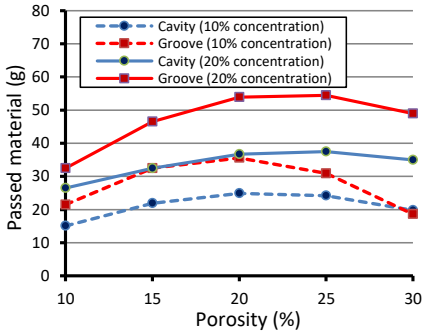

Figure 11. Variations of materials passing over obstacles with different porosities and concentrations

TABLE 3. Material trapping data for different porosities and concentrations

Porosity (%)	Material trapping (g) 10% concentration		Material trapping (g) 20% concentration	
	Groove	Cavity	Groove	Cavity
10	5010.1	5016.5	10030.6	10036.6
15	4999.1	5009.7	10016.6	10030.6
20	4996.0	5006.7	10009.2	10026.4
25	5000.7	5007.4	10008.6	10025.6
30	5013.0	5011.8	10014.1	10028.1

trapping materials. Also, at high porosity, the performance of the two types of obstacles was close together. In this case, the lowest trapping was observed in 20% porosity for 10% concentration and in 25% porosity for 20% concentration. By repeating the tests and further examining the optimal porosity, which has the highest amount of passed material, it was determined about 22% for the groove type and about 19% for the cavity type. The trapping decreases for the porosities lower than this amount and increases for the higher porosities.

3. 3. Effect of Obstacle Installation Angle In the first stage of tests, the obstacles were considered perpendicular to the flow direction (90° angle). To investigate the effect of the installation angle, the obstacles were rotated in the flow direction at the same previous location. According to Figure 12, the angles 90, 105, 120 and 135° were selected relative to the horizontal bed direction. The variations of the materials passing over the obstacles for different obstacle angles are shown in Figure 13. Table 4 also reports the data on the trapping performance for different obstacle installation angles (10% porosity) and different concentrations.

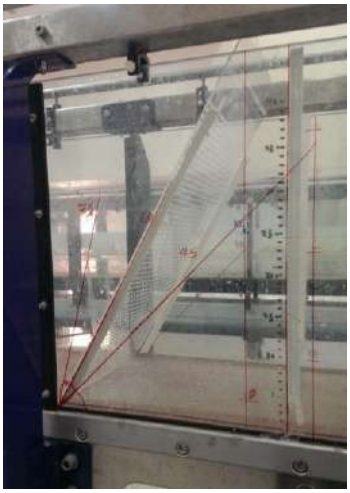

Figure 12. Selected angles of obstacle installation beyond 90°

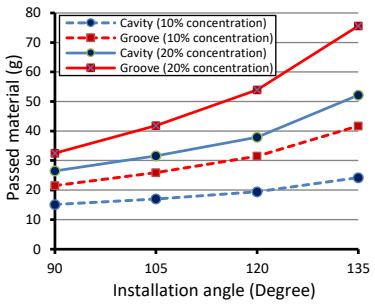

Figure 13. Variations of passed materials with obstacle installation angle at different concentrations

TABLE 4. Data on trapping performance for different obstacle installation angles (10% porosity) and concentrations

Installation Angle (Dgree)	Material trapping (g) 10% concentration		Material trapping (g) 20% concentration	
	Groove	Cavity	Groove	Cavity
90	5005.7	5016.5	10030.6	10036.6
105	5000.1	5014.6	10021.3	10031.6
120	4989.9	5012.2	10009.2	10025.2
135	5031.6	5007.4	9987.5	10010.9

The results showed that by increasing the angle of installation reduces the trapping level in both types of obstacle. In addition, at two different concentrations used, the observed reduction in the trapping level in the groove obstacles was more than that in the cavity obstacles. According to Figure 14, the correlation coefficients in the groove and cavity obstacles were 0.9994 and 0.9967 for 10% and 20% of concentration, respectively. This can be attributed to the easier passage of flow and discharge of materials due to the water pressure on the cavity obstacle. For this reason, the trapping reduction rate in the groove obstacles was more than that in the cavity obstacles.

3. 4. Effect of Obstacle Thickness or Dimension To investigate the effect of obstacle thickness and dimension in the flow direction, one of the groove obstacles with 10% porosity was selected. Due to the operational limitations, according to Figure 15, this obstacle was used at a 90° angle in perpendicular direction. The passed current was constant with the same base current at both 10 and 20% concentrations. In addition to the thickness of the main obstacle (3 mm), the 5, 10 and 15cm thicknesses were also considered.

Figure 16 shows the amount of passed sediment for different obstacle thicknesses in both currents at 10 and 20% concentrations. As can be seen in Figure 16, the

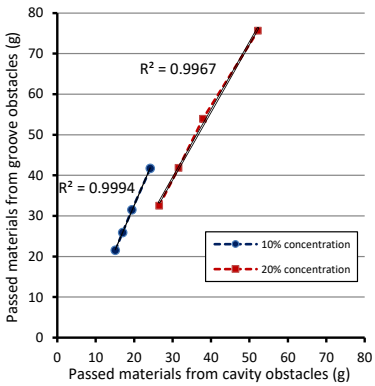

Figure 14. Relative fitting of materials passed over obstacles with different installation angles and concentrations

Figure 15. Example of obstacle with dimension for testing impact of obstacle thickness

amount of passed materials is higher for the increased obstacle thickness at both concentrations. However, at high concentration resulted in high increased rate. As such, the slope of fitting line of the 20% concentration data was observed about 2.3 times that of the 10% concentration. Also, the correlations of recorded data of the obstacle-passed materials with different thicknesses at the 10 and 20% concentrations were 0.981 and 0.995, respectively. The reason for the general increase in the passed materials was found to be the impact of the current passing along the obstacle on the current flowing into the obstacle and created suction conditions. Also, the higher correlation coefficient at higher concentration was attributed to the easier flow of suspended materials into the obstacle due to the inside flow tension. In the case of obstacles with low thickness, the flow is released as it passes over and has no effect on the upstream and, as a result, on the flow of materials through and over the obstacle.

3. 5. Effect of Second Obstacle Layer Due to the frequent application of sediment control structures such as slit dams, an obstacle was used to investigate the effect of the second obstacle upstream of the main one. The tests were performed for all previously used obstacles with the same specifications but with a half-height obstacle. The relevant experiments were repeated at the same conditions as before with two concentrations of 10 and 20% and the materials deposited behind an obstacle and the conditions of two obstacles were compared. Figure 17 illustrates the second-layer obstacle and the obstacle valve for the passage of second-layer materials. A view of the deposited material with the second layer of obstacle is shown in Figure 18.

The amount of sediment passed over a single obstacle, two obstacles, comparison of the obstacle types in two obstacles, and the remaining amount behind the second obstacle are shown in Figures 19, 20, 21 and 22, respectively.

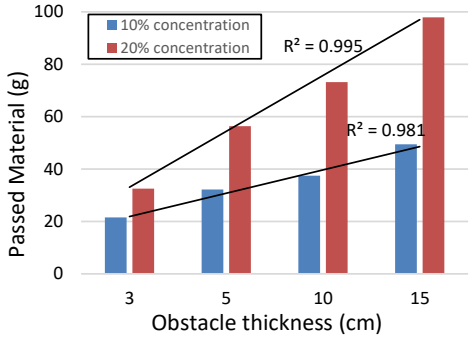

Figure 16. Amount of passed sediment for different thicknesses of first obstacle with two rows and 10 and 20% concentrations

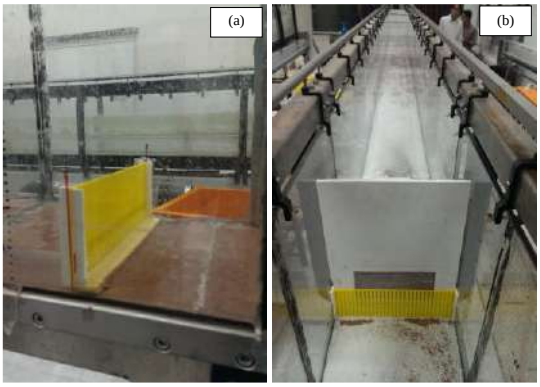

Figure 17. a) Example of second-layer obstacle; b) valve for passage of second-layer

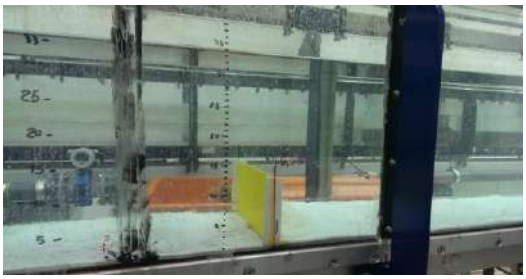

Figure 18. View of deposited material with second layer of obstacle

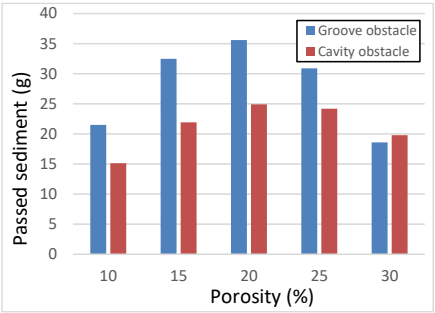

Figure 19. Amount of sediments passed over single obstacle

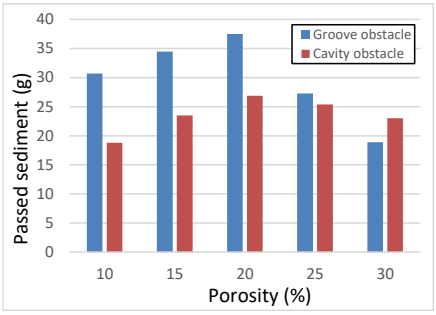

Figure 20. Amount of sediments passed over two obstacles

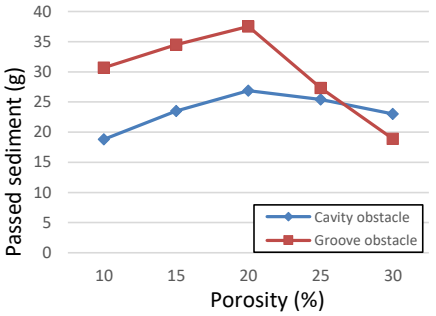

Figure 21. Comparison of sediment amounts passed over first obstacle in case of two obstacle rows

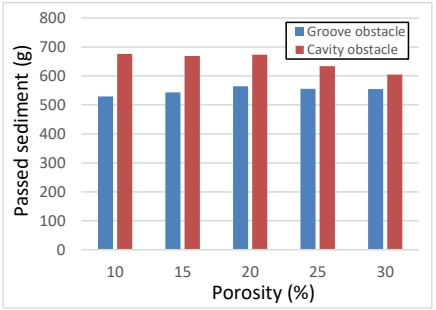

Figure 22. Amount of sediment remained behind second obstacle

As shown in Figures 19 and 20, by addition of the second layer of obstacle, the amount of passage over the first layer slightly increased compared to the single-obstacle conditions. The average amounts of increased for the cavity and groove obstacles were 2.34% and 1.96%, respectively. The reason for such increase was the effect of turbulent flow passing over the second obstacle towards the first obstacle downstream and the tendency of the materials to the passage. The behavior of groove and cavity obstacles was similar to the single-layer case. As such, the optimal porosity in this case was also observed about 20% where the passage of materials over the obstacle before and after that had an increasing and decreasing trend, respectively. In this case, the efficiency of the cavity-type obstacle was better than the groove type.

Comparing the behavior of the two types of cavity and groove obstacles in Figure 21 showed that by addition of the second obstacle row, the materials passing over the first obstacle downstream in the cavity type had less changes than the groove type. Particularly for the porosities higher than the optimum porosity (about 20%), the groove-type conditions were improved so that at high porosities, the efficiency was higher than the cavity type. This is due to low permeability of the obstacle than the cavity type resulted from the flow turbulence.

The examination of the materials deposited behind the second obstacle in Figure 22 showed that with an increasing the porosity before the optimum porosity, the trapping process decreased, but that of the groove type increased. For the porosity more than the optimal porosity, due to high permeability of the cavity type, the same process was continued, but in the groove type, as the flow passes over obstacle, the trapping and sedimentation of materials behind the obstacle were stabilized. However, the performance of both types of obstacle showed that the second layer was effective in improving the obstacle efficiency. Of course, it was affected by the distance of the second obstacle from the first obstacle.

To investigate the effect of location and installation of second obstacle to the first one, the experiments were carried out from 2 m upstream the first obstacle at 25cm intervals to the end of flume. The reason for choosing 2 m was that in the lower distances, the turbulence of the flow passing over the second obstacle had a great effect on the first obstacle and the performance of obstacles could not be distinguished. As such, for the performed experiments, the optimal distance of the second obstacle from the first one downstream was determined based on the highest trapping and sedimentation efficiencies. The selection criterion was to compare the deposited materials between the two obstacles and upstream of the second obstacle layer. Figures 23 and 24 showed the amount of the sediment passed over the first and second obstacle in terms of the distance from the first obstacle, respectively.

The studies showed that the greater the distance between the second and first obstacles, the better the effectiveness in improving the efficiency. Figure 24 shows that the process of sediment deposition behind the second obstacle is greater with an increased distance from the first obstacle. Also, according to Figure 23, it was found that with the existing tools and limitations, the sedimentation process changed from a certain distance to higher ones. The reason for this was also the effect of turbulence caused by the base flow inlet, especially the effect density current injection. As a result, at the end parts of the flume, the function of the second layer was

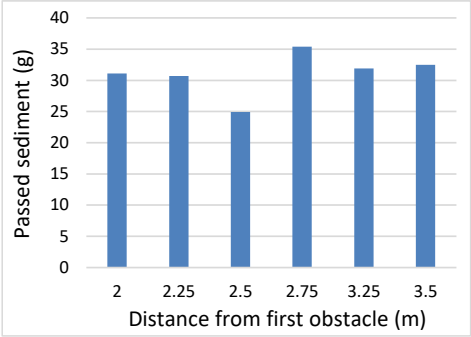

Figure 23. Amount of sediment passed over first obstacle in terms of distance from first obstacle

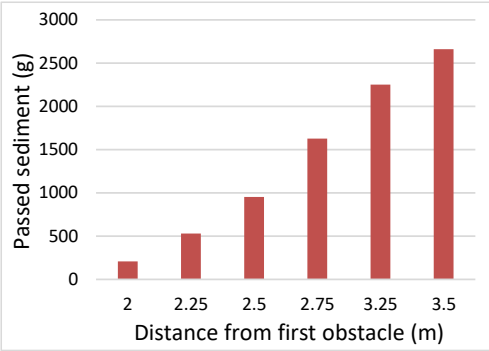

Figure 24. Amount of sediment behind second obstacle in terms of distance from first obstacle

not practically recognizable. Consequently, the optimum distance between the second and first obstacles was about 2.25 m.

6. CONCLUSION

This paper explores the effect of porosity and installation angle, thickness (dimension) and second layer of permeable obstacles on the density current control and trapping in the laboratory. Two types of groove and cavity obstacles with the groove width and cavity diameter equal to 3 mm were selected and built from the plexiglass sheets. An insoluble suspended polymer with the density of 1.135 g/l and average diameter of 1.15 mm was used to create the density current. The experiments were conducted at two different concentrations of 10 and 20%, five different porosities, four different angles, four different thicknesses and two obstacle layers:

1) The analysis of laboratory results showed that the optimum porosity for cavity and groove obstacles were 22 and 19%, respectively. However, an increasing porosity, the trapping up to the optimum porosity decreased and then increased.
2) In all tests, the trapping level of cavity obstacles was higher than the groove obstacles. The trapping level of cavities obstacles at t 10 and 20% concentrations were 0.13 and 0.14% higher than the groove obstacles, respectively.
3) The evaluation of different angles of obstacles relative to the direction perpendicular to the stream bed showed that by increasing the angle, the amount of trapping decreased. The reduction in the trapping level with the correlation coefficients of 0.995 and 0.981 in the groove obstacles was higher than the cavity ones.
4) The average flow velocity in the cavity obstacles was 3.62% higher than that in the groove obstacles.
5) For the increased thickness with 10% porosity and groove type, the passage of materials from the obstacle further increased. This was attributed to high flow velocity along with obstacle and the induced tensile force and its effect on the upstream inflow.
6) By creating the second layer of obstacle, the passage of materials from the obstacle in both groove and cavity obstacles increased, so that the amounts of 1.96% and 2.34% were recorded in the groove and cavity types, respectively. The reason for such increase was the effect of turbulent flow passing over the second obstacle. Therefore, higher the distance between the second and first obstacles resulted in improvement in trapping and sedimentation efficiencies. As such, the optimal distance from the second obstacle to the first one was obtained equal to 2.25 m. Beyond this distance, due to the effect of the turbulent flume inflow and injection of density current, the share of second obstacle was not noticeable. However, the effect of second layer on the overall trapping and sedimentation efficiencies was found to be positive. According to all obtained results, the cavity obstacles always outperformed the groove obstacles under similar conditions.

7. REFERENCES

1. Jawaduddin, M., Memon, S. A., Bheel, N., Ali, F., Ahmed, N., and Abro, A. W., "Synthetic Grey Water Treatment Through $FeCl_3$-Activated Carbon Obtained from Cotton Stalks and River Sand." ***Civil Engineering Journal***, Vol. 5, No. 2, (2019), 340-348, doi: 10.28991/cej-2019-03091249.
2. Alavi, S. R., Lay, E. N., and Makhmali, Z. A., "A CFD study of industrial double-cyclone in HDPE drying process", ***Emerging Science Journal***, Vol. 2, No. 1, (2018), 31-38, doi: 10.28991/esj-2018-01125.
3. Li, N., Sheng, G. P., Lu, Y. Z., Zeng, R. J. and Yu, H. Q., "Removal of antibiotic resistance genes from wastewater treatment plant effluent by coagulation', ***Water Research***, Vol. 111,No. 1, (2017), 204-212, doi: 10.1016/j.watres.2017.01.010.
4. Massoudinejad, M., Hashempour, Y., and Mohammad, H. "Evaluation of Carbon Aerogel Manufacturing Process in Order to Desalination of Saline and Brackish Water in Laboratory

Scale.", ***Civil Engineering Journal***, Vol. 4, No. 1, (2018), 212-220, doi: 10.28991/cej-030980.

5. Barahmand, N., and Shamsai, A., "Experimental and theoretical study of density jumps on smooth and rough beds, Lakes & Reservoirs" ***Research and Management***, Vol. 15, No. 4, (2010) 285-306, doi: 10.1111/j.1440-1770.2010.00442.x.
6. Hu, P., Cao, Z., Pender, G., and Tan, G., "Numerical modelling of turbidity currents in the Xiaolangdi reservoir, Yellow River, China", ***Journal of Hydrology***, Vol. 464, (2012), 41-53, doi: 10.1016/j.jhydrol.2012.06.032.
7. Vladimirov, I.Y., Korchagin, N., and Savin, A., "Wave influence of a suspension-carrying current on an obstacle in the flow", in Doklady Earth Sciences, Springer Science & Business Media, (2015), 286-293, doi: 10.1134/S1028334X15030162.
8. Farizan, A., Yaghoubi, S., Firoozabadi, B., and Afshin, H., "Effect of an obstacle on the depositional behaviour of turbidity currents", ***Journal of Hydraulic Research***, Vol. 57, No. 1, (2019), 75-89, doi: 10.1080/00221686.2018.1459891.
9. Chamoun, S., De Cesare, G., and Schleiss, A.J., "Managing reservoir sedimentation by venting turbidity currents: A review", ***International Journal of Sediment Research***, Vol. 31, No. 3, (2016), 195-204, doi: 10.1016/j.ijsrc.2016.06.001.
10. Asghari Pari, S.A., Kashefipour, S.M., and Ghomeshi, M., "An experimental study to determine the obstacle height required for the control of subcritical and supercritical gravity currents", ***European Journal of Environmental and Civil Engineering***, Vol. 21, No. 9, (2017), 1080-1092, doi: 10.1080/19648189.2016.1144537.
11. Yaghoubi, S., Afshin, H., Firoozabadi, B., and Farizan, A., "Experimental investigation of the effect of inlet concentration on the behavior of turbidity currents in the presence of two consecutive obstacles", ***Journal of Waterway, Port, Coastal, and Ocean Engineering***, Vol. 143, No. 2, (2016), 6018-6029, doi: 10.1061/(ASCE)WW.1943-5460.0000358.
12. Keshtkar, MM. and Amiri, B., "Numerical simulation of radiative-conductive heat transfer in an enclosure with an isotherm obstacle", ***Heat Transfer Engineering***, Vol. 39, No. 1, (2018), 72-83, doi: 10.1080/01457632.2017.1280293.
13. De Cesare, G., Oehy, C.D., and Schleiss, A.J., "Circulation in stratified lakes due to flood-induced turbidity currents", ***Journal of Environmental Engineering***, Vol. 132, No. 1, (2006), 1508-1517, doi: 10.1061/(ASCE)0733-9372(2006)132:11(1508).
14. Asghari Pari, S. A., Habibagahi, G., Ghahramani, A., and Fakharian, K., "Improve the design process of pile foundations using construction control techniques.", ***International Journal of Geotechnical Engineering***, Vol. 1, No. 1, (2019), 1-8, doi: 10.1080/19386362.2019.1655622.
15. Oehy, C.D., and Schleiss, A.J., "Control of turbidity currents in reservoirs by solid and permeable obstacles", ***Journal of Hydraulic Engineering***, Vol. 133, No. 6, (2007), 637-648, doi: 10.1061/(ASCE)0733-9429(2007)133:6(637).
16. Kordnaeij, A., Kalantary, F., Kordtabar, B. and Mola-Abasi, H., "Prediction of recompression index using GMDH-type neural network based on geotechnical soil properties", ***Soils and Foundations***, Vol. 55, No. 6, (2015), 1335-1345, doi: 10.1016/j.sandf.2015.10.001.
17. Asghari Pari, S.A, Habibagahi, G., Ghahramani, A. and Fakharian, K., "Reliability-Based Calibration of Resistance Factors in LRFD Method for Driven Pile Foundations on Inshore Regions of Iran", ***International Journal of Civil Engineering***, Vol. 17, No. 12, (2019), 1859-1870, doi: 10.1007/s40999-019-00443-0.
18. Samadi-koucheksaraee, A., Ahmadianfar, I., Bozorg-Haddad, O., and Asghari-pari, S. A., "Gradient evolution optimization algorithm to optimize reservoir operation systems", ***Water Resources Management***, Vol. 33, No. 2, (2019) 603-625, doi: 10.1007/s11269-018-2122-2.
19. Marosi, M., Ghomeshi, M., and Sarkardeh, H., "Sedimentation control in the reservoirs by using an obstacle", ***Sadhana***, Vol. 40, No. 4, (2015), 1373-1383, doi: 10.1007/s12046-015-0333-2.
20. Alves, M., Gaillard, F., Sparrow, M., Knoll, M., and Giraud, S., "Circulation patterns and transport of the Azores Front-Current system", ***Deep Sea Research Part II: Topical Studies in Oceanography***, Vol. 49, No. 19, (2002), 3983-4002, doi: 10.1016/S0967-0645(02)00138-8.
21. Nogueira, W., Litvak, L., Edler, B., Ostermann, J., and Büchner, A., "Signal processing strategies for cochlear implants using current steering ***EURASIP Journal on Advances in Signal Processing***, Vol. 1, (2009), 213-224, doi: 10.1155/2009/531213.
22. Janocko, M., Cartigny, M., Nemec, W., and Hansen, E., "Turbidity current hydraulics and sediment deposition in erodible sinuous channels: laboratory experiments and numerical simulations", ***Journal of Marine Petroleum Geology***, Vol. 41, (2013), 222-249, doi: 10.1016/j.marpetgeo.2012.08.012.
23. McArthur, J. M., Sikdar, P. K., Nath, B., Grassineau, N., Marshall, J. D. and Banerjee, D. M., "Sedimentological control on Mn, and other trace elements, in groundwater of the Bengal Delta", ***Journal of Marine Petroleum Geology***, Vol. 46, No. 2, (2012), 669-676, doi: 10.1021/es202673n.
24. Oshaghi, M. R., Afshin, H. and Firoozabadi, B., "Experimental investigation of the effect of obstacles on the behavior of turbidity currents", ***Canadian Journal of Civil Engineering***, Vol. 40, No. 4, (2013), 343-352, doi: 10.1139/cjce-2012-0429.
25. Bogdanov, I. I., Mourzenko, V. V., Thovert, J. F. and Adler, P. M., "Effective permeability of fractured porous media in steady state flow", ***Water Resources Research***, Vol. 39, No. 1, (2003), 13-24, doi: 10.1029/2001WR000756.
26. Abhari, M.N., Iranshahi, M., Ghodsian, M., and Firoozabadi, B., "Experimental study of obstacle effect on sediment transport of turbidity currents", ***Journal of Hydraulic Research***, Vol. 56, No. 5, (2018), 618-629, doi: 10.1080/00221686.2017.1397778.
27. Wilson, R. I. and Friedrich, H., "Coupling of Ultrasonic and Photometric Techniques for Synchronous Measurements of Unconfined Turbidity Currents", ***Water***, Vol. 10, No. 9, (2018), 1246-1258, doi: 10.3390/w10091246.
28. Tokyay, T., Constantinescu, G., and Meiburg, E., "Lock-exchange gravity currents with a high volume of release propagating over a periodic array of obstacles", ***Journal of Fluid Mechanics***, Vol. 672, (2011), 570-605, doi: 10.1017/S0022112010006312.
29. Tokyay, T., Constantinescu, G., Gonzalez-Juez, E., and Meiburg, E., "Gravity currents propagating over periodic arrays of blunt obstacles: Effect of the obstacle size", ***Journal of Fluids and Structures***, Vol. 27, No. 6, (2011), 798-806, doi: 10.1016/j.jfluidstructs.2011.01.006.
30. Nasr-Azadani, M., and Meiburg, E., "Turbidity currents interacting with three-dimensional seafloor topography", ***Journal of Fluid Mechanics***, Vol. 745, (2014), 409-443, doi: 10.1017/jfm.2014.47.

Persian Abstract

چکیده

در این پژوهش، اثر تخلخل و زاویه‌ی نصب، ضخامت (بعد) و لایه دوم موانع نفوذپذیر بر کنترل و تله‌اندازی جریان غلیظ در آزمایشگاه بررسی شده است. برای این منظور، از یک پلیمر نامحلول و معلق و موانع از صفحات پلاکسی گلاس انتخاب شدند که از دو نوع شیاری و حفره‌ای استفاده شد. آزمایش‌ها با دو غلظت متفاوت، پنج تخلخل گوناگون، چهار زاویه‌ی مختلف، چهار ضخامت متفاوت و با دو لایه مانع انجام شدند. نتیجه‌ها نشان دادند که با افزایش تخلخل، میزان تله‌اندازی تا تخلخل بهینه روند کاهشی و سپس افزایشی دارد. بر این اساس، تخلخل بهینه برای موانع حفره‌ای و موانع شیاری به ترتیب ۲۲ و ۱۹ درصد به‌دست آمد. در همه‌ی آزمایش‌ها، تله‌اندازی حفره‌ای، با ۰/۱۳ و ۰/۱٤ درصد به‌ترتیب در غلظت‌های ۱۰ و ۲۰ درصد، بیشتر از شیاری بود. علاوه بر این، با افزایش زاویه، مقدار تله‌اندازی کاهش یافت و مقدار آن در شیاری نسبت به حفره‌ای به‌ترتیب با ضریب همبستگی‌هایی برابر ۰/۹۹۵ و ۰/۹۸۱، بیشتر مشاهده شد. اثر عمده موانع، کاهش سرعت و ایجاد کندی جریان تشخیص داده شد که متوسط سرعت در حفره‌ای ۳/٦۲ درصد بیشتر از شیاری به‌دست آمد. به ازای افزایش ضخامت با تخلخل ۱۰ درصد و نوع شیاری روند عبور مواد از مانع بیشتر شد. با ایجاد لایه دوم مانع عبور موارد از مانع هم در شیاری و هم در حفره‌ای روند افزایشی پیدا کرد و فاصله بهینه مانع دوم از اول معادل ۲/۲۵ متر به دست آمد.

IJE TRANSACTIONS C: Aspects Vol. 33, No. 9, (September 2020) 1721-1730

International Journal of Engineering

Journal Homepage: www.ije.ir

An Investigation of the Seismic Interaction of Surface Foundations and Underground Cavities Using Finite Element Method

E. Shoja, H. Alielahi*

Department of Civil Engineering, Zanjan Branch, Islamic Azad University, Zanjan, Iran

P A P E R I N F O

Paper history:
Received 26 April 2020
Received in revised form 09 May 2020
Accepted 12 June 2020

Keywords:
Surface Foundation
Underground Cavities
Finite Element Method
Seismic Interaction

A B S T R A C T

In this study, the seismic interaction of surface foundations and underground cavities was investigated. For this purpose, a parametric study of geometric dimensions of the foundation and cavity, their location, and the effect of the interaction between surface foundations and underground cavities was evaluated. The variable parameters include the ratio of the overburden height to the foundation width (H/B = 0.5, 1 and 2), the location ratio of the cavity to the foundation width (X/B=0, 2 and 8) and the ratio of the cavity diameter to the foundation width (d/B=0.5, 1 and 2), respectively. The accuracy of the finite element method was evaluated using a laboratory study and it was found that the used method provides an accurate prediction of tunnel behavior. The results indicated that by increasing the overburden height, the stress on the tunnel surfaces was increased for all values of X/B (the horizontal tunnel distance to the foundation width). Therfore, in the case where the tunnel is located exactly along the center at the bottom of the foundation (X/B=0, d/B=2), the maximum stress generated is approximately 2.13 times greater than its corresponding value in the ratio of the depth to width of 0.5 (X/B=0, d/B=0.5). It can be concluded that the higher overburden height, the greater stresses caused by the dynamic loads of the earthquake on the tunnel wall.

***doi**: 10.5829/ije.2020.33.09c.04*

1. INTRODUCTION

In recent years, tunneling has been focused on creating spaces suitable for transportation and utilities in urban environments. In fact, development of technology in machinery and drilling equipment makes it relatively easy to build such underground structures. Moreover, the limitations of surface spaces for implementation of construction projects as well as security issues have attracted the attention in construction of underground structures for civilian, military, and mining applications [1-6].

On the other hand, according to the seismicity of Iran and the dominant of seismic lateral forces arising from the earthquake in the design of structures, in most cases, it is necessary to have an adequate understanding of the behavior of the foundations when applying seismic forces in addition to static forces [7]. Many complex analysis and dynamic problems in earthquake engineering level are being carried out by various researchers around the world. The soil environment or the stone surrounding the structure and the foundation behavior has a significant impact on the structure's behavior against earthquake [8-13].

The site conditions, the structure geometric, the mechanical properties of the soil and the foundation behavior can be effective on the dynamic response of the structures. Therefore, given the increasing importance of using underground structures such as tunnels as well as the need for the foundations to be built around tunnels and the dynamic load caused by seismic load and the effect of the waves generated by the dynamic load on underground tunnels. Also, given the destructive effects that dynamic forces can have, an investigation on seismic interaction of surface foundations and underground tunnels required due to limited studies conducted in this area. Considering the increasing development of underground structures and high cost of construction for

*Corresponding Author Email: *H.alielahi@iauz.ac.ir* (H. Alielahi)

Please cite this article as: E. Shoja, H. Alielahi, An Investigation of the Seismic Interaction of Surface Foundations and Underground Cavities Using Finite Element Method, Journal of Engineering (IJE), IJE TRANSACTIONS C: Aspects Vol. 33, No. 9, (September 2020) 1721-1730

any of these structures as well as their importance in the intercity and inland transportation network, it is necessary to study their sustainability against the dangers of the earthquake and their resulting vibrations.

Various studies have been conducted on interaction of tunnels and the soil surroundings. Asakereh et al. [14] examined the behavior of the reinforced strip foundations on the reinforced sand with cavity under cyclic loading. To this end, several experiments were carried out on strip foundation located in reinforced or non-reinforced sand with geogrid with a cavity inside it. The number of reinforced layers and cyclic load range were evaluated. The presence of the cavity causes an increase in failure in the areas where foundations are under successive loading [14]. Asheghabadi and Matinmanesh [15] studied the seismic behavior of tunnel considering the interaction of soil-tunnel. The seismic analysis was conducted using the finite element method. This analysis was performed by considering three real history of ground movements. The results indicated that the existence of a tunnel exacerbates the seismic waves at the surface of the soil and the maximum amount of exacerbation occurs at the surface of the tunnel and soil contact [15]. Sabouni [16] studied variations of the displacement and effective stresses of the strip foundation in the presence of single and double cavities. For this purpose, the Plaxis 2D finite element software was used and the parameters such as size, location of the cavity, number of cavity and placement position (single cavity, two adjacent cavities and two cavities on each other) were investigated [16]. Lee et al. [17]studied the resistance of strip foundations in clay in the presence of underground cavities using the finite element method. Tsinidis et al. [18] studied tunels seismic response in soft soil. In the aforementioned study, several experiments were conducted to examine the response of box tunnels, which were under sinus and seismic stimulation in dry sand and soil to investigate the relative flexibility of the soil and tunnel as well as the interaction of soil and structure. The system was investigated using full-time history analysis with the exact implementation of the finite element models. The results indicate a vibrational deformation state along with known racking rocking for tunnels with box cross-section under seismic stimulation [18]. In a numerical parametric study, Tsinidis et al. [19] examined different rectangular soil-tunnel systems with the aim of identifying characteristics of the critical response of rectangular tunnels under transverse vibration. Numerical results showed that when the soil around the tunnel was unstable, a hybrid deformation pattern of vibrational and racking shape was developed for tunnels exposed to vibration, as well as internal deformations in the floor and lateral walls of the flexible tunnels [19]. Alielahi et al. [20] studied the seismic behavior of the ground in the presence of unlined tunnels exposed to the vertical waves of S and P using the boundary element method. Several simple and practical relationships presented for estimating the seismic zoning of environments in which unlined tunnels were used [20].

Most underground structures in urban areas, such as subway tunnels, are buried in shallow soil, and there are countless buildings on them. The presence of buildings around the tunnel in urban areas makes the seismic behavior of the tunnel different from the tunnel located in the suburban areas. When a tunnel is affected by dynamic loads, it vibrates and the vibration propagates in the soil in a wave motion. When a wave reaches the earth surface, it causes vibrations in buildings. In contrast, the vibration of buildings under dynamic loads also causes the tunnel to vibrate. If the tunnel or building is subjected to a critical force such as an earthquake or the distance between them is small, the interaction between the tunnel and the building foundation can cause serious damage to them. In order to investigate the problem, the dynamic interaction between the tunnel and the adjacent building should be examined and all the parameters that can be effective should be discussed so that if there is a building near the tunnel, its effect on the tunnel's internal forces should be determined. According to the explanations, the seismic interaction of surface foundations and underground cavities is investigated in this study. For this purpose, a parametric study of geometric dimensions of the foundation and cavity and their location and the effect that they can have on the interaction between surface foundations and underground cavities is evaluated using the finite element method. ABAQUS software [21] is used for simulation. One of the most important aspects of innovation and novelty in this study is considering the study of seismic interactions between surface foundations and underground cavities along with applying the effect of the earthquake on these structures.

2. THE PROCEDURE

The variable parameters in this study include the ratio of the overburden height to the foundation width (H/B: 0.5, 1 and 2), the location ratio of the cavity to the foundation width (X/B: 0, 2 and 8) and the ratio of the cavity diameter to the foundation width (d/B: 0.5, 1 and 2), respectively. These cases are shown in Table 1. According to the study conducted by Pais [22] at MIT (U.S.A.), the width and height of the foundation under investigation were considered 12 and 1.00 meters, respectively. So, due to the mentioned variables, 27 finite element models were simulated. The applied loads on the model of this study are dynamically considered.

3. FINITE ELEMENTS SIMULATION

The details of modeling in ABAQUS were presented in this part. These details include the definition of element type, material characteristics, boundary conditions,

TABLE 1. Introducing the cases in the present study

Number	Symbol	H/B	X/B	d/B
1	d/B: 0.5, X/B:0, H/B:0.5	0.5	0	0.5
2	d/B:1, X/B:0, H/B:0.5	0.5	0	1
3	d/B: 2, X/B:0, H/B:0.5	0.5	0	2
4	d/B: 0.5, X/B:2, H/B:0.5	0.5	2	0.5
5	d/B:1, X/B:2, H/B:0.5	0.5	2	1
6	d/B:2, X/B:2, H/B:0.5	0.5	2	2
7	d/B:0.5, X/B:8, H/B:0.5	0.5	8	0.5
8	d/B: 1, X/B:8, H/B: 0.5	0.5	8	1
9	d/B: 2, X/B:8, H/B: 0.5	0.5	8	2
10	d/B:0.5, X/B:0, H/B:1	1	0	0.5
11	d/B:1, X/B:0, H/B:1	1	0	1
12	d/B:2, X/B:0, H/B:1	1	0	2
13	d/B:0.5, X/B:2, H/B:1	1	2	0.5
14	d/B:1, X/B:2, H/B:1	1	2	1
15	d/B:2, X/B:2, H/B:1	1	2	2
16	d/B:0.5, X/B:8, H/B:1	1	8	0.5
17	d/B:1, X/B:8, H/B:1	1	8	1
18	d/B:2, X/B:8, H/B:1	1	8	2
19	d/B:0.5, X/B:0, H/B:2	2	0	0.5
20	d/B:1, X/B:0, H/B:2	2	0	1
21	d/B:2, X/B:0, H/B:2	2	0	2
22	d/B:0.5, X/B:2, H/B:2	2	2	0.5
23	d/B:1, X/B:2, H/B:2	2	2	1
24	d/B:2, X/B:2, H/B:2	2	2	2
25	d/B:0.5, X/B:8, H/B:2	2	8	0.5
26	d/B:1, X/B:8, H/B:2	2	8	1
27	d/B:2, X/B:8, H/B:2	2	8	2

loads, analysis type, interaction between surfaces, mesh, and the element used for mesh.

The geometric properties of the model are shown in Figure 1. The solid technique was used to simulate all the sections (Figure 2).

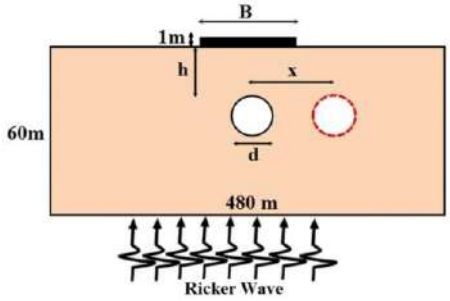

Figure 1. The geometric properties of the models

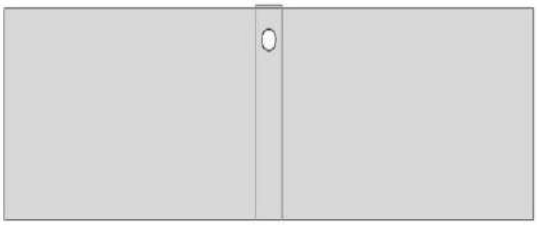

Figure 2. A sample of the defined geometric model

The behavior of sections is also three-dimensional and deformable. The deformable section is one of the five sections used in this software to model the deformable sections in two and three-dimensional spaces [21]. The characteristics of the soils are presented in Table 2. These parameters were selected based on the study of Jafari et al. [23].

The damping of materials in the soil generally results in from viscosity, friction, and plasticity development. A soil damping matrix is required for soil and structural analysis. The coefficients α and β of the damping matrix are calculated according to Riley's method (Equations (1) and (2)) [15].

$$[c]= \alpha [m]+ \beta [k] \quad (1)$$

$$\frac{1}{2}\begin{bmatrix} \frac{1}{\omega i} & \omega i \\ \frac{1}{\omega j} & \omega j \end{bmatrix}\begin{Bmatrix} \alpha \\ \beta \end{Bmatrix} = \begin{Bmatrix} \xi i \\ \xi j \end{Bmatrix} \quad (2)$$

Given the half-infinity of the real model, the seismic energy applied into the model must be exited through the boundaries (geometric damping). There are several methods to apply the energy-absorbing boundary. One of these methods is the viscose boundary. In this method, the damper elements are placed on the boundaries. The coefficiency of these damper elements is obtained from Equations (3) and (4) [15] in which ρ is the soil density, Cse is the shear wave velocity and A is the lining surface.

$$Fd=Cd.\dot{u} \quad (3)$$

$$Cd=\rho.Cse.A \quad (4)$$

There are two types of spring and damper elements in ABAQUS software [21]. In ABAQUS/Standard, there is just one node element. A dual-mode element can only be used in ABAQUS/Explicit. ABAQUS/Explicit has been used to perform nonlinear dynamic analysis. The spring and damper elements are defined in the interaction module using the Springs/Dashpots menu. Explicit

TABLE 2. Parameters of the used materials

β	α	n	E (kPa)	ρ (kg/m3)	Material name
0.08	0.001	0.30	40000	1900	Soil layer
---	---	0.20	20560000	2400	Concrete

dynamic analysis was used to analyze the models. Ricker type with a PGA scale of 0.3g and a central frequency of 4.3 Hz was used to apply the vertical invasive wave, and a shear wave velocity of 400 m/s was considered at the bottom of the soil block (Figure 3).

Also, in order to reduce the effect of the reflection coefficient applied to the model boundaries, the dimensions of the model were considered to be large enough.

For the regularity of the meshing or more simplicity in some parts of the modeling, there is a need for different parts of the model to be built and interconnected separately. In places where two parts of a model are to be connected, the degrees of freedom of the connected surfaces should be conjuncted to each other. The interaction tool is used for this purpose. By fixing the nodes on the two surfaces, this tool keeps their positions relative to each other by analyzing the displacements of the two nodes in a problem-orientation

In areas where a collision occurs during nonlinear analysis between two separated elements, the collision characteristics must be defined on two levels. Otherwise, the collision is not considered, and the two elements collapse into each other. In order to define the property of the collision, the nature of the collision of the elements should be defined in the software in terms of the nature of the collision. In normal collisions, the surface of the collision has tangential and frictional behavior. The use of contact behavior in modeling has the capability of simulating the collision and separating two levels from each other [21].

Since the materials used in the models include the soil and concrete of the tunnel, the interaction and contacts between the surfaces should be properly simulated. To this end, through the interaction module which is commonly used to define contacts and interactions between surfaces, using the Tie interaction, the interaction between the soil and concrete of the tunnel is applied to the models.

Tie interaction is one of the practical interactions in civil engineering which can be used to integrate the soil interaction and the concrete tunnel in which both are modeled with solid elements [21, 24].

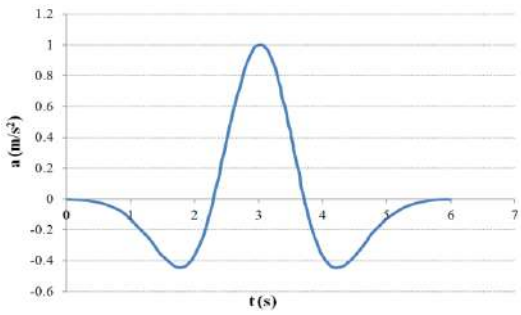

Figure 3. History of the Ricker wave

One of the most important parts of ABAQUS [21] software is defining or attributing mesh attribution. This part can be called the most important part of the software. In the finite element analysis of this study, models with large elements analyze at first (few numbers of elements) and one of the output quantities such as the maximum stress value generated at a desired point in the model is noted. Then the elements become finer and the problem is analyzed again. The process of subtracting the elements continues until the difference between the results becomes very low. Meshing or gridding which is representative of the model is sufficiently good enough to ensure that the applied forces are exactly calculated (Figure 4).

C3D8R soil elements were selected in which linear fragile eight nodes cube elements are reduced by an integral method. In each node, these elements have three degrees of freedom in three directions which in total constitute 24 degrees of freedom for each element and they are practical and reliable in terms of efficiency and accuracy.

4. VALIDATION OF THE NUMERICAL MODEL

Validation of the finite element method was carried out according to study conducted by Jiang et al. [24]. In Jiang's study, the seismic response of underground tunnels was studied using a laboratory study and the finite element. The laboratory study was conducted by the shaking table. The length, width, and height of the shear box of the soil were 3, 1.80, and 1.91 m, respectively. It consists of 16 steel frames which are placed on each other (Figure 5).

Each frame is made up of a square steel tube with dimensions of 2×100×100 mm. The tunnel laboratory model was selected based on Shanghai tunnel. The cross-section of this tunnel is 3000×3000 mm and the thickness of the walls is 300 mm. According to the laboratory facilities, the laboratory model was constructed on a scale of 1:5 as shown in Figure 6.

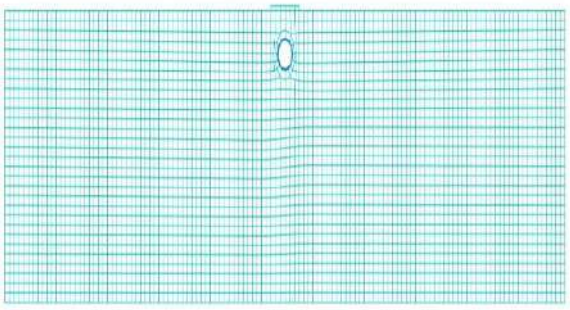

Figure 4. Cross-section meshing of one of the models understudy

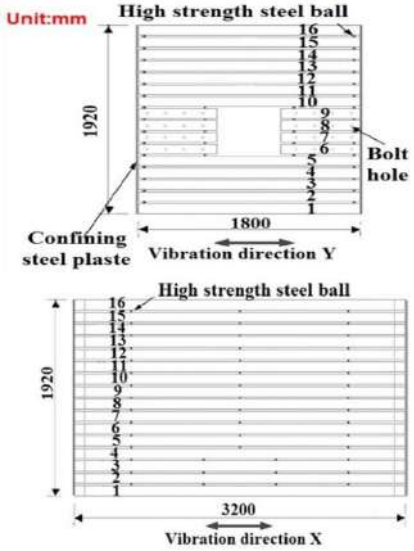

Figure 5. The shear box of the soil used in Jiang et al. study [25]

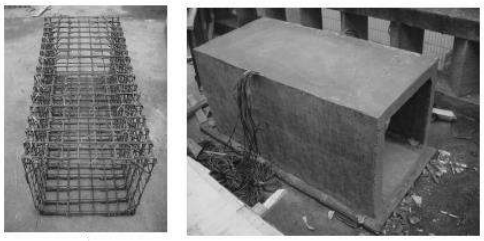

Figure 6. The tunnel modeling of Jiang et.al study [25]

Saturated clay was used in the experiment. Soils were poured into 20 cm layers in a box. Each layer was knocked into a specific density. Table 3 summarized the soil specifications used by Jiang et al. [25].

To measure the response of the structure, the soil, the shear box, accelerometers, pressure measurement devices, and sensors for measuring displacement at different points inside and outside the soil were embedded (Figure 7). El Centro earthquake characteristics were used for seismic stimulation. Figure 8 shows the history of the stimulus applied. Loading was applied from the bottom of the model and the outputs related to the center of the foundation and the tunnel were extracted. The outputs related to the two points A6 and A12 are shown in Figures 9 and 10.

TABLE 3. The physical characteristics of the soil in Jiang et.al study [24]

Special Dry Weight (g/cm^3)	Porosity Coefficient (e)	Adhesion Resistance (kPa)	Internal Friction Angle (°)
1.53	0.943	24.40	**27.9**

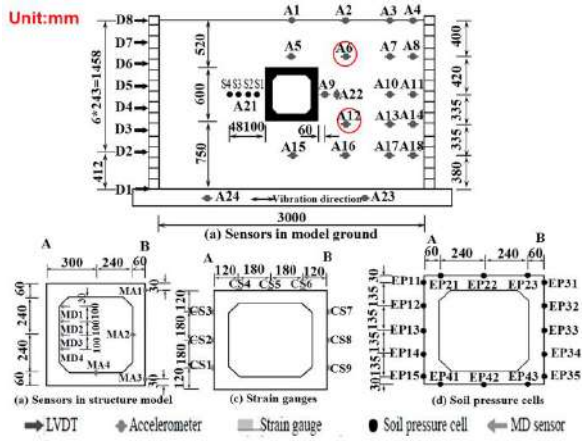

Figure 7. Shear box of the soil used in Jiang et al. study [25]

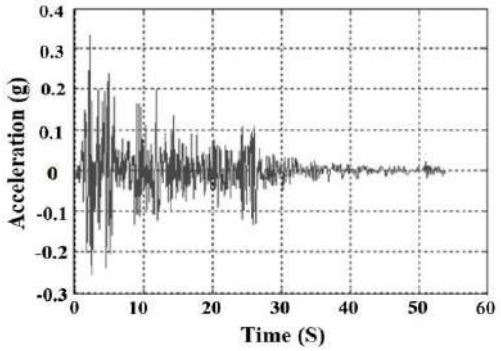

Figure 8. El Centro Earthquake record [25]

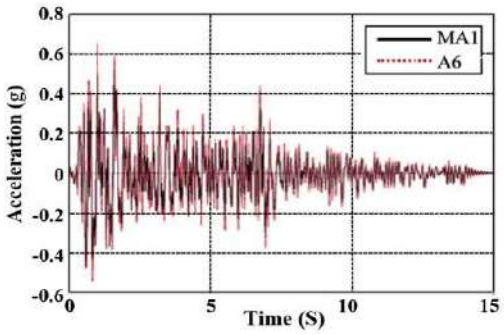

Figure 9. The soil acceleration at A6 in Jiang et al. study [25]

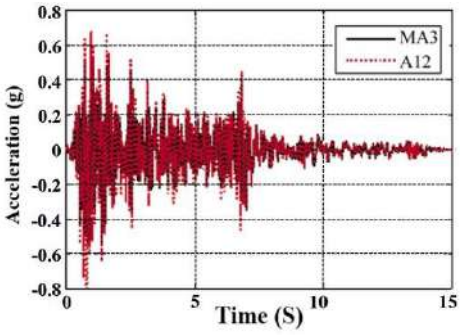

Figure 10. The soil acceleration at A12 in Jiang et al. study [25]

The model introduced in Jiang et al. [25] study was simulated according to the specifications mentioned using the finite element method used in the present study (Figures 11 and 12). The outputs which include the acceleration generated at points A6 and A12 are extracted (Figures 13 and 14). The details of the used method were presented in the previous part.

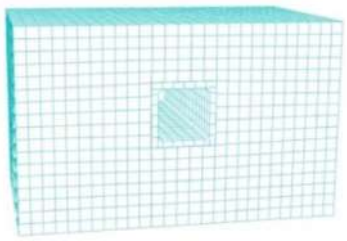

Figure 11. The meshing of Jiang et al model using the finite element method in the present study

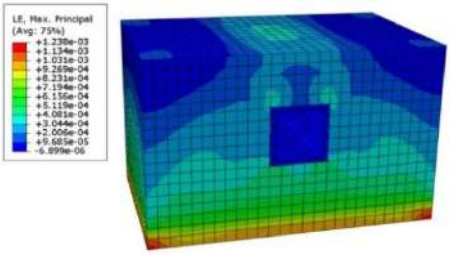

Figure 12. The strain distribution in the simulated model using the finite element method in the present study

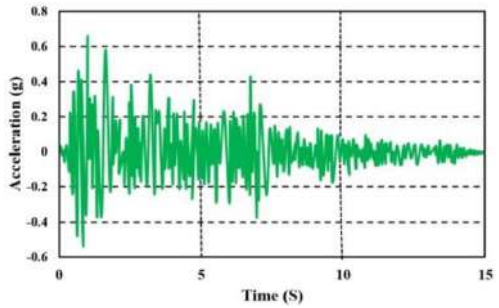

Figure 13. The acceleration generated at point A6 in the ABAQUS software

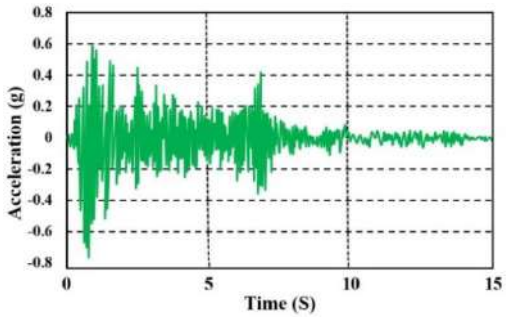

Figure 14. The acceleration generated at point A12 in the ABAQUS software

Figures 15 and 16 compare the results of the study conducted by Jiang et al. [25] and the simulated model using the finite element method used in this study. Given the obtained values, it is seen that the results are very close to each other. Therefore, the use of finite element simulation is accurate.

5. RESULTS OF THE PARAMETRIC STUDIES

The outputs are stress, displacement, and acceleration, respectively. The performance of simulated cases is compared using various diagrams, so that the parameters in the present study which include the tunnel diameter, the depth of tunnel location, the tunnel distance, and the foundation depth can be evaluated. For this purpose, each output of acceleration, stress, and displacement are interpreted separately according to the variables which are H/B, X/B, and d/B ratios, respectively.

5. 1. Evaluating the Maximum Acceleration of the Tunnel Acceleration response of tunnels for different values of X/B (0, 2, and 8) is illustrated in Figures 17a to 17c. The studied parameters are shown on each of the figures for better understanding the diagrams. Also in Figure 18d, the acceleration responses of all the tunnels (27 models) are presented to evaluate their

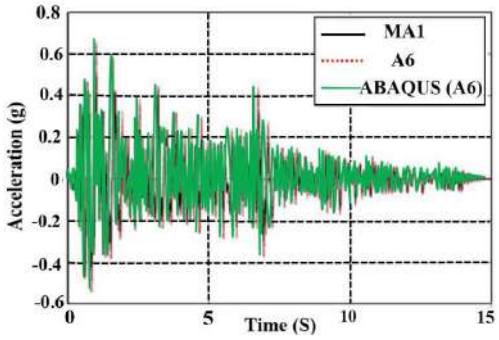

Figure 15. The acceleration generated at point A6 in ABAQUS software

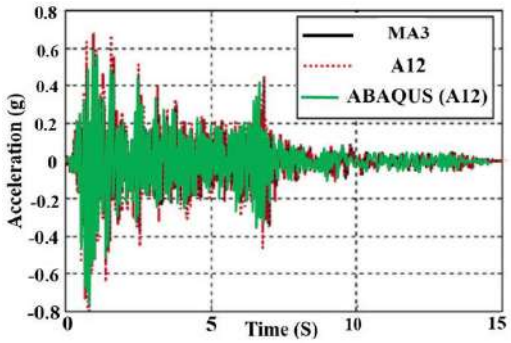

Figure 16. The acceleration generated at point A12 in ABAQUS software

overall behavior. According to these diagrams, when the ratio of tunnel location depth to the foundation width is equal to 2 (H/B=2.0), the generated acceleration value in all cases is less than other cases (H/B=0.5 and H/B=1.0). The reason for this is that whatever the overburden height is lower, (the depth of tunnel location), the soil becomes more vibrational under the influence of an earthquake, and its characteristics and parameters change. Thereby the acceleration applied to the tunnel lining is increased.

Another issue that can be seen from the illustrations in Figure 17 is that the acceleration created in the tunnel lining for different location depths (H/B=0.5, H/B=1, H/B=2) is very close when the ratio of horizontal distance of the tunnel from the center of the foundation is 2 and the diameter-to-width ratio is 2. In other words, the difference between the acceleration in the tunnel lining is very close to each other. Another parameter that can influence the acceleration in the tunnel lining is the horizontal distance of the tunnel relative to the center of the foundation which can be seen according to Figure 17. The acceleration generated in the tunnel lining is reduced in most cases by increasing the horizontal distance of the tunnel to the center of the foundation. According to the results, it can be stated that the horizontal distance of the tunnel relative to the center of the foundation has an effective role on the acceleration generated on the tunnel lining and this should be considered when designing tunnels near urban areas.

Another variable parameter which is also considered in this study is the diameter variation ratio of the tunnel diameter. As can be seen in Figure 17, any changes in the diameter parameter when the horizontal distance of the tunnel to the width of the foundation is equal to 2 (X/B = 2), the changes in the diameter parameter results in more changes in the generated acceleration. In other words, the slope of acceleration in this case is higher than other cases.

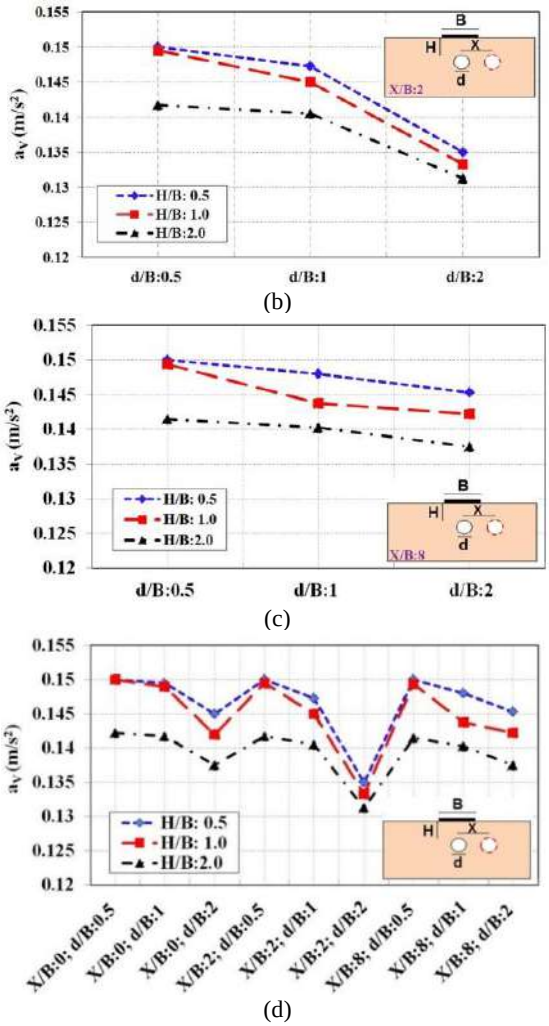

Figure 17. Comparison of the generated acceleration values in simulated tunnels a: X/B:0 b: X/B:2 c: X/B:8 d: total comparison

5. 2. Comparison of Maximum Stress Values in the Tunnel Figure 18 compares the stress values generated in simulated tunnels with the aim of examining H/B ratios for various horizontal distances (X/B). As can be seen, by increasing the overburden height, the stress on the tunnel surfaces is increased for all X/B values.

For example in the case where the tunnel is located exactly along the center and at the bottom of the foundation (X/B=0) and the diameter to width ratio of the foundation is equal to 2, the maximum stress generated in the depth to width ratio of the foundation is 2 and this is approximately 2.13 times greater than its corresponding value in the ratio of depth to width of 0.5.

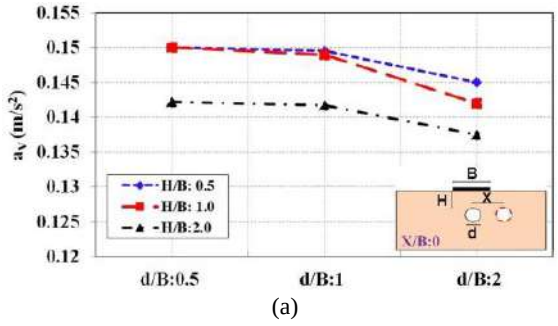

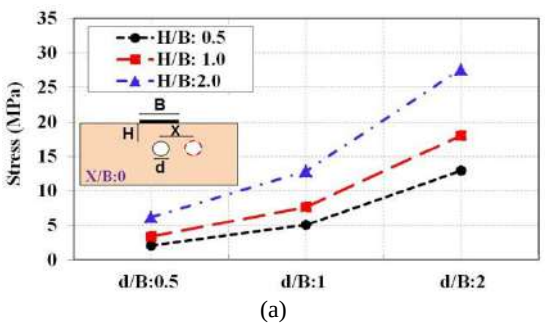

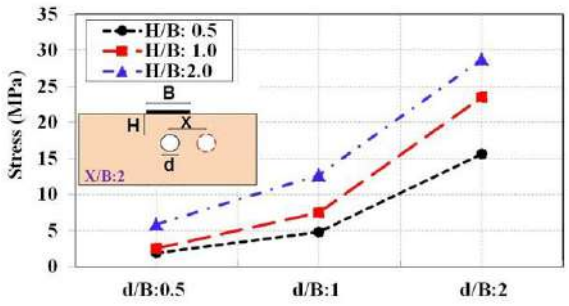

(b)

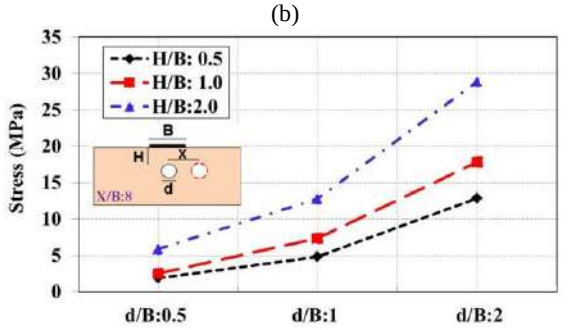

(c)

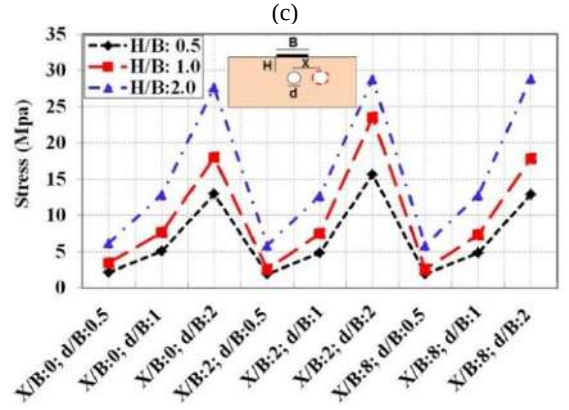

(d)

Figure 18. Comparison of the generated stress values in simulated tunnels **a:** X/B:0 **b:** X/B:2 **c:** X/B:8 **d:** total Comparison

So it can be concluded that the higher the overburden height, the greater the stresses caused by the dynamic loads of the earthquake on the tunnel wall. When the effect of the dynamic loading of earthquake forces is applied to the models, the depth of tunnel location is directly related to the overburden weight on the tunnel, and whatever this depth increases, the tunnel is placed under less stress.

5. 3. Comparison of the Maximum Displacement Values in the Tunnel The tunnel walls displacement values are compared in Figure 19. As shown in these diagrams, the tunnel lining displacement has been reduced by increasing the depth of the tunnel at all the different horizontal distances of the tunnels. For the case that the tunnel is located exactly along the center and at the bottom part of the foundation (X/B=0) and the diameter to width ratio of the foundation is equal to 0.5, the maximum displacement in the depth to width ratio of the foundation is approximately 5% lower than its corresponding value in the depth ratio to width of the foundation 0.5. On the other hand, according to Figure 19, it can be seen that by increasing the horizontal distance of the tunnel to the central axis of the foundation, the tunnels which have the same diameter to width ratio of foundation (X/B=1) carry lower displacements by increasing depth of location. Therefore, it can be concluded that when underground tunnels are exposed to dynamic earthquake loading, selecting the diameter of the tunnels can affect the displacement of the tunnel lining.

When the tunnel is located exactly along the center and at the bottom of the foundation (X/B=0) and the diameter to width ratio of the foundation is equal to 0.5, the maximum displacement generated in the depth-to-width ratio of the foundation 2 is 5 percent lower than its corresponding value in the depth to width ratio of 0.5. On

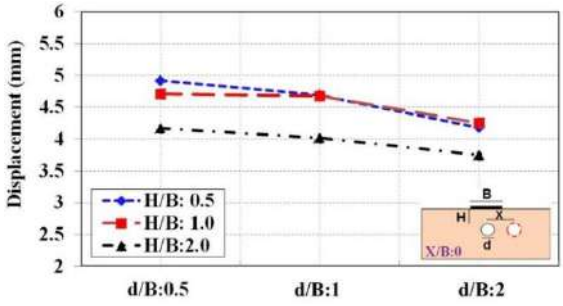

(a)

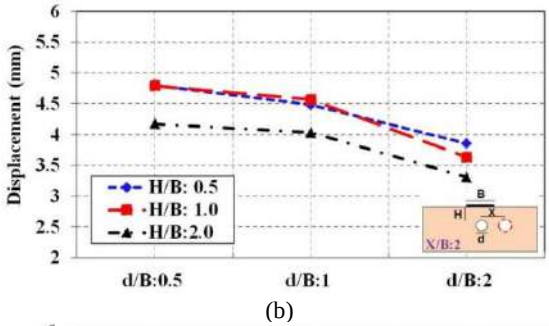

(b)

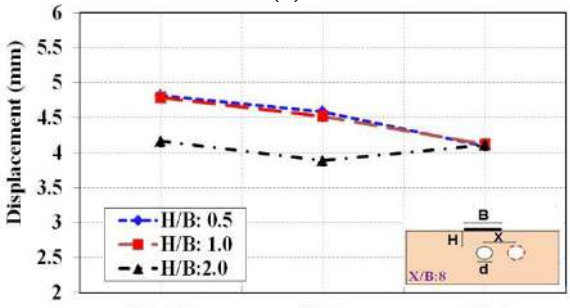

(c)

Figure 19. Comparison of the generated displacement values in simulated tunnels **a:** X/B:0 **b:** X/B:2 **c:** X/B:8

the other hand, according to Figure 19, it can be seen that by increasing the horizontal distance of the tunnel to the central axis of the foundation, the tunnels which have the same diameter to width ratio of foundation (X/B=1) carry lower displacements by increasing depth of location. This can be deduced when the underground tunnels are exposed to dynamic earthquake loading, selecting the diameter of the tunnels can affect the displacement of the tunnel lining.

5. CONCLUSION

In the present study, the seismic interaction between the surface foundation and underground cavities was investigated. For this purpose, a parametric study of the geometric dimensions of the foundation and cavity and their location and the effect that they can have on the interaction between surface foundations and underground cavities is evaluated using a finite element method. ABAQUS software was used for simulation. Variable parameters include the ratio of the overburden height to the foundation width (0.5, 1 and 2), the ratio of the cavity location to the foundation width (0, 2 and 8) and the ratio of the cavity diameter to the foundation width (0.5, 1 and 2). The most important results are presented below:

- Whatever the overburden height (depth of tunnel deployment) is lowered, the soil will become more vibrational under the influence of an earthquake, and its characteristics and parameters change, thereby increasing the acceleration applied to the tunnel lining.
- The horizontal distance of the tunnel towards the center of the foundation plays a significant role in the acceleration generated on the tunnel lining and when designing tunnels near urban areas, this should be taken into consideration.
- When the dynamic loading effect of seismic forces is applied to the models under investigation, the depth of the tunnel has a direct relationship with the weight of the overburden on the tunnel, and whatever this depth increases, the tunnel will be under less stress.
- Comparison of the displacement values generated in the tunnel walls shows that when the tunnel is located exactly below the central axis of the foundation (X/B = 0), the displacement of tunnel lining is increased by increasing depth of tunnel location. For the case where the tunnel is located exactly along the center and at the bottom of the foundation (X/B=0) and the diameter to width ratio of the foundation is equal to 0.5, the maximum stress generated in the depth to width ratio of the foundation 2 is approximately 2.13 times greater than its corresponding value in the ratio of depth to width of 0.5.
- By increasing the horizontal distance of the tunnel to the central axis of the foundation, the tunnels which have the same diameter to width ratio of foundation (X/B=1), carry lower displacements by increasing depth of location. So it can be concluded that when the underground tunnels are exposed to dynamic earthquake loading, selecting the diameter of the tunnels can affect the displacement of the tunnel lining.

6. REFERENCES

1. Rasti, A. and Marandi, S.M., "Parameters analysis of the covering soil of tunnels constructed in liquefiable soils", ***International Journal of Engineering*, *Transactions A: Basics,*** Vol. 25, No. 4, (2012), 333-346. doi: 10.5829/idosi.ije.2012.25.04a.05
2. Nikbakht, R., Moghtaderi Esfahani, A., Behnamfar, F. and Ghandil, M., "Analysis of structural vibrations due to passage of underground trains", ***International Journal of Engineering*, *Transactions C: Aspects,*** Vol. 29, No. 6, (2016), 742-751. doi: 10.5829/idosi.ije.2016.29.06c.00
3. Tsinidis, G., de Silva, F., Anastasopoulos, I., Bilotta, E., Bobet, A., Hashash, Y.M., He, C., Kampas, G., Knappett, J. and Madabhushi, G., "Seismic behaviour of tunnels: From experiments to analysis", ***Tunnelling and Underground Space Technology***, Vol. 99, (2020), 103334. https://doi.org/10.1016/j.tust.2020.103334
4. Karabin, M., Kitsakis, D., Koeva, M., Navratil, G., Paasch, J.M., Paulsson, J., Vučić, N., Janečka, K. and Lisec, A., "Layer approach to ownership in 3d cadastre in the case of underground tunnels", Land Use Policy, (2020), 104464. https://doi.org/10.1016/j.landusepol.2020.104464
5. Xu, Q., Overview of underground space utilization and standardization suggestions, in Data processing techniques and applications for cyber-physical systems (dpta 2019). 2020, Springer.195-204.
6. Cui, J. and Nelson, J.D., "Underground transport: An overview", ***Tunnelling and Underground Space Technology***, Vol. 87, (2019), 122-126. https://doi.org/10.1016/j.tust.2019.01.003
7. Jahani, M., Oulapour, M. and Haghighi, A., "Evaluation of the seismic bearing capacity of shallow foundations located on the two-layered clayey soils", ***Iranian Journal of Science and Technology, Transactions of Civil Engineering***, Vol. 43, No. 1, (2019), 49-57. https://doi.org/10.1007/s40996-018-0122-3
8. Saberi, M., Annan, C.-D. and Konrad, J.-M., "Implementation of a soil-structure interface constitutive model for application in geo-structures", ***Soil Dynamics and Earthquake Engineering***, Vol. 116, (2019), 714-731. https://doi.org/10.1016/j.soildyn.2018.11.001
9. Achouri, A. and Amrane, M.N., "Effect of structures density and tunnel depth on the tunnel-soil-structures dynamical interaction", ***Pollack Periodica***, Vol. 15, No. 1, (2020), 91-102. https://doi.org/10.1556/606.2020.15.1.9
10. Asheghabadi, M.S. and Rahgozar, M.A., "Finite element seismic analysis of soil–tunnel interactions in clay soils", ***Iranian Journal of Science and Technology, Transactions of Civil Engineering***, Vol. 43, No. 4, (2019), 835-849. https://doi.org/10.1007/s40996-018-0214-0
11. Ozturk, B., "Free vibration analysis of beam on elastic foundation by the variational iteration method", ***International Journal of Nonlinear Sciences and Numerical Simulation***, Vol. 10, No. 10, (2009), 1255-1262. https://doi.org/10.1515/IJNSNS.2009.10.10.1255
12. Ozturk, B. and Coskun, S.B., "The homotopy perturbation method for free vibration analysis of beam on elastic foundation", ***Structural Engineering and Mechanics***, Vol. 37, No. 4, (2011), 415-425. http://doi.org/10.12989/sem.2011.37.446

13. Ozturk, B. and Coskun, S.B., "Analytical solution for free vibration analysis of beam on elastic foundation with different support conditions", ***Mathematical Problems in Engineering***, Vol. 2013, (2013). https://doi.org/10.1155/2013/470927
14. Asakereh, A., Moghaddas Tafreshi, S. and Ghazavi, M., "Strip footing behavior on reinforced sand with void subjected to repeated loading", ***International Journal of Civil Engineering***, Vol. 10, No. 2, (2012), 139-152.
15. Asheghabadi, M.S. and Matinmanesh, H., "Finite element seismic analysis of cylindrical tunnel in sandy soils with consideration of soil-tunnel interaction", ***Procedia Engineering***, Vol. 14, (2011), 3162-3169. https://doi.org/10.1016/j.proeng.2011.07.399
16. Sabouni, R., "Displacement and effective stresses changes underneath strip footing on stiff ground with single and double voids", in Published in the proceeding of GeoMontreal 2013 Conference, Montreal, Canada, 29th October-3rd September. DOI: 10.13140/2.1.1334.1447
17. Lee, J.K., Jeong, S. and Ko, J., "Undrained stability of surface strip footings above voids", ***Computers and Geotechnics***, Vol. 62, (2014), 128-135. https://doi.org/10.1016/j.compgeo.2014.07.009
18. Tsinidis, G., Pitilakis, K. and Madabhushi, G., "On the dynamic response of square tunnels in sand", ***Engineering Structures***, Vol. 125, (2016), 419-437. https://doi.org/10.1016/j.engstruct.2016.07.014
19. Tsinidis, G., "Response characteristics of rectangular tunnels in soft soil subjected to transversal ground shaking", ***Tunnelling and Underground Space Technology***, Vol. 62, (2017), 1-22. https://doi.org/10.1016/j.tust.2016.11.003
20. Alielahi, H., Kamalian, M. and Adampira, M., "Seismic ground amplification by unlined tunnels subjected to vertically propagating sv and p waves using bem", ***Soil Dynamics and Earthquake Engineering***, Vol. 71, (2015), 63-79. https://doi.org/10.1016/j.soildyn.2015.01.007
21. Hibbitt, H., Karlsson, B. and Sorensen, P., "Abaqus theory manual, version 6.3", Pawtucket, Rhode Island, USA, (2006).
22. Pais, A.L., "Dynamic coupling of multiple structures through soil", Massachusetts Institute of Technology, (1988),
23. Jafari, H., Atrchian, M. and Daghigh, Y., "Dynamic response of buried pipelines retrofitted with concrete canvas panels under blast loading", ***Iranian Journal of Science and Technology, Transactions of Civil Engineering***, (2020), 1-15. https://doi.org/10.1007/s40996-020-00392-y
24. Jiang, L., Chen, J. and Li, J., "Seismic response of underground utility tunnels: Shaking table testing and fem analysis", ***Earthquake Engineering and Engineering Vibration***, Vol. 9, No. 4, (2010), 555-567. https://doi.org/10.1007/s11803-010-0037-x

Persian Abstract

چکیده

در مطالعه ی حاضر به بررسی اندرکنش لرزه‌ای پی های سطحی و حفره های زیرزمینی پرداخته شد. برای این منظور با استفاده از مطالعه پارامتریک ابعاد هندسی پی و حفره و موقعیت قرار گیری آن‌ها و تاثیری که می توانند بر اندرکنش بین پی های سطحی و حفره های زیرزمینی داشته باشند، ارزیابی شد. متغیرها به ترتیب شامل نسبت ارتفاع روباره به عرض پی H/B (۰.۵، ۱ و ۲)، نسبت موقعیت قرارگیری حفره به عرض پی X/B (۲،۰ و ۸) و نسبت قطر حفره به عرض پی d/B (۰.۵، ۱ و ۲) می باشند. بارهای اعمال شده به صورت بار لرزه ای به کف مدل به صورت دینامیکی در نظر گرفته شدند. اعتبارسنجی روش اجزاء محدود به کار رفته، با استفاده از شبیه سازی یک مطالعه‌ی آزمایشگاهی مورد بررسی قرار گرفت و نشان داده شد که تحلیل عددی صورت گرفته، از تطابق خوبی نسبت به واقعیت برخوردار می باشد. مقایسه مقادیر تنش ایجاد شده در تونل های شبیه سازی شده نشان می دهد با افزایش ارتفاع روباره، تنش ایجاد شده برروی سطوح تونل به ازای تمامی مقادیر X/B (فاصله ی افقی تونل نسبت به پی) افزایش یافته است. بطوریکه به عنوان مثال در حالتی که تونل دقیقاً در امتداد مرکزی و در قسمت تحتانی پی قرار گرفته (X/B=۰) و نسبت قطر به عرض پی برابر ۲ می باشد، بیشینه تنش ایجاد شده در نسبت عمق به عرض پیِ ۲، حدوداً ۲.۱۳ برابر از مقدار متناظرش در نسبت عمق به عرض ۰/۵۰ بیشتر شده است. از این موضوع می توان به این نتیجه دست یافت که هر چقدر ارتفاع روباره بیشتر باشد، تنش های ناشی از بارهای دینامیکی زلزله بر جداره ی تونل ها بیشتر می شود. به عبارتی می توان بیان نمود هنگامی که اثر بارگذاری دینامیکی ناشی از نیروی زلزله بر روی مدل های مورد بررسی اعمال شود، عمق قرار گیری تونل رابطه ای مستقیم با وزن سربار وارده بر روی تونل دارد و هر چقدر این عمق بیشتر شود، تونل تحت تنش‌های کمتری قرار می گیرد.

International Journal of Engineering

Journal Homepage: www.ije.ir

Intrusion of Geomesh in Gypseous Soil Under Single Footing

W. A. Zakaria*

Engineering College, Civil Department, University of Diyala, Iraq

P A P E R I N F O

Paper history:
Received 27 April 2020
Received in revised form 10 June 2020
Accepted 12 June 2020

Keywords:
Footing
Geo-grid Reinforcement
Geo-mesh Reinforcement
Laboratoryl
Soil Improvement

A B S T R A C T

Methods to improve bearing capacity of footing resting of collapsing soil can, in fact, take two approaches, improving soil strength properties and intrusion of reinforcing sorces into soil. The footing is modeled by a square steel plate 0.1 by 0.1 m. The footing is loaded as to have a stress of 40 kPa and settlement is receded in dry and in soaking conditions. Two depths of the geo-mesh reinforcement are used, one B (B is width of footing) and 0.5B. For one B depth, three different square sizes of geo-mesh are used, 4B, 6B, and 8B. For the reinforcement depth of 0.5B the three sizes of the geo-mesh used are, 3.5B, 5.5B, and, 7.5B. Results reveal that the best improvement obtained is the case of square geo-mesh width of 7.5B and located at depth of B/2 under footing, with an improvement in terms of collapse settlement of 35%, and a settlement reduction in dry condition of 50%. The least improvement is the case of square geo-mesh with width of 4B and depth of one B, and it was really negligible, about 4% decrease in collapse settlement. Other cases varied between the two mentioned ratios. For findings of study, author recommends not to use geomesh size less than size of footing and not to place it in a depth more than half footing width. As such, in a whole, the effectiveness of geomesh in reducing the settlement of collapsing soil is obvious if used in proper way.

***doi**: 10.5829/ije.2020.33.09c.05*

1. INTRODUCTION

The concept of reinforcing waek soil is rather old and had come into effect to touch the collapsing soil. Gemesh or geogrid had been well perfected into use here in this country and abroad. Problematic soils are widely exist in the dry surface of the global. In this type of soil, the soil grains are attached by bridges of salts acting as a cementing or bonding material, as the case of the gypseous soil [1, 2]. The salts bridging soil exists in countries such as China, Australia, and also in Europe [3]. Some Arab Countries are also include in the list, such as, Iraq, Iran, Algeria, Syria, and, Bahrain. In these places the gypsum may range between 10-70%. The fundamental property of such soils is that it can bear large loads when dry and run out in large reduction in volume, without additional stress, when water finds its way to the soil grains and by dissolution breaking out the bonding bridges of gypsum [2]. It is worth to mention that gypsum dissolves at a rate of 2.6 gram per liter at 25˚C and the rate of dissolution increases by three-fold as the temperature changes from 5 to 23˚C [4]. According to literature [5] mainly water can get to soil from top by raining, for instance, or it can penetrate from bottom as there is a rise in water table. The methods for improving the gypseous soil can take three aspects; the first is deal with the soil without the intrusion of any type of materials or reinforcement into soil, such as using heavy compaction or even deep detonation using small and safe charges. The second aspect is to introduce effective stabilizing materials or some types of reinforcement [6]. The last aspect is to carry out a soil replacement. Each method of the three aspects has its own limitations and condition for use. The use of the geo-grid reinforcement has been in progress for many decades in normal soil. It was used not only in soil foundation engineering, but also in highways and so on. The reinforcement of soil has a long tradition. Already 3500 years ago the Sumerians

*Corresponding Author Email: *waadzakariya@yahoo.com* (W. A. Zakaria)

Please cite this article as: W. A. Zakaria, Intrusion of Geomesh in Gypseous Soil Under Single, International Journal of Engineering (IJE), IJE TRANSACTIONS C: Aspects Vol. 33, No. 9, (September 2020) 1731-1736

under King Kurigalzu erected the temple of Aqar Quf in Mesopotamia near Bagdad/ Iraq. They used reed mats to stabilize the foundations and the brick walls [7]. The main function of geo-grids is reinforcement. Depending on the application under consideration, reinforcement could either be uniaxial (strength in one direction) or biaxial (strength in all directions). They are graded by a number of performance properties for instance tensile strength, junction efficiency, and so on. The best depth of first geogrid layer in granular soil was found at depth of 0.15 from thickness and from height of soil layer [8]. On the other hand, that the permanent strain soil reinforced geogrid samples have decreased by 44% compared to that in unreinforced soil samples [9].

According to karim et al. [10], studied the effect of cyclic loading on foundations for different engineering structures constructed on soft ground. They improved soil by fly ash, geogrid and both. They demontrated that settlement of footing resting on treated models with fly ash and geogrid layers performed better than other improving techniques. Using PLAXIS FE program, the study conducted by Emeka et al. [11] recommended of 30%of existing soil should be replaced by mixture of lateritic soil and quarry dust. They stated that it is advisable to replace some quantities of problematic soil with mixture stated for purposes of soil improvement. The study conducted by Al-Amli et al. [12] carried out a non-linear analysis for reinforced concrete members on saturated and unsaturated soil using the FE ABAQUS program. They showed that plastic strains in reinforced concrete members in unsaturated soil was about 54, 58, 53, and 52% when geogrid ratios are (without geogrid 60, 40, 20%) respectively with some value of applied stress. It is worth to mention that size and depth of empedment of geogrids had not been mathematically formulated and standarized, and design formula did not flaot to surface yet. Additional knowledge to such subject is still sticking to the state-of-the-art review.

2. METHOD

2. 1. Properties of Soil Used The soil used in this study is totally brought by a pickup car from the western desert, Al-Anbar governorate, about 200 km west of the capital Baghdad. Al-Anbar governorate, in addition to Salahuldeen north of Baghdad, is quit famous with its soil as being rich in gypsum content, (as such, those places have great issues in their engineering facilities). The mass of soil is brought from a depth of 0.60 m below the natural ground level and packed into double nylon bags and transported to the laboratory in Baghdad. It is believed that the top soil does not represents a homogeneous soil as it was much contaminated with other materials, as such, a depth of 0.6 m is found adequate for study. These bags are dumped together as a mass on to a large sheet of thick nylon, remixed thoroughly as to get homogeneous soil, packed again into nylon bags, and stored in place in concern ready to be used when needed. To determine the gypsum content in soil, four specimens are taken from different random bags (after thorough mixing). Another three specimens are tested for collapsibility test using the consolidation apparatus (one dimensional compression) and following the Knight method (namely, compressing soil in dry state until 200 kPa then completing in saturated state) [13]. And finally two specimens are tested for shear strength using the direct shear device. The two collapsibility tests using the Knight Method reveal collapse potential of 7.5 and 8%, which is rather high. On the other hand, shear strength for the two tests show an angle of friction of 32 and 34^o tested in soaked state, and 34 and 36^o tested in dry basis. According to literature [14], there was a little decrease in friction angle of gypseous soil tested using the shear box as soil is tested in dry and soaked states. Also, similar results are reached regerding soaked and unsoaked friction angle of gypseous soil by other authors [15, 16].

One specific gravity test using the white spirit is conducted, and Gs is 2.39. Ordinary Proctor test show that the maximum Proctor dry density (unit weight more precisely) is 15.98 kN/m^3. The maximum and minimum unit weight are 16.32, 11.81 kN/m^3, respectively. The last tests are conducted once per each test. Table 1 shows summary of the average test results.

A primitive look on Table 1 shows that soil has high and dangerous collapse potential. This is because soil has low specific gravity, maximum dry unit weight, and high gypsum content, and collapse potential. As stated before this type of soil has high strength when in dry condition and experiences high immediate settlement upon wetting.

2. 2. Laboratory Testing Model The testing model is totally manufactured by author using components available in local market in Baghdad, the setup is quite simple and has no complicated parts. It is shown schematically in Figure 1. Most of the parts are made of steel and the major components are described for convenience.

TABLE 1. Summary of soil test results

Test	Result
Gypsum content	66 %
Shear strength (Ave.)	33^o soaked, 35^o dry
Collapse potential	8%
Soil type	Sandy
Specific gravity	2.351
Maximum Proctor dry unit weight	15.98 kN/m^3
Maximum dry unit weight	16.32 kN/m^3
Minimum dry unit weight	11.81 kN/m^3

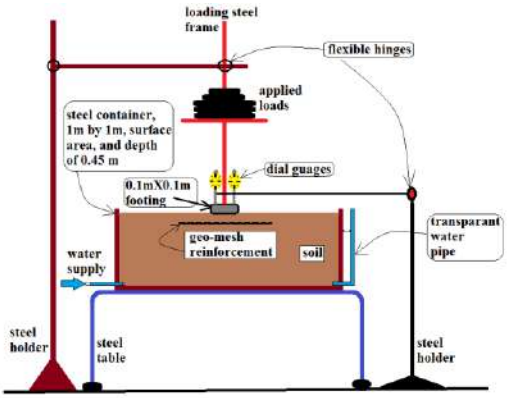

Figure 1. Setup used in this study

The soil is placed into the steel container, densifided in layers of 100 mm each using portable-electrical compactor. Also, it is intended to place the geo-mesh (or geo-grid) into two depth positions. The first is embeded at depth of one width dimension of footing (B) beneath the bottom surface of footing, the second is at depth of embedment of (B/2) below footing level. And since the footing is placed directly on soil surface, the geo-grid is now understood to be embeded at depths of B and (B/2) below soil surface. The soil is continued to be compacted easily layer after layer until the level of placement of the grid reinforcement is reached. The geo-grid is placed, (in a specified lateral dimensions for each test), and soil is continued to be compacted until the surface of soil, and that is a total depth of soil equals 0.5 m. At each specified depth of the geo-mesh reinforcement, three dimensions (sizes) of the grid are used, please care for Figure 2 for details.

Three extensions are used for each geo-mesh depth, namely, 1B, 2B, and 3B. Table 2 shows the relationship between the extensions of the geo-mesh, their depths, and the total lateral length of the grid.

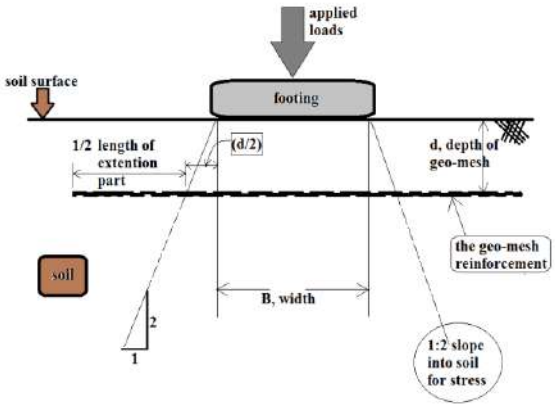

Figure 2. Schematic diagram for footing and location of geomesh reinforcement

TABLE 2. Depth of geo-mesh versus extension and its size

Extension of geo-mesh	Depth of geo-mesh	Total length (size) of the mesh
1B	B**	4B by 4B
2B	B	6B by 6B
3B	B	8B by 8B
1B	B/2	3.5B by 3.5B
2B	B/2	5.5B by 5.5B
3B	B/2	7.5B by 7.5B

**B is the width of the square footing = 100 mm

The basic idea of this research is to investigate the effect of depth and size of the geo-mesh reinforcement in getting a notable improvement in reducing the collapse potential of the gypseous soil. It worth to mention that one type of geo-mesh reinforcement is used for the totality of the study as author believes that changing the geometry of the grid will have some changes on the results.

2. 4. Testing Method The testing procedure for the laboratory model can be listed through the following points.

1. After completing the job of compacting the soil in tank, carefully levelling off the soil surface, the footing is placed onto soil and the two dial gauges are positioned and set to zero.
2. Now the soil is in its air-dried condition. Loads are applied gradually onto the loading steel frame up to a stress of 40 kPa. The settlement recording is initiated with time until no further depression in footing is taking place. The gypseous soil has the property of owning a high strength when dry, thus little footing settlement is expected in this stage. The water inlet valve is opened to let soil to be saturated. The soaking stage is now just started and the settlement of footing begins to increase. This settlement is recorded until the dial readings runs out to a negligible settlement. This takes about 3 days. It is worth to mention that no leaching process is carried out and only soaking process is conducted. The water level is monitored through a transparent pipe installed for that purpose in the container. When water level reaches soil surface, water inlet valve is closed off.
3. Upon ending of test, soil in container is removed and not be used again in any test, that is, always new soil is used in each test.
4. Very low head of water is utilized to saturate the soil as to avoid soil boiling condition, since water inlet is located in the bottom on the container.
5. The dial readings is recorded for the first ten hours, in increments of one reading per hour. Then after the settlement reading is recorded for each next 24

hours. It has been observed that at the initial stages of soaking, dial readings changes considerably with time, and only experience little changes then after.

6. In case of footing rotation, the average dial readings is recorded. On the other hand, if large differential settlement (rotation of footing) takes place then the whole test is stopped, ignored, and repeated once again with new soil.
7. For connivance, the test in which no geo-grid is used, has been repeated twice and the average settlement is taken into account. This test is the reference test for measuring any improvement in the soil, as it will be compared with it. Thus the reference test is considered important.

3. RESULTS AND DISCUSSION

Figures 3 to 8 show the cases plotted individually, in each figure two curves are plotted, one is for the unreinforced (untreated) soil, and the other belongs to the case of geo-mesh reinforcement in concern. The curve for the untreated soil is inserted in each figure for convenience as a measure for improvement. In each of the forgoing figures, the settlement which is presented as a ratio of s/B (settlement/width of footing) is plotted versus Time in minutes and in logarithmic scale. A primitive look on the mentioned figures indicates that the general trend of behavior is quite similar for all tests. The settlements regarding the initial (pre-soaked) stage are quite small compared to the total settlement. This stage lasted for as hour at most for all cases. The case of (3B, B/2) is exceptional, and by (3B, B/2) it is meant and extension of geo-mesh reinforcement equal to 3B and located at depth of B/2 under soil surface. Again, the case (3B, B/2) show the least initial settlement. It is half the settlement recorded compared to the other cases. In other words, extending the geo-mesh for 3B seems to be effective in reducing the dry stage of loading by about 50%. The other cases do not show such significant differences in any reduction of initial settlement. After one hour of dry loading, the soaking stage comes after by allowing water to preclude and saturate the gypseous soil directed from bottom to top of soil. The water rise is monitored in the container via a transparent pipe as mentioned earlier. As can be seen in all figures, there is a drastic increase in the settlement, namely the collapse settlement, for all cases. The best case for obtaining a reduction in the settlement is the case of (3B, B/2). The percentages of improvement recorded with respect the untreated soil is show in Table 5. These percentages are based on the final settlement measured (after 72 hours) for the case in concern divided on that for the untreated soil. There is a reduction in settlement by 35% and by settlement it is meant the collapse settlement. In foundation engineering terminology, it is considered good improvement. The next in improvement comes the case of (2B, 0.5B), which was successful in reducing the collapse potential by a ratio of 16%. The case of (B, B), which has an improvement ration of 4% only, is regarded as insignificant and ineffective in reducing the collapse potential of a footing. The use of such size and death of reinforcement is immaterial. Also, the two curves in Figure 8 seems to converge in the initial stages of test and in its final. The curves convergence of untreated soil and the reinforced soil, indicates that the type of reinforcement in concern is ineffective in reducing the collapse potential and has no impact in real engineering live.The case of (3B, B), shown in Figure 6, has improvement ratio of 10% which is rather a low number. It can be realized from Table 3 that decreasing the geo-grid by 0.5B reduced the settlement improvement ratio from 35 to 10%. This indicates that large amount of the collapse settlement is actually taking place in the zone beneath the footing and the improvement ratio for all cases of depth B are less than all cases of depth 0.5B, although the size of the mesh is little larger. Similar results are noticed by Hassan [17] on the sabkha soil (salty) when using geomesh. This insures the forgoing conclusion. Also extending the geo mesh increases the improvement (which is physically understood) and the extension of 1B is not effective in reducing the collapse settlement. Now referring to Figures 3 to 8, it can be seen that the curve of case 3B, 0.5B is in a higher position than the others, meaning that the collapse settlement is always and all the time is well below the other cases. All curves are rather smooth and do not intersect of overlap each other (in general), except the case of (1B, B/2). There is

TABLE 3. Percentage of collapse potential improvement with respect to the untreated soil

Length of geo-grid Reinforcement	d = Depth of geo-grid Reinforcement	
	B/2 (%)	B (%)
3B	35	10
2B	16	7.5
1B	7	3

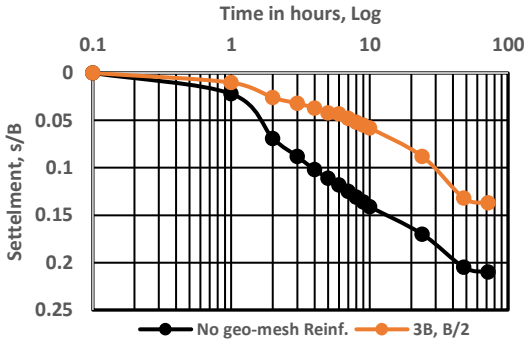

Figure 3. Settlement in terms of s/B versus time in logarithmic scale, for (3B, B/2)

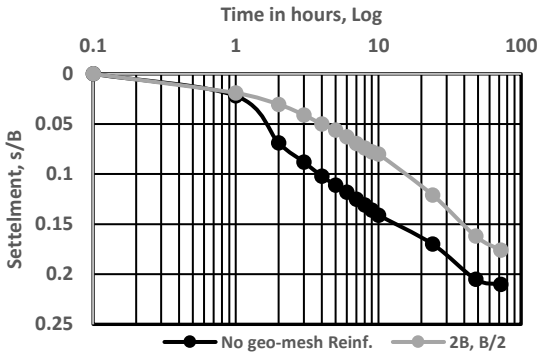

Figure 4. Settlement in terms of s/B versus time in logarithmic scale, for (2B, B/2)

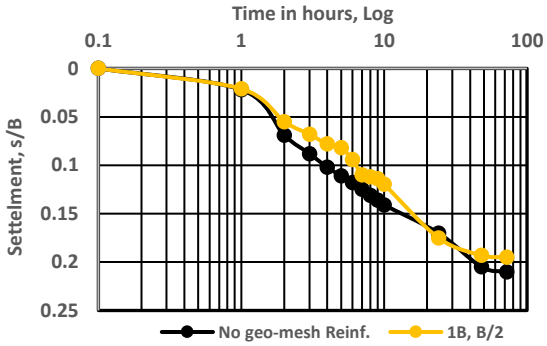

Figure 5. Settlement in terms of s/B versus time in logarithmic scale, for (1B, B/2)

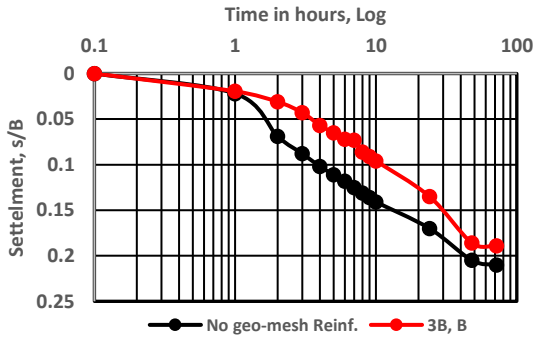

Figure 6. Settlement in terms of s/B versus time in logarithmic scale, for (3B, B)

a fluctuation in this curve as it intersects other curves and not in a trend of harmony like the other cases. Author believes that this is attributed to (maybe) experimentation error as it is the only one that deviates from the general trend of the other cases. So as stated earlier, very small initial settlement is recorded as a whole when soil is almost dry (and as curves in figures show) and a sharp increase in settlement is mesured uopn wetting, it is worth mentioning that quit similar resluts were obrained by Ibrahim and Zakaria [18].

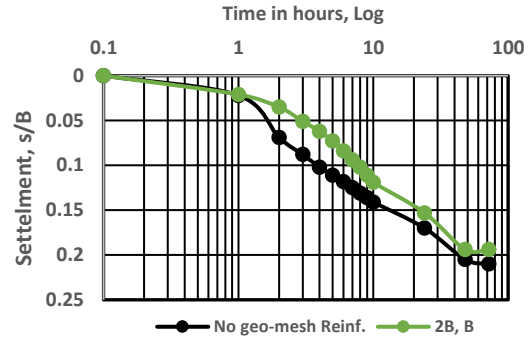

Figure 7. Settlement in terms of s/B versus time in logarithmic scale, for (2B, B)

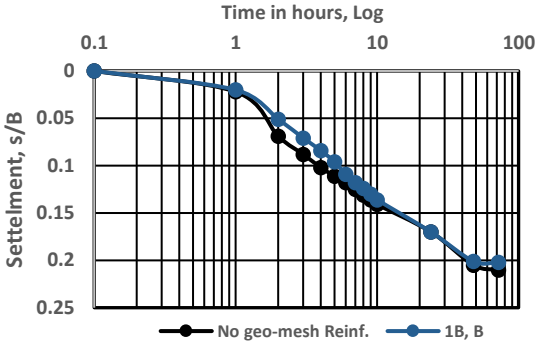

Figure 8. Settlement in terms of s/B versus time in logarithmic scale, for (1B, B)

4. CONCLUSIONS

Conclusions of this study are summarized as follows:

1. The settlement of footing in dry gypseous soil is quite small, and all cases of reinforcement and the case of untreated soil experience almost the same initial settlement except the cace of (3B, 0.5B), in which footing show about half the depression experienced by the other cases.
2. The best collapse settlement improvement ratios recorded is for the case of (3B, 0.5B) and it is 35%. The improvement is measured with respect to settlement of the untreated soil. The worst case for improvement ratio measured is the case (1B, B), with only 4%. This is an immaterial improvement ratio and thus this detail of reinforcing the gypseous soil should not be followed off.
3. Next in improvement ratio is the case (2B, 0.5B) with a value of 16%. The other types of reinforcements have improvement ratios confined between 4-16%.
4. All reinforcement cases for the depth of 0.5B show higher improvement ratios than the similar cases for depth one B, indicating that the majority of collapse potential is taking place in the zone of soil almost directly beneath footing. In addition to that the sizes of the geo-mesh in the first case are smaller than that for the latters.

5. All settlement-time curves plotted show similar trend of behavior and settlement almost seized after 72 hours of the start of tests.
6. The settlement in soaking stage is very much higher (considered drastic) compared to the dry stage. This is physically normal since gypseous soil has high strength properties when dry, loses bond and collapse when saturated, or even wetted.

5. REFERENCES

1. Al-Jumaily, F., "Gypsum and its mechanical effect on the engineering properties of soil", ***Journal of Arab Universities***, Vol. 1, (1994), 40-50.
2. Clemence, S.P. and Finbarr, A.O., "Design considerations for collapsible soils", ***Journal of the geotechnical Engineering Division, ASCE***, Vol. 107, No. GT3, Proc. Paper, 16106, (1981), 305-317.
3. Ismail, H., "The use of gypseous soils", in Symposium on the Gypseous Soils and Their Effect on Strength, NCCL, Baghdad.
4. James, A. and Lupton, A., "Gypsum and anhydrite in foundations of hydraulic structures", ***Geotechnique***, Vol. 28, No. 3, (1978), 249-272. doi:10.1680/geot.1978.28.3.249
5. Noor, S.T., Hanna, A. and Mashhour, I., "Numerical modeling of piles in collapsible soil subjected to inundation", ***International Journal of Geomechanics***, Vol. 13, No. 5, (2013), 514-526. doi:10.1061/(asce)gm.1943-5622.0000235
6. Awn, S.H.A. and Abbas, H.O., "Improvement of gypseous soil by compaction and addition of cement", ***Journal of Engineering and Sustainable Development***, Vol. 16, No. 2, (2012), 74-88.
7. Ziegler, M., "Application of geogrid reinforced constructions: History, recent and future developments", ***Procedia Engineering***, Vol. 172, No., (2017), 42-51. doi:10.1016/j.proeng.2017.02.015
8. Fakhraldin, M.K., "Improvement of loose granular soil by using geogrid reinforcement", ***Kufa Journal of Engineering***, Vol. 7, No. 3, (2016), 66-79.
9. Ahmed Kamel, M., Chandra, S. and Kumar, P., "Behaviour of subgrade soil reinforced with geogrid", ***International Journal of Pavement Engineering***, Vol. 5, No. 4, (2004), 201-209. https://doi.org/10.1080/1029843042000327122
10. Karim, H.H., Samueel, Z.W. and Jassem, A.H., "Behaviour of soft clayey soil improved by fly ash and geogrid under cyclic loading", ***Civil Engineering Journal***, Vol. 6, No. 2, (2020), 225-237. doi:10.28991/cej-2020-03091466
11. Emeka, A.E., Chukwuemeka, A.J. and Okwudili, M.B., "Deformation behaviour of erodible soil stabilized with cement and quarry dust", ***Emerging Science Journal***, Vol. 2, No. 6, (2018), 383-387. http://dx.doi.org/10.28991/esj-2018-01157
12. Amli, A., Sabah, A., Al-Ansari, N. and Laue, J., "Study numerical simulation of stress-strain behavior of reinforced concrete bar in soil using theoretical models", ***Civil Engineering Journal***, Vol. 11, No. 5, (2019), 2349-2358. doi:10.28991/cej-2019-03091416
13. Lutenegger, A.J. and Saber, R.T., "Determination of collapse potential of soils", ***Geotechnical Testing Journal***, Vol. 11, No. 3, (1988), 173-178. doi:10.1520/gtj10003j
14. Muarik, H.O.A.S.M., "Behavior of compacted gypsiferous sandy soil during soaking and leaching process", ***Journal of Wassit for Science & Medicine***, Vol. 5, No. 1, (2012), 165-176.
15. Al-Busoda, B.S. and Al-Rubaye, A.H., "Bearing capacity of bored pile model constructed in gypseous soil", ***Journal of Engineering***, Vol. 21, No. 3, (2015), 109-128.
16. Noman, B.J., Abd-Awn, S.H. and Abbas, H.O., "Effect of pile spacing on group efficiency in gypseous soil", ***Civil Engineering Journal***, Vol. 5, No. 2, (2019), 373-389. doi:10.28991/cej-2019-03091252
17. Abbas, H.O., "Improvement of sabkha soil by using geomesh and addition of polycoa", ***Engineering and Technology Journal***, Vol. 30, No. 4, (2012), 568-576.
18. Ibrahim, S.K. and Zakaria, W.A., "Effect of vibrating footing on a nearby static–load footing", ***Civil Engineering Journal***, Vol. 5, No. 8, (2019), 1738-1752. doi:10.28991/cej-2019-03091367

Persian Abstract

چکیده

در حقیقت روشهایی برای بهبود ظرفیت تحمل استراحت کف پا در حال فروپاشی خاک می تواند دو رویکرد را بهبود بخشد ، از این رو بهبود خصوصیات استحکام خاک و نفوذ سوراخهای تقویت شده به خاک است. پایه توسط یک صفحه فولادی مربع ۰.۱ در ۰.۱ متر مدل سازی می شود. پایه بارگذاری می شود که دارای استرس ٤٠ کیلو پاسکال بوده و محل استقرار در شرایط خشک و در حالت خیساندن اصلاح می شود. از دو عمق تقویت جغرافیایی مش استفاده می شود ، یک B) B عرض پا) و B۰.۵ است. برای یک عمق B ، از سه اندازه مربع مختلف از ژئو مش استفاده می شود ، ٤ B، ٦ B و B۸ .برای عمق تقویت شده از B ۰.۵، سه اندازه از جغرافیایی مش استفاده شده ، B ۳.۵ ، 5.5B و ، B۷.۵ است. نتایج نشان می دهد که بهترین پیشرفت به دست آمده ، مورد عرض جغرافیایی مربعی با عرض B ۷.۵ و در عمق B/2 در زیر پایه است ، با پیشرفت از نظر حل و فصل سقوط ۳۵٪ و کاهش تسویه در شرایط خشک ۵۰٪ کمترین پیشرفت در مورد ژئو مش مربع با عرض B٤ و عمق یک B است و واقعاً بسیار ناچیز بود ، حدود ٤٪ کاهش در تسویه سقوط. موارد دیگر بین این دو نسبت متفاوت بود. برای یافته های مطالعه ، نویسنده توصیه می کند از اندازه ژئومش کمتر از اندازه پایه استفاده نکند و آن را در عمق بیش از نیمی از عرض پایه قرار ندهد. به همین ترتیب ، در کل ، تأثیر ژئومش در کاهش محل استقرار خاک در حال فروپاشی واضح است اگر به روش مناسب استفاده شود

International Journal of Engineering

Journal Homepage: www.ije.ir

Collapse Problem Treatment of Gypseous Soil by Nanomaterials

A. L. Hayal[a], A. M. B. Al-Gharrawi[a], M. Y. Fattah*[b]

[a] *Civil Engineering Department, University of Kufa, Kufa, Iraq*
[b] *Civil Engineering Department, University of Technology, Baghdad, Iraq*

PAPER INFO

Paper history:
Received 27 April 2020
Received in revised form 18 May 2020
Accepted 12 June 2020

Keywords:
Collapse Soil
Gypseous Soil
Nano Materials
Soil Improvement

ABSTRACT

Investigation of the effect of using nanomaterials for improving and Stabilizing the gypseous soil was carried out using laboratory works. The gypseous soils were collected from a site of intake in Bahar Al-Najaf and mixed with two types of nanomaterials (Nano-silica and, Nano-clay) where the nanomaterials were added in small amounts as a percent of the dry weight of the soil sample. Tests to determine the sieve analysis, specific gravity, and collapse potential were performed. The results of the experimental work showed significant modification in the geotechnical properties of the soil sample. The collapse potential decreases as soon as the used nanomaterials were increased until they reach a percentage after which the collapse potential will be increased. Thus, addition of nanomaterials, even at a low percentage, could improve the properties of gypseous soil. When adding the nano-silica to the soil, the collapse potential (CP) is decreased whenever the nano-silica increases until 1% of the added nanomaterials and then further stabilizer increases the (CP), the percent of decrease in CP is about 91% where the effect of the additive (nano-silica) changes the classification of severity of collapse from "moderate trouble" case to "no problem" case.

***doi**: 10.5829/ije.2020.33.09c.06*

NOMENCLATURE

Cc	coefficient of curvature	ΔH_e	changing in height of specimen which results from the wetting
C_u	coefficient of uniformity	Ho	specimen initial height
SP	poorly graded sands	Δe	changing of specimen void rate which results from wetting,
CP	collapse potential	e_o	natural void ratio
SOT	Singule Oedometer Test		

1. INTRODUCTION

The soil texture, as a term, refers to the orientation and mineralogical composition of particles, the nature of properties of soil water and the forces of interaction between particles and soil water in a soil mass. An understanding of the soil structure is necessary because it influences the physical characteristics like swelling and engineering characteristics like strength and other properties of soil.

Collapsible soils are having metastable structure. This kind of soil has different properties due to various water conditions. It shows high strength and toughness when it is at normal water condition while at the wetting condition, the soil will suffer an unexpected plastic deformation. Existing of collapsible soil can result in structural damages to the construction projects such as cracks in floor, foundations, and walls.

The saturation of soils without the flow of water under specific pressure is referred to as soaking such as site flooded with water during heavy rainfall, irrigation or breaking of sewerage and water pipes. Changing of water contents in gypsum makes the gypsum function as solidifying operator to debauch inside the soils mass which brings about single or mix of three procedures, firstly separating any bond that exists within soil particles

*Corresponding Author Email: *myf_1968@yahoo.com* (M. Y. Fattah)

Please cite this article as: A. L. Hayal, A. M. B. Al-Gharrawi, M. Y. Fattah, Collapse Problem Treatment of Gypseous Soil by Nanomaterials, International Journal of Engineering (IJE), IJE TRANSACTIONS C: Aspects Vol. 33, No. 9, (September 2020) 1737-1742

bolstered via the gypseous followed by the collapsing of soils construction and this procedure happens very quickly. The subsequent procedure is union, while the third is draining procedure which shows up when the water stream proceeds through the dirt mass. Mixing such procedures can make the soils to be settled extensively as the load gets subjected [1].

In Iraq, particularly over the most recent three decades, broad improvements have been proved in the locales of gypseous soils because of the need for the development of numerous quantities of key ventures.

Numerous experimental researches in the world and Iraq motivated on remedial measures of collapsible gypseous soils. All of these techniques are focusing on governing the volume change and decreasing the permeability coefficient or inhibiting any interaction of moisture between the gypseous soil and water source to reduce the gypsum agent's dissolution. In general, the treatment measures of gypseous soils can be summarized as follows:

1) Chemical treatment: in which the remedial materials recommended are primarily cement, lime and crude and/or west oil products.
2) Physical treatment: these measures are based upon improvement of the geotechnical properties of gypseous soils to control the consequences of dissolution of gypsum.

The work presented by Fattah et al. [2] introduced the findings of tests conducted on four gypseous soils of various features and different contents of gypsum. Undisturbed soil specimens were tested to calculate the compressibility subjected to many conditions. An acrylate liquid was used as grouting material in which soil specimens were treated. The remediated specimens exhibited the ability of acrylate liquid to decrease the compressibility of the gypseous soil by more than 60–70%. The parameters of shear strength were influenced by acrylate liquid via the increase in the cohesion plus the decrease in the internal friction angle.

Ibrahim and Schanz [3] analyzed the enhancement of the features of gypsiferous soils by utilizing silicone oils to limit the impacts of dampness and gypsum losing. The analysis had been directed on fake gypsiferous soils (30% Silber sand and 70% unadulterated gypsum) treated with silicone oil in different percentages. Silicone oil was selected as an additive because of leakages of oil-related products from an oil refinery north of Iraq built on gypsiferous soil. Thus, this oil product provides a suitable analogue for that which has infiltrated the foundation soil of the refinery buildings. The results showed that the silicone oil is a suitable material for modifying the basic properties of the gypsiferous soil, such as collapsibility and shear strength.

Verma and Maheshwari [4] stated that there are various types of nano materials such as nano silica (SiO_2), nano titanium oxide (TiO_2) etc. are available. They carried out experiment in which the nano silica was mixed with soil samples (CI) in varying proportions of (0.0%, 0.25%, 0.50%, 0.75% and 1.0%) to study the geotechnical properties of soil. The results showed that the unconfied compressive strength and CBR characteristics of soils get increases with increasing the percentages upto 0.75 % of nano SiO_2 and afterwards a gradual decrease was obtained.

The objectives of the present study is to enhance the collapsibility of gypseous soils using two types of nanomaterial; nano clay and nano silica. Collapse tests were conducted in samples treated by different percentages of these materials.

2. LABORATORY INVESTIGATION

2. 1. Material The soils utilized in the current work represents disturbed regular gypsums soils (collapsible soil).

Soil samples of this study were collected from several sites in Bahar Al-Najaf south west Baghdad city in Iraq. All samples are representing disturbed soils brought together from a depth (1.5-2.5) m under the ground surface and the samples are collected from the bed of the intake. Figure 1 presents the geological conditions of the study area. The intake region is located at about (10) km from the city center of Al-Najaf.

The filed dry unit weight of the soil was measured by the sand replacement method. It was found to be 15.2 kN/m^3.

2. 2. Laboratory Work

2. 2. 1. Sieve Analysis Particle size analysis is used to determine the particle size distributing. The sample got washed via a number of sieves having

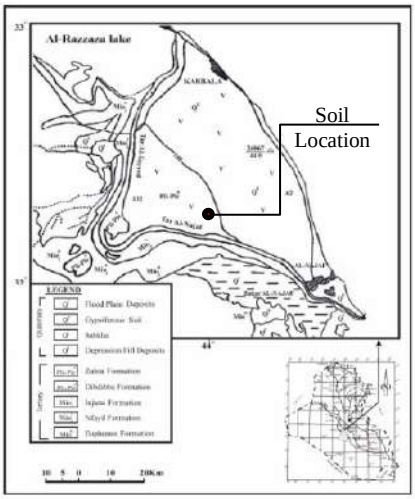

Figure 1. Location and geologic map of Karbala – Najaf area in Iraq

dimensions of gradually smaller screen to define the percentages of sand-sized particles of the examples consistent with ASTM D-422 [5] specification. Approximately 50 grams of dry soil which was passing sieve No. 200 was treated with a dispersing agent and analyzed using a hydrometer. From Figure 2, the coefficient of uniformity C_u is 4.34 and the coefficient of curvature C_c is 0.59, so the soil is classified as SP (poorly graded sand) according to the unified soil classification system.

2. 2. 2. Specific Gravity Values for specific gravity of the soil solids were determined according to ASTM D-854 [6]. Kerosene was used instead of water to avoid dissolution of gypsum. The result shows that the specific gravity value for the untreated gypseous soil is 2.34.

2. 2. 3. Collapse Test Such testing was performed through utilizing oedometer tool. A single oedometer test had been conducted to decide the collapsing potential (CP) for the soils. At that point, the testing proceeds by extra load and emptying as in the customary consolidating testing. Table 1 presents the criterion used to classify gypseous soils based on collapse potential. It is evident that the increase in CP refers to increase of the prolem of gypseous soil collapse upon wetting.

The samples were prepared at the field dry unit weight of 15.2 kN/m^3 by making a gentle tamping on sample in a compaction mold. Then an oedometer ring was pressed on the soil to get the collapse test specimen.

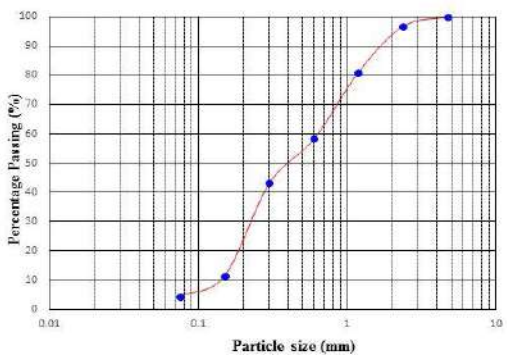

Figure 2. Grain size distributing of the soil used

TABLE 1. Relationship of collapsing potential to the severity of Foundation problems [7]

CP (%)	Severity of problem
0-1	No problem
1-5	Moderate trouble
5-10	Trouble
10-20	Severe trouble
20	Very severe trouble

For singule oedometer testing (sot) such testing, the soil's sample is stacked steadily at starting condition till the sample arrives at vertical stress of (200 kPa) with loading increase proportion (LIR) of 1. After that, the sample gets soaked with water within 24 hours. The extra settling was recorded at (200 kPa) stress because of splashing process. The collapse potential (CP) can be determined by utilizing the accompanying condition:

$$c_P = \frac{\Delta H_e}{H_o}\frac{\Delta e}{1+e_o} x100 \quad (1)$$

3. NANO MATERIALS

There are two types of additives material as nanomaterials (nano-clay and nano-silica) that are used in this study in different ways by mixing and grouting while nano-silica as (0.5%, 1%, 2% and 3%) and nano-clay as (2.5%, 5% and 10%).

Nanoclay is composed of phyllosilicates which include groups of minerals such as talc, Mica, kaolin, montmorillonite, Serpentine or sepiolite. Among other things, nanoclay differs in the size and sequence of the regions in which the SiO_4 tetrahedra are oriented upwards or downwards in the layers. Montmorillonite, the most technically significant clay mineral as the main constituent of bentonite, is composed of SiO_4 tetrahedron bilayers with deep-rooted octahedral layers of aluminium, iron, and hydroxide ions. A common montmorillonite particle comprises of approximately 1 nm thick alumina-silicate layers with lateral sizes in the series of 700 nm to about 10 µm, which accumulate into big stacks.

Also amorphous nano-silica powder was used with a solid content of more than 99.8%, an average size of 12 nm and surface area of 200 ± 25 m^2/g. Nano-silica consists of 48.83% silicon and 53.33 oxygen.

4. RESULTS AND DISCUSSION

4. 1. Collapsible Test Results without Nanomaterial Figure 3 delineates a normal reaction where a seating stresses of 25 kPa had been utilized to set up an initial state. Each compressing under such stress was credited to specimen disturbing. The initial compressing bend refers to the soil's reaction at its in situ water content. Weight was applied until the stress on the sample was equivalent to, or bigger than, the normal one in the field or up to 200 kPa as standardized by ASTM D-5333 [8].

Figure 3 illustrates a typical response in which a seating stress of 25 kPa was used to establish an initial state. Any compression under this stress was attributed to sample disturbance. The initial compression curve

represents the response of the soil at its in situ water content. Pressure was applied until the stress on the sample was equal to, or greater than, that expected in the field or up to 200 kPa as standardized by ASTM D-5333 [8].

The result of collapse test shows that collapse potential (CP) of the sample of the soil is equal to (3.6) %, so the soil is classified as moderately trouble according to Table 1.

Generally, collapsible soils are under unsaturated conditions in the dry state, with negative pore pressure resulting in higher effective stresses and greater shear strength. Additionally, cementing agents such as $CaCO_3$ can also contribute to maintaining an open ''honeycombed'' structure. Upon wetting, the pore pressure become less negative and the effective stresses are reduced causing a decrease in shear strength. Additionally, the water can dissolve or soften the bonds between the particles, allowing them to take a denser packing. This mechanism, referred to as wetting-induced collapse, or hydrocompression, can take place with or without extra loading.

4. 2. Effect of Adding Nanomaterials

4. 2. 1. Nano-Clay This type is classified as montmorillonite K 10 and this substance is not classified as dangerous material. The Nano-clay is added to the soil of percentage as (2.5%, 5% and 10%) and the results showed the following improvement.

Figure 4 presents single collapse test result on gypsum saturated soil samples treated with 2.5% of Nano- clay and at pressure equal to 200 kPa. It is noticed that the vertical strain changed from (2%) to (5.35%) and the collapse potential was decreased to 3.25%.

The Collapse mechanism can be explained by initial collapse of metastable texture of soil due to dissolution of gypsum when the soil is subjected to the wetting condition by which bonds between grains are broken down.

Molecular forces between particles are the weakest and the strength decreases with an increase in water saturation. The ionic-electrostatic force and capillary force are similar in magnitude, however ionic-electrostatic force is not stable in the presence of water, and capillary forces only exist at degrees of saturation between 0.35 and 0.80. Chemical agents, such irons present in nano-materials, can form cementation bridges with the strongest force. In addition, the collapsibility of stabilized gypseous soils also depends on the distortion and size of the inter-aggregate and intra-aggregate pores.

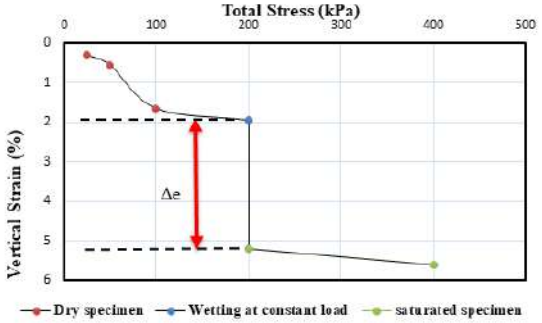

Figure 4. Collapse test results on the gypseous soil treated with 2.5% Nano clay

From Figure 5 that presents single collapse test result on gypsum soil samples treated with 5% Nano clay the outcomes show that changing of vertical strain at pressure equaled to 200 kPa frome a value of (2.5%) to (4%) which makes the collapse potential 1.44%.

Figure 6 presents single collapse test result on gypsum soil samples treated with 10% of Nano clay. The collapse potential was decreased to 0.945% because of the vertical strain change from 2.3% to 3.4% in consequence of applying 200 kPa (stress).

4. 2. 2. Nano-Silica It is added to the soil of percentage (0.5%,1%, 2% and 3%). The results illustrated the following values of the collapsing potential (CP) and the following curves indicated the effect of adding nanomaterials.

Figure 7 presents single collapse test result on gypsum soil samples treated with 0.5% of Nano silica where the vertical strain shifted from (2.4%) to (3.3%) under the compression at 200 kPa making the collapse

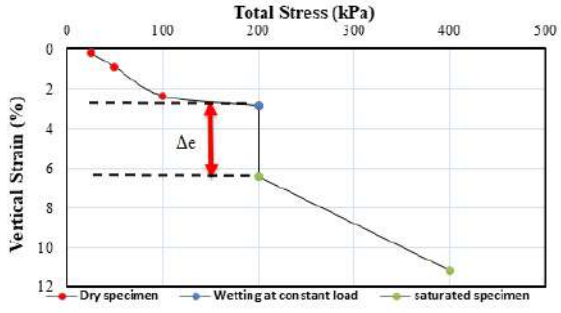

Figure 3. Collapse test results on the natural soil

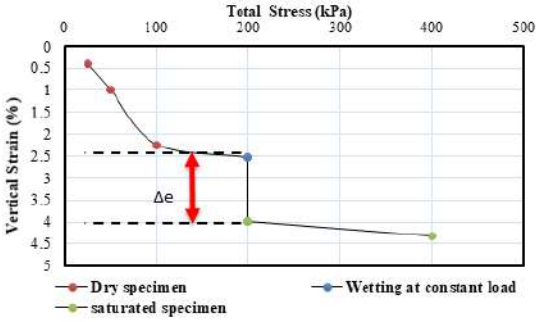

Figure 5. Collapse test results on the gypseous soil treated with 5% Nano clay

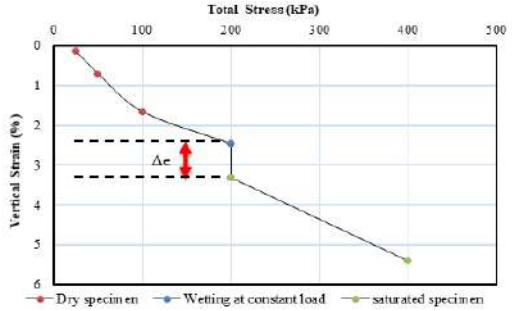

Figure 6. Collapse test results on the gypseous soil treated with 10% Nano clay

potential decrease to 1.89%. The lower collapse potential in treated samples can be related to stronger bond in the binder. Figure 8 presents single collapse test result on saturated gypsum soil samples treated with 1% of nano silica. In this curve, when the total stress reaches 200 kPa, the value of vertical strain changed from (1.75%) to (2.3%) and the collapse potential was decreased to 1.537%.

Figure 9 presents single collapse test result on saturated gypsum soil samples treated with 2% of nano silica where the vertical strain value is changed from (2.2%) to (4.8%) because under the stress 200 kPa the collapse potential was decreased to 2.45%.

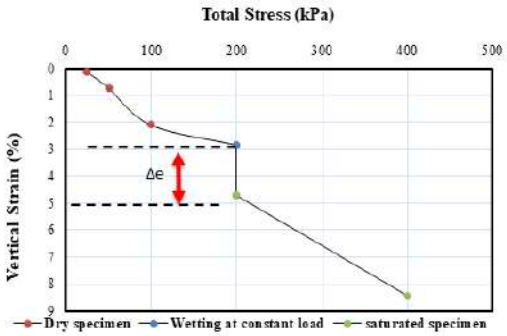

Figure 7. Collapse test results on the gypseous soil treated with 0.5% Nano silica

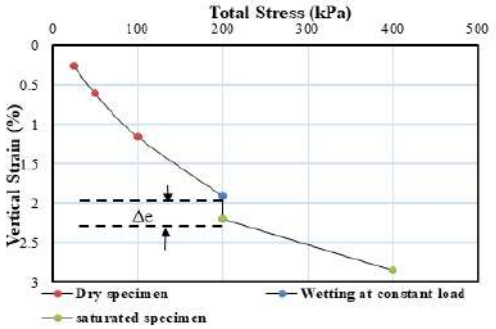

Figure 8. Collapse test results on the gypseous soil treated with 1% Nano silica

Figure 10 presents result of single collapse test on the saturated gypseous soil treated with 3% of Nano silica. The collapse potential is equal to 0.945% as a result to adding a constant stresss of 200 kPa which makes the vertical strain change from (1.9%) to (2.8%).

Table 2 summarizes the results of collapse test on treated samples. The table reveals that the gypseous soil collapse potential decreases by about 9.7%, 60% and 73.8% when the soil is mixed with 2.5, 5 and 10% Nano clay. While the decrease of CP by about 73.8% required adding only 3% of Nano silica.

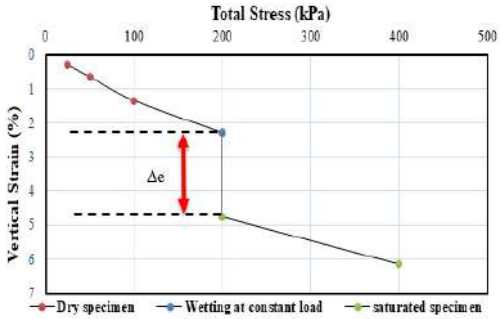

Figure 9. Collapse test results on the gypseous soil treated with 2% Nano silica

Figure 10. Collapse test results on the gypseous soil treated with 3% Nano silica

TABLE 2. Results of single collapse test

Without treatment	Treated with Nano-clay					
	CP (%)	% change in CP	CP (%)	% change in CP	CP (%)	% change in CP
	2.5		5		10	
3.6	3.25	9.027	1.44	60	0.945	73.8
Without treatment	**Treated with Nano-silica**					
	CP (%)	**% change in CP**	**CP (%)**	**% change in CP**	**CP (%)**	**% change in CP**
	1		2		3	
3.6	1.537	57.3	2.45	32.0	0.945	73.8

After full inundation of collapsible soil, the cementing bonds between particles get broken, and the remaining shear strength is derived from the inter-granular frictional forces. Consequently, the angle of internal friction can be utilized as an adequate measure of shear strength [9, 10]. In addition, nanomaterials provide another type of bond that resists inundation of collapsible soil, it is added to cohesion of soil particles.

5. CONCLUSIONS

In this paper, some of the experiment work was performed on collapsible soil mixed with different percentages of nano-clay and nano-silica fume stabilizers, to investigate the collapse potential (CP). The following conclusions may be written:

1. Nano-clay; when increasing the additive nano-clay to the soil sample, a decrease in (CP) was obtained.
2. The increment of the nano- clay leads to decrease in the collapse potential (CP) as a ratio of (73.75%) and this means that the additive modifies the soil to no problem case.
3. When adding the nano-silica to the soil, the collapse potential (CP) is decreased whenever the nano-silica increases until 1% of the added nanomaterials and then further stabilizer increases the (CP), the percent of decrease in CP is about 91% where the effect of the additive (nano-silica) changes the classification of severity of collapse from "moderate trouble" case to "no problem" case.

6. REFERENCES

1. AlNouri, I., and Saleam, S. "Compressibility Characteristics of Gypseous Sandy Soils." ***Geotechnical Testing Journal***, Vol. 17, No. 4, (1994), 465-474. https://doi.org/10.1520/gtj10307j
2. Fattah, M. Y., Al-Ani, M. M., and Al-Lamy, M. T. A. "Treatment of collapse of gypseous soils by grouting." ***Proceedings of the Institution of Civil Engineers - Ground Improvement***, Vol. 166, No. 1, (2013), 32–43. https://doi.org/10.1680/grim.11.00020
3. Ibrahim, A. N., and Schanz, T. "Improvement of Gypsiferous Soil Strength by Silicone Oil." ***Soil Mechanics and Foundation Engineering***, Vol. 54. (2017), 117-121. https://doi.org/10.1007/s11204-017-9443-7
4. Verma, D. K. and Maheshwari, U. K., "Effect of Nano Silica on Geotechnical Properties of Clayey Soil." ***International Journal of Science and Research***, Vol. 6, No. 12, (2017), 974–976. https://doi.org/10.21275/ART20178874.
5. ASTM D-422, 2007: "Standard Test Methods for Particle-size Analysis of Soils". Annual Book of ASTM Standards, ASTM international, West Conshohocken, PA.
6. ASTM D854 (2010), "Standard Test Methods for Specific Gravity of Soil Solids by Water Pycnometer". Annual Book of ASTM Standards, Vol.04.08, Philadelphia, P&A, ASTM, USA. Copyright, ASTM International, 10&0 Barr Harbor Drive, PO Box C700, West Conshohock.
7. Pells, P., Robertson, A., Jennings, J. E., and Knight, K. "A guide to construction on or with materials exhibiting additional settlement due to collapse of grain structure." In Proceedings of 6th Regional Conference for Africa on soil mechanics and Foundation Engineering, Durban, South Africa, (1975), 99–105. Retrieved from https://trid.trb.org/view/41906
8. ASTM D5333 (2018), "Standard Test Method for Measurement of Collapse Potential of Soils". Annual Book of ASTM Standards, Vol.04.08, Philadelphia, PA, ASTM, USA. Copyright, ASTM International, 100 Barr Harbor Drive, P&O Box C700, West Conshohocken, P&A 19428-2959, United States.
9. Changizi, F., and Haddad, A. "Improving the geotechnical properties of soft clay with nano-silica particles." ***Proceedings of the Institution of Civil Engineers - Ground Improvement***, Vol. 170, No. 2, (2017), 62–71. https://doi.org/10.1680/jgrim.15.00026
10. Ashour, M., Abbas, A., Altahrany, A., and Alaaeldin, A. "Modelling the behavior of inundated collapsible soils." ***Engineering Reports***, Vol. 2, No. 4, (2020). https://doi.org/10.1002/eng2.12156

Persian Abstract

چکیده

بررسی تأثیر استفاده از نانومواد برای بهبود و تثبیت بررسی تأثیر استفاده از نانومواد برای بهبود و تثبیت خاک گچ با استفاده از کارهای آزمایشگاهی انجام شد. خاکهای گچی از محلی از بهار النجف جمع آوری و با دو نوع نانومواد (نانو سیلیس و ، نانو رس) مخلوط شدند که در آن نانومواد به مقدار درصد به عنوان درصد وزن خشک خاک اضافه می‌شوند. نمونه آزمایش‌هایی برای تعیین تحلیل غربال، وزن مخصوص و پتانسیل فروپاشی انجام شد. نتایج حاصل از آزمایش آزمایشی اصلاحات قابل توجهی در خصوصیات ژئوتکنیکی نمونه خاک نشان داد. پتانسیل فروپاشی به محض افزایش نانومواد مورد استفاده کاهش می‌یابد تا رسیدن به درصد و در نتیجه پتانسیل فروپاشی افزایش می‌یابد. بنابراین، افزودن نانومواد، حتی با درصد کمی، می‌تواند باعث بهبود خواص خاک گچی شود. با افزودن نانو سیلیس به خاک، هرگاه نانو سیلیس افزایش یابد تا ۱٪ از نانومواد اضافه شده افزایش یابد و سپس تثبیت‌کننده بیشتر باعث افزایش (CP) شود، پتانسیل فروپاشی (CP) ۹۱٪ کاهش می‌یابد، جایی که اثر افزودنی (نانو سیلیس) طبقه‌بندی شدت سقوط را از پرونده "مشکل متوسط" به پرونده "بدون مشکل" تغییر می‌دهد.

IJE TRANSACTIONS C: Aspects Vol. 33, No. 9, (September 2020) 1743-1750

International Journal of Engineering

Journal Homepage: www.ije.ir

Plant Classification in Images of Natural Scenes Using Segmentations Fusion

N. Nikbakhsh[a], Y. Baleghi Damavandi*[a], H. Agahi[b]

[a] *Department of Electrical & Computer Engineering, Babol Noshirvani University of Technology, Babol, Iran*
[b] *Department of Mathematics, Faculty of Basic Science, Babol Noshirvani University of Technology, Babol, Iran*

PAPER INFO

Paper history:
Received 25 April 2020
Received in revised form 30 June 2020
Accepted 22 August 2020

Keywords:
G-calculus
Image Segmentation Fusion
Mutual Information
Plant Classification
Tsallis Entropy

ABSTRACT

This paper presents a novel approach to automatic classifying and identifying of tree leaves using image segmentation fusion. With the development of mobile devices and remote access, automatic plant identification in images taken in natural scenes has received much attention. Image segmentation plays a key role in most plant identification methods, especially in complex background images. Where there are no presumptions about leaf and background, segmentation of leaves in images with complex background is very difficult. In addition, each image has special conditions, so parameters of the algorithm must be set for each image. In this paper, image segmentation fusion is used to overcome this problem. A fast method based on maximum mutual information is used to fuse the results of leaf segmentation algorithms with different parameters. Applying Tsallis entropy and *g*-calculus, generalized mutual information equations are derived and used to obtain the best consensus segmentation. To evaluate the proposed methods, a dataset with tree leaf images in natural scenes and complex backgrounds is used. These images were taken from Pl@ntLeaves dataset and modified so that they do not have a presumption. The experimental results show the use of Tsallis entropy and *g*-calculus in image segmentation fusion, improves plant species identification.

doi: *10.5829/ije.2020.33.09c.07*

1. INTRODUCTION

Classification and identification of plant species are essential for plant extinction prevention, the use and development of plant resources, herbal medicines and separation of products from undesired plants in automation systems. However, identification of plants requires expert knowledge, and is a challenging and tedious task. Automatic plant identification through digital images helps the classification and identification of plant species according to time and human energy consumption. Unfortunately, despite the widespread biodiversity of plants, current processes of identification and classification are both error prone and slow [1]. In recent years, with the development of mobile devices and remote access, automatic plant identification in images taken in natural scenes has received much attention. Compared to other plant organs, leaves are the most widely used part for automatic plant identification using computer vision techniques because they are accessible throughout the year and easy to analyze. Automatic tree leaf classification is very accurate in images with white and uniform light background, but very difficult in natural scene images that are acquired in uncontrolled conditions.

To increase the accuracy of the classification, the classifier can use several features such as leaf color, overall shape, edge and vein structure. In most approaches, the accuracy of identification depends on the accuracy of the segmentation, which is the most difficult task in a complex natural scene [2, 3]. Because there are no specific conditions for image acquisition in natural scenes, an unsupervised segmentation algorithm with constant parameters leads to poor results for some images. In general, there is no best algorithm for segmentation of various images. In this paper, fusing the results of different algorithms or different parameters is used to overcome this problem. The clustering ensemble combines the results of different clustering algorithms to obtain a more accurate final clustering which is called consensus clustering. Mutual information is one of the most common parameters used in clustering ensemble. It

*Corresponding Author Institutional Email: *y.baleghi@nit.ac.ir* (Y. Baleghi Damavandi)

Please cite this article as: N. Nikbakhsh, Y. Baleghi Damavandi, H. Agahi, Plant Classification in Images of Natural Scenes Using Segmentations Fusion, International Journal of Engineering (IJE), IJE TRANSACTIONS C: Aspects Vol. 33, No. 9, (September 2020) 1743-1750

shows the amount of dependency between the two variables. However, if clusters have a large amount of data, fusion of them using criteria such as maximum mutual information requires a fast methods.

Plant leaf identification has been a hot research topic in recent years [4, 5]. Although a number of methods have been designed to identify plant species, new methods are still needed to improve the identification accuracy and speed, especially in complex background images. Most of tree leaves datasets have images with plain and uniform background. In addition, most of image datasets for tree leaves with natural scene use defaults such as color, position or orientation of leaf in the image. Pl@antLeaves dataset [2, 6] contains tree leaf images in the real world. These images are divided into three categories that were taken under different conditions. The scan category includes images with a white background, and the scan-like category includes images with a uniform background. There is no occlusion or overlap in both of them. However, the photograph category includes photos directly taken from the trees in nature. These photographs have a non-uniform background with optical distortions, shadows, color and luminance variations, and other problems such as overlapping. The most important advantage of this dataset is that it contains images that are very close to what a smartphone user may take from nature.

Most plant identification methods require images with simple background, or assumptions about leaf color or shape, and many of them need user interaction. Very few works handle the automatic segmentation and identification of plants in images with complex background [3]. A system called LeafSnap [7] was introduced to identify plant species in the mobile system that uses leaf shape in plain background images, but does not work well in complex and natural background images. In [8], the authors employed the semi-supervised Fuzzy C-Mean (FCM) classifier on different features to classify a number of images in the Pl@ntLeaves dataset (scan, scan-like, and photo) In [4] the authors used the Support Vectore Mechine (SVM) classifier with the color, shape and texture characteristics to classify tree leaf images. They reached an accuracy of about 61% for a number of scan and scan-like images on the Pl@antLeaves dataset, but this accuracy was only 8.5% for photo images. In [9] using Tsallis entropy and truth table, a new fast method was proposed for segmentation of tree leaves in images with complex background. In [10] the authors obtained 63.4 % of accuracy for 70 classes of species with simple background images (the scan and scan-like images). In [11], an approach was proposed to identify tree leaves using hand-crafted features, however, this method requires the leaf image without any occlusion and with a uniform background.

In recent years, another approach called the convolutional neural networks (CNN) has been used to identify plants, in which the leaf features are directly represented [6, 12]. In [13], the authors achieved a classification accuracy of 71% by testing a variety of CNNs on a combination of scan, scan-like and photo images. However, there are still many problems. In addition to hardware restrictions, this method requires a large number of well-categorized data which makes it impossible to use it in many cases, especially in datasets with a limited number of samples. These methods are not sensitive to image details. Also they are not accurate in overlapping images, and the relationship between pixels is not fully considered [14].

The purpose of the present work is to introduce a novel approach to automatic classification and identification of tree leaves using image segmentation fusion. The proposed method based on the two different methods for image segmentation fusion, and the dataset are described in Section 2. The experimental results are reported in Section 3, and the conclusion is given in Section 4.

2. MATERIALS AND METHODS

Automatic identification of plants in images taken from natural scenes is very difficult when prior information about the leaf or background is not available. Leaf image segmentation is the most important step in plant identification in leaf images with complex background. However, each segmentation algorithm requires special settings for each image. In this paper, image segmentation fusion is used to overcome this problem. In Figure 1, the flow diagram of the proposed method is shown.

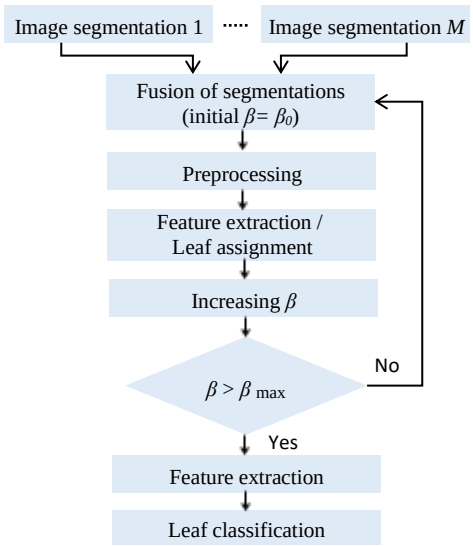

Figure 1. Flow diagram of the proposed method

Image segmentation fusion is usually a two-step algorithm. In the first step, the base clusterings are generated by different clustering algorithms or an algorithm with different parameters. Then, using a consensus function, the base clusterings are combined to find a new clustering so that it is most similar to the base clusterings. In this paper, fusion of unsupervised segmentations is done using maximum mutual information and a *g*-function [15] or Tsallis entropy.

2. 1. Image Segmentation Fusion Suppose X is an N-pixel image, and there are M different unsupervised segmentation algorithms. Each algorithm $S^j = \{S_i^j, [i]_1^N\}$, divides the image into background and object segments (labeled 0 and 1). Unlike supervised classification, the labels produced by these algorithms do not match. Table 1 shows an example of the labels produced by the different segmentation algorithms. A set of all segmentation results for the pixel i, provides a feature vector for representation of this pixel, $x_i = \{S_i^j, [j]_1^M\}$. Image segmentation fusion, combines the base segmentation results into S^*, and gets the best segmentation (S_{best}^*) which divides the image pixels into two parts so that this segmentation is most compatible with all the base segmentation results.

If the labels of the two segmentation results are in full correspondence, the mutual information between them is maximum. The mutual information between X, Y is defined as:

$$I(X,Y) = H_X + H_Y - H_{X,Y} \quad (1)$$

where H_X and H_Y are the classical entropy, and $H_{X,Y}$ is the joint entropy. The classical Shannon entropy is defined as$H = -\sum_x P(x)\, ln\, P(x)$, and is a measure of uncertainty of the random variable X with probability distribution $P(x)$. Mutual information between S^* and all of the base segmentation results (S) is obtained as follows:

$$I(S^*,S) = \sum_{j=1}^{M} I(S^*,S^j) \quad (2)$$

The results of the different base segmentation algorithms for each pixel, are considered as a new feature vector for it. In an image with N pixels and M segmentation algorithms as in Table 1, there are only 2^M different feature vectors. A state table can be created which includes all of the different feature vectors or 2^M state vectors [9, 16]. This table has 2^M rows or state vectors (SV). The number of repetitions for each of the state vectors in all pixels from the image is computed as f_i. The first row in this state table is selected as b_1, and the vector with maximum distance with b_1 is selected as b_2.

TABLE 1. The results of different segmentation algorithms

X	S^1	S^2	S^3	…	S^M	S^*
x_1	1	0	0	…	1	$S_1^* \; S_N^* \; S_N^* \; S_1^* \; S_1^* \; S_1^*$
x_2	0	1	1	…	0	$S_2^* \; S_2^* \; S_2^*$
…	…	…	…	…	…	…
x_N	1	0	0	…	1	$S_N^* \; S_N^* \; S_N^* \; S_N^*$

Then all state vectors are grouped into two categories based on similarity to b_1 or b_2. A new segmentation (S^*) is created by assigning the value of 0 or 1 to each state vector in this truth table. The value of each state vector is denoted byu_i^*, and is equal to 0 for vector b_1 and similar vectors, and 1 for vector b_2 and similar vectors. After generating this new segmentation (S^*), the mutual information between the new segmentation and the base segmentations is calculated. In the next step, the second vector in truth table is selected as the base vector b_1, and the above process is repeated. This procedure is repeated for half of the state vectors, and the segmentation which has the maximum mutual information is selected as the best consensus clustering as Equation (3).

$$S_{\text{best}}^* = \underset{S^*}{argmax} I_\beta(S^*,S) \quad (3)$$

This method greatly reduces the complexity of computations. In an N-pixel image and M segmentation algorithms, the time complexity in the exhausting search is $O(2^{N-1})$, and in the Bayesian clustering ensemble method [17] is $O(2NT)$, where T is the number of iterations until the convergence. However; in the proposed method, the time complexity is $O(2^{M-1})$, and the mutual information is calculated only for $2^M/2$ cases.

In calculation of maximum mutual information, the use of Tsallis entropy or *g*-calculus can lead to better results because these two methods have an additional parameter. By varying this parameter from the initial value to the maximum, a better final consensus segmentation will be obtained. These two methods are described below.

Method 1: Mutual information based on Tsallis entropy (I_β) betweenS^* and S^j is calculated as follows:

$$I_\beta(S^*,S^j) = H_\beta(S^j) + H_\beta(S^*) - H_\beta(S^j,S^*) \quad (4)$$

$H_\beta(S^j)$ and$H_\beta(S^*)$ represent Tsallis entropies, and are calculated as follows:

$$H_\beta(S^j) = (1-\beta)^{-1}\left(\sum_{k=0}^{1} P_k\,(S^j)^\beta - 1\right), \quad (5)$$

where $P_0(S^j)$ is obtained by dividing the number of pixels in which $S^j = 0$ by the total number of pixels.$P_0(S^j)$ and $P_1(S^j)$ are obtained as follows:

$$P_k(S^j) = \frac{1}{N}\sum_{i=1}^{2^M} f_i \quad \text{if} \quad SV_i^j = k, \quad (6)$$

whereSV_i^jrefers to the jth bit of SV_i (ith state vector) in the state table, and f_i is the frequency of each state vector in all pixels.

$$H_\beta(S^*) = (1-\beta)^{-1}(\sum_{k=0}^{1} P_k\,(S^*)^\beta - 1), \quad (7)$$

$$P_k(S^*) = \frac{1}{N}\sum_{i=1}^{2^M} f_i \quad \text{if} \quad u_i^* = k, \quad (8)$$

where u_i^* refers to the value of SV_i (0 or 1).

$H_\beta(S^j, S^*)$ represents the joint entropy that is the entropy of a joint probability distribution for a pair of random variables, and is calculated as Equation (9).

$$H_\beta(S^j, S^*) = (1-\beta)^{-1}(\sum_{k=0}^{1}\sum_{l=0}^{1} P_{kl}^{\beta} - 1), \quad (9)$$

where,

$$P_{kl} = \frac{1}{N}\sum_{i=1}^{2^M} f_i \quad \text{if} \quad SV_i^j = k \text{ and } u_i^* = l \quad (10)$$

For example, P_{01} is obtained by dividing the number of pixels in which $S^j = 0$ and $S^* = 1$ by the total number of pixels.

In this case, the classical Shannon entropy for mutual information is obtained by β =1.

Method 2: The *g*-calculus [15] is a development in Mathematics. Assuming that $-\infty \le a < b \le +\infty$ and $g:[a, b] \rightarrow [0, +\infty)$ is a continuous monotonic function, then $\oplus$ (pseudo-addition), the generalization of the classical operation, is defined by using the generating function g as follows:

$$x \oplus y = g^{-1}(g(x) + g(y)). \quad (11)$$

The function used by *g*-calculus is called the *g*-function. Using a *g*-function, new mutual information equations are generated which we call them *g*-mutual information equations. Using pseudo-addition:

$$I_\oplus(S^*, S) = \oplus_{j=1}^{M} \quad I(S^*, S^j) \quad (12)$$

If g is a strictly upward and continuous function such that $g(a) = 0$, then we get the following equation:

$$I(S^*, S) = g^{-1}\left[\sum_{j=1}^{M} \quad g(I(S^*, S^j))\right]. \quad (13)$$

Assuming $g: [-\infty, +\infty] \rightarrow [0, +\infty), g(x) = e^{\beta x}, \beta > 0$, then mutual information is obtained as follows:

$$x \oplus y = \frac{1}{\beta} ln\left(e^{\beta x} + e^{\beta y}\right), \quad (14)$$

$$I_\beta(S^*, S) = \frac{1}{\beta}\ln \sum_{j=1}^{M} \quad e^{\beta I(S^*, S^j)} \quad (15)$$

$$I_\beta(S^*, S) = \frac{1}{\beta}\ln \sum_{j=1}^{M} \quad e^{\beta\left(H_{Sj} + H_{S^*} - H_{Sj,S^*}\right)} \quad (16)$$

where $H_\beta(S^j)$, $H_\beta(S^*)$ and $H_\beta(S^j, S^*)$ are obtained as follows:

$$H_\beta(S^*) = \sum_{k=0}^{1} \quad P_k(S^*)\, ln\, P_k\,(S^*), \quad (17)$$

$$H_\beta(S^j) = \sum_{k=0}^{1} \quad P_k(S^j)\, ln\, P_k\,(S^j), \quad (18)$$

$$H_\beta(S^j, S^*) = \sum_{k=0}^{1} \quad \sum_{l=0}^{1} \quad P_{kl}\, ln\, P_{kl}, \quad (19)$$

In these equations, $P_k(S^*)$, $P_k(S^j)$ and P_{kl} are obtained from Equations (6), (8) and (10).

2. 2. Preprocessing The segmented image may contain undesirable noise, false classified pixels and connected regions. After the fusion of segmentations, morphological operations such as hole filling, opening and closing are used to improve the segmented image [9]. Morphological closing applies dilation process to an image, followed by an erosion process, while morphological opening is a reverse process. After these operations, boundary correction and separation of the overlapping parts that have different colors with the main part or the shadow are performed. By morphological dilation (or erosion) and subtraction of the source image, several pixels are selected around the borders. The pixels in this area, which are different in color from the object, are considered as background. The color dissimilarities of pixel $x(i,j)$ with the object and background (d_1, d_2), are obtained using Hue, Saturation and Value components in the *HSV* color space as follows:

$$d_1(x(i,j)) = \sum_{k=1}^{3} \frac{(x(i,j,k)-\mu_1)^2}{\sigma_1^2} \quad (20)$$

$$d_2(x(i,j)) = \sum_{k=1}^{3} \frac{(x(i,j,k)-\mu_2)^2}{\sigma_2^2} \quad (21)$$

where, the mean and variance of the object and background are assumed as $(\mu_1, \sigma_1^2, \mu_2, \sigma_2^2)$, respectively. If $d_1 > d_2$ then the pixel $x(i,j)$ is considered as the background. The example of these operations are shown in Figure 2.

2. 3. Shape Features Extraction The accuracy of classifiers largely depends on the accuracy of the segmentation and feature extraction process. A feature is an object characteristic that is different from other objects. Leaf color may vary in different seasons and geographical locations. In addition, different plant species may have leaves of the same color. Shape is an important feature of image description. The accuracy of feature extraction from the shape depends greatly on the quality of the image segmentation. After the object is segmented from the image by fusion of the results of

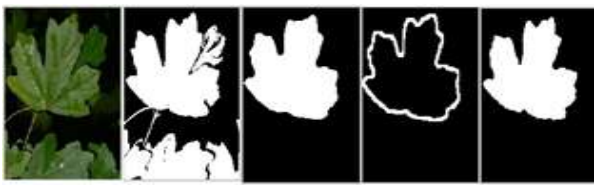

(a) (b) (c) (d) (e)

Figure 2. (a) Original image; (b) Result of fusion of segmentation algorithms; (c) After opening, selecting the largest segment, and closing; (d) The pixels around the borders; (e) After boundary correction

segmentation algorithms, it is necessary to calculate the similarity between the segmented shapes and the predefined ones. To do this, a feature vector including 6 digital morphological features [4, 9], 6 elliptical Fourier descriptors (EFD) [6] and the first Hu invariant moment [4, 6] is extracted from shapes.

Let the longest distance between two points on the border of the leaf be indicated by L, and the length of the longest line perpendicular to L by W (width). Also, A is the leaf area which indicates the number of pixels in the leaf and P is the leaf perimeter which counts the number of pixels at the leaf border. Then 13 features are obtained as follows.

Rectangularity feature, which shows the similarity of a leaf and its rectangle is calculated by $L.W/A$. Form factor, which shows the difference between a leaf and a circle, is defined by $4\pi A/P^2$. Perimeter to length ratio, is calculated by P/L. Perimeter ratio of length and width, is calculated by $P/(L+W)$. Aspect ratio shows the ratio of leaf length and leaf width (L/W). Vein feature, which defines the skeletal structure of the leaf, is calculated by dividing the total vein pixels by the total number of pixels in the leaf.

Elliptical Fourier Descriptors are used as a set of elliptical harmonics to approximate a closed edge. We select the first 6 harmonics as 6 features.

The first Hu invariant moment of an intensity function $f(x,y)$ is defined as:

$$M_1 = \left(\frac{\mu_{20}}{\mu_{00}^2}\right) + \left(\frac{\mu_{02}}{\mu_{00}^2}\right) \quad (22)$$

where μ_{00}, μ_{02} and μ_{20} are calculated as:

$$\mu_{pq} = \sum_x \sum_y (x - \bar{x})^p (y - \bar{y})^q f(x,y) \quad (23)$$

$$\bar{x} = \left(\frac{m_{10}}{m_{00}}\right) \quad , \bar{y} = \left(\frac{m_{01}}{m_{00}}\right) \quad (24)$$

$$m_{pq} = \sum_{x=0}^{M-1} \sum_{y=0}^{N-1} x^p y^q f(x,y). \quad (25)$$

Thus, a feature vector containing 13 components is created.

In each value of β, after determining the S^*_{best}, which has the maximum mutual information, the segments of the leaf and background classes are examined. The features of these two segments are extracted and their similarities are calculated with the features of predefined shapes. The leaf class is determined with the maximum similarity by calculating the minimum distance with the stored features of the predefined shapes. The similarity is measured using the Euclidean distance between the shape features of these two classes (segments) and the features of the predefined shapes. Figure 3 shows the predefined leaf shapes for the 30 plant species used in this paper.

The new mutual information equations, made by Tsallis entropy or g-function, have an additional parameter, so that by changing this parameter the best result can be obtained for the fusion of segmentations.

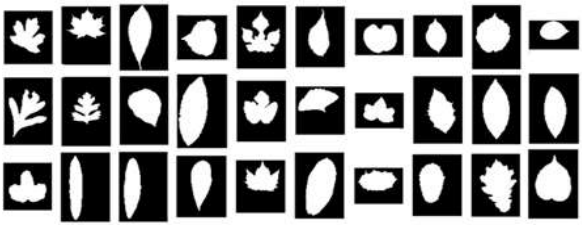

Figure 3. Predefined leaf shapes for the 30 plant species

First, with initial parameter of β, the resulting segments in the leaf and background classes are examined, and using the Euclidean distance, their similarity with predefined shapes are calculated. In the next step, β increases, and this process is repeated until β reaches the maximum value. In each step, the Euclidean distance between the features of each resulting segments and features of the predefined shapes is calculated. Finally, a segmentation with one β is selected that makes the least Euclidean distance with one of the predefined shapes. In the fusion using Tsallis entropy, β can vary from 0.1 to 1, and if $\beta = 1$, then the fusion with the Shannon entropy method is obtained.

2. 5. Dataset Most datasets used to evaluate plant classification algorithms have defaults that cannot be applied to real cases. For this reason, we generated a dataset of leaf images with natural scenes and without presumptions, to evaluate the segmentation and identification algorithms. This dataset consists of 200 tree leaf images with natural scenes extracted from Pl@ntLeaves dataset with segmentation ground truth that we have extracted manually. It can be downloaded from "ftp://doc.nit.ac.ir/cee/electronic/baleghi.yaser/Plants_Dataset/". Some of these photograph images have been modified so that the leaf is not always vertical or in the middle of the image. These images are classified into 30 species of plants and can be used to evaluate unsupervised algorithms for leaf segmentation and identification. Figure 3 shows an example of each class, and Figure 4 shows the sample images of this dataset. The images of this dataset are taken in natural conditions and have problems such as different shades and lighting, overlapping, different colors and defects.

2. 6. Performance Metric Average top-n accuracies are ususally used with n=1, 5 or 10. Assuming that m is the number of evaluation samples, and y_i is the

Figure 4. Sample images from dataset

correct species class for input sample x_i, i=1,...,m, then:

$$\text{Top-}n \text{ accuracy} = \frac{1}{m}\sum_{i=1}^{m}\sum_{j=1}^{n} I(f_j(x_i) = y_i) \quad (26)$$

where j=1,…,n, is the highest ranked species predictions according to their probability values, and I(.) is the indicator function which returns 1 for the true expressions and 0 for otherwise.
The other metric is F1-measure that is defined as:

$$F1\text{-measure} = \frac{1}{C}\sum_{i=1}^{C}\frac{2*TP_i}{2*TP_i+FP_i+FN_i} \quad (27)$$

where, TP_i indicates the number of correct predictions on class i, FP_i indicates the samples that do not belong to class i but are predicted in this class, and FN_i indicates the samples that belong to class i but are not predicted in this class.

3. RESULTS AND DISCUSSION

3. 1. Evaluation and Results Since an algorithm with a fixed parameter is not suitable for segmentation of all images, the fusion of four different algorithms is used in this work. To do this, the FCM [18] and *k*-means algorithms with different parameters are used as individual image segmentation methods. In the *k*-means clustering algorithm, each pixel is assigned to the nearest cluster, but in the FCM algorithm each pixel is assigned to clusters with different degrees of membership. FCM uses a procedure to minimize the weighted summation of distances from the pixels to the M cluster centers as follows:

$$J = \sum_{i=1}^{N}\sum_{l=1}^{M}\mu_{li}^{k}\,\|X_i - C_l\|^2 \quad (28)$$

where X is an N-pixel image, k is a coefficient greater than 1, and $0 \le \mu_{li} \le 1$ is the degree of membership of image pixel X_i to the cluster l with center C_l .

Since the *YCbCr* and *Lab* color spaces have separate luminance and chrominanc components, the *RGB* color leaf image is converted to *YCbCr* and *Lab* color spaces. Segmentation Algorithms 1 and 2 divide the image into two parts using the fuzzy c-mean clustering algorithm and the *a*, *b* components in the *Lab* color space. Algorithm 1, uses the membership degree of less than 0.1, and Algorithm 2 uses the membership degree of less than 0.9. Algorithm 3 is *k*-means clustering using *L*, *a*, *b* components in the *Lab* color space, and Algorithm 4 is *k*-means clustering using *Y*, *Cb*, *Cr* components in the *YCbCr* color space.

In Figure 5, the results of four segmentation algorithms for three sample images are shown in (b) to (e). In (f) and (g), the fusion results of these segmentations are shown using the classic Shannon entropy and the proposed method with Tsallis entropy. The results of the proposed method are obtained with β=0.5 for images 1-2, and β=0.75 for image 3 while the classical Shannon entropy is obtained with β=1. As shown in this figure, changing the parameter β, can lead to a good improvement in image fusion.

(a) (b) (c) (d) (e) (f) (g)

Figure 5. (a) Original image; (b) to (e) Results of four segmentation algorithms; (f) Fusion by β=1(Shannon); (g) Fusion by proposed method (Tsallis entropy)

For the computation time comparison, these three images were tested in MATLAB on a PC with Intel core (i3) CPU, 3.7GHz processor and 8GB RAM. The average time required for image segmentation fusion by BISF [17] is approximately 94 seconds but with the proposed method is about 0.7 seconds. The computation time for fusion in the proposed method is greatly improved.

3. 2. Comparison of Performance on the Whole Dataset In Table 2, the average performances of classification algorithms are compared on all images of tree leaves from the dataset. To get these results, the average scores over 200 tree leaf images is calculated. As shown in this table, the proposed methods are better than all individual algorithms in terms of average classification accuracies (Top-1, Top-2, Top-5, and F1-measure). The mean and standard deviation of accuracy (F1-measure) over 5 runs for the two different proposed methods of fusion are approximately 0.63, 0.02, and almost similar.

TABLE 2. Comparison of average classification results based on the whole dataset

Method	Top-1 accuracy	Top-2 accuracy	Top-5 accuracy	F1-measure
FCM (Algorithm1, *a*,*b*)	0.38	0.46	0.62	0.35
FCM (Algorithm2, *a*,*b*)	0.36	0.41	0.59	0.34
k-means(Algorithm3, *L*,*a*,*b*)	0.38	0.48	0.65	0.34
k-means(Algorithm4, *Y*,*Cb*,*Cr*)	0.40	0.49	0.64	0.38
Fusion (Tsallis entropy)	0.64	0.70	0.84	0.63
Fusion (g-calculus)	0.65	0.72	0.85	0.64

Each image needs to its own settings, so each segmentation algorithm only works well in some images. Due to the complexity of the background of these images, there is no algorithm that is suitable for all of the images. For this reason, the fusion of the results of differnent algorithms, leads to a good improvement in classification accuracy.

3. 3. Comparison with Other Methods In Table 3, the proposed methods are compared with some other existing methods. This comparison is obtained using the average classification accuracies (Top-1, Top-2, Top-5, and $F1$-measure) on all tree leaf images from the dataset.

In this table, Shannon fusion approach is obtained through the proposed method with Tsallis entropy and β=1. The results of MP+B/A+CS, FCM methods were reported in [8] using a number of images in the Pl@ntLeaves dataset (Scan, Scan-like and Photograph categories) and a semi-supervised FCM procedure.

The results of Table 3 show that the proposed fusion methods using Tsallis entropy and g-calculus are better in terms of classification accuracy than other methods. Mutual information equations using Tsallis entropy or g-calculus have a parameter which may lead to the best consensus clustering. These results indicate that the image fusion using Tsallis entropy and g-calculus, improves the average performance of image fusion with classical Shannon entropy. Also, these results indicate that the proposed methods, can overcome the problems in unsupervised identification algorithms.

TABLE 3. Comparison of the proposed methods with other methods

Method	Top-1 accuracy	Top-2 accuracy	Top-5 Accuracy
Mean shift [19]	0.31	0.39	0.48
Snakes [20]	0.33	0.41	0.49
FCM [18]	0.38	0.46	0.62
MP+B/A+CS, FCM [8]	0.45	0.55	0.70
Fusion (BISF) [17]	0.41	0.49	0.58
Fusion (Shannon entropy)	0.44	0.51	0.68
Fusion (Tsallis entropy)	0.64	0.70	0.84
Fusion (g-calculus)	0.65	0.72	0.85

4. CONCLUSIONS

In this paper, we presented a new method for classifying plants in complex background images based on image segmentation fusion with maximum mutual information. Classification of plant leaf images with complex background is very challenging when there is no presumption about the color or location of the leaves in the image.

The most important factor influencing the classification accuracy is the leaf segmentation. Segmentation algorithms require specific parameters and settings for each image. In this paper, we solve this problem by fusing the results of four different segmentation algorithms with different parameters. Experiments were performed on the Pl@ntLeaves dataset. To get the best consensus segmentation we introduced new equations for maximum mutual information by using Tsallis entropy and g-calculus.

The evaluation results show that in general, the fusion of results is better than the result of a single algorithm. Each image needs its own settings, so each algorithm only works well on some images. The use of Tsallis entropy or g-calculus, results in a large improvement on the overall classification result, and offers a promising way to combine clusterings, especially in big data. It can be used to identify plants by a mobile phone as a terminal and is not just limited to leaf images. This method is fast and does not depend on the user's subjective judgment. This fast and simple method can help people to get to know the plant more quickly and better.

5. ACKNOWLEDGEMENT

The authors acknowledge the funding support of Babol Noshirvani University of Technology through Grant programs No. BNUT/370123/99 and BNUT/392100/99.

6. REFERENCES

1. Mata-Montero, E. and Carranza-Rojas, J., "Automated plant species identification: Challenges and opportunities", ***IFIP Advances in Information and Communication Technology***, Springer, Vol. 481, (2016), 26-36, doi: 10.1007/978-3-319-44447-5_3.
2. Grand-Brochier, M., Vacavant, A., Cerutti, G., Kurtz, C., Weber, J. and Tougne, L., "Tree leaves extraction in natural images: Comparative study of preprocessing tools and segmentation methods", ***IEEE Transactions on Image Processing***, Vol. 24, No. 5, (2015), 1549-1560, doi: 10.1109/TIP.2015.2400214.
3. Wäldchen, J. and Mäder, P., "Plant species identification using computer vision techniques: A systematic literature review", ***Archives of Computational Methods in Engineering***, Vol. 25, No. 2, (2018), 507-543, doi: 10.1007/s11831-016-9206-z.
4. Wang, Z., Li, H., Zhu, Y. and Xu, T., "Review of plant identification based on image processing" ***Archives of Computational Methods in Engineering***, Vol. 24, No. 3, (2017), 637-654, doi: 10.1007/s11831-016-9181-4.
5. Zhang, S., Zhang, C. and Wang, X., "Plant species recognition based on global-local maximum margin discriminant projection", ***Knowledge-Based Systems***, Vol. 200, (2020), doi: 10.1016/j.knosys.2020.105998.
6. Zhang, S., Huang, W., Huang, Y.A. and Zhang, C., "Plant Species Recognition Methods using Leaf Image: Overview",

Neurocomputing, (2020), doi: 10.1016/j.knosys.2020.105998.

7. Kumar, N., Belhumeur, P.N., Biswas, A., Jacobs, D.W., Kress, W.J., Lopez, I.C. and Soares, J.V., "Leafsnap: A computer vision system for automatic plant species identification", in European Conference on Computer Vision, Springer, (2012), doi: 10.1007/978-3-642-33709-3_36.
8. Cerutti, G., Tougne, L., Coquin, D. and Vacavant, A., "Curvature-scale-based contour understanding for leaf margin shape recognition and species identification", International Conference on Computer Vision Theory and Applications (2013), doi: 10.5220/0004225402770284.
9. Nikbakhsh, N., Y. Baleghi, and H. Agahi, "Maximum mutual information and Tsallis entropy for unsupervised segmentation of tree leaves in natural scenes", ***Computers and Electronics in Agriculture***, Vol. 162, (2019), 440-449, doi: 10.1016/j.compag.2019.04.038.
10. Le, T.-L., D.-T. Tran, and N.-H. Pham. "Kernel descriptor based plant leaf identification", in 2014 4th International Conference on Image Processing Theory, Tools and Applications (IPTA), IEEE, (2014), doi: 10.1109/IPTA.2014.7001990.
11. Saleem, G., Akhtar, M., Ahmed, N. and Qureshi, W.S., "Automated analysis of visual leaf shape features for plant classification", ***Computers and Electronics in Agriculture***, Vol. 157, (2019), 270-280, doi: 10.1016/j.compag.2018.12.038.
12. Kaya, A., Keceli, A.S., Catal, C., Yalic, H.Y., Temucin, H. and Tekinerdogan, B., "Analysis of transfer learning for deep neural network based plant classification models", ***Computers and Electronics in Agriculture***, Vol. 158, (2019), 20-29, doi: 10.1016/j.compag.2019.01.041.
13. Hedjazi, M.A., I. Kourbane, and Y. Genc. "On identifying leaves: A comparison of CNN with classical ML methods", in 2017 25th Signal Processing and Communications Applications Conference, IEEE, (2017), doi: 10.1109/SIU.2017.7960257.
14. Kamilaris, A. and F.X. Prenafeta-Boldú, "Deep learning in agriculture: A survey", ***Computers and Electronics in Agriculture***, Vol. 147, (2018), 70-90, doi: 10.1016/j.compag.2018.02.016.
15. Mehri-Dehnavi, H., H. Agahi, and R. Mesiar, "Pseudo-exponential distribution and its statistical applications in econophysics", ***Soft Computing***, Vol. 23, No. 1, (2019), 357-363, doi: 10.1007/s00500-018-3623-x.
16. Nikbakhsh, N. and Y. Baleghi. "A New Fast Method of Image Segmentation Fusion Using Maximum Mutual Information", in 2019 27th Iranian Conference on Electrical Engineering, IEEE, (2019), doi: 10.1109/IranianCEE.2019.8786371.
17. Wang, H., Zhang, Y., Nie, R., Yang, Y., Peng, B. and Li, T., "Bayesian image segmentation fusion", ***Knowledge-Based Systems***, Vol. 71, (2014), 162-168, doi: 10.1016/j.knosys.2014.07.021.
18. Arora, J., K. Khatter, and M. Tushir, "Fuzzy c-means clustering strategies: A review of distance measures", ***Software Engineering***, Springer, (2019), 153-162, doi: 10.1007/978-981-10-8848-3_15.
19. Comaniciu, D. and P. Meer, "Mean shift: A robust approach toward feature space analysis", ***IEEE Transactions on Pattern Analysis & Machine Intelligence***, Vol. 5, (2002), 603-619, doi: 10.1109/34.1000236.
20. Chan, T.F., B.Y. Sandberg, and L.A. Vese, "Active contours without edges for vector-valued images", ***Journal of Visual Communication and Image Representation***, Vol. 11, No. 2, (2000), 130-141, doi:10.1006/jvci.1999.0442.

Persian Abstract

چکیده

در این مقاله یک رویکرد جدید برای طبقه بندی و شناسایی بدون نظارت برگ درخت با استفاده از همجوشی تصاویر قطعه بندی شده ارائه شده است. با توسعه دستگاه‌های تلفن همراه و دسترسی از راه دور، شناسایی اتوماتیک گیاهان در تصاویر گرفته شده با زمینه طبیعی مورد توجه بسیاری قرار گرفته است. در اکثر روش‌های شناسایی گیاه به ویژه در تصاویر با زمینه پیچیده، قطعه‌بندی برگ‌های گیاه نقش بسیار مهمی دارد. در جایی که پیش فرض هایی در مورد برگ و زمینه وجود ندارد، قطعه‌بندی برگ‌ها در تصاویر با پس‌زمینه پیچیده بسیار دشوار است. علاوه بر این، با توجه به این که هر تصویر شرایط ویژه‌ای دارد، برای هر تصویر باید پارامترهای الگوریتم تنظیم شود. در این مقاله برای رفع این مشکل از همجوشی تصاویر قطعه‌بندی شده استفاده شده است. نتایج چهار الگوریتم بدون نظارت قطعه‌بندی برگ با پارامترهای مختلف استخراج می‌شود. برای ادغام نتایج این قطعه‌بندی‌ها، از یک روش سریع و بر اساس حداکثر اطلاعات متقابل استفاده می‌شود. با استفاده از آنتروپی Tsallis و g-calculus، معادلات اطلاعات متقابل تعمیم یافته به دست آمده و برای بدست آوردن بهترین قطعه‌بندی استفاده می‌شوند. برای ارزیابی روش‌های پیشنهادی از یک پایگاه داده تصویر برگ درخت در صحنه‌های طبیعی و با زمینه پیچیده استفاده شده است. این تصاویر از پایگاه داده Pl@ntLeaves گرفته شده و طوری اصلاح شده‌اند تا هیچ پیش فرضی نداشته باشند. نتایج تجربی نشان می‌دهد که استفاده از آنتروپی Tsallis و g-calculus در ادغام نتایج قطعه‌بندی تصویر، شناسایی گونه‌های گیاهی را بهبود می‌بخشد.

International Journal of Engineering

Journal Homepage: www.ije.ir

Quay Cranes and Yard Trucks Scheduling Problem at Container Terminals

S. Behjat, N. Nahavandi*

Industrial & Systems Engineering Faculty, Tarbiat Modares University, Tehran, Iran

P A P E R I N F O

Paper history:
Received 03 March 2020
Received in revised form 16 March 2020
Accepted 12 June 2020

Keywords:
Quay Crane Scheduling
Yard Truck Scheduling
Non-crossing
Simulated Annealing Algorithm
Grouping
Safety Margin
Container Terminals

A B S T R A C T

A bi-objective mathematical model is developed to simultaneously consider the quay crane and yard truck scheduling problems at container terminals. Main real-world assumptions, such as quay cranes with non-crossing constraints, quay cranes' safety margins and precedence constraints are considered in this model. This integrated approach leads to better efficiency and productivity at container terminals. Based on numerical experiments, the proposed mathematical model is effective for solving small-sized instances. Two versions of the simulated annealing algorithm are developed to heuristically solve the large-sized instances. Considering the allocation of trucks as a grouping problem, a grouping version of the simulated annealing algorithm is proposed. Effectiveness of the presented algorithms is compared to the optimal results of the mathematical model on small-sized problems. Moreover, the performances of the proposed algorithms on large-sized instances are compared with each other and the numerical results revealed that the grouping version of simulated annealing algorithm outperformed simulated annealing algorithm. Based on numerical investigations, there is a trade-off between the tasks' completion time and the cost of utilizing more trucks. Moreover increasing the number of YTs leads to better outcomes than increasing the number of QCs. Besides two-cycle strategy and using dynamic assignment of yard truck to quay cranes leads to faster loading and unloading procedure.

***doi**: 10.5829/ije.2020.33.09c.08*

1. INTRODUCTION

Particularly over the past decades, container terminals have been playing a significant role in the global transportation system [1]. According to a review by the Maritime Transport [2], the global container port throughput has grown to 752 million 20-foot equivalent units (TEUs) in 2017. This reflects the addition of 42.3 million TEUs in that year. The report estimates 5% growth in total TEU capacity by January 2019 [2]. Given the progressive growth rate of the transported containers volume in the last decade, the operational efficiency of container terminals must be optimized .

In this study, the assignment of containers to the quay cranes and trucks as well as the sequence of tasks performed by each quay crane and each truck are determined. The objective function of the presented model is a linear combination of the makespan of the vessel and the sum of the quay cranes' completion times. The management of these complicated operations is an attractive issue for researchers, especially in the past years. In 1989, Daganzo [3] for the first time presented a mathematical model for the quay crane scheduling problem assuming a certain number of vessels and QCs in the berth. Kim and Park [4] proposed a mixed integer programming (MIP) model considering several constraints regarding the quay crane scheduling problem. The model was later modified by Moccia et al. [5]. There are a plethora of other hypothesis on the real-world instances in works of researchers including assumptions such as a safety distance between cranes (e.g. Nguyen et al., [6]; Kaveshgar et al., [7]), cranes non-crossing (e.g. Tavakkoli-Moghaddam et al. [8]; Emde, [9]), precedence relationship between containers (e.g. Kim and Park, [4] ; Sammarra et al., [10]) and unidirectional schedules for quay cranes (e.g. Legato et al., [11]; Chen and Bierlaire, [12]). A comprehensive categorization and review of various articles in this field was carried out by Bierwirth and Meisel [13, 14].

*Corresponding Author's Email: *n_nahavandi@modares.ac.ir* (N. Nahavandi)

Please cite this article as: S. Behjat, N. Nahavandi, Quay Cranes and Yard Trucks Scheduling Problem at Container Terminals, International Journal of Engineering (IJE), IJE TRANSACTIONS C: Aspects Vol. 33, No. 9, (September 2020) 1751-1758

Beside works studying the independent scheduling problems of quay cranes (QCs) and yard trucks (YTs); there are several studies carried out in the recent years approaching both problems in integration. Chen et al. [15] considered and formulated the integrated operational management problem of QCs, YTs and YCs as a hybrid flowshop scheduling problem. Furthermore, considering precedence and blocking constraints, they developed a Tabu search algorithm with an objective function to minimize the makespan [15]. A mathematical model to solve the joint quay crane and truck scheduling problem was proposed by Tang et al. [16]. Considering both inbound and outbound containers, besides developing several valid inequalities, they proposed two lower bounds for their presented model. Kaveshgar and Huynh [17] studied the joint scheduling problem of QCs and YTs. Also they developed a mixed integer programming (MIP) model as well as a genetic algorithm for solving the presented problem. Based on the solution for several numerical problems, the proposed algorithm showed suitable results [17]. In 2019, to solve the problem of simultaneous allocation of vessels to the berths, QCs to vessels and YTs to QCs, Vahdani et al. [18] proposed an integer programming model plus two metaheuristic approaches based on genetic algorithm and particle swarm optimization (PSO) algorithm. The results showed that the simultaneous solving of such problems could lead to an improvement in the efficiency of these resources and reduce the completion time [18]. Fazli et al. [19] addresed quay crane assignment and scheduling problem and proposed a mathematical model and Red Deer Algorithm (RDA) for solving this problem. At the same time, assuming the cranes do not cross each other, Behjat and Nahavandi [20] investigated the simultaneous and integrated scheduling and allocation of QCs and YTs. For solving this problem, they developed an integer programming model and a metaheuristic solving method regarding to the imperialist competitive algorithm [20].

The assumption that quay cranes do not cross each other is a practical constraint in the management of container port operations. In the current study it is assumed that prior to solve the scheduling problem there were no assumptions about how QCs would be assigned to vessels or containers. This assumption could improve the efficiency in the allocation of the valuable resources at container terminals and increase their productivity by decreasing the constraints on the assignment of QCs. Moreover, along with other real-world assumptions, such as assuming precedence relationships or safety margin which are considered in this study, such an assumption leads to an increase in the complexity of problem-solving. Taking the safety margin between QCs into consideration is a real-world assumption which was neglected in Behjat and Nahavandi's study [20]. In this paper, considering the main real-world assumptions, a novel integrated bi-objective mathematical model based on the flexible jobshop problem concept is developed. To the best of our knowledge, there is no published work in the related literature that have modelled this problem considering the below mentioned assumptions the way presented in this study. Moreover, a solving method based on simulated annealing algorithm and the grouping concept is developed for solving the proposed problem, especially for large-sized problems.

2. PROBLEM STATEMENT

It is expected that the integrated management of QCs and YTs help improve the efficiency of container management operations. Furthermore, with the dynamic assignment of yard trucks to containers (rather than vessels or QCs), an improvements in the utilization of YTs is expected. In this study, the assignment of containers to the quay cranes and trucks as well as the sequence of tasks performed by each quay crane and each truck are determined. The objective function of the presented model is a linear combination of the makespan of the vessel and the sum of the quay cranes' completion times. Utilizing a weighted linearization method to convert a multi-objective problem to a single objective one is a typical method for solving such problems.

The vessel's completion time is reduced to the lowest value by minimization of the makespan. Additionally, the minimization of the sum of the QCs completion times leads to the better utilization of quay cranes. In addition to the faster completion of tasks, this objective function will reduce the idle time of quay cranes. Among different schedules with equal makespan values, the schedule with the minimum sum of completion time for quay cranes is commonly considered as the most desirable solution. Nevertheless, the minimization of makespan enjoys greater significance. Accordingly, the makespan minimization weight in the objective function is more important than the reduction in the completion time of quay cranes.

In this study, it is assumed that at the same time, each crane or truck can only serve one container. Due to the linear placement of QCs on the rail, it is impossible for them to cross one another. In the literature, this practical assumption is known as the non-crossing assumption. There are no preset restrictions on the assignment of QCs to vessels or bays. Depending on the location of the containers at the vessel based on the stowage plan, there is a precedence relationship between containers that should be considered while loading and unloading. The cranes working on adjacent bays should have a certain distance as safety margin from one another. The purpose is to find a sequence of processing containers on QCs and YTs which minimizes the makespan of the vessel and the sum of the completion times of the containers on the QCs.

As previously mentioned, in order to increase the efficiency and utilization of YTs, each truck can serve several QCs. Basically, there are two types of operations for yard trucks. One is the one-cycle strategy in which each truck is assigned to and merely serves one crane. The other operation is called the two-cycle strategy where the trucks work with different cranes leading to a better utilization for them.

3. MATHEMATICAL MODEL

The presented model in this study is developed based on the model proposed by Behjat and Nahavandi [20] and is inspired from the concept of flexible jobshop problem for the modelling of integrated assignment and scheduling problem of QCs and YTs. The problem under study here is to consider quay cranes and yard trucks as machines, and containers are tasks that need to be processed on these machines. As both inbound and outbound containers are investigated, the issue can be considered as a special case of a flexible jobshop scheduling problem. The existence of real-world assumptions, such as the non-crossing cranes and the presence of a safety margin between them, make this problem more complex than a flexible jobshop problem.

There are two operations on QCs and YTs required for the completion of every container's task. To show these operations, notation O_hj is used where h stands for the number of operations and j shows the number of containers. For each inbound container, Operation 1 is performed by quay cranes and Operation 2 is proceeded by yard trucks. For the outbound containers, this operation count will be reversed. For instance, in the case of outbound containers, O_2j is the operation which is done by QCs on containers. In the proposed model, a dummy container is considered as the first container to be processed on each QC or YT. The parameters, decision variables, and the model are as follows:

Parameters:

m	Number of machines (sum of the number of QCs and YTs)
n	Number of jobs (containers)
Q	Number of quay cranes
i, j	Jobs index
l, h, l'	Operations index
k	Machines index
q_j	Location of job j (bay number)
Ω	Set of precedence constrained containers
J_1	Set of inbound containers
J_2	Set of outbound containers
Φ	Set of operations which should be processed on QCs
δ	Safety margin among quay cranes based on the number of bays
f_{hjk}	1, if machine k is capable to process the O_{hj} 0, o.w.
M	A large number
$\propto_1$	The weight of the makespan component of the objective function
$\propto_2$	The weight of the sum of the quay cranes completion times in the objective function
p_{hjlik}	The processing time of O_{hj} on machine k if it is processed immediately after O_{li} on machine k

Variables:

X_{hjlik}	1, if operation O_{hj} is processed immediately after the operation O_{li} on machine k 0, o.w.	$h, l = 1,2$ $i, j = 1, \dots, n$ $k = 1, \dots, m$
s_{hj}	The start time of operation O_{hj}	$h = 1,2$ $j = 1, \dots, n$
c_{hj}	Completion time of operation O_{hj}	$h = 1,2$ $j = 1, \dots, n$
C_k	Completion time of the last job on quay crane k	
Y_{hjk}	1, if operation O_{hj} is processed on machine k 0, o.w.	$h = 1,2$ $j = 1, \dots, n$ $k = 1, \dots, m$
Y'_{hjli}	1, if operation O_{hj} is processed after operation O_{li} (not immediately) 0, o.w.	$h, l = 1,2$ $i, j = 1, \dots, n$

The model:

$$Min \ \propto_1 C_{max} + \propto_2 \sum_{k=1}^{Q} C_k$$

$$\sum_l \sum_{i=0} \sum_k X_{hjlik} = 1 \qquad \forall h = 1,2;\ \forall j = 1, \dots, n \qquad (1)$$

$$\sum_h \sum_j \sum_k X_{hjlik} \leq 1 \qquad \forall l = 1,2;\ \forall i = 1, \dots, n \qquad (2)$$

$$\sum_l \sum_i X_{hjlik} \leq f_{hjk} \qquad \forall h = 1,2;\ \forall j = 1, \dots, n;\ \forall k = 1, \dots, m \qquad (3)$$

$$\sum_h \sum_j X_{hj10k} \leq 1 \qquad \forall k = 1, \dots, m \qquad (4)$$

$$\sum_h \sum_j X_{hjlik} \leq \sum_{l'} \sum_{i'} X_{lil'i'k} \qquad \forall k = 1, \dots, m \qquad (5)$$

$$c_{hj} \geq c_{(h-1)j} + \sum_l \sum_i \sum_k X_{hjlik} \cdot p_{hjlik} \quad \forall h = 1,2 \quad \forall j = 1, \dots, n \tag{6}$$

$$c_{hj} \geq c_{li} + \sum_k X_{hjlik} \cdot p_{hjlik} - M(1 - \sum_k X_{hjlik}) \quad \forall h, l = 1,2 \quad \forall i, j = 1, \dots, n \tag{7}$$

$$s_{hj} \geq c_{li} \quad \forall (i,j) \in \Omega \quad \forall h, l = 1,2 \tag{8}$$

$$\sum_l \sum_i X_{hjlik} = Y_{hjk} \quad h = 1,2 \quad j = 1, \dots, n \quad k = 1, \dots, m \tag{9}$$

$$M\left(Y'_{hjli} + Y'_{lihj}\right) \geq \sum_k k \times Y_{hjk} - \sum_{k'} k' \times Y_{lik'} + 1 \quad h, l = 1,2 \quad j, i = 1, \dots, n \quad \forall q_j < q_i \quad O_{hj}, O_{li} \in \Phi \tag{10}$$

$$M\left(Y'_{hjli} + Y'_{lihj}\right) \geq \delta \times \left(\sum_k k \times Y_{hjk} - \sum_{k'} k' \times Y_{lik'}\right) + q_j - q_i \quad h, l = 1,2 \quad j, i = 1, \dots, n \quad \forall q_j < q_i \quad O_{hj}, O_{li} \in \Phi \tag{11}$$

$$s_{hj} + \sum_l \sum_i \sum_k X_{hjlik} \times p_{hjlik} = c_{hj} \quad h = 1,2 \quad j = 1, \dots, n \tag{12}$$

$$c_{li} - s_{hj} + M \times Y'_{hjli} \geq 0 \quad \forall h, l = 1,2 \quad \forall i, j = 1, \dots, n \tag{13}$$

$$c_{li} - s_{hj} - M \times (1 - Y'_{hjli}) \leq 0 \quad \forall h, l = 1,2 \quad \forall i, j = 1, \dots, n \tag{14}$$

$$C_k \geq c_{hj} - M \times (1 - Y_{hjk}) \quad \forall j = 1, \dots, n \quad h = 1,2 \quad \forall k = 1, \dots, Q \tag{15}$$

$$s_{hj}, c_{hj}, C_k \geq 0 \quad \forall h = 1,2\,, \quad \forall j = 1, \dots, n, \quad k = 1, \dots, Q \tag{16}$$

As mentioned earlier, the objective function is the minimization of a weighted sum of the vessel makespan and the sum of completion times of the quay cranes. Reducing a multi-objective optimization model to a single objective problem through a linear combination of the objective functions is a common approach in similar problems. In cases with the same makespan, solutions that also minimize quay cranes' idle times are preferred in order to enhance the utilization of cranes. Since minimizing the makespan is more important than the utilization of QCs, it is assumed that $\propto_1 = 0.99 \; and \; \propto_2 = 0.01$.

The constraint set (1) ensures that the operation O_{hj} is processed after exactly one operation. The constraint set (2) guarantees that at most one operation can be processed after the previously completed operation. The constraint set (3) ensures that the operation O_{hj} is processed on the machine that is capable to process the operation. For example, the first operation of outbound containers ($O_{1j}, j \in J2$) cannot be processed on a quay crane. Based on the constraint set (4), following the dummy jobs, only one job can be processed. The constraint set (5) ensured that if the operation O_{li} is not processed on machine k, any other operation cannot be processed after this operation on the mentioned machine. Constraint set (6) is incorporated into the model to calculate the completion time of the operation O_{hj}. The constraint set (7) ensures that each machine processes no more than one operation at the same time. The precedence relationship between containers is considered in the constraint set (8). The constraint set (9) is incorporated into the model to determine which operation is processed on which machine. The constraint set (10) constitutes the quay crane's non-crossing limitation. For two containers, if $Y'_{hjli} + Y'_{lihj} = 0$ (*i.e.* O_{li} and O_{hj} are processed simultaneously), if the position of container *j* is on the left side of the container *i* then the QC that processes operation O_{hj} is on the left side of the QC processing O_{li}. The constraint set (11) is incorporated in the model to ensure the safety margin among quay cranes. Assume that there should be a two-bay margin among adjacent quay cranes, and cranes 3 and 5 are processing containers simultaneously, there should be at least a 4 ((5-3) ×2=4) bay-margin between the cranes. The constraint set (12) computes the start time of operations. The constraint sets (13) and (14) are incorporated into the model to compute the Y'_{hjli} variable, showing the simultaneous processing of two operations. Lastly, the completion time of the last job on the quay crane k is calculated based on the constraint set (15).

Applying some simplification and assuming only inbound containers and the assumption that there is only one vessel at the terminal, the problem proposed in this research can be transformed into the jobshop scheduling problem with the makespan minimization objective function. Thus, the new simplified problem is of an NP-hard one as mentioned in the literature [21]. Therefore, it could be concluded that the former intricate problem is also an NP-hard problem. Hence, there is no possible way to precisely solve large-scale instances, and search-based metaheuristic methods are required to be developed to solve the problems.

4. SIMULATED ALGORITHM

The simulated annealing (SA), first proposed by Kirkpatrick et al. [22] in 1983, is a metaheuristic optimization algorithm which is effective in solving combinational optimization problems. This algorithm was inspired by an annealing treatment in metallurgy. The algorithm works by starting from an initial answer and moves to the next one based on the neighborhood search structure at each step of the algorithm. The condition for accepting a new neighborhood solution and moving on to that answer is that the new answer must be better than the current one. If not, it will be accepted with a defined probability. This probability is calculated based on the number of iterations performed and the objective function difference between the new and the current answers. The algorithm accepts the new solution with a probability of $e^{-E/T}$ if the problem has a minimization objective (or $e^{E/T}$ if the problem has a maximization objective), where E is the difference of objective function values between the current and the new solutions, and T is the current temperature [23].

4. 1. Solution Representation In this study, the initial solution is randomly generated. The proposed algorithm's solution representation has two main parts; the first one is the containers' processing sequence on the quay cranes and the allocation of the cranes to the containers, and the second part is the processing sequence of containers on the yard trucks and their assignment to each truck.

4. 2. Neighborhood Search Structure Two different operators are defined for generating a neighbor solution. Based on Operator 1, one point is randomly chosen along the array, thereafter, the position of tasks is replaced with each other with respect to the point (Figure 1).

Based on the second operation, the positions related to two elements along the array are swapped with each other. These movements are repeated for a random number of times (Figure 2).

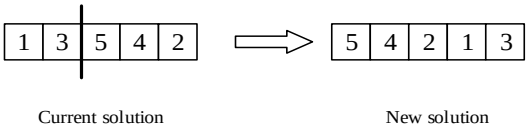

Figure 1. How Operator 1 works

Figure 2. How Operator 2 works

4. 3. Grouping Simulated Annealing The grouping problems are somehow categorized as optimization problems in which the members of an arbitrary set of G are divided into several subgroups with the intersection of null and a sum equal to the set G. The key assumption in such problems is that the order of groups is of no importance. Some problems in optimization, including graph coloring, bin packing, batch-machine scheduling, and packing/partitioning problems, could be considered as the grouping problems. The allocation of QCs and YTs to containers are two assignment problems being discussed in this study. Since the arrangement of the quay cranes is important in their assignment (due to assumptions such as the safety distance or lack of crossing movements of the cranes), this problem cannot be considered as a grouping problem. Nevertheless, the problem of allocating yard trucks to containers is assumed to be a grouping problem because these trucks are similar and there is no specific spatial constraint on their allocation [24].

In the grouping version of the algorithm (G-SA), to update the allocation and sequence of containers on QCs in each iteration, Operators 1 and 2 are used according to Figures 1 and 2. The container group's allocation and sequence on the YTs, though, will be updated according to Figure 3.

4. 4. Stopping Criteria If the temperature reaches its minimum, the proposed SA will stop. This algorithm also stops when after a predetermined number of iterations, no improvement has been occurred in the current best solution.

5. NUMERICAL RESULTS

54 random sample instances are solved to evaluate the performance of the proposed mathematical model and the solution quality of the presented metaheuristic algorithms. To generate such random problems, the ranges proposed by Behjat and Nahavandi were used [20].

The design parameter values of the proposed SA (T_0, T_{final}, α) affect the performance and results of the algorithm. T_0 and T_{final} respectively represent the initial and final temperatures, and α is used as the cooling rate in each iteration (temperature in iteration n is equal to $\alpha \times$ temperature in iteration n-1). The parameters of the proposed SA are tuned by setting a trade-off between time and quality of the solutions. In order to find appropriate values for the parameters of algorithm, different combinations of parameters were tested on a large number of test instances, and 100, 0.01 and 0.96 values selected as the best values for T_0, T_{final} and α, respectively.

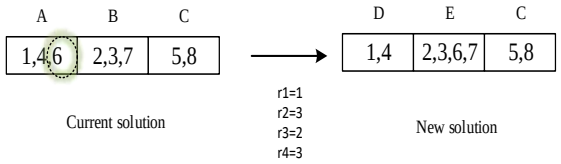

Figure 3. How G-SA crossover works

Problems in smaller dimensions can be precisely solved using CPLEX software which in addition to validating the presented model, create a situation to evaluate the performance of the developed algorithms. The proposed SA was able to obtain one optimal results from 6 proposed examples. For the rest of the examples, the difference between the answer obtained from the SA and the optimal mathematical model is between 1.67 and 3.43. This is while the G-SA was able to obtain an optimal solution of 3 examples out of 6. The mean difference between the optimal solutions obtained from the mathematical model and the near-optimal solutions of the SA and G-SA algorithms are 1.89 and 0.71, respectively, indicating the superiority of G-SA performance.

In Table 1 the relative percentage deviations (RPDs) values are presented for larger instances with three and four QCs in order to evaluate the performance of the developed algorithms. RPD as a performance measure is calculated based on the following equation:

$$RPD = (\sum_i \frac{OFV_i - OFV_i^{min}}{OFV_i^{min}})/n \times 100 \quad (17)$$

where n is the total number of solved instances, OFV_i stands for the objective function value for the given algorithm after solving the i^{th} instance and OFV_i^{min} is the best objective function value resulted from the given algorithm for the i^{th} instance.

For further evaluation of the proposed metaheuristics, the impact of the number of YTs on the makespan was also investigated. In Figure 4 the impact of the using a greater number of yard trucks and quay cranes on the objective function value is demonstrated. For this, an instance with 15 containers was solved for 2 to 4 QCs and 2 to 10 YTs. The results showed that there is a significant inverse correlation between the objective function value and the number of YTs.

The efficiency of two-cycling strategy versus one-cycling strategy for assignment of containers to the YTs has been studied by solving 9 random instances with two QCs and variable number of YTs. In the one-cycling scenario specific number of YTs are assigned to a quay crane at the beginning. However in two-cycling scenario, it is allowed to assign YTs in a dynamic manner during the time span of processing the containers. The results of solving these instances are shown in Figure 5.

TABLE 1. The RPD values for the proposed algorithms

No. of QCs	No. of YTs	No. of instances	Algorithms RPD (%)	
			SA	G-SA
Three-QC	6	8	11.90	0
	8	8	4.81	1.95
	10	8	8.34	2.02
	Total	24	8.35	1.32
Four-QC	6	8	7.81	2.50
	8	8	6.83	0.38
	10	8	6.95	0.29
	Total	24	7.19	1.05

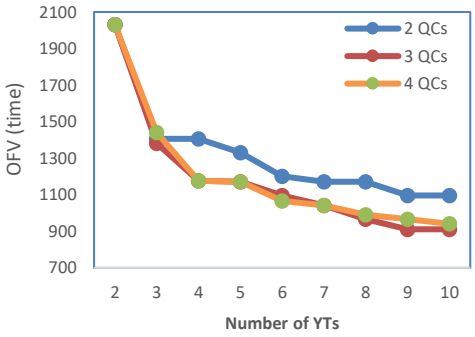

Figure 4. Effect of increasing the number of resources (YTs and QCs) on the objective function

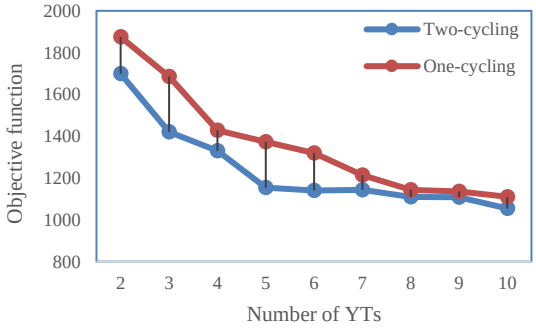

Figure 5. Comparison of the YT assignment strategies (two-cycling vs. one cycling)

6. CONCLUSION AND FUTURE STUDIES

An integrated scheduling and allocation problem of quay cranes and yard trucks at container ports is presented in this study. A mathematical model of bi-objective integer programming was developed taking into account real-world constraints, such as no quay cranes passing through each other, precedence relationships and safety distance between cranes. Since the presented problem

falls into the category of NP-hard problems, two different versions of SA are presented for solving the problem. Based on the several numerical experiments, these algorithms can obtain optimal or near-optimal solutions, especially for small-scale problems. Moreover, given the concept of grouping in hybrid optimization problems, G-SA is proposed considering the allocation of yard trucks as a grouping problem. This algorithm produces better solutions than SA.

There are some limitations in the presented research which need to be considered in the future studies. There are a few sources of uncertainty in the real world that affects the scheduling of quay cranes and yard truck. Deviation of loading and unloading operation times of vessels from the estimated time, equipment failures, and other unforeseen events may cause disorders in the deterministic schedule. This leads to significant increasing of handling costs and dissatisfaction of the customers. So considering these uncertainties and dynamics of the real world is important and could be focused in the future researches.

Moreover there are vessel stability constraints which refer to appropriate distribution of containers weight on the vessel. That affects the sequence of loading or unloading containers on the vessel. This is a critical factor that should be considered during loading and unloading containers. Otherwise it may cause sagging, twisting or even overturning of the vessel.

In this research it is simplified by considering a pre-defined stowage plan. But some modifications of containers processing sequence may be needed during the loading/unloading process of the vessel. In other words, dynamic and real time rescheduling of containers may be required in the real world problems. This is another future research direction that could be followed by researchers.

Considering uncertainties in assumptions such as container processing time, proposing real time approaches based on the vessel stability constraints and offering a method to find a lower bound for evaluation of the metaheuristic algorithm are among what may be of interest to other researchers as a future research direction.

7. REFERENCES

1. Zegordi, S. H., and Nahavandi, N., “Measuring productivity indexes and efficiency in the container terminal at port Rajaei”, ***Scientia Iranica***, Vol 9, No. 3, (2002), 248-254.
2. UNCTAD, “Review of maritime transport 2018”. United Nations Conference on Trade and Development, (2018). https://doi.org/10.18356/cd4440fc-en
3. Daganzo, C. F., "The crane scheduling problem", ***Transportation Research Part B: Methodological***, Vol. 23, No. 3, (1989), 159-175. https://doi.org/10.1016/0191-2615(89)90001-5
4. Kim, K. H., Park, Y. M., "A crane scheduling method for port container terminals", ***European Journal of Operational Research***, Vol 156, No. 3 (2004), 752-768. https://doi.org/10.1016/s0377-2217 (03)00133-4
5. Moccia, L., Cordeau, J. F., Gaudioso, M., Laporte, G. "A branch-and-cut algorithm for the quay crane scheduling problem in a container terminal", ***Naval Research Logistics***, Vol 53, No. 1 (2006), 45-59. https://doi.org/10.1002/nav.20121
6. Nguyen, S., Zhang, M., Johnston, M., Tan, K. C. "Hybrid evolutionary computation methods for quay crane scheduling problems." ***Computers and Operations Research***, Vol. 40, No. 8 (2013), 2083-2093. https://doi.org/10.1016/j.cor.2013.03.007
7. Kaveshgar, N., Huynh, N., Rahimian, S. K., "An efficient genetic algorithm for solving the quay crane scheduling problem", ***Expert Systems with Applications,*** Vol. 39, No. 18, (2012), 13108-13117. https://doi.org/10.1016/j.eswa.2012.05.091
8. Tavakkoli-Moghaddam, R., Makui, A., Salahi, S., Bazzazi, M., Taheri, F., "An efficient algorithm for solving a new mathematical model for a quay crane scheduling problem in container ports", ***Computers and Industrial Engineering,*** Vol. 56, No. 1 (2009), 241-248. https://doi.org/10.1016/j.cie.2008.05.011
9. Emde, S. "Optimally scheduling interfering and non-interfering cranes", ***Naval Research Logistics***, Vol. 64, No. 6, (2017), 476-489. https://doi.org/10.1002/nav.21768
10. Sammarra, M., Cordeau, J. F., Laporte, G., Monaco, M. F., "A tabu search heuristic for the quay crane scheduling problem", ***Journal of Scheduling***, Vol 10, No. 4-5 (2007), 327-336. https://doi.org/10.1007/s10951-007-0029-5
11. Legato, P., Trunfio, R., & Meisel, F. “Modeling and solving rich quay crane scheduling problems” ***Computers and Operations Research,*** Vol. 39, No. 9, (2012), 2063-2078. https://doi.org/10.1016/j.cor.2011.09.025
12. Chen, J. H., Bierlaire, M., “The study of the unidirectional quay crane scheduling problem: complexity and risk-aversion. European”, ***Journal of Operational Research***, Vol. 260, No. 2, (2017), 613-624. https://doi.org/10.1016/j.ejor.2017.01.007
13. Bierwirth, C., Meisel, F., "A survey of berth allocation and quay crane scheduling problems in container terminals", European ***Journal of Operational Research***, Vol 202, No. 3 (2010), 615-627. https://doi.org/10.1016/j.ejor.2009.05.031
14. Bierwirth, C., Meisel, F., "A follow-up survey of berth allocation and quay crane scheduling problems in container terminals", ***European Journal of Operational Research***, Vol. 244, No. 3 (2015), 675-689. https://doi.org/10.1016/j.ejor.2014.12.030
15. Chen, L., Bostel, N., Dejax, P., Cai, J., & Xi, L. "A tabu search algorithm for the integrated scheduling problem of container handling systems in a maritime terminal", ***European Journal of Operational Research,*** Vol 181, No. 1 (2007), 40-58. https://doi.org/10.1016/j.ejor.2006.06.033
16. Tang, L., Zhao, J., & Liu, J. "Modeling and solution of the joint quay crane and truck scheduling problem." European ***Journal of Operational Research,*** Vol 236, No. 3, (2014), 978-990. https://doi.org/10.1016/j.ejor.2013.08.050
17. Kaveshgar, N., & Huynh, N. "Integrated quay crane and yard truck scheduling for unloading inbound containers." International ***Journal of Production Economics,*** Vol 159 (2015), 168-177. https://doi.org/10.1016/j.ijpe.2014.09.028
18. Vahdani, B., Mansour, F., Soltani, M., & Veysmoradi, D. "Bi-objective optimization for integrating quay crane and internal truck assignment with challenges of trucks sharing." ***Knowledge-Based Systems,*** Vol 163, (2019), 675-692. https://doi.org/10.1016/j.knosys.2018.09.025
19. Fazli, M., Fathollahi-Fard, A. M., Tian, G., “Addressing a Coordinated Quay Crane Scheduling and Assignment Problem by Red Deer Algorithm”, ***International Journal of Engineering, Transactions B: Applications,*** Vol. 32, No. 8, (2019), 1186-1191.

https://doi.org/10.5829/ije.2019.32.08b.15

20. Behjat, S., & Nahavandi, N. "A Mathematical Model and Grouping Imperialist Competitive Algorithm for Integrated Quay Crane and Yard Truck Scheduling Problem with Non-crossing Constraint" ***International Journal of Engineering, Transcation A: Basics***, Vol. 32, No. 10, (2019), 1464-1479. https://doi.org/10.5829/ije.2019.32.10a.16
21. Pinedo, M. Scheduling. New York: Springer, 2012. https://doi.org/10.1007/978-1-4614-2361-4
22. Kirkpatrick, S., Gelatt, C. D., Vecchi, M. P. "Optimization by simulated annealing", ***Science***, Vol. 220, No. 4598, (1983), 671-680. https://doi.org/10.1126/science.220.4598.671
23. Nikabadi, M., & Naderi, R. "A hybrid algorithm for unrelated parallel machines scheduling." ***International Journal of Industrial Engineering Computations***, Vol. 7, No. 4, (2016), 681-702. https://doi.org/10.5267/j.ijiec.2016.2.004
24. Kashan, A. H., Kashan, M. H., Karimiyan, S. "A particle swarm optimizer for grouping problems." ***Information Sciences***, Vol. 252, (2013), 81-95. https://doi.org/10.1016/j.ins.2012.10.036

Persian Abstract

چکیده

زمان‌بندی و تخصیص جرثقیل‌های اسکله‌ای در بنادر کانتینری از مسائل مهم و کاربردی در بهبود بهره‌وری این ترمینال ها به شمار می‌رود. در این تحقیق یک مدل ریاضی با هدف مدیریت یکپارچه جرثقیل‌های اسکله‌ای و کامیون‌های محوطه ارائه شده است. در این مدل فرضیات کلیدی دنیای واقعی از جمله فرض عدم عبور جرثقیل‌ها از روی یکدیگر و نیز فاصله ایمنی بین جرثقیل‌های در حال کار در نظر گرفته شده اند. نتایج عددی نشان می‌دهد که مدل عدد صحیح پیشنهادی، می‌تواند در حل مسائل با ابعاد کوچک به تصمیم گیران کمک کند. با این وجود به دلیل NP-hard بودن مساله پیشنهادی، الگوریتم های فراابتکاری به منظور حل مساله در ابعاد بزرگ تر پیشنهاد شده‌اند. همچنین با توجه به اینکه کامیون‌های محوطه به عنوان یکی از منابع اصلی مساله، تفاوت خاصی با هم ندارند، می‌توان از رویکرد گروه‌بندی در حل مساله استفاده نمود. از این رو الگوریتم شبیه سازی تبرید با رویکرد گروه‌بندی توسعه داده شده است که براساس آزمایش‌های صورت گرفته عملکرد بهتری نسبت به الگوریتم شبیه سازی تبرید عادی دارد.

International Journal of Engineering

Journal Homepage: www.ije.ir

Investigation on Mechanical and Electrical Properties of Cu-Ti Nanocomposite Produced by Mechanical Alloying

R. M. Babaheydari, S. O. Mirabootalebi*, G. H. Akbari

Department of Material Science and Engineering, Shahid Bahonar University of Kerman, Iran

P A P E R I N F O

Paper history:
Received 25 January 2020
Received in revised form 02 August 2020
Accepted 02 August 2020

Keywords:
Copper-Titanium Alloys
Mechanical Alloying
Electrical Resistance
Mechanical Properties

A B S T R A C T

In this paper, Cu-Ti nanocomposite synthesized via ball milling of copper-titanium powders in 1, 3, and 6 of weight percentage compounds. The vial speed was 350 rpm and ball to powder weight ratio kept at 15:1 under Argon atmosphere, and the time of milling was 90 h. Obtained powders were studied by scanning electron microscopy (SEM), X-ray diffraction (XRD), and dynamic light scattering (DLS). Crystallite size, lattice strain, and lattice constant were calculated by Rietveld refinement with Maud software. The results show a decrease in the crystallite size, and an increase in the internal strain and lattice parameter. Furthermore, the lattice parameter grew by increasing the percentage of titanium. Then, the powders compressed by the cold press and annealed at 650˚C. Finally, their micro-hardness and electrical resistance were measured. These analyses show that via increasing the proportion of titanium, Cu-6wt%Ti with 312 Vickers had the highest micro-hardness; due to the increasing the work hardening. Moreover, the results of the electrical resistance illustrate through increasing the amount of alloying material, the electrical resistance grew which the highest electrical conductivity was Cu-1wt%Ti with 0.36 Ω.

***doi**: 10.5829/ije.2020.33.09c.09*

1. INTRODUCTION

For the best performance of copper nanocomposites, it is necessary to make a good balance between its electrical and mechanical properties [1]. This means the alloy can be strengthened without a considerable reduction in the electrical properties of copper [2]. Increasing the mechanical properties through the formation of a saturated solid solution and the formation of fine nanometer-scale sediments is always a suitable way to increase the strength, toughness, thermal stability, creep resistance and at the same time, reduce changes in the electrical properties of copper [3-6]. A very good example here is Cu-Be alloys which have attracted very much attention by providing a strength of more than 1000 MPa and maintaining electrical conductivity of copper. But the main drawback of this alloy, which has limited its industrial use, is the high cost and toxicity of beryllium [7]. Cu-Ti alloys are the best alternative to Cu-Be and some similar alloys, because of the high strength, corrosion resistance, antibacterial property, high electrical conductivities and thermal stability [2, 8-11]. Some applications of Cu-Ti nanocomposite include relay controls [12], prosthetic dental applications [13], solar cells [14], anticorrosive applications [15], electrochemical denitrification [16], and, etc.

A variety of methods have been used to produce Cu-Ti alloys, for instance melting and casting processes or solid-state processing like powder metallurgy. In particular, new methods such as rapid solidification, severe plastic deformation (SPD), accumulative roll-bonding (ARB), electrolysis, high-energy milling and sol-gel have been proposed to prepare Cu-Ti alloys [17-22]. Among these approaches, mechanical alloying (MA) due to simplicity and cheapness of the process, being eco-friendly and homogenous dispersion of the second phase, has a special place for the production of Cu-Ti alloys.

Several studies have been carried out on Cu-Ti alloys produced by MA. Shkodich et al. and Sheibani et al. [23, 24], studied the formation and nanocrystalline phases of

*Corresponding Author Institutional Email: *oveis@eng.uk.ac.ir*
(S. O. Mirabootalebi)

Please cite this article as: R.M. Babaheydari, S.O. Mirabootalebi, G.H. Akbari, Investigation on Mechanical and Electrical Properties of Cu-Ti Nanocomposite Produced by Mechanical Alloying, International Journal of Engineering (IJE), IJE TRANSACTIONS C: Aspects Vol. 33, No. 9, (September 2020) 1759-1765

Cu-Ti by mechanical alloying. Preparing Cu-Ti via wet ball-milling was investigated by Eryomina et al. [25, 26]. Nagarjuna investigated the thermal conductivity of Cu-Ti alloy [27] and Guwer et al. discuss the micro-hardness of produced Cu-Ti alloys [28]. Likewise, Pourfereidouni and Akbari [29] analyzed the nano-structures of Cu-Ti Alloys in MA. Despite a wide range of studies on copper-titanium alloys in MA process, none of them focused on simultaneous changes in the crystal structure, micro-hardness, and electrical conductivity.

In the present study, the supersaturated solid solution copper with different percentages of titanium synthesized by high energy ball milling. The fabricated Cu-Ti nanocomposites were investigated by XRD, SEM and DLS analyses and the changing in the crystallite size, internal strain, the lattice constant, structure of the particles and particle-size distribution at different amount of Ti were investigated. Subsequently, heat treatment was performed and the hardness of the nanocomposite alloys was studied by the Vickers Micro-hardness test. Finally, the specimens were placed in an electrical circuit and their electrical resistance was evaluated.

2. MATERIALS AND METHODS

Precursors were pure Cu (99.7%,<6μm) and Ti (97%,10 μm). Samples with three compounds of 1, 3 and 6 weight percentages of Ti were milled for 90 h in a planetary ball mill at Ar atmosphere. The initial amount of powders was 15 g, the balls were 10 and 15 mm in diameter and the ball-to-powder weight ratio was kept at 15:1, and the vial speed was 350 rpm.

The structural changes in obtained samples were studied by an X-ray diffractometer (Philips X'Pert, Cu-Kα, λ=0.1542 nm). Rietveld refinement was used to calculate the copper crystallographic parameters including lattice parameter, crystal size, and internal strain. Morphology and size of ball-milled samples were analyzed by using scanning electron microscopy (Cam Scan mv2300) and the size distribution of samples was analyzed by zeta-seizer (ZEN3600). For sintering the mixed powders, the specimens were first molded to a diameter of 1 cm and thickness of 1 mm. Hence, 1.4 grams of the synthesized Cu-Ti powders were under pressure a coaxial cold press machine (12 ton). Sintering process applied in a tube furnace for a half-hour at 650˚C in Ar. The Vickers microscopy test was performed according to ASTM E 348-89 standard (Duramin20 Strues microprocessor) and micro-hardness was performed with a force of 98.7 mN at 400 magnification for 5 s. The electrical resistance of the samples was measured by using an electrical circuit. In this approach, the produced samples were placed in the circuit and by applying a voltage, the passing current through the tablets calculated and then by the Ohm's law, the resistance of the samples was obtained.

3. RESULTS AND DISCUSSION

Figure 1 shows the XRD pattern of Cu-1, 3, 6 wt% Ti powders after 90 hours of ball milling. By comparing the peaks, the highest and the lowest peaks were observed in Cu-1wt%Ti and Cu-6wt%Ti, respectively. The low amount of the alloying element makes it difficult to detect the peaks of alloying elements in the XRD pattern.

During the ball milling of Cu-Ti, powder particles were severely deformed by the impact of the balls. This process leads to an increase in the local temperature and as a result, atomic diffusion occurs. Furthermore, density of crystalline defects such as vacancies, dislocations and stacking faults are greatly increased. Therefore, the particles get work hardening over time and as the effects of work hardening expanded, the internal strain and the width of the peaks were increased. The crystal defects are diffusion pathways for Ti atoms to dissolve in the copper matrix. On the other hand, after long milling time and increasing internal strains, the dislocations were regularly incorporated into the copper lattice and create subgrain boundaries. By continuing the milling process and increasing the density of the dislocations at the subgrain boundaries, they provide the basis for rotating these boundaries and converting them to the original boundaries.

Figure 2 provides information about lattice constant of Cu-1, 3, 6 wt% Ti after 90 h of milling. We can see with the increasing the amount of titanium, the lattice parameter increased. As well as, by increasing the percentage of Ti to 6 weight percentages, the lattice constant increases at a higher rate. The presence of large titanium atoms (0.147 nm radius) in the copper matrix increased the copper lattice parameter and is a sign of the formation of a solid solution. The high concentration gradient in the presence of large quantities of the reinforcement element in the primary powder mixture will help the titanium atoms to diffuse in copper lattice, therefore, a more saturated solid solution is formed. In fact, the possibility of collisions increased by raising

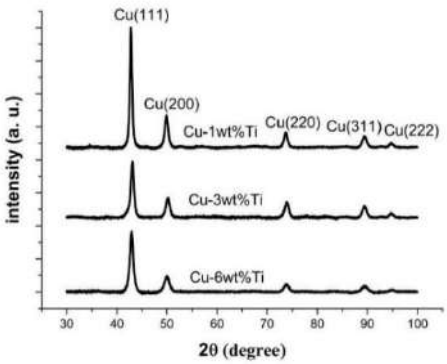

Figure 1. X-ray diffraction pattern of Cu-1, 3, 6 wt% Ti samples after ball milling for 90 hours

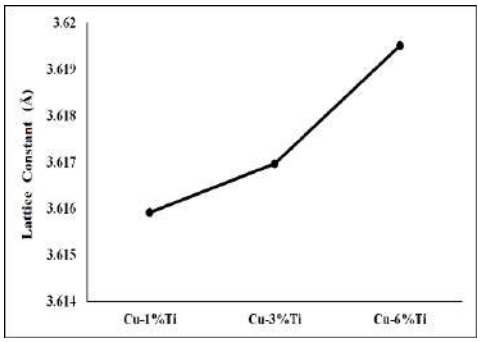

Figure 2. Diagram of changes in the copper lattice constant of 1, 3, 6wt% Ti after 40 h of ball milling

in the proportion of titanium, thereby the lattice parameter increased.

The crystallite size of copper for the Cu-1, 3, 6wt% Ti samples after 90 h of ball milling is shown in Figure 3. The crystallite size of all samples was in the range of 9-32 nm, and Cu-6wt% Ti has the largest reduction in crystal size (9 nm), while the Cu-1wt% Ti powder has the highest crystal crystallite size (17 nm).

Generally, the crystallite size is determined by the competition between plastic deformation through the motion of dislocations and the recovery and recrystallization [30]. Indeed, recovery and recrystallization increased by reducing the plastic deformation, conversely, the crystallite size decreases.

In this study, due to the low speed (350 rpm) and 15 min stop after 30 minutes of ball milling, the vial temperature did not increase and so the recovery and recrystallization phenomenon did not occur and the crystallite size decreased uniformly with increasing plastic deformation. The higher initial proportion of titanium accelerates work hardening, fraction, diffusion and segmentation of crystallite. Thus, Ti is dissolved and the hardness of the matrix increase. The reason for the more reduction of the crystal size in the compositions with more fraction of titanium is the aggregation of the effect of cold working and saturation of the copper matrix. Moreover, by increasing the percentage of Ti, the effects of the cold working become more apparent, and as a result, subgrain boundaries and dislocations create more and more.

Figure 4 shows the strain of the copper lattice for Cu-1, 3, 6wt%Ti samples. The internal strain and its rate grow by increasing the proportion of Ti. Initial powders are strain-free, but by starting the milling process, there is a rapid increase in the number of dislocations and other crystallographic defects. Gradually, with the formation of dislocations and reaching the crystallite size to a few nanometers, the number of dislocations has reached the saturated extent and under this situation, no new dislocations are created by increasing milling time. On the other hand, Ti atoms have also been entered into the Cu lattice during this period, these two phenomena impose strains on the lattice of copper. As shown in Figure 4, by increasing Ti percentage, the lattice strain of all samples is grown. In copper composites due to combination with the higher amount of Ti, the effects of cold working were much more severe, and the dissolutions of alloying elements increased. Consequently, matrix structure more affected due to the cold working and more defects, and eventually a much higher strain on the lattice is produced. Indeed, titanium by dissolving in the copper matrix and forming a solid solution, create more strain on the copper lattice.

The particle size distribution of Cu-1, 3, 6wt% Ti samples is shown in Figure 5. The average particle sizes for Cu-1, 3, 6wt% Ti were 188, 165 and 141 nm, respectively. According to Figure 5, sizes of particles were decreased by increasing the proportion of second phase and creation the richer solid solution, which leads to an expand the work hardening of the samples. Therefore, the samples with higher amounts of Ti were more fractured and the powder particles due to the more work hardening of the solid solution, have the smaller size. It should be noted that in all the samples some large particles of powder in the solution are deposited and the results illustrate the smaller particles. Although, the important point in this analysis is proving the achievement of the nano-sized particles in Cu-Ti composites by the MA method.

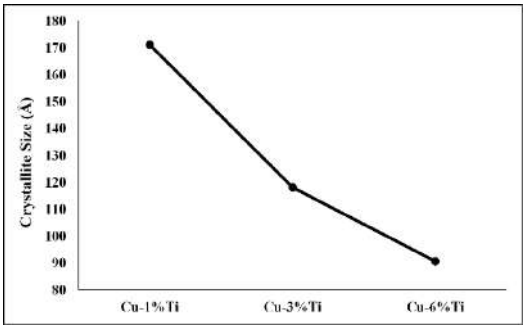

Figure 3. Crystallite size of Cu-1, 3, 6wt%Ti samples after 90 h of milling

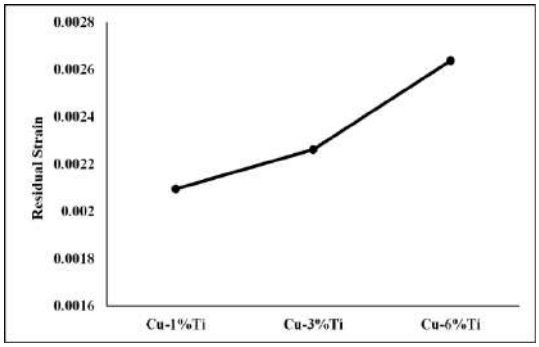

Figure 4. Strain changes of Cu-1, 3, 6wt%Ti samples

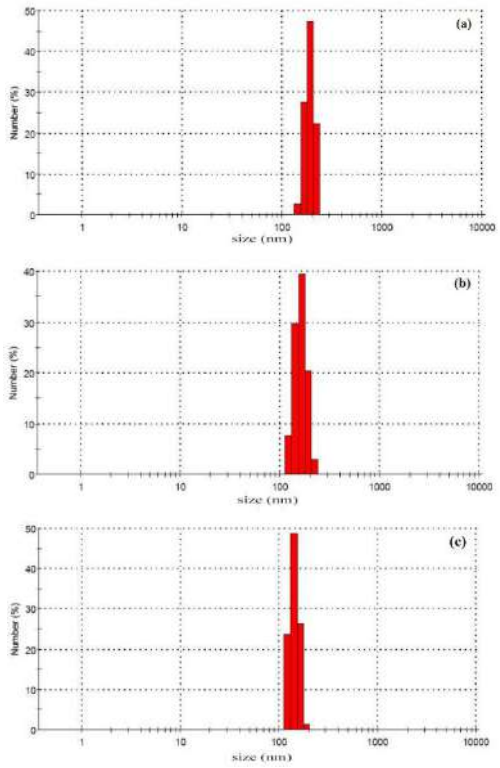

Figure 5. The particle size distribution Cu-1, 3, 6wt% Ti in a, b and c, respectively

The morphology and particle size of the powder mixtures are shown in Figure 6. Cu-1wt% Ti has the largest particle size and the size of particles decreased with increasing the amount of Ti. Due to the long milling time (90 h) of copper-titanium powder and making a balance between cold welding and fracture, the particle size distribution is reduced and have a uniform shape and dimensions, they also became agglomerated.

Titanium particles have an HCP structure and trapped between copper particles with FCC structure, which have been faster work hardening than copper. At this stage, the brittle titanium particles are distributed among the softer copper particles and create tiny cracks in their edges. As these cracks grow and spread into the powder grains, failure would occur more rapidly. On the other hand, in the compounds with a high initial titanium percentage, a rich solid solution was obtained. That is a reason for the higher hardness of these compounds. Hence, the samples with higher titanium content were more fractured and the powder particles, due to the higher hardness by the formation of the richer solid solution, had the smaller sizes.

Figure 7 gives information about the hardness changes of Cu-1, 3, 6wt% Ti after annealing at 650˚C. As can be seen, the micro-hardness increases by increasing the percentage of Ti. Cu-6wt% Ti with a hardness of 312

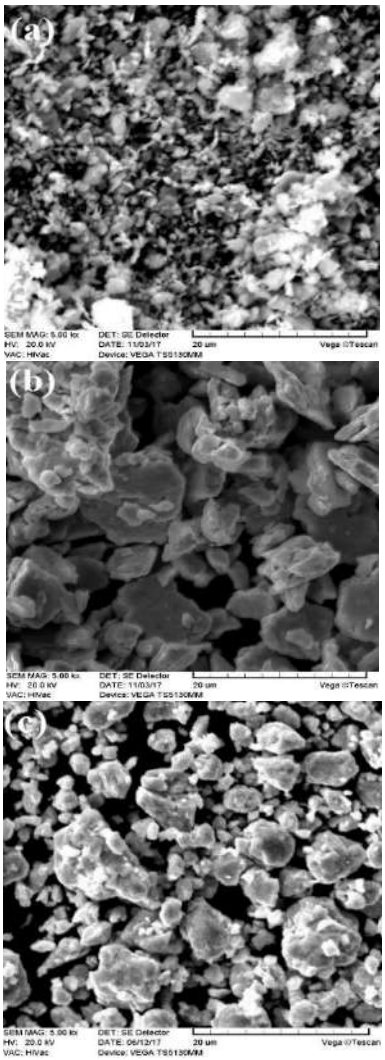

Figure 6. SEM images of Cu-1, 3, 6wt% Ti samples (a, b and c, respectively) after 90 hours of milling

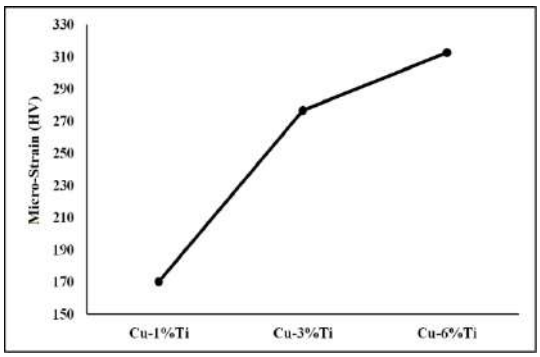

Figure 7. Micro-hardness changes of Cu-1, 3, 6wt% Ti after 90 hours of milling

Vickers had the highest hardness and the rate of increasing hardness decreased with an increasing amount of titanium. Due to the high work hardening of the

powders at the ball-milling process, the applied force during compression does not cause significant changes in micro-hardness [30].

The solubility of titanium in copper is very low at room temperature (<0.1 atomic percentage). In the mechanical alloying of copper-titanium, the concentration of titanium in the copper matrix is increased and reached to more value of the steady-state condition. This over-dissolution of titanium in the field of copper by MA and annealing at 650˚C provides a suitable situation for the deposition of titanium atoms in nanometer-sized particles. Therefore, the formation of titanium-rich nanoparticles in the matrix of copper in the sintering step, simultaneous with recovery and recrystallization of the processes will not only delay the softening process but also halt in many cases.

In general, the Cu4Ti sediments in the early stages of sintering are in the form of a coherent and fine nanometer. These sediments which were created inside the grains are obstacles to dislocation movement. Thus, delays recovery and recrystallization increases the micro-hardness.

Figure 8 shows the electrical resistance changes of the Cu-1, 3, 6wt% Ti. The electrical resistance increased by increasing the percentage of titanium. Cu-6wt% Ti with 0.44 Ω and Cu-1wt%Ti with 0.36 Ω, had the highest and lowest electrical resistance, respectively. Furthermore, the electrical resistance rate grows by increasing the proportion of Ti.

The main reason for increasing the electrical resistance by increasing the proportion of titanium is the lower conductivity of titanium than copper, which has a great effect on electrical conductivity. The higher density of defects and the richer solid solution lead to work hardening along the increasing amount of titanium and provide a high volume fraction of the sediments. Consequently, movements of electrons are prevented and the electrical resistance has increased, by these crystallographic defects and the sediments.

Regarding the percentage of the second phase and micro-hardness of the samples, electrical resistance in all fabrication of Cu-Ti alloys, such as the aging and severe drawing, and laser welding [31, 32]. It seems high capability of the ball-milling to mono-dispersion of the second phase particles cause to strengthen the grain boundaries and better precipitate of the titanium. On the other hand, the low content solution of Ti in the copper lattice has a minor effect on the electrical properties of the copper composites. The comparison of the micro-hardness and the electrical resistivity results represents the maintaining of mechanical strength simultaneous with the proper electrical conductivity of the produced Cu-alloys.

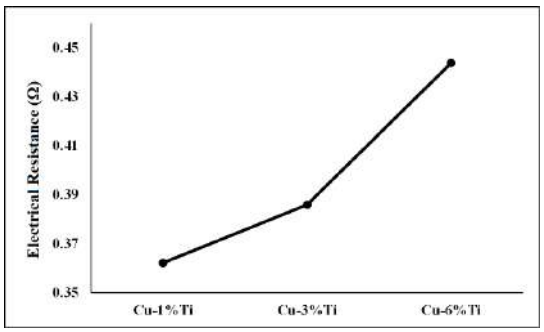

Figure 8. Electrical resistance of Cu-1, 3, 6wt% Ti compounds after 90 hours of milling

4. CONCLUSION

1. By mechanical alloying of copper and titanium with different percentages, it is possible to produce nanostructured Cu-Ti with nanometer-scale particle size.
2. The lattice constant increased by increasing the proportion of titanium.
3. The crystallite size is decreased and the internal strain is increased as the proportion of the titanium was increased.
4. Higher percentage of titanium lead to smaller particle size. Cu-6wt%Ti with average size of 141 nm has the smallest particle size.
5. Micro-hardness is increased by increasing the proportion of titanium.
6. Addition of titanium to the copper leads to homogeneous morphology.
7. The electrical resistance grew by increasing the amount of titanium.

5. REFERENCES

1. Wang, W, Li, R, "Effect of direct current pulses on mechanical and electrical properties of aged Cu–Cr–Zr alloys", ***Materials & Design***, Vol. 92, (2016), 135-142, https://doi.org/10.1016/j.matdes.2015.12.013.
2. Eze, A.A, Tamba, Jamiru, "Effect of titanium addition on the microstructure, electrical conductivity and mechanical properties of copper by using SPS for the preparation of Cu-Ti alloys", ***Journal of Alloys and Compounds***, Vol. 736, 2018, 163-171, https://doi.org/10.1016/j.jallcom.2017.11.129 .
3. Nadutov, V, "Thermal stability of solid solutions formed by ultrasonic milling of Cu–Co and Cu–Fe powder mixtures", ***Journal of Physics***, Vol. 62, No. 8, (2017), 685-691, doi: 10.15407/ujpe62.08.0685.
4. Bachmaier, A, "High strength nanocrystalline Cu–Co alloys with high tensile ductility", ***Journal of Materials Research***, Vol. 34, 2019, p. 58-68, DOI: https://doi.org/10.1557/jmr.2018.185.
5. Rabiee, M., H. Mirzadeh, and A. Ataie, "Processing of Cu-Fe and Cu-Fe-SiC nanocomposites by mechanical alloying", ***Advanced Powder Technology***, Vol. 28, (2017), 1882-1887, https://doi.org/10.1016/j.apt.2017.04.023

6. Chabri, S., S.Bera, "Microstructure and magnetic behavior of Cu–Co–Si ternary alloy synthesized by mechanical alloying and isothermal annealing", ***Journal of Magnetism and Magnetic Materials***, Vol. 426, (2017), 454-458, https://doi.org/10.1016/j.jmmm.2016.08.029.
7. Shah, A.N, "Beryllium in the environment: Whether fatal for plant growth?" ***Reviews in Environmental Science and Bio/Technology***, Vol. 15, (2016), 549-561, https://doi.org/10.1007/s11157-016-9412-z.
8. Wang, "Cu–Ti–C alloy with high strength and high electrical conductivity prepared by two-step ball-milling processes", ***Materials & Design***, Vol. 61, (2014), 70-74, https://doi.org/10.1016/j.matdes.2014.04.034.
9. Wang, F, "In-situ fabrication and characterization of ultrafine structured Cu–TiC composites with high strength and high conductivity by mechanical milling", ***Journal of Alloys and Compounds***, Vol. 657, (2016), 122-132, https://doi.org/10.1016/j.jallcom.2015.10.061.
10. Karakulak, E., "Characterization of Cu–Ti powder metallurgical materials". ***International Journal of Minerals, Metallurgy***, and Materials, Vol. 24, (2017), 83-90, https://doi.org/10.1007/s12613-017-1381-x.
11. Liu, J., "Effect of Cu content on the antibacterial activity of titanium–copper sintered alloys", ***Materials Science and Engineering***, Vol. 35, (2014), 392-400, https://doi.org/10.1016/j.msec.2013.11.028.
12. Semboshi, S., E. Hinamoto, and A. Iwase, "Age-hardening behavior of a single-crystal Cu–ti alloy", ***Materials Letters***, Vol. 131, (2014). 90-93, https://doi.org/10.1016/j.matlet.2014.05.128.
13. Liu, X, "Binary titanium alloys as dental implant materials—a review", ***Regenerative Biomaterials***, Vol. 4, No. 5, (2017). 315-323, https://doi.org/10.1093/rb/rbx027.
14. Saha, S, S.B. Abd Hamid, and T.H. Ali, "Catalytic evaluation on liquid phase oxidation of vanillyl alcohol using air and H2O2 over mesoporous Cu-Ti composite oxide", ***Applied Surface Science***, Vol. 354, (2017), 205-218, https://doi.org/10.1016/j.apcatb.2019.04.026.
15. Zhang, E, " Effect of the existing form of Cu element on the mechanical properties, bio-corrosion and antibacterial properties of Ti-Cu alloys for biomedical application", ***Materials Science and Engineering: C***, Vol. 69, (2016), 1210-1221, https://doi.org/10.1016/j.msec.2016.08.033.
16. Liu, F, "Fabrication and characterization of Cu/Ti bilayer nanoelectrode for electrochemical denitrification", ***International Journal of Electrochemical Science***, Vol. 11, (2016), 8308-8322, doi: 10.20964/2016.10.49.
17. Hosseini, Pardisa, N, "Structural characteristics of Cu/Ti bimetal composite produced by accumulative roll-bonding (ARB)", ***Materials & Design***, Vol. 113, (2017), 128-136, https://doi.org/10.1016/j.matdes.2016.09.094.
18. Shkodich, Vadchenkoa, S.G, "Crystallization of amorphous Cu50Ti50 alloy prepared by high-energy ball milling", ***Journal of Alloys and Compounds***, Vol. 741, (2018), 575-579, https://doi.org/10.1016/j.jallcom.2018.01.062.
19. Kursun, C, and M. Gogebakan, "Structure and Mechanical Behaviour of Cu-Zr-Ni-Al Amorphous Alloys Produced by Rapid Solidification", Metallic Glasses–Formation and Properties, (2016), DOI: 10.5772/63513.
20. Sundeev, R.V, Shalimovab, A.V, "Difference between local atomic structures of the amorphous Ti2NiCu alloy prepared by melt quenching and severe plastic deformation: ***Materials Letters***, Vol. 214. (2018), 115-118, https://doi.org/10.1016/j.matlet.2017.11.110.
21. Vorotilo, S, Loginov, PA, "Manufacturing of Conductive, Wear-Resistant Nanoreinforced Cu-Ti Alloys Using Partially Oxidized Electrolytic Copper Powder", ***Nanomaterials***, Vol. 10. No. 7, (2020), 1261, https://doi.org/10.3390/nano10071261.
22. Zeng, Y, Wang. T, "Sol–gel synthesis of CuO-TiO2 catalyst with high dispersion CuO species for selective catalytic oxidation of NO", ***Applied Surface Science***, Vol. 411, (2017), 227-234, https://doi.org/10.1016/j.apsusc.2017.03.107.
23. Sheibani, S., S. Heshmati-Manesh, and A, "Ataie, Structural investigation on nano-crystalline Cu–Cr supersaturated solid solution prepared by mechanical alloying", ***Journal of Alloys and Compounds***, Vol. 495, No. 1, (2010), 59-62. https://doi.org/10.1016/j.jallcom.2010.02.034.
24. Shkodich, NF, Rogachev, AS, "Formation of amorphous structures and their crystallization in the Cu–Ti system by high-energy ball milling", ***Russian Journal of Non-Ferrous Metals***, Vol. 59. No. 5, (2018), 543-549, https://doi.org/10.3103/S1067821218050176.
25. Eryomina, MA., Lomayeva, SF, "Microstructure Characterization and Properties of Ti Carbohydride/Cu–Ti/GNP Nanocomposites Prepared by Wet Ball Milling and Subsequent Magnetic Pulsed Compaction", ***Metals and Materials International***, (2019), 1-11, https://doi.org/10.1007/s12540-019-00531-9.
26. Eryomina, M. and S. Lomayeva, "Composites prepared by multistage wet ball milling of Ti and Cu powders: Phase composition and effect of surfactant addition", ***Advanced Powder Technology***, Vol. 31, No. 5, (2020), https://doi.org/10.1016/j.apt.2020.02.014.
27. Nagarjuna, S, "Thermal conductivity of Cu-4.5 Ti alloy", ***Bulletin of Materials Science***, Vol. 27, No. 1, (2004), 69-71, https://doi.org/10.1007/BF02708488.
28. Guwer, A., Nowosielski, R, "Fabrication of copper-titanium powders prepared by mechanical alloying", ***Indian Journal of Engineering and Materials Sciences*** , Vol. 21, (2014).
29. Pourfereidouni, A. and G.H. Akbari, "Development of Nano-Structure Cu-Ti Alloys by Mechanical Alloying Process", ***Advanced Materials Research***, Vol. 829, (2014), 168-172, https://doi.org/10.4028/www.scientific.net/AMR.829.168.
30. Suryanarayana, C, Mechanical alloying and milling. Progress in materials science, Vol. 46, No. 1-2, (2001), 1-184, https://doi.org/10.1016/S0079-6425(99)00010-9.
31. Zhao, Y, Wang, W, "Microstructure and properties of Cu/Ti laser welded joints", ***Journal of Materials Processing Technology***, Vol. 257, (2018), 244-249, https://doi.org/10.1016/j.jmatprotec.2018.03.001.
32. Semboshi, S, Kaneno, Y, "High strength and high electrical conductivity Cu-Ti alloy wires fabricated by aging and severe drawing", ***Metallurgical and Materials Transactions A***, Vol. 49, No. 19, (2018), 4956-4965, https://doi.org/10.1007/s11661-018-4816-8.

Persian Abstract

چکیده

در این مقاله ، نانوکامپوزیت مس-Ti از طریق آسیاکاری گلوله‌ای مخلوط پودرهای مس - تیتانیوم در ترکیبات ۱ ، ۳ و ٦ درصد وزنی سنتز گردید. سرعت کاپ ۳۵۰ دور در دقیقه و نسبت وزن گلوله به پودر ۱۵: ۱ بود. فرآیند در اتمسفر آرگون انجام شد و همچنین زمان آسیاب ۹۰ ساعت بود. پودرهای به دست آمده توسط (SEM)، (XRD) و (DLS) مورد بررسی قرار گرفت. اندازه کریستالی ، کرنش شبکه و ثابت شبکه با آنالیز Rietveld و نرم افزار Maud محاسبه شد. نتایج حاکی از کاهش در اندازه کریستالیت و افزایش کرنش و پارامتر شبکه است. علاوه بر این ، پارامتر شبکه با افزایش درصد تیتانیوم افزایش می‌یابد. سپس پودرها توسط پرس سرد فشرده شده و در دمای ٦۵۰ درجه سانتیگراد آنیل می شود و در نهایت میکرو سختی و مقاومت الکتریکی آنها اندازه گیری شد. تجزیه و تحلیل این تست ها نشان می دهد که Cu-6wt%Tiبا ۳۱۲ ویکرز بالاترین میزان میکرو سختی را دارد و با افازیش تیتانیوم سختی افزایش می‌یابد. نتایج مقاومت الکتریکی نشان می دهد که با افزایش مقدار عنصر آلیاژی تیتانیوم، مقاومت الکتریکی بیشتر می‌شود که بیشترین هدایت الکتریکی مربوط به Cu-1wt%Ti با $0.36\ \Omega$. است.

International Journal of Engineering

Journal Homepage: www.ije.ir

Effect of Mechanical Alloying and Sintering on Phase Transformation, Microstructural Evolution, Mechanical Properties and Density of Zr-Cr Alloy

J. Arasteh*

Department of Materials Science and Engineering, Shahid Bahonar University of Kerman, Kerman, Iran

P A P E R I N F O

Paper history:
Received 30 June 2020
Received in revised form 18 July 2020
Accepted 02 August 2020

Keywords:
Mechanical Alloying
Microhardness
Nanostructured
Sintering
Solubility

A B S T R A C T

The purpose of present research was production of Zr-based alloy as the nuclear fuel cladding by mechanical alloying (MA) and sintering process. Firstly, Zr and Cr powders were mechanically alloyed to produce the refractory and hard Zr-10 wt% Cr alloy, and then, the powder mixtures were consolidated by press and following sintering at temperature of 800˚C min. The phase evolution, microstructural changes, microhardness, and density of the Zr-10 wt% Cr alloy were studied using X-ray diffraction (XRD), scanning electron microscopy (SEM), microhardness measurement, and the Archimedes method. The results showed that the MA increased the solid solubility of the immiscible powders of Cr and Zr; therefore, the Cr atoms were completely dissolved in the Zr lattice after 24 h of the milling time and the nanostructured Zr(Cr) solid solution was obtained with the high microhardness value of about 491 Hv. Also, the results of the density measurement indicated that the resulted density was close to 98% of the theoretical density.

***doi**: 10.5829/ije.2020.33.09c.10*

1. INTRODUCTION

Zirconium alloys are considered as a high temperature structural materials owing to proper corrosion resistance, good thermal stability, desired mechanical and physical properties, and low thermal neutron absorption properties [1]. Cr is a useful alloying element for Zr-based alloys owing to high melting point, and also, Zr-Cr alloys can be used as a high temperature material with good strength, proper erosion resistance, and excellent corrosion resistance. So far, extensive research has been done on Zr-Cr alloys. The microstructural examination of the rapidly cooled Zr-0.15% Cr alloy showed that a Zr-rich solid solution was formed. This solid solution phase was precipitated in the grain boundaries of Zr which increased the microhardness and strength of the Zr-Cr alloy [2]. The Zr-Cr multilayer coating on Zr surface by vacuum arc vapor method was significantly increased the hot corrosion resistance of the Zr-based alloy [3]. The Cr ion implantation was subjected on the Zr-1Nb alloy to improve the corrosion behavior of Zr-based alloy, which the result showed the laves phase was homogeneously precipitated within the α-Zr matrix. Also, the oxidation resistance of the Zr-based alloy was improved at high temperature due to the Cr ion implantation on the surface of Zr [4]. Huang et al. [5] have produced Cr coated Zr-based alloy by electroplating which the result indicated that the oxidation resistance of Zr-based alloy cladding was significantly improved. Also, pulsed laser treatment was subjected to the commercial Zr alloy to perform the Cr alloying on the Zr surface. The results of this research displayed that the microhardness of Zr was noticeably increased due to the microstructure improvement and grain refinement [6].

So far, many methods have been used to produce the Zr-Cr alloys, but the mechanical alloying method has always attracted the attention of the researchers due to the low cost of the instrument and primary powders [7], production of the stable and metastable phases [8, 9] no need for high temperatures [10], alloying of the elements with high difference in the melting points [11], independency of the limitation of the phase diagram

*Corresponding Author Email: *javadaraste68@gmail.com* (J. Arasteh)

Please cite this article as: J. Arasteh, Effect of Mechanical Alloying and Sintering on Phase Transformation, Microstructural Evolution, Mechanical Properties and Density of Zr-Cr Alloy, International Journal of Engineering (IJE), IJE TRANSACTIONS C: Aspects Vol. 33, No. 9, (September 2020) 1766-1772

[12], ability to the uniform distribution of the components, and production of the nanostructure materials and quasi-stable microstructures [13-14]. The mechanical alloying accelerated the kinetic of the chemical reactions and changed the metallurgical transformations which led to occur the reactions at room temperature [15]. Researchers have proven that chromium is a very suitable additive element to improve the mechanical properties [16] and corrosion resistance [17] of Zr which indicates that the Zr-Cr alloys have the special importance among the Zr-based alloys. But in the Zr-Cr alloy system, the solid solubility of Cr in Zr is very low at the equilibrium state [18]. The solubility of these elements can be increased by nonequilibrium processes such as mechanical alloying. The purpose of this research was to produce a solid solution of Zr-Cr alloy with high hardness by mechanical alloying and sintering process. Also, the phase evolution, structural and morphological changes, mechanical properties, and physical properties of the Zr-Cr alloys were investigated.

2. MATERIALS AND METHODS

In the present research, planetary ball mill (84 D, Sepahan) was used to produce Zr- 10% Cr alloy. Therefore, the Cr and Zr powders (99.9% purity, prepared by Alpha Aesar) were firstly mixed according to the weight ratio of Zr-10 wt% Cr. Then, 10 g powder mixtures of Cr and Zr along with the 200 g steel balls were put into a steel vial. Milling was performed under argon gas atmosphere with a rotational speed of 400 rpm. The milling process was stopped for 15 minutes after every 30 minutes of the work to prevent the temperature rise inside the vial. Some powders were taken out the vial within 8, 16, 24, and 32 hours of milling to analyze the phase transformation at various milling times.

In order to consalidation of the milled powders, the powders were pressed into a cylindrical steel mold with a load of 300 MPa. It should be noted that the dimensions of the produced billet were 30 mm in the length and the diameter of 27 mm. Then, the pressed samples were subjected to sintering process at a temperature of 800 ℃ for 30 min under the argon gas atmosphere.

In this study, X-ray diffraction analysis (XRD, D8 advance Bruker system, CuKα radiation) was performed to identify the phases during the MA. Also, the crystallite size and the lattice strain was measured by Williamson-Hall formula. The microstructure, morphology, and the particle size change at various stages of milling were studied by scanning electron microscopy (SEM, Camscan mv2300 system). The Archimedes method was used to measure the density of the samples according to ASTM, C-373 standard [19]. Also, the mixtures law was used to calculate the theoretical density. The microhardness test was performed based on Vickers hardness by Coopa mh1 microhardness tester according to the standard of ASTM, E 384-99. The microhardness test was done at the load of 200 g for the loading time of 15 s.

3. RESULTS AND DISCUSSION

The X-ray diffraction patterns of the as-milled Zr-Cr powders and the milled powders are shown in Figure 1 to identify the phase evolution at milling times of 8, 16, 24, and 32 h. The Zr peaks were moved to the lower angles after 8 h of milling. The peak height of the elements is significantly reduced as compared with the initial powders and some peaks related to Zr and Cr were removed at 8 h. In addition, the width of the peaks was increased at that time.

The transition of Zr diffraction peaks to the lower angles indicated the dissolution of Cr in the Zr lattice. Factually, the dissolution of the Cr atoms with an atomic radius less than the atomic radius of the Zr atoms caused to solute the Cr atoms in the Zr lattice through two substitution and interstitial ways [20]. This matter led to apply the severe strain into Zr lattice, and so, the Zr lattice parameter was increased. Finally, the Zr peaks moved to the lower angles as the Zr lattice parameter was increased. It should be noted that the dissolution of the Cr atoms within Zr lattice in two forms of substitution and interstitial is owing to the high difference in the atomic radius of Zr and Cr.

Also, the Zr lattice parameter was calculated using Bragg's law [21]. Figure 2 is depicted the values of the lattice parameter versus milling time. The Zr lattice parameter was significantly increased up to 24 h of milling, but after 32 h, there was no noticeably change in the Zr lattice parameter which indicated the Cr atoms were completely dissolved in the Zr lattice after 24 h. The dissolution of Cr in the Zr lattice led to form the Zr(Cr) supersaturated solid solution phase with hcp crystalline lattice.

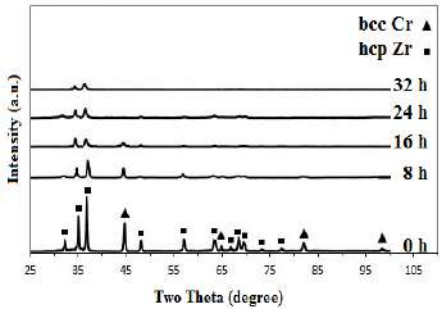

Figure 1. X-ray diffraction patterns of Zr-Cr powder mixtures versus milling time

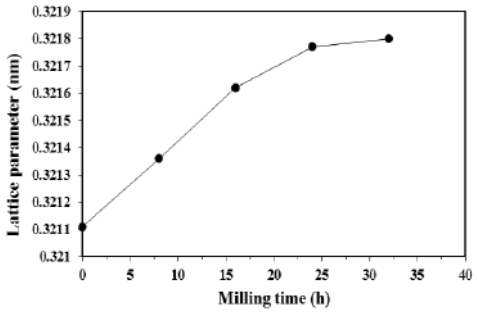

Figure 2. The change of Zr lattice parameter at different milling times

As mentioned, the atomic radius of Cr is lower than Zr atomic radius which led to solute Cr in Zr lattice both through an interstitial and a substitution way. This matter led to apply the severe strain into the Zr-rich phase and facilitated the amorphous phase formation [22]. So, the height of Zr peaks gradually decreased at the milling time of 8, and also, some peaks of Zr were eliminated at 16 h. On the other hands, the MA process was applied a severe plastic deformation to Zr lattice which led to work hardening of the powder particles. Therefore, a distortion in the Zr lattice was created which led to prepare the amorphous phase. The disappearance of Zr crystalline peaks is a sign of amorphous structure at the milling time of 16 h.

After 24 h of milling, the Zr peak at the angle of 32.5° was appeared. This appearance of Zr peak at 24 h was related to the local temperature rise in the milled powder which caused the nonequilibrium phases such as amorphous phase transformed to the more stable phases such as crystalline phase after 24 h of milling. The temperature of the milled powders could increase up to 300 ℃ at high milling times which led to occur the recovery and recrystallization phenomena [23]. In general, the recovery and recrystallization can significantly decrease the lattice strain due to the rearrangement of the dislocation, and the reduction of defect densities [24]. In fact, MA technique is considered to be a method for production of nonequilibrium phases but at milling, the local temperature enhancement due to the kinetic energy of the balls led to transformation of amorphous phase to more stable crystalline phase. In other words, the generation of the heat during milling increased the diffusivity of atoms and then, increased the tendency of formation the more stable phases. Principally, the change in the peak intensity depended on the plastic deformation in the recovery and recrystallization operation [25]. In other words, plastic deformation caused to decrease the peak intensity while, the recovery and recrystallization increased the peak intensity. Finally, the Zr peak at the angle of 32.5° was removed after 32 h of milling due to the severe deformation. The reduction of the peak intensity continued up to 24 h and the Cr peaks were totally eliminated and also, the Zr peaks remains as the only crystalline phase. The peak widening continued as the milling time was increased, especially at 24 h of milling, which confirmed that many crystalline defects were created in the powders during the milling process. In other words, defects were the main reason of the enhancement of the peak width. The plot of the lattice strain and crystallite size versus milling time are shown in Figure 3. The lattice strain enhancement and crystallite size refinement were occurred as the milling time was enhanced, which confirmed that the responsible for the increase in the peak width was the crystallite size refinement and lattice strain enhancement. As observed in Figure 3, it is clear that the decrement rate of the crystallite size was decreased after 16 h of milling. Finally, after 32 h of milling, the crystallite size was found to be 19 nm, indicating that the MA process is a proper technique to produce the nanostructured powders.

When the crystallite size is nanometer scale, it is possible to dissolve the elements in each other and the formation of a solid solution in the alloy systems with a positive enthalpy [26]. In fact, the strain increased the distances between the atomic planes in the crystal lattice [24], which ultimately led to increase the diffusion of Cr in the Zr lattice. Finally, Zr(Cr) supersaturated solid solution was produced after 24 h.

However, this study indicated that the mechanical alloying of powders can enhance the solid solubility, and led to form the Zr(Cr) supersaturated solid solution phase. The high density of dislocation can significantly increase the solid solubility. In general, the effect of cold welding and fracture phenomena on the MA process led to apply the severe plastic deformation (SPD) on the powders. SPD increased the defect density, which led to facilitate the diffusion of the atoms. Finally, the alloying treatment was improved.

The morphology of the powders were studied by SEM images. Figure 4(a) shows the morphology of the primary powders of Zr and Cr. The particle size of the primary powders was approximately 5-50 µm, and the

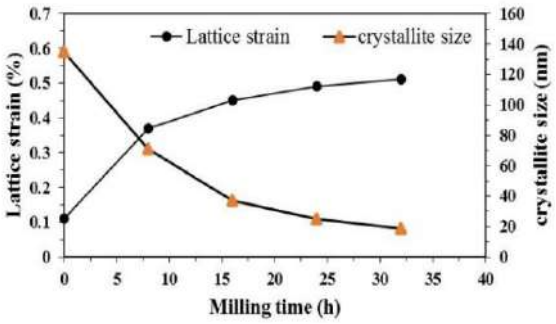

Figure 3. The change of lattice strain and Crystallite size of Zr element at various milling times

particle size distribution was irregular. The powder particles are very soft at the start of MA due to the low dislocation density, and high energy collisions was applied to the soft powders during the milling process. This high energy led to occur the plastic deformation in the powder particles, and the particles morphology became coarse-grained particles at 8 h which is indicated in Figure 4(b). In fact, the cold welding mechanism caused to stock the powder particles together. At 8 h, the particle size of the powder mixtures was about 75-175 µm with a heterogeneous distribution. In Figure 4(c), the mechanical bonding and cold welding among the Cr and Zr particles were happened after 16 h owing to the impact of the balls. It can be concluded that the particle size was increased as compared with the previous stage. They were randomly distributed with a size of about 1-80 µm. After 24 h, the work hardening was occurred due to the enhancement of the dislocation density which led to breakdown the particles. Therefore, the particle size was reduced to less than 30 µm which is shown in Figure 4(d).

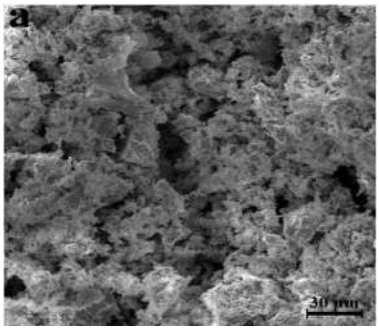

(a)

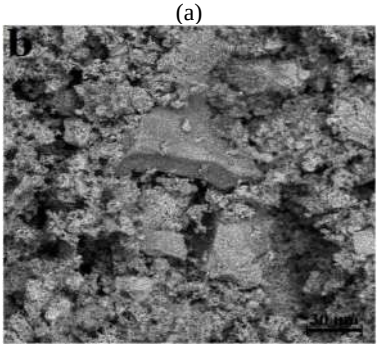

(b)

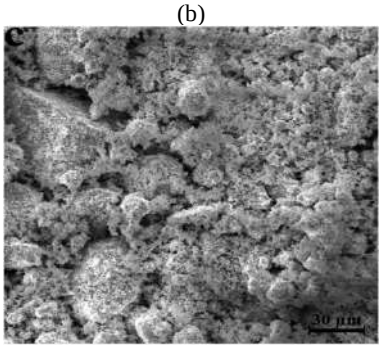

(c)

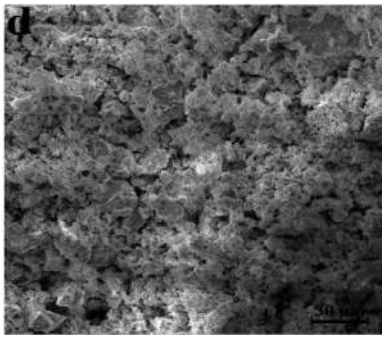

(d)

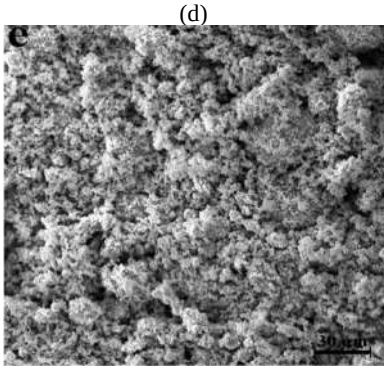

(e)

Figure 4. The SEM image of Zr(Cr) alloy at: (a) 0 h, (b) 8 h, (c) 16 h, (d) 24 h, and (e) 32 h of milling

In fact, the fracture of powder particles was the prodominant phenomenon. Finally, the particle size was reduced with an irregular distribution of the particle size. Of course, another factor that can contribute to the fragmentation of the particles was the dissolution of the elements, and work hardening owing to the formation of Zr(Cr) supersaturated solid solution phase [27]. The powder particles fracture continued after 32 h which is shown in Figure 4(e). At this time, the particle morphology was close to the spherical shape with a size of less than 20 µm which more regularly distributed as compared with the previous steps. In fact, the thickness of the particles was reduced owing to the severe deformation; thus, the diffusion distances were reduced. As a result, the decrement of the diffusion distances and the enhancement of the crystalline defects led to be more diffusion of the atoms which enhanced the solid solubility of the elements.

Figure 5 shows the results of the density measuring based on the Archimedes method. In this figure, the empirical values were compared with the theoretical values. As can be seen, the density of Zr-Cr alloy samples is close to the theoretical density (about 98% of the theoretical density). This can be attributed to the excessive deformation in the milling process. At the start of milling process, the density of the produced alloy was decreased which may be due to the agglomeration of powder particles at the beginning of the milling. Of course, the powder particle size can

greatly effect on the pressing and consolidation of the powder particles.

According to Figure 5, the density of Zr-Cr alloy was increased from 6.344 g/cm^3 at 8 h to 6.359 g/cm^3 after 24 h of milling. This is owing to the crystallite size refinement as well as the reduction in the powder particle size at longer milling times. Also, the density of the as-milled Zr-10 wt% Cr powders was increased from 6.349 g/cm^3 to 6.359 g/cm^3 after 24 h of milling. This is due to the reduction in the powder particle size, reduction in the crystallite size, complete diffusion of Cr into the Zr lattice, and the formation of Zr(Cr) phase during the milling process. Finally, the density of Zr-10 wt% Cr alloy reached to 6.362 g/cm^3 after 32 h of milling which is equal to 98% of the theoretical density.

To investigation of the mechanical properties of Zr(Cr) alloy, the microhardness test was performed and their results are depicted in Figure 6. The microhardness was enhanced as the milling time was enhanced. It should be noted that the microhardness of the primary powders was in the range of 118-129 Hv; which the lowest value was corresponding to Zr and the largest value was related to Cr. At 8 h, the microhardness was

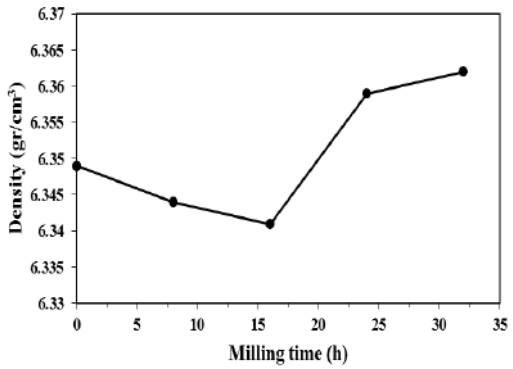

Figure 5. Density of the Zr-Cr alloy versus milling times

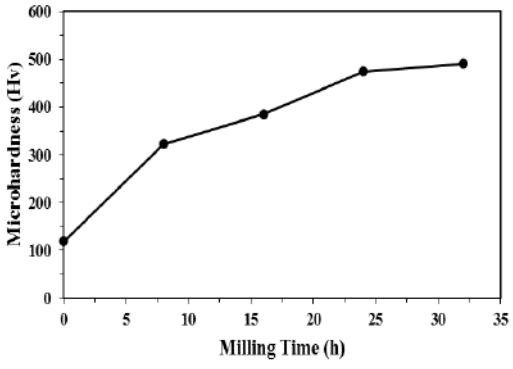

Figure 6. Vickers microhardness value of the Zr(Cr) alloy versus milling time

severely increased. This is due to the sharp decline in the crystallite size at the early stages of the milling. In fact, the primary powders are very soft and the work hardening of the powders due to the severe strain was responsible for the enhancement of the microhardness after 8 h.

After 16 h, the rate of the microhardness enhancement was decreased as compared with the previous stage. This trend continued up to 24 h. The microhardness value reached to 475 Hv after 24 h, indicating the microhardness was significantly increased. In fact, several factors including the crystallite size decrement, formation of the supersaturated solid solution, and the severe strain had a significant effect on the microhardness enhancement. The formation of the supersaturated solid solution of Zr(Cr) can improve the microhardness of Zr due to the solution hardening. In other words, the solution of Cr in Zr lattice through interstitial and substitution ways can prevent the movement of the dislocation which led to increase the microhardness of Zr-based alloy [24]. Eventually, after 32 h of milling, the microhardness reached to about 491 Hv, indicating that the microhardness didn't significantly change after 24 h and was almost stable. In fact, the Zr(Cr) supersaturated solid solution was formed at 24 h and no significant phase evolution was observed after the 32 h. However, homogenization of nanostructures and grain size reduction can effect on the microhardness.

4. CONCLUSION

In the present research, the effect of MA process and sintering on the behaviour of Zr and Cr powder mixtures in the immiscible Zr-Cr alloy system was investigated. As well-known, the solid solubility of Cr in Zr lattice is about 1% at the equilibrium state. The results revealed that MA led to enhance the solid solubility of Cr in Zr lattice. Finally, a nanostructure supersaturated solid solution of Zr(Cr) was formed. Therefore, the crystallite size of Zr was decreased to about 19 nm. The SEM images analysis indicated that at the beginning of MA, the cold welding was the dominant mechanism which led to agglomerate the powder particles, so that, the largest powder particle size reached to 80 µm after 16 h. the particle fracture dominated cold welding at 24 h of milling. After 32 h of milling, the particle size reached to 20 µm with a spherical shape and homogeneous distribution. The density of the Zr-10 wt% Cr alloy was close to 98% of the theoretical density. Also, the microhardness measurement revealed that MA could noticeably enhance the microhardness value of the Zr-10 wt% Cr alloy up to 491 Hv after 32 h.

5. REFERENCES

1. Zhang, X., Liu, S. G., Wang, S. H., Zhang, B., Zhang, X. Y., Ma, M. Z. and Liu, R. P., "Dynamic precipitation-induced simultaneous enhancement of the strength and plasticity of hot-rolled Zr–9Al alloy", ***Journal of Alloys and Compounds***, Vol. 829, (2020), 154577. DOI: https://doi.org/10.1016/j.jallcom.2020.154577
2. Gault, B., Felfer, P. J., Ivermark, M., Bergqvist, H., Cairney, J. M. and Ringer, S. P., "Atom probe microscopy characterization of as quenched Zr-0.8 wt% Fe and Zr-0.15 wt% Cr binary alloys", ***Materials Letters***, Vol. 91, (2013), 63-66. DOI: https://doi.org/10.1016/j.matlet.2012.09.059
3. Kuprin, A. S., Belous, V. A., Voyevodin, V. N., Bryk, V. V., Vasilenko, R. L., Ovcharenko, V. D., Reshetnyak, E. N., Tolmachova, G. N. and Vyugov, P. N., "Vacuum-arc chromium-based coatings for protection of zirconium alloys from the high-temperature oxidation in air", ***Journal of Nuclear Materials***, Vol. 465, (2015), 400-406. DOI: https://doi.org/10.1016/j.jnucmat.2015.06.016
4. Ryabchikov, A. I., Kashkarov, E. B., Shevelev, A. E. and Syrtanov, M. S., "High-intensity chromium ion implantation into Zr-1Nb alloy", ***Surface and Coatings Technology***, Vol. 383, (2020), 125272. DOI: https://doi.org/10.1016/j.surfcoat.2019.125272
5. Huang, M., Li, Y., Ran, G., Yang, Z. and Wang, P., "Cr-coated Zr-4 alloy prepared by electroplating and it's in situ He^+ irradiation behavior", ***Journal of Nuclear Materials***, Vol. 538, (2020), 152240. DOI: https://doi.org/10.1016/j.jnucmat.2020.152240
6. Chen, K., Zeng, L., Li, Z., Chai, L., Wang, Y., Chen, L.Y. and Yu, H., "Effects of laser surface alloying with Cr on microstructure and hardness of commercial purity Zr", ***Journal of Alloys and Compounds***, Vol. 784, (2019), 1106-1112. DOI: https://doi.org/10.1016/j.jallcom.2019.01.097
7. Prosviryakov, A. S., Bazlov, A. I. and Loginova, I. S., "Effect of Cu addition on microstructural evolution and hardening of mechanically alloyed Al−Ti−O in-situ composite", ***Transactions of Nonferrous Metals Society of China***, Vol. 30, No. 5, (2020), 1135-1147. DOI: https://doi.org/10.1016/S1003-6326(20)65284-0
8. Akbari, G. H. and Taghian, M., "Behavior of Cu-Cr Powder Mixtures During Mechanical Alloying", ***International Journal of Engineering***, Transactions B: Applications, Vol. 23, No. 1, (2010), 69-76. DOI: 10.5829/IJE.2010.23.01B.05
9. Mirvakili, S. A., Zakeri, M. and Yazdani Rad, R., "Effect of Chromium Content on Formation of $(Mo_{1-x}Cr_x)Si_2$ Nanocomposite Powders via Mechanical Alloying", ***International Journal of Engineering***, Transactions C: Aspects, Vol. 25, No. 2, (2012), 99-104. DOI: 10.5829/IJE.2012.25.02C.02
10. Suryanarayana, C. and Al-Joubori A. A., "Effect of initial composition on phase selection in Ni-Si powder blends processed by mechanical alloying", ***Materials and Manufacturing Processes***, Vol. 33, No. 8, (2018), 840-848. DOI: 10.1080/10426914.2017.1401714
11. Akbari, G. H. and Khajesarvi, A., "Effect of Mo Addition on Nanostructured $Ni_{50}Al_{50}$ Intermetallic Compound Synthesized by Mechanical Alloying", ***International Journal of Engineering***, Transactions C: Aspects, Vol. 28, No. 9, (2015), 1328-1335. DOI: 10.5829/IJE.2015.28.09C.10
12. Verdian, M. M., "Fabrication of supersaturated NiTi(Al) alloys by mechanical alloying", ***Materials and Manufacturing Processes***, Vol. 25, No. 12, (2010), 1437-1439. DOI: https://doi.org/10.1080/10426914.2010.501093
13. Azazari khosroshahi, R., Abbasi Nargesi, F. and parvini ahmadi, N., "Synthesis of Nanostructure Ti-45Al-5Cr Alloy by Mechanical Alloying and Study the Effect of Cr Addition on Microstructure of TiAl Alloy", ***International Journal of Engineering, Transactions A: Basics***, Vol. 24, No. 2, (2011), 123-130. DOI: 10.5829/IJE.2011.24.02C.03
14. Rahaei, M. B., Yazdani-Rad, R. and Kazemzadeh, A., "Synthesis and Characterization of Nanocrystalline Ni_3Al Intermetallic during Mechanical Alloying Process", ***International Journal of Engineering, Transactions C: Aspects***, Vol. 25, No. 2, (2012), 89-98. DOI: 10.5829/IJE.2012.25.02C.01
15. Kristl, M., Ban, I. and Gyergyek, S., "Preparation of Nanosized Copper and Cadmium Chalcogenides by Mechanochemical Synthesis", ***Materials and Manufacturing Processes***, Vol. 28, No. 9, (2013), 1009-1013. DOI: https://doi.org/10.1080/10426914.2013.811736
16. Zhang, X., Li, Y., He, X., Sun, Y., Pang, S., Su, G., Liu, X., and Yang, Z., "Influence of Cr addition on microstructure and mechanical properties of Zr-based alloys corresponding to Zr-C-Cr system", ***Journal of Alloys and Compounds***, Vol. 640, (2015), 240-245. DOI: https://doi.org/10.1016/j.jallcom.2015.03.240
17. Ali, F., Mehmood, M., Qasim, A. M., Ahmada, J., Rehman, N., Iqbal, M., and Qureshi, A. H., "Comparative study of the structure and corrosion behavior of Zr-20%Cr and Zr-20%Ti alloy films deposited by multi-arc ion plating technique", ***Thin Solid Films***, Vol. 564, (2014), 277-283. DOI: https://doi.org/10.1016/j.tsf.2014.05.041
18. Massalski, T. B., Okamoto, H., Subramanian, P.R. and Kacprzak, L., Binary Alloy Phase Diagrams, ASM International, Ohio: Materials Park, 1990.
19. Kumar, A. A., Patton, M. R., Hennek, J. W., Lee, S. Y. R., Alesio-Spina, G. D., Yang, X., Kanter, J., Shevkoplyas, S. S., Brugnara, C. and Whitesides, G. M., "Density-based separation in multiphase systems provides a simple method to identify sickle cell disease", ***Proceedings of the National Academy of Sciences***, Vol. 111, No. 5, (2014), 14864-14869. DOI: https://doi.org/10.1073/pnas.1414739111
20. Burr, P. A., Wenman, M. R., Gault, B., Moody, M. P., Ivermark, M., Rushton, M. J. D., Preuss, M., Edwards, L. and Grimes, R. W., "From solid solution to cluster formation of Fe and Cr in α-Zr", ***Journal of Nuclear Materials***, Vol. 467, No. 1, (2015), 320-331. DOI: https://doi.org/10.1016/j.jnucmat.2015.10.001
21. Cullity, B. D. and Stock, S. R., Elements of X-ray Diffraction, New York: Pearson, 2001.
22. Nowroozi, M. A., and Shokrollahi, H., "Magnetic and structural properties of amorphous/nanocrystalline $Fe_{42}Ni_{28}Zr_8Ta_2B_{10}C_{10}$ soft magnetic alloy produced by mechanical alloying", ***Advanced Powder Technology***, Vol. 24, No. 6, (2013), 1100-1108. DOI: https://doi.org/10.1016/j.apt.2013.03.016
23. Suryanarayana, C., "Mechanical alloying and milling", ***Progress Materials Science***, Vol. 46, No. 1-2, (2001), 1-184. DOI: https://doi.org/10.1016/S0079-6425(99)00010-9
24. Dieter, G.E., mechanical metallurgy, New York: McGraw-Hill Book Co., 1986.
28. Lou, T., Fan, G., Ding, B., and Hu, Z., "The synthesis of $NbSi_2$ by mechanical alloying". ***Journal of Materials Research***, Vol. 12, No. 5, (1997), 1172-1175. DOI: https://doi.org/10.1557/JMR.1997.0162
25. Costa, M.B., Mateus, R., Guedes, M. and Ferro, A. C., "Mechanical alloying in the Li-Sn system", ***Materials Letters: X***, Vol. 6, No. 1, (2020), 100045. DOI: https://doi.org/10.1016/j.mlblux.2020.100045
26. Annan, K. A., Daswa, P., Motumbo, K. and Siyasiya, C. W., "Influence of milling parameters on the structural and phase

formation in Ti-20%Al alloy through mechanical milling", ***Materials Today***, (2020). DOI: https://doi.org/10.1016/j.matpr.2020.04.524

27. Zhao, C., Lu, H., Wang, H., Tang, F., Nie, H., Hou, C., Liu, X., Song, X. and Nie, Z., "Solid-solution hardening of WC by rhenium", ***Journal of the European Ceramic Society***, Vol. 40, No. 2, (2020), 333-340. DOI: https://doi.org/10.1016/j.jeurceramsoc.2019.09.050

Persian Abstract

چکیده

هدف از پژوهش حاضر، تولید آلیاژ پایه Zr به عنوان روکش سوخت هسته‌ای با استفاده از فرآیند آلیاژسازی مکانیکی (MA) و تفجوشی است. بدین منظور، پودرهای Zr و Cr برای تولید آلیاژ دیرگداز و سخت Zr-10 wt% Cr به صورت مکانیکی آلیاژسازی شدند و سپس، مخلوط پودر بوسیله پرس و سینتر در دمای ۸۰۰ °C به مدت ۳۰ دقیقه فشرده شد. تغییر فاز، تغییرات ریزساختار، ریزسختی و چگالی آلیاژهای حاصل با استفاده از پراش اشعه ایکس (XRD)، میکروسکوپ الکترونی روبشی (SEM)، اندازه‌گیری میکروسختی و روش ارشمیدوس مورد بررسی قرار گرفت. نتایج نشان داد که MA باعث افزایش حلالیت پودرهای غیرقابل امتزاج Cr و Zr در حالت جامد می‌شود، به طوری که اتم‌های Cr پس از ۲٤ ساعت آسیاکاری به طور کامل در شبکه Zr حل شدند و محلول جامد نانوساختار Zr(Cr) با مقدار سختی 491 Hv حاصل شد. همچنین، نتایج اندازه‌گیری چگالی نشان داد که چگالی حاصل نزدیک به ۹۸٪ چگالی نظری است.

International Journal of Engineering

Journal Homepage: www.ije.ir

Experimental Study on Warm Incremental Tube Forming of AA6063 Aluminum Tubes

F. Rahmani[a], S. M. H. Seyedkashi*[b], S. J. Hashemi[c]

[a] *Department of Mechanical Engineering, Kar higher Education Institute, Qazvin, Iran*
[b] *Department of Mechanical Engineering, University of Birjand, Birjand, Iran*
[c] *Department of Mechanical Engineering, Faculty of Enghelab-e Eslami, Tehran Branch, Technical and Vocational University (TVU), Tehran, Iran*

PAPER INFO

Paper history:
Received 6 March 2020
Received in revised form 01 April 2020
Accepted 12 June 2020

Keywords:
Warm Incremental Tube Forming
Expansion Ratio
Surface Roughness
Temperature

ABSTRACT

Effect of temperature on formability of AA6063 aluminum tubes in incremental forming process was investigated. Experiments are performed on AA6063 aluminum tubes. A spirally moving tool incrementally expands the tube wall. The tube is clamped from both ends while the deformation zone is not in contact with the die. A circumferential heating system is used to heat the tube due to the low formability of aluminum alloys at ambient temperature. The effects of process parameters including temperature, radial feed, axial feed and tool linear velocity are investigated in order to obtain the highest formability and surface quality. The results show that with a temperature rise from 100°C to 300°C, the expansion ratio increases from 28% to 34%. Axial feeding and temperature are the most effective parameters on the surface roughness and bulge diameter, respectively.

***doi**: 10.5829/ije.2020.33.09c.11*

1. INTRODUCTION

Single-point incremental forming (SPIF) process is a technique for forming of sheet metals in job shop manufacturing, especially for rapid prototyping [1]. The sheet is first clamped along its circumference using a fixture or a blank-holder. Then a forming tool, usually having a spherical tip, contacts the sheet and moves incrementally along a predetermined path to form a desired shape. Tool rotational speed, linear velocity, and feeding depth are the most important parameters affecting the formability, surface roughness and thickness distribution of the product. This process has been considered by researchers to produce prototype sheet metal parts because of its high flexibility and low production cost [2].

Aluminum alloys exhibit low formability at room temperature. Therefore, high temperatures are typically used to enhance their formability. The single-point incremental forming of different materials at elevated temperatures has been studied by several researchers. Ambrogio et al. [3] showed that the highest formability of AZ31 magnesium alloy in incremental forming is achieved at 250°C. Ji and Park [4, 5] numerically and experimentally studied the incremental forming of magnesium sheets at various temperatures up to 250°C. They concluded that the highest formability was obtained at 150°C. Fan et al. [6, 7] used electric current for heating the sheet in incremental forming process.

Zhang et al. [8] showed that the anisotropy effect on the surface quality of the AZ31 sheets is decreased by increasing the temperature during the incremental forming. Kim et al. [9] increased the limit drawing ratio (LDR) of magnesium products using a localized heating and cooling technique. Al-Obaidi et al. [10] investigated the incremental forming of high-strength steels with the local heating at the tool/sheet contact point using an induction coil. They showed that the forming angle is increased in addition to the reduction of the forming force. Galdos et al. [11] used hot fluid to achieve a uniform temperature distribution in incremental forming of magnesium sheets. Based on their results, the maximum formability of AZ31 alloy obtained by this heating method is 250°C. VanSy and ThanhNam [12]

*Corresponding Author Institutional Email: *seyedkashi@birjand.ac.ir* (S. M. H. Seyedkashi)

Please cite this article as: F. Rahmani, S. M. H. Seyedkashi, S. J. Hashemi, Experimental Study on Warm Incremental Tube Forming of AA6063 Aluminum Tubes, International Journal of Engineering (IJE), IJE TRANSACTIONS C: Aspects Vol. 33, No. 9, (September 2020) 1773-1779

incrementally formed AZ31 and AA5055 sheets at high temperatures and examined the effect of temperature on the surface quality of the products.

Metal tubes are widely used in the construction of lightweight structures [13]. One of the widely used processes for changing the cross-sections of metal tubes is the tube hydroforming process (THF). In this process, the internal pressure and feed loading paths have a significant effect on the formability. Seyedkashi et al. [14] used the simulated annealing (SA) optimization method to achieve the highest expansion ratio in the hydroforming of copper tubes. Elevated temperatures are also used in this process to increase the formability. Several heating mechanisms have been used in the THF process, such as hot fluid bath [15], induction coil and heating element in the fluid [16], and using a preheated fluid [17]. However, in addition to the sealing problems and the need for high fluid pressure, the warm hydroforming process has a temperature limitation due to the maximum temperature of the available fluids.

It is also possible to form metal tubes using a single-point incremental tube forming (ITF) process. For this purpose, a rotary tool changes the tube cross-section by moving along a predetermined path inside or outside of the tube. This process can be very effective, especially for the production of centrally bulged tubular products. There is limited literature about ITF process. Several researchers have focused on incremental forming of a flange on the perforations formed on the tube surface. Teramae et al. [18] investigated the forming of flanges on the tube numerically and experimentally. According to their results, by increasing the work hardening exponent of the material, the thickness distribution in the formed flange becomes more uniform. Yang et al. [19] showed that the flange dimension depends on the tube diameter and the hole size. Wen et al. [20] carried out the ITF process under four different conditions and compared the produced parts with die casting. Seyedkashi et al. [21] performed free bulging of copper tubes by incremental tube forming, and studied the effect of process parameters on the thickness distribution and surface roughness. Rahmani et al. [22] experimentally studied the incremental tube forming to convert copper circular tubes into square cross-sectional parts. In addition, quantifying the residual stresses, is a key step in determination of the integrity of engineering and structural components. Faghidian et Al. [23] predicted the residual stresses by elastic–plastic bending using an approximate analysis and the finite element method. Axisymmetric bulging of tubes can be done using different processes. Rubber pad forming is one of these processes which can be used for axisymmetric bulging of tubes [24]. In the tube hydroforming process, quality of final product depends on forming parameters like internal pressure and axial feeding [25]. Many researchers have investigated the bulging of tubes using hydroforming process.

In this paper, the axisymmetric bulging of aluminum tubes using the warm incremental tube forming (WITF) is proposed. The forming tool moves spirally inside the tube and incrementally increases its diameter at each step. During the forming process, the middle part of the tube is free without any contact with the die. The effects of different process parameters, such as temperature, radial feed, axial feed, and linear velocity of the tool, have been experimentally studied. The radial feed is increased until the tube rupture. After the forming process, the final tube length, the inner surface roughness, and the maximum bulge height before rupture are measured and the effects of studied parameters on these responses are compared.

2. MATERIAL AND METHODS

Aluminum tubes used in this research are made of AA6063 alloy and have an outer diameter of 40 mm, initial thickness of 1.5 mm and initial length of 60 mm. The seamless tubes had been produced by extrusion. Chemical composition of AA6063 is given in Table 1.

There is no limitation on the cross-sectional shape of the final piece in the ITF process. Even an asymmetric cross-section can be formed. The forming tool is mounted on a CNC milling machine and the die assembly is clamped to the machine table. At the beginning, the forming tool enters into the tube and stops where the bulge is about to start. Then, it moves radially and causes the tube to deform. This amount of radial movement is called "radial feed, F_r". The longitudinal tool axis always remains parallel to the tube axis. Then, the forming tool moves spirally along the tube free length. Therefore, the free section of the tube will expand. In this research, the tool is not rotatable. The tool's linear velocity is constant along the path. This value is one of the most important parameters affecting the process. Due to the free space between the top and bottom dies, various shapes can be produced based on the tool path. "Axial feed, F_a" is the distance that the tool moves along the tube axis in each rotation, same as the "pitch" in a spring. After the first forming stage, the tool vertically returns to the initial starting point. If higher expansion is required, the next stage begins again with subsequent radial feed and spiral movement. In order to increase the dimensional accuracy of the corner fillets of the final product, the tool starts and ends each stage with a full circular movement without any axial feed.

TABLE 1. Chemical composition of tube material

Al	Mg	Si	Fe	Zn	Cu	Mn	Pb	Ti	Sn	Ni	Ga
Base	0.47	0.44	0.30	0.08	0.06	0.03	0.03	0.03	0.017	0.02	0.01

Figure 1 shows the experimental setup and tool path. Two ends of the tube are placed in the upper and lower clamps (die). The height of each die is 20 mm and the inside diameter is equal to the outer diameter of the tube. So, the radial movement of the tube is restricted by the die, while its axial movement is limited only by friction force at the tube/die interface. The tube is heated by a ceramic heating element which is shown in Figure 1(a).

The main objective of this paper is to investigate the effects of process parameters on the final form of the aluminum tubes in the incremental forming process. For this purpose, important parameters including temperature (T), radial feed (F_r), and axial feed (F_a) are selected at different levels. Then, the forming process has been performed. The full factorial design of experiments (DOE) is used to study all the main effects and interactions of effective parameters. Three levels are considered for each parameter as shown in Table 2. Hence, 27 experiments are needed to be performed with three replications. The linear velocity of the tool is held constant at 800 mm/min. Three responses are also considered; tube length (L), surface roughness (R_z) and maximum bulge (D) after forming.

Based on the experimental tests and measurements, the obtained response values for each treatment are presented in Table 3.

3. RESULTS AND DISCUSSION

Three samples formed at different temperatures with axial and radial feeds of 0.5 mm are compared in Figure 2. By increasing the temperature, the bulge height increases, but the tube length decreases.

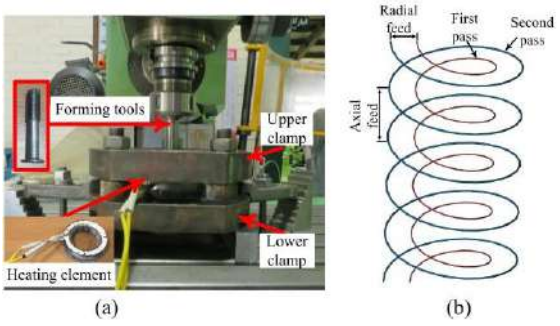

Figure 1. a) Experimental setup; b) Tool path

TABLE 2. Input parameters and their levels

Parameter	Level 1	Level 2	Level 3
Axial feed, F_a (mm)	0.5	1	1.5
Radial feed, F_r (mm)	0.5	0.75	1
Temperature, T (°C)	100	200	300

TABLE 3. Tube length, diameter and roughness values obtained in experiments

Factors			Responses		
T (°C)	F_a (mm)	F_r (mm)	L (mm)	D (mm)	Rz (µm)
300	0.5	1	60.3	54	6.91
300	1	1	60.18	53.5	7.9
200	1	0.75	61.35	51.95	7.34
300	0.5	0.75	61.1	54.57	6.84
100	0.5	0.75	62.11	52.05	5.02
200	0.5	0.5	61.6	53.54	5.45
100	1.5	0.75	61.83	51.56	7.32
200	1.5	1	60.64	50.7	7.98
200	0.5	0.75	61.2	53.02	5.92
200	0.5	1	60.8	52	6.327
100	1	1	61.7	50.22	6.51
200	1	1	60.85	50.75	7.64
300	1	0.75	60.85	54.02	7.92
200	1.5	0.5	61.5	51.9	7.74
300	0.5	0.5	61.15	54.69	5.83
100	0.5	0.5	62.74	52.82	4.75
300	1.5	0.75	60.8	53.28	8.34
300	1	0.5	61.25	54.44	7.83
300	1.5	0.5	61.4	52.76	8.14
100	1.5	1	61.05	50.3	7.98
100	1	0.75	62	50.62	5.92
100	1	0.5	62.4	51.08	5.56
200	1	0.5	61.51	52.7	7.49
300	1.5	1	60.56	51.48	8.78
100	1.5	0.5	62.54	51.66	6.62
100	0.5	1	61.7	51.01	5.55
200	1.5	0.75	60.96	51.3	7.82

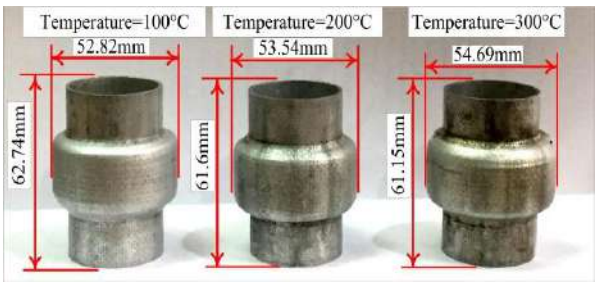

Figure 2. Bulge diameter and length of the formed samples at different temperatures

Table 4 shows the analysis of variance (ANOVA) table for the parameters affecting the bulge diameter. The most important parameter which is critical for interpretation is P-value. The others are used mainly for intermediate computational purposes. If the p-value is less than the significance level of 0.05, the corresponding parameter is statistically significant.

Temperature is the most effective parameter on the bulge diameter with a contribution of 54.96%, while radial feed has the lowest effect with a 16.45% contribution. As shown in Figure 3, bulge diameter is also increased by increasing the temperature. Nevertheless, the increase in diameter is doubled with the temperature change from 200 to 300 °C compared to the temperature change from 100 to 200 °C. This happens due to the changes in aluminum microstructure at about 300 °C, which alter its mechanical properties. By increasing the axial feed, the bulge diameter is reduced. The rupture of all specimens occurs near the upper side of the bulge. The lower the axial feed, the more uniform thickness distribution in a longitudinal direction is. However, when the axial feed is increased, the tube wall in the corner becomes more elongated and thinning increases. The radial feed effect is similar to that of the axial feed, and the tube formability is decreased with its increase (see Figure 3).

TABLE 4. ANOVA table for the bulge diameter

	DF	Seq SS	Contrib. %	Adj SS	Adj MS	F-Value	P-Value
T	2	26.777	54.96	26.777	13.388	145.67	0.000
F_a	2	9.353	19.20	9.353	4.676	50.88	0.000
F_r	2	8.013	16.45	8.013	4.006	43.59	0.000
$T \times F_a$	4	3.103	6.37	3.103	0.775	8.44	0.001
Er.	16	1.471	3.02	1.471	0.091		
R^2			98.34				

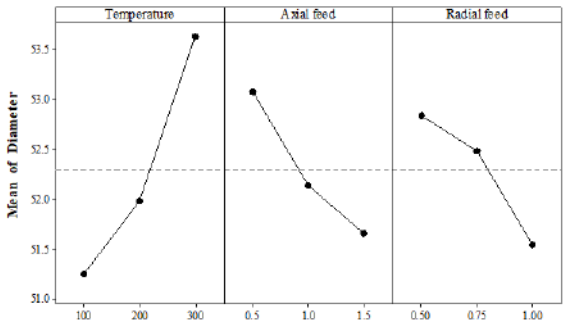

(a) (b) (c)

Figure 3. Effect of a) temperature, b) axial feed and c) radial feed on the bulge diameter

According to Table 4, the interaction between temperature and axial feed on the bulge diameter has a high significance as shown in Figure 4. Here, it is seen that the highest bulge diameter is achieved when the process is carried out at the highest temperature and the lowest axial feed. In fact, the material is in its highest formable state by choosing these values, because the fracture strain is increased at higher temperatures. On the other hand, by decreasing the axial feed, the forming velocity and hence the strain rate decreases.

Table 5 shows the effects of process parameters on the final length of the samples. Temperature and radial feed have a high level of significance, while the axial feed is not significant.

As shown in Figure 5(a), the length of the formed specimens is reduced when temperature increases. This is consistent with the increase in the bulge diameter at high temperatures. The higher the temperature, the higher the amount of material flow between the dies is. Thus, the sample length decreases. The decrease of the sample length by increasing the temperature can also be related to the increase of friction coefficient at high temperatures, as explained before.

According to Figure 5(b), the axial feed has no considerable effect on the tube length after the forming. Based on Figure 5(c), the tube length decreases when the radial feed increases.

One of the important issues in incremental forming is the surface roughness of the formed section. The internal surface roughness increases due to the contact with the

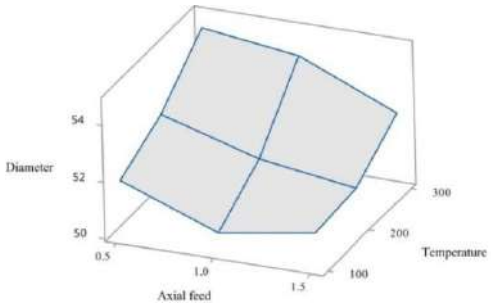

Figure 4. The interaction effect of axial feed and temperature on the bulge diameter

TABLE 5. ANOVA results for the final tube length

	DF	Seq SS	Contrib. %	Adj SS	Adj MS	F-Value	P-Value
T	2	6.5355	58.80	6.5355	3.26775	104.44	0.000
F_a	2	0.1128	1.01	0.1128	0.05638	1.80	0.191
F_r	2	3.8417	34.56	3.8417	1.92083	61.39	0.000
Er.	20	0.6257	5.63	0.6257	0.03129		
R^2			94.37				

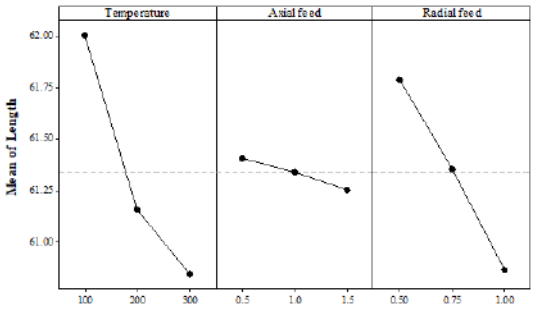

(a) (b) (c)

Figure 5. Effect of a) temperature, b) axial feed and c) radial feed on the final tube length

tool. The average roughness (R_z) of the tubes before forming was 0.83 μm.

According to Table 6, the analysis of variance for surface roughness shows that in addition to the significance of the main parameters, the interaction between temperature and axial feeding is also significant. In terms of the relative importance of input parameters, axial feed with a 57.23% contribution is the most influential parameter on surface roughness, while the contribution of temperature is 30.68%, radial feed 6.47%, and the interaction of temperature and axial feed 2.51%.

As shown in Figure 6(a), surface roughness is increased by increasing the temperature. This increase can be related to the amount of friction at the tube/tool interface which depends on the temperature. The coefficient of friction increases at higher temperatures, hence the surface quality decreases. In fact, the higher the linear velocity of the tool, the longer the tube will remain at a high temperature creating more coarse grains. As shown in Figure 6(b), the surface roughness increases by increasing the axial feed. Figure 6(c) shows that increasing the radial feed leads to higher surface roughness, but the effect of this parameter is far less than temperature and axial feed. The higher the radial feed, the larger the contact area of the tube/tool is, which leads to a decrease in the surface quality.

TABLE 6. ANOVA table for surface roughness

	DF	Seq SS	Contrib. %	Adj SS	Adj MS	F-Value	P-Value
T	2	10.0209	30.68	10.0209	5.0104	79.16	0.000
F_a	2	18.6920	57.23	18.6920	9.3460	147.66	0.000
F_r	2	2.1131	6.47	2.1131	1.0565	16.69	0.000
$T \times F_a$	4	0.8213	2.51	0.8213	0.2053	3.24	0.040
Er.	16	1.0127	3.10	1.0127	0.0633		
R^2			96.90				

Figure 7 shows the interaction between axial feed and temperature. As the axial pitch increases, a more heterogeneous and non-uniform deformation occurs in coarse grains, and the surface roughness is increased. If the goal is to achieve a high surface quality, the lowest temperature and axial feed should be used. However, it should be noticed that lower temperatures reduce the formability.

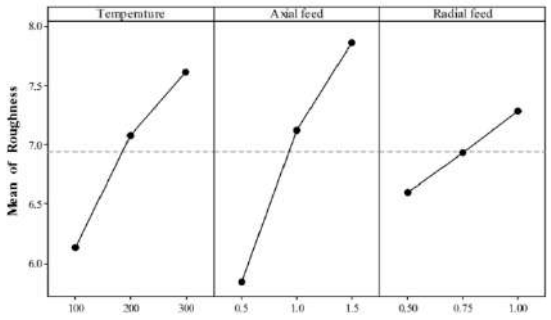

(a) (b) (c)

Figure 6. Effect of a) temperature, b) axial feed and c) radial feed on surface roughness

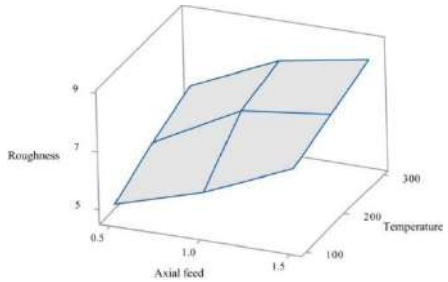

Figure 7. Interaction effect of axial feed and temperature on surface roughness on the bulge diameter

4. CONCLUSIONS

In this paper, warm incremental tube forming process was used to create an axisymmetric bulge in AA6063 aluminum tubes. The tubes are uniformly heated to increase the formability.

The maximum expansion of 36.7% was achieved at 300°C. Temperature, axial feed and radial feed are the most effective parameter on the bulge height, respectively. To achieve the maximum bulge diameter, the lowest axial and radial feeds should be used. According to the experiments, there is no significant relation between the bulge diameter and the final tube length. The radial feed has the largest effect on the tube length, while the axial feed is not significant. On the other hand, the results show that the axial feed is the most important parameter affecting the surface roughness. The friction between the tool and the tube is increased by temperature, hence increases the surface roughness.

5. REFERENCES

1 Martins, P., Bay, N., Skjødt, M., and Silva, M., "Theory of single point incremental forming", ***CIRP Annals***, Vol. 57, No. 1, (2008), 247-252. doi:10.1016/j.cirp.2008.03.047.

2. Jeswiet, J., Geiger, M., Engel, U., Kleiner, M., Schikorra, M., Duflou, J., Neugebauer, R., Bariani, P., and Bruschi, S., "Metal forming progress since 2000", ***CIRP Journal of Manufacturing Science and Technology***, Vol. 1, No. 1, (2008), 2-17. doi:10.1016/j.cirpj.2008.06.005.

3. Ambrogio, G., Filice, L., and Manco, G., "Warm incremental forming of magnesium alloy AZ31", ***CIRP Annals***, Vol. 57, No. 1, (2008), 257-260. doi:10.1016/j.cirp.2008.03.066.

4. Ji, Y., and Park, J., "Formability of magnesium AZ31 sheet in the incremental forming at warm temperature", ***Journal of Materials Processing Technology***, Vol. 201, No. 1-3, (2008), 354-358. doi:10.1016/j.jmatprotec.2007.11.206.

5. Ji, Y., and Park, J., "Incremental forming of free surface with magnesium alloy AZ31 sheet at warm temperatures", ***Transactions of Nonferrous Metals Society of China***, Vol. 18, (2008), s165-s169. doi: 10.1016/S1003-6326(10)60195-1.

6. Fan, G., Gao, L., Hussain, G., and Wu, Z., "Electric hot incremental forming: A novel technique", ***International Journal of Machine Tools and Manufacture***, Vol. 48, No. 15, (2008), 1688-1692. doi:10.1016/j.ijmachtools.2008.07.010.

7. Fan, G., Sun, F., Meng, X., Gao, L., and Tong, G., "Electric hot incremental forming of Ti-6Al-4V titanium sheet", ***International Journal of Advanced Manufacturing Technology***, Vol. 49, No. 9-12, (2010), 941-947. doi: 10.1007/s00170-009-2472-2.

8. Zhang, Q., Guo, H., Xiao, F., Gao, L., Bondarev, A., and Han, W., "Influence of anisotropy of the magnesium alloy AZ31 sheets on warm negative incremental forming", ***Journal of Materials Processing Technology***, Vol. 209, No. 15-16, (2009), 5514-5520. doi:10.1016/j.jmatprotec.2009.05.012.

9. Kim, S., Lee, Y., Kang, S., and Lee, J., "Incremental forming of Mg alloy sheet at elevated temperatures", ***Journal of Mechanical Science and Technology***, Vol. 21, No. 10, (2007), 1518. doi: 10.1007/BF03177368.

10. Al-Obaidi, A., Kräusel, V., and Landgrebe, D., "Hot single-point incremental forming assisted by induction heating", ***International Journal of Advanced Manufacturing Technology***, Vol. 82, No. 5-8, (2016), 1163-1171. doi: 10.1007/s00170-015-7439-x.

11. Galdos, L., Sáenz de Argandoña, E., Ulacia, I., and Arruebarrena, G., "Warm incremental forming of magnesium alloys using hot fluid as heating media", In: Key Engineering Materials, Trans Tech Publ (2012), 815-820. doi:10.4028/www.scientific.net/KEM.504-506.815.

12. VanSy, L., and ThanhNam, N., "Hot incremental forming of magnesium and aluminum alloy sheets by using direct heating system", ***Proceedings of the Institution of Mechanical Engineers, Part B: Journal of Engineering Manufacture***, Vol. 227, No. 8, (2013), 1099-1110. doi:10.1177/0954405413484014.

13. Hashmi, M., "Aspects of tube and pipe manufacturing processes: meter to nanometer diameter", ***Journal of Materials Processing Technology***, Vol. 179, No. 1-3, (2006), 5-10. doi:10.1016/j.jmatprotec.2006.03.104.

14. Seyedkashi, S.M.H, Naeini, H.M., Liaghat, G., Mashadi, M.M., Mirzaali, M., Shojaee, K., and Moon, Y.H., "The effect of tube dimensions on optimized pressure and force loading paths in tube hydroforming process", ***Journal of Mechanical Science and Technology***, Vol. 26, (2012), 1817-1822. doi: 10.1007/s12206-012-0430-7.

15 Aue-u-lan, Y., "Hydroforming of tubular materials at various temperatures", The Ohio State University, PhD thesis, (2007).

16 Seyedkashi, S.M.H., Naeini, H.M., and Moon, Y.H., "Feasibility study on optimized process conditions in warm tube hydroforming", ***Journal of Mechanical Science and Technology***, Vol. 28, No. 7, (2014), 2845-2852. doi: 10.1007/s12206-014-0638-9.

17 Kim, B., Van Tyne, C., Lee, M., and Moon, Y.H., "Finite element analysis and experimental confirmation of warm hydroforming process for aluminum alloy", ***Journal of Materials Processing Technology***, Vol. 187, (2007), 296-299. doi:10.1016/j.jmatprotec.2006.11.201.

18 Teramae, T., Manabe, K., Ueno, K., Nakamura, K., and Takeda, H., "Effect of material properties on deformation behavior in incremental tube-burring process using a bar tool", ***Journal of Materials Processing Technology***, Vol. 191, No. 1-3, (2007), 24-29. doi:10.1016/j.jmatprotec.2007.03.039.

19 Yang, C., Wen, T., Liu, L., Zhang, S., and Wang, H., "Dieless incremental hole-flanging of thin-walled tube for producing branched tubing", ***Journal of Materials Processing Technology***, Vol. 214, No. 11, (2014), 2461-2467. doi:10.1016/j.jmatprotec.2014.05.027.

20 Wen, T., Yang, C., Zhang, S., and Liu, L., "Characterization of deformation behavior of thin-walled tubes during incremental forming: a study with selected examples", ***International Journal of Advanced Manufacturing Technology***, Vol. 78, No. 9-12, (2015), 1769-1780. doi: 10.1007/s00170-014-6777-4.

21 Seyedkashi, S.M.H., Hashemi Ghiri, S.J., Rahmani, F., "Experimental investigation of effective parameters on a new incremental tube bulging method using rotary tool", ***International Journal of Advanced Design and Manufacturing Technology***, Vol. 10, No. 2, (2017), 83-91.

22 Rahmani, F., Seyedkashi, S.M.H., Hashemi, S.J., "Converting circular tubes into square cross-sectional parts using incremental forming process", ***Transactions of Nonferrous Metals Society of China***, Vol. 29, No. 11, (2019), 2351-2361. doi: 10.1016/S1003-6326(19)65141-1.

23 Faghidian, S.A., Goudar, D., Farrahi, G.H., Smith, D.J., "Measurement, analysis and reconstruction of residual stresses", ***The Journal of Strain Analysis for Engineering Design***, Vol. 47, No. 4, (2012), 254-264. doi: 10.1177/0309324712441146.

24 Tabatabaei, S. M. R., Alasvand Zarasvand, K., "Investigating the Effects of Cold Bulge Forming Speed on Thickness Variation and Mechanical Properties of Aluminum Alloys: Experimental and Numerical", ***International Journal of Engineering, Transactions C: Aspects***, Vol. 31, No. 9, (2018), 1602-1608. doi: 10.5829/ije.2018.31.09c.17.

25 Taheri Ahangar, A., Bakhshi-Jooybari, M., Hosseinipour, S. J., Gorji, H., "Improvement of Die Corner Filling of Stepped Tubes Using Warm Hybrid Forming", ***International Journal of Engineering , Transactions A: Basics***, Vol. 32, No. 4, (2019), 587-595. doi: 10.5829/ije.2019.32.04a.17.

Persian Abstract

چکیده

روش جدیدی برای شکل‌دهی یک برآمدگی مطلوب با استفاده از فرآیند شکل‌دهی تدریجی گرم لوله بررسی شده است. آزمایش‌های تجربی روی لوله‌های آلومینیومی AA6063 صورت گرفته است. در این روش، یک ابزار چرخان با حرکت مارپیچ خود و به‌صورت تدریجی، دیواره‌ی داخلی لوله را بسط می‌دهد. در زمان انجام فرآیند شکل‌دهی، لوله از دو انتها مهار شده و در ناحیه‌ی تغییر شکل، سطح خارجی لوله با قالب در تماس نمی‌باشد. به دلیل پایین بودن شکل‌پذیری آلیاژهای آلومینیوم در دمای محیط از یک سیستم گرمایش محیطی برای ایجاد توزیع دمای یک‌نواخت در سطح لوله استفاده شده است. به منظور دست‌یابی به بیشترین شکل‌پذیری و بالاترین کیفیت در قطعات، اثر پارامترهای فرایند شامل دما، تغذیه‌ی شعاعی، تغذیه‌ی محوری و سرعت خطی حرکت ابزار بر نتایج بررسی شده است. نتایج نشان می‌دهد که با افزایش دما از ۱۰۰ به ۳۰۰ درجه، نسبت انبساط متوسط لوله‌ها از ۲۸٪ به ۳٤٪ رسیده است. تغذیه‌ی محوری و دما به ترتیب مؤثرترین پارامترها بر زبری سطح داخلی لوله و قطر برآمدگی می‌باشند.

IJE TRANSACTIONS C: Aspects Vol. 33, No. 9, (September 2020) 1780-1791

International Journal of Engineering

Journal Homepage: www.ije.ir

Effects of Drying Temperature and Aggregate Shape on the Concrete Compressive Strength: Experiments and Data Mining Techniques

K. Reza Kashyzadeh*[a], S. Ghorbani[a], M. Forouzanmehr[b]

[a] *Department of Mechanical and Instrumental Engineering, Academy of Engineering, Peoples' Friendship University of Russia (RUDN University), 6 Miklukho-Maklaya Street, Moscow, Russian Federation*

[b] *School of Science & Engineering, Division of Solid Mechanics, Sharif University of Technology, International Campus, Kish Island, Iran*

P A P E R I N F O

Paper history:
Received 21 March 2020
Received in revised form 31 March 2020
Accepted 12 June 2020

Keywords:
Concrete
Compressive Strength
Aggregates
Drying Process
Temperature

A B S T R A C T

The main purpose of this paper is to assess the impact of the geometry and size of the aggregate, as well as the drying temperature on the compressive strength of the ordinary concrete. To this end, two aggregates with sharp and round corners were prepared in three different aggregate sizes. After preparing concrete samples, the drying operations were carried out in the vicinity of room temperature, cold wind, and hot wind. Next, the linear relationship between the concrete strength and the studied parameters was estimated using Multiple Linear Regression (MLR) method. Finally, the Taguchi Sensitivity Analysis (TSA) and Decision Tree Analysis (DTA) were applied in order to determine the importance of the parameters on the compressive strength of concrete. As a result, it is obtained that the aggregate size has the greatest influence on the compressive strength of the ordinary concrete followed by drying temperature as stated by method TSA and DTA. In addition, the influence percentages reported for each parameter by Taguchi approach and decision tree method are matched. The prediction of the strength obtained by Taguchi method and second-order regression with the experimental data are in a good agreement. It was concluded that the impact of drying temperature on the concrete strength is several times greater than the effect of the aggregate geometry. Finally, the main conclusion of this research is related to the application of cold wind for drying operation, which leads to an increase of the compressive strength by 8.67% and 11.55% for ordinary concrete containing a constant aggregate size of 20 and aggregate geometries of round and sharp corners, respectively.

***doi**: 10.5829/ije.2020.33.09c.12*

1. INTRODUCTION

Concrete as one of the most famous building materials is widely applied due to its easy operation, low cost, and responsiveness to the requirements. Today, ordinary concrete is not used in construction of a new building. In addition, civil engineers are attempted to use reinforced concrete to increase the strength of the building. However, there are many old buildings in the world that require their ordinary concrete to be partially repaired. Therefore, researchers are still looking for different methods to improve the strength of ordinary concrete and finding various techniques to predict concrete strength based on the composition of the raw material and changes in its manufacturing process. Besides, the knowledge of concrete compressive strength is major factor in assessing the strength and lifetime of structures and buildings. It is obvious that the strength of concrete is mainly dependent on the aggregate's sizes and geometries as a raw material. In addition, another parameter that greatly affects the concrete strength is its drying temperature. However, finding a general concept of the relationship between these parameters with concrete strength is still problematic. Therefore, one of the main tasks that plays important role is to determine the aggregate's size and type as well as the drying temperature.

*Corresponding Author's Email: *reza-kashi-zade-ka@rudn.ru* (K. Reza Kashyzadeh)

Please cite this article as: K. Reza Kashyzadeh, S. Ghorbani, M. Forouzanmehr, Effects of Drying Temperature and Aggregate Shape on the Concrete Compressive Strength: Experiments and Data Mining Techniques, International Journal of Engineering (IJE), IJE TRANSACTIONS C: Aspects Vol. 33, No. 9, (September 2020) 1780-1791

In this regard, recently, much research has been performed on both ordinary and reinforced concrete using different statistical analysis methods.

Study performed by Benidir et al. [1] on the aggregate size influence on the core compressive strength of concrete has shown the increase of compressive strength by increasing the drilled core diameter. It was also found that as the aggregate size increases the concrete compressive strength increases.

Ogundipe et al. have studied the impact of different aggregate sizes (coarse and fine) on the compressive strength of concrete [2]. They stated that increase in aggregate size increases the compressive strength. The authors claimed that application of very big aggregate sizes in normal concrete do not produce the desired result, which is related to the difficulty in compacting the concrete to a dense state, unworkable concrete mix, and the greater voids that is created in the mix. Kilic et al. have presented a new model for compressive strength assessment of ordinary concrete based on the physico-mechanical properties of aggregate rock [3]. In this study, nine different materials for aggregates (different mechanical and physical properties) are used to fabricate concrete samples. The authors concluded that increase in unit weight of the aggregate rock, compressive strength of rock, and young's modulus of aggregate rock lead to an increase in concrete compressive strength. Li et al. have studied how the specimens' shape and size affect the concrete behavior under static and dynamic loading conditions [4]. They found that the influence of specimen shape on the results of static compressive tests is trivial. In addition, as the aspect ratio of the specimen decreases the concrete strength increases. Moreover, the experimental results showed that the size and shape impacts on the static compressive strength are independent of the concrete grades. Also, the different effective parameters of pipe cooling system have been analyzed on the temperature regime and the thermal stress state during construction massive concrete [5]. Dmitry has studied the deformation of concrete modified by adding chemical and fine mineral elements under shrinkage phenomenon [6]. Zinevich has presented a new numerical modelling in order to design technology, heat and concrete solidification in monolithic structures [7]. Darayani et al. have studied the effect of the application of styrofoam artificial lightweight aggregate in the self-compacting concrete on the compressive strength, modulus of elasticity, and its workability [8]. The authors stated that as the amount of artificial lightweight aggregate increases the compressive strength and workability for both conventional and self-compacting concrete decrease. In addition, the elasticity modulus of concrete decreases as the styrofoam artificial lightweight aggregate replacement increases. Buller et al. have investigated the influence of 12-hours fire on the reinforced concrete beams (made by using 50% replacement of natural coarse aggregates with recyclable concrete aggregates from demolished concrete) [9]. The authors claimed that, as a result, the deflection increases, whereas the pick load decreases for all studied beams. It was also concluded that dominant failure pattern in all beams is shear failure with shear cracks.

Moreover, ANN and MLR techniques have been used to estimate the static strength of the 28-day concrete [10]. In this study, the parameters such as the largest size of aggregate, the content of cement and sand, the modulus of fitness, the ratio of water-cement, and gravel were used as input parameters. It was shown that the MLR techniques should be used for designing the preliminary mix of concrete and the ANN model should be used in order to get to the optimum mode. Also, Self Organization Feature Map (SOFM) has been optimized by the genetic algorithm and utilized to predict the concrete strength [11]. The obtained results by ANN and regression technique were compared, and then importance of the parameters was determined using this technique. They have listed the parameters in order of degree of importance as follows: 1- slump; 2- water-cement ratio; 3- the gravel maximum size; 4- cement content; 5- Sand. Nikoo et al. applied the ANN to estimate the concrete strength [12]. They investigated four optimal network structures (different learning algorithms, transfer function, number of hidden layers, and number of hidden neurons) based on the proposed by genetic algorithm. Eventually, the best network structure which has special capability in nonlinear mapping is introduced. Besides these methods, the fuzzy logic method has been applied in order to determine how the concrete raw material affect the compressive strength [13]. The results showed that the ANN technique could predict concrete strength more accurately than fuzzy logic approach in terms of R^2. Young et al. have estimated the concrete strength by knowing the mixture proportions and using machine learning methods [14]. They also reported the most optimal mixture for concrete considering the cost analysis. Moreover, the discrepancy between the predicted compressive strength of concrete using this proposed model and the experimental results is less than 10%. Moreover, Rastegarian and Sharifi have proposed equations while studying the relationship between inter-story drift and structural performance objectives of reinforced concrete intermediate moment frame [15]. By means of the proposed equations, the inter-story drift at performance levels with a bit of story information can be predicted. The effect of application of recycled aggregates on concrete strength has been reviewed by Silva et al. [16]. The laboratory data of the compressive strength of 28-day concrete in terms of coarse and fine recycled aggregate contents, age, additional material (fly ash), and oven-dried density was collected. In addition, in order to predict the recycled concrete strength under static axial compression load, the

Deep Learning (DL) technique was used [17]. Nouri and Guneyisi have presented a new strength assessment model based on the genetic algorithm [18], by means of which the compressive strength of recycled aggregate concrete-filled steel tube columns was obtained. Moreover, Kazemi et al. employed the Schmidt rebound hammer and core testing to assess the compressive strength of recycled aggregate concrete [19]. The results demonstrated an increase in compressive strength of recycled aggregate concrete by raising the curing days.

Anwar has studied the impact of nano-clay, nano-silica, and hybrid nanoparticles on the concrete strength in vitro [20]. The findings of this research revealed that the nano-silica in wet conditions and nano-clay in dry conditions have remarkable improvement on the compressive strength. Also, the optimum value for replacement of cement with nanoparticles is 0.75 and 3% for nano-silica and nano-clay, respectively. Moreover, the wet mix for nano-clay is more efficient than dry mix with approximately 24% improvement in compressive strength. The effect of adding nanoparticles such as titanium dioxide has been investigated on the strength of cementitious concrete [21]. The compressive strength of high-performance concrete, which contains nano-silica and copper slag has been investigated by Chithra et al. [22]. For this purpose, they have used various statistical techniques including regression and ANN. The authors used the following parameters as input variables in their statistical models: parameters of cement content, nano-silica content, fine aggregate content, copper slag content, age of specimen, and super plasticizer dosage. In addition, the coarse aggregate content and water content are constant in all the concrete mixes. Recently, a modified firefly algorithm-artificial neural network has been presented for predicting strength of high-performance concrete [23]. In addition to that, in order to study the strength of self-compacting concrete, the Adaptive Neuro Fuzzy Inference System (ANFIS) has been applied [24].

In summary, all studies conducted on the improvement of concrete compressive strength classify into two categories. The first group focuses on adding nanoparticles and finally recommend to use reinforced concrete. Therefore, the concrete strength based on the characteristics and the adding particles amount has been predicted by applying some different algorithm. The impact of raw materials of concrete on the compressive strength was examined by the second group, and the most optimal combination was suggested in order to increase the strength. The brief review presented here shows that predicting the concrete strength under different conditions (raw material rates, production process, and material additives) is a quite serious problem. In the present paper, for the first time, the effects of drying temperature and the aggregate shape on the concrete compressive strength were investigated. To this end, different data mining techniques including Taguchi approach, multiple linear regression, and decision tree analysis were used. Finally, the main aims of this paper are related to the following issues:

-To investigate experimentally the impact of aggregate geometry (round and sharp corners) and its size on the concrete compressive strength.

-To determine the effects of cold and hot air-dried on the concrete strength in vitro.

-To provide the decision tree to select the most optimal mode for adjusting various parameters in order to increase the concrete strength.

-To develop a new mathematical equation based on multiple linear regression method in order to assess the compressive strength of the concrete.

-To detect the greatest and least important factors on the concrete compressive strength using Taguchi approach.

2. METHODS

In the present research, the American Concrete Institute recommendations (ACI-211.1-91) was considered to select the proportions of concrete elements [25]. Moreover, water/cement ratio was considered to 0.5 and finally superplasticizer was added to the mix (2% of total weight of cement). River stone as aggregate with different types of geometrical shapes (sharp and round corners) were used as the objective of this study. Also, each type of aggregate was prepared in three different sizes. To this end, the results of particle size distribution for the aggregates using different sieve sizes (2.36, 4.75, 10, 12.5, 20, 25, and 32) are shown in Figure 1.

The 28-days concrete samples were developed in the cubic shape (with a height of 150 mm and a square cross-section of 50×50 mm) based on the ISO-1920-3 standard [26]. Totally, 54 specimens were prepared in 18 different groups according to the Taguchi design (each group consists of three specimens). The characteristics and raw

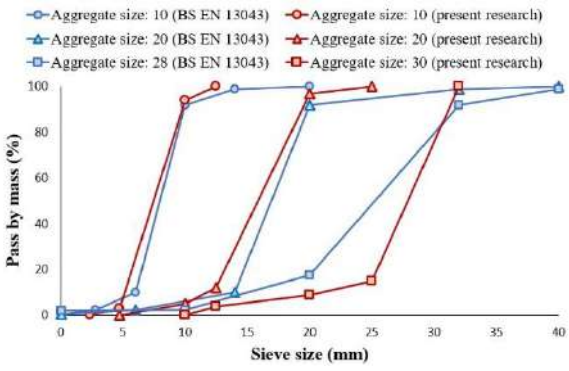

Figure 1. Particle size distribution curves in comparison with BS EN 13043 standard for aggregate

material proportions are presented in Table 1. For drying operations, the specimens were air-dried at different temperatures (temperature of 10 °C as cold wind, temperature of 20 °C as room temperature, and temperature of 30 °C as hot wind). Eventually, Figure 2 shows the working flowchart to clarify the research methodology in this study.

3. EXPERIMENTAL PROCEDURE

Firstly, different types of concrete specimens were classified using below designing code. For example, the sample code of R1020 represents the concrete which is made of aggregate with round corner geometry and size of 10 with a drying temperature of 20 °C.

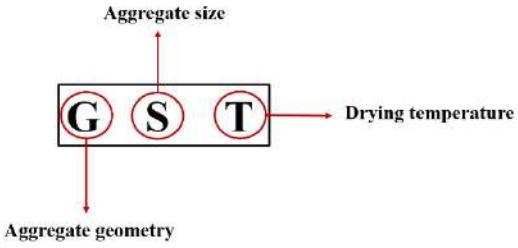

TABLE 1. The characteristics and raw material proportions

Parameters	Unit	Value
Slump	mm	50
Water-cement ratio	-------	0.5
Cement	Kg/m^3	238
Sand 3/8	Kg/m^3	2411
Sand ¾	Kg/m^3	1224

The hydraulic universal compression testing machine (Amsler brand made in USA) with a capacity of 60 tons was employed in order to perform the tests and report the concrete compressive strength. In accordance with ISO-1920-4 standard [27], a constant rate of loading equal to 1000 N/sec (0.4 Mpa/sec) was applied continuously and without shock. All tests were carried out at room temperature. Moreover, the authors repeated each test three times in order to ensure the accuracy of the experimental results and then the mean value was reported as sample strength.

4. FRACTURE SURFACE ANALYSIS

Different failure modes of cubic concrete are shown in Figure 3. When the stress reaches 75-90 % of ultimate failure load, the cracks are initiated in the mortar through the concrete samples. In ideal state, under pure uniaxial compression loading, the cracks are approximately parallel to the load direction. In practice, due to the Poisson's effect, concrete cube tends to lateral expansion, but rigid plates on both sides of sample have not any movement. In other words, the degree of two sides plates restrain on the concrete is related to surface friction [28].

Three failure modes were observed in the tests (Figure 4). It means that the air temperature had a significant effect on the concrete bonding by considering the same conditions (proper mortar and mix design).

5. STATISTICAL ANALYSIS

In order to get the linear relationship between dependent and several independent variables, the MLR method is mostly used in various industries and academic researches [10, 22, 29]. However, the order of the

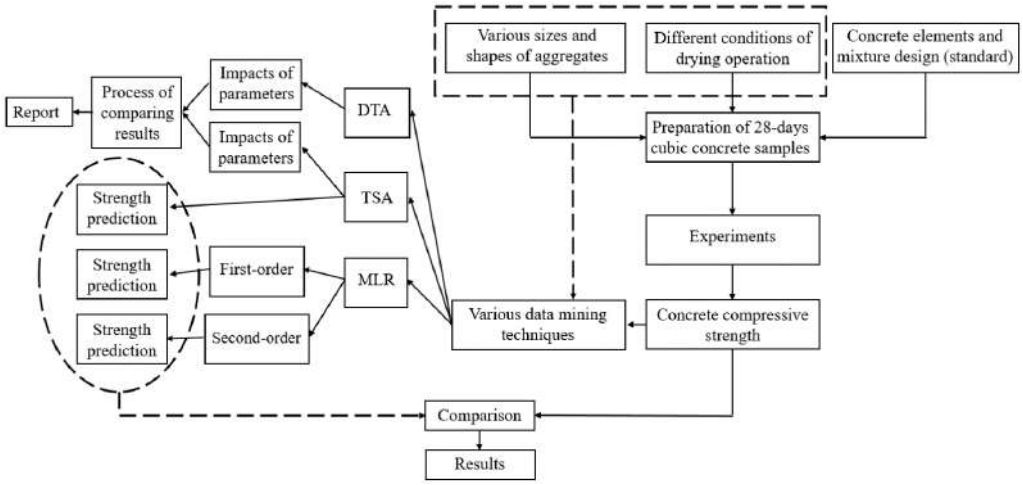

Figure 2. The working flowchart used in this research.

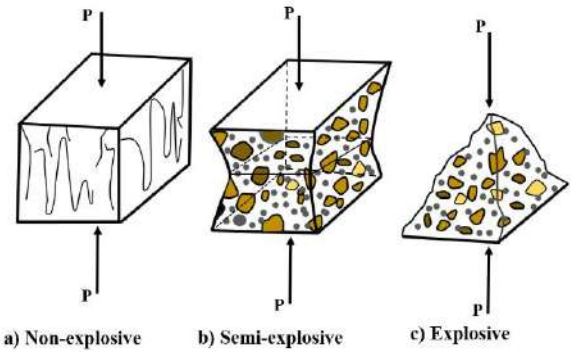

Figure 3. Different failure modes of cubic concrete [27]

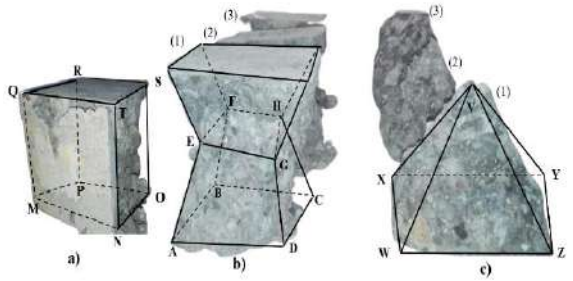

Figure 4. a) fracture surface of a rejected case in the GS30 samples, b) fracture surfaces in the GS20 samples, and c) fracture surfaces in the GS10 samples.

equation and interaction with the input parameters affect the accuracy of the response. Nevertheless, generally, using such relationships is very cost-effective in comparison with the high cost of mechanical tests.

In this study, the authors have presented separate relationships for each of the aggregate geometries with sharp and round corners to predict the compressive strength in terms of aggregate size and drying temperature. This is because there are two quantitative variables (the size of the aggregate and drying temperature) and one qualitative variable (aggregate geometry) and it is impossible to consider the impact of the qualitative parameter in such relationships. In addition, the Minitab software was applied to get the first-order and the second-order of linear regression equations, by means of which the influence of order condition on response accuracy was investigated and compared to experimental data.

Next, application of TA made it possible to determine the impact of aggregate geometry, aggregate size, and drying temperature on the compressive strength of the concrete. This section mainly aims at determination of the most important factor and prediction of the concrete compressive strength under different conditions without tests. This method uses the minimum number of samples needed for sensitivity analysis in comparison with the other methods of Design of Experiments (DOE) [29]. Figure 5 illustrates the applied algorithm in this study, which includes the input and output variables. Three different levels were considered for each aggregate size and drying temperature parameters. Also, the aggregate geometry is qualitatively coded so that the numbers 1 and 2 represent the sharp and the round aggregate, respectively. Variables and their levels considered as input data are presented in Table 2.

The main goal of this research focuses on the increase of the concrete compressive strength. Hence, the equation "the larger is the better" is used (Equation (1)) [30]:

$$\frac{S}{N} = -10\,log\left[\frac{1}{n}\left(\frac{1}{y_1^2}+\frac{1}{y_2^2}+\ldots+\frac{1}{y_n^2}\right)\right] \quad (1)$$

where y1, y2, and y_n demonstrate the bent angles measured during bending process. It should be mentioned that the authors repeated n time each bending condition.

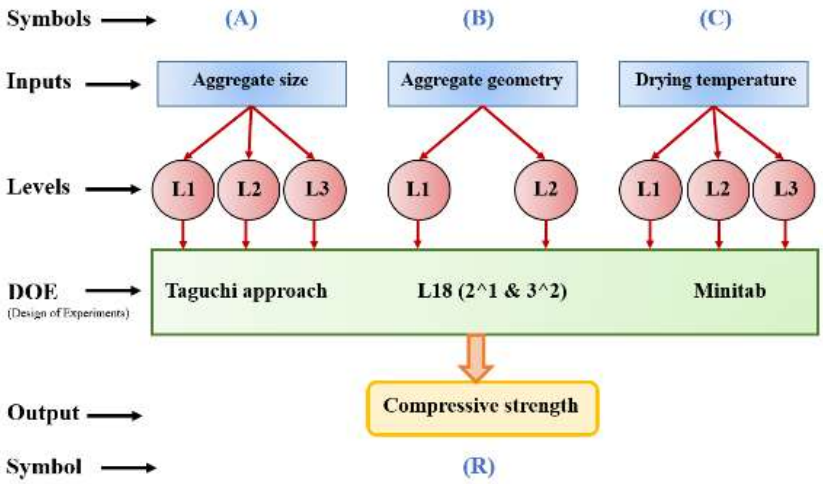

Figure 5. Design of experiments based on the Taguchi method

TABLE 2. Variables and their levels used as input data in the Taguchi-based DOE

Parameter	Symbol	Level		
		L1	L2	L3
Aggregate size	A	10	20	30
Aggregate geometry	B	1	2	-------
Drying temperature	C	10	20	30

In addition, the compressive strength of the concrete was considered as positive values. Because it is not possible to enter negative values in Taguchi sensitivity analysis [31]. In this research, a mixed-mode design of Taguchi (2^1 & 3^2) consist of 18 tests was used. The Taguchi orthogonal matrix including different test conditions is presented in Table 3.

Moreover, DTA is a widely used classifier in machine learning. This method has a tree structure that splits the input data into groups to explain the variation of a single response which may be numeric and/or categorical [32]. The features are represented by nodes and the values of the nodes are also represented by branches. A decision tree is described graphically which makes it easy to explore and understand. This method is also easy to interpret and able to handle missing values in both response and explanatory variables [33]. A decision tree forest evaluates the parameters sensitivity or parameter combinations. Random forest consisting of many decision trees is a classifier that evolves from decision trees. Each classifier in decision tree represents a "weak" classifier but in ensemble, they form a strong classifier. In random forest approach, each decision tree depends on the random vector values, which are sampled independently. Moreover, the important parameters determined by the algorithm through branching of inputs.

TABLE 3. The orthogonal matrix extracted from the mixed-mode design of Taguchi for L18

Run No.	A	B	C
1	L1	L1	L1
2	L1	L1	L2
3	L1	L1	L3
4	L2	L1	L1
5	L2	L1	L2
6	L2	L1	L3
7	L3	L1	L1
8	L3	L1	L2
9	L3	L1	L3
10	L1	L2	L1
11	L1	L2	L2
12	L1	L2	L3
13	L2	L2	L1
14	L2	L2	L2
15	L2	L2	L3
16	L3	L2	L1
17	L3	L2	L2
18	L3	L2	L3

A decision tree forest is an ensemble of single decision trees formed by various methods, by different subsamples of observations over one and the same phenomenon, by applying different characteristics. Finally, the predictions are combined to make the overall prediction for the forest as it is shown in Figure 6.

In decision tree forest, the improvement of a large number of independent trees and laws of the researched phenomenon grow in parallel, and problem consideration makes it possible to better understand the fact that they interact only when all of them have been built. The basis of bagging incorporated in decision tree forest are bootstrap resampling method and aggregating. Different training sub-sets are drawn randomly with replacement from the training data set. From these sub-sets separate models can be produced and applied to predict the entire data. Next, by applying majority voting for classification problems or the mean for regression problems the estimated models can be aggregated.

$$D_i^* = (Y_i^*, X_i^*) \quad (2)$$

where D_i^* represents a bootstrapped sample according to the empirical distribution of the pairs Di = (Xi, Yi), and (i=1, 2, . . . ; n).

In the second step, by applying plug-in principle the bootstrapped predictor is estimated using the following Equation [32]:

$$C_n^*(x) = h_n(D_i^*, \ldots, D_i^*)(x) \quad (3)$$

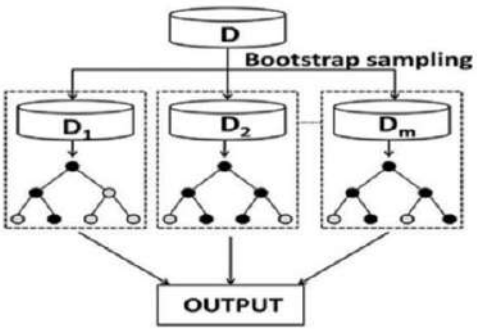

Figure 6. Conceptual diagram of decision tree forest

where Cn(x)=hn(Di, ...,Dn)(x) represents the n-th hypothesis. In the final step, the bagged predictor is determined using the following equation [32]:

$$C_{nB}^{*}(x) = E^{*}[D_{n}^{*}(x)] \quad (4)$$

Bagging reduces the variance with a good performance when combined with the base learner generation. The out of bag data rows for model validation is applied for the decision tree forest gaining strength from bagging technique. By this way the independent test set is provided, which does not require a separate data set or holding back rows from the tree construction. The decision tree forest algorithm is highly resistant to over-fitting due to the stochastic element in it.

In the present research, the random forest method was applied in order to predict the compression strength in terms of aggregate size, drying temperature, and aggregate geometry.

6. RESULTS AND DISCUSSION

The experimental results of the concrete strength under axial compression loading for different types of concrete samples are reported in Table 4. In addition, the diagram of concrete strength in terms of aggregate size (the drying process performed at room temperature) is depicted in Figure 7. According to the experimental result, the compressive strength of the concrete increases as the aggregate size for both sharp and round corners increases which is completely consistent with the results achieved by the authors published paper in literatures [34-35]. It is stated that the compressive strength of concrete of the same mix is directly proportional with increase in coarse aggregate size. However, an inverse relationship has been observed between the size of the aggregate and concrete flexural strength. Moreover, it was revealed that the concrete compressive strength of round corner aggregates is much greater than that of sharp corner. It is worth to mention that some researchers have stated it and is reported in literatures [36-37]. However, they only studied the effects of different types of aggregate shapes with a specific aggregate size on the concrete compressive strength. In addition, they conclude that the application of rounded corner aggregates increases the concrete compressive strength. However, in this study, the author considered three different aggregate sizes in order to investigate the effect of aggregate geometry. Additionally, as it is shown in Figure 7, the trend of increasing concrete compressive strength with aggregate size does not depend on the type of aggregate geometry.

Next, the designed decision tree using the random forest method is demonstrated in Figure 8. This is presented to easily identify the path for achieving the desired target (maximum compressive strength of concrete).

TABLE 4. Experimental results for compressive strength of different types of concrete samples

Experiment No.	Specimen No.	Strength (N)
1	S1010	56391.1
2	S1020	63010.9
3	S1030	96700.9
4	S2010	60510.3
5	S2020	91000.5
6	S2030	101249.1
7	S3010	40844.7
8	S3020	45949
9	S3030	70529.1
10	R1010	43761
11	R1020	66372
12	R1030	73665.8
13	R2010	63308.4
14	R2020	71245.5
15	R2030	107317.5
16	R3010	68967.4
17	R3020	98894.7
18	R3030	115963.1

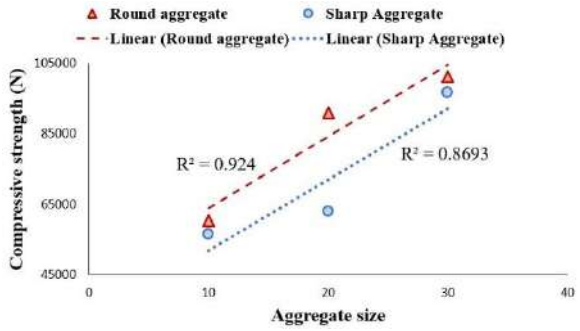

Figure 7. Concrete compressive strength graph in terms of aggregate size (drying temperature = room temperature)

Based on the results obtained by both TA and DTA the compressive strength of ordinary concrete is mainly affected by aggregate size following by drying temperature (Figure 9). Moreover, the results showed that the aggregate geometry has the least impact, which is about 1/4 of the effective weight in comparison with the aggregate size parameter.

In TA, the main effect plot is used to compare the relative strength of the effects against other factors [38] as shown in Figure 10.

From the highest S/N ratio given in the Figure 10, it is conducted that the highest compressive strength of concrete is obtained with the round aggregate, largest

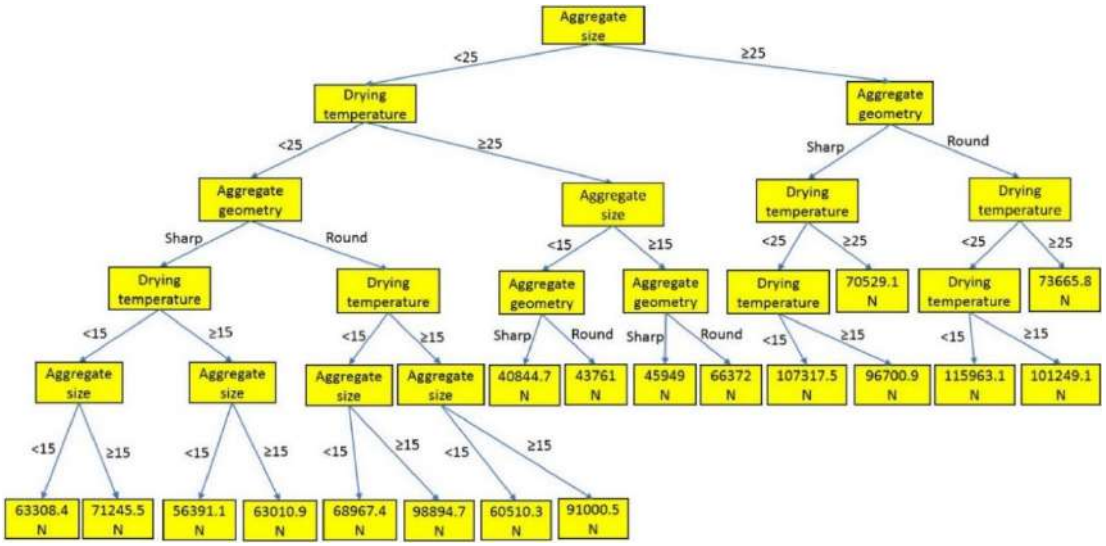

Figure 8. Decision tree graph based on the random forest method

aggregate size, and the lowest drying temperature. Figure 11 shows the relationship between the response and variables. This contour graph is useful to find the optimal output value via area range for each variable [38].

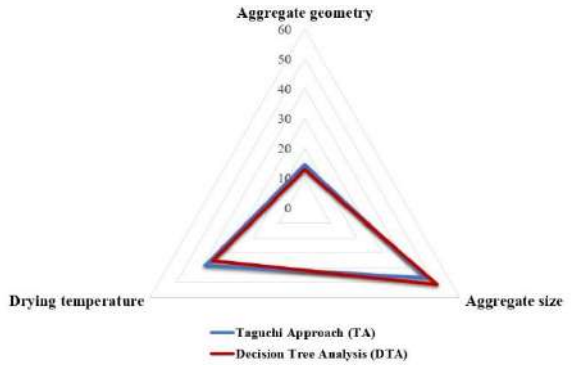

Figure 9. Most effective parameter on the concrete compressive strength using DTA and TA

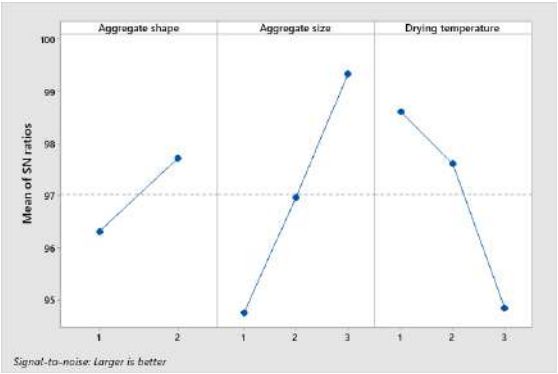

Figure 10. The Main effects plot S/N ratios compressive strength

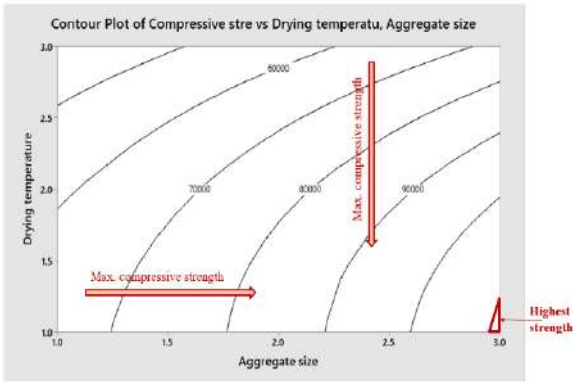

Figure 11. Contour plot of concrete compressive strength via both parameters of aggregate size and drying temperature

Next, the concrete compressive strength under different conditions was predicted using TA and MLR, and compared with laboratory data. In the following, the Taguchi sensitivity analysis and Taguchi prediction algorithm were performed in Minitab software. Nevertheless, in MLR method, since the aggregate geometry is a qualitative quantity and cannot be directly incorporated into the mathematical model, the mathematical model for each of the aggregate forms including sharp and round corners was obtained separately.

The first-order and the second-order equations obtained by MLR for different geometrical shapes of the aggregates are as follows:

<u>For sharp aggregate</u>

First-order

$$R = 58548 + 1900 \times A - 1409 \times C \quad (5)$$

Second-order

$$R = 81698 - 3079 \times A + 792 \times C + 124.5 \times A^2 - 55 \times C^2 \quad (6)$$

For round aggregate

First-order

$$R = 74172 + 1961 \times A - 1667 \times C \quad (7)$$

Second-order

$$R = 26220 + 5189 \times A + 859 \times C - 80.7 \times A^2 - 63.2 \times C^2 \quad (8)$$

where R represent concrete compressive strength and parameters of A and C are aggregate size (mm) and drying temperature (℃), respectively.

Concrete strength prediction via aggregate size and drying temperature are illustrated in Figure 12 and Figure 13, respectively.

The results showed that as the aggregate size increases, generally, the concrete compressive strength increases. However, the increasing trend varies with aggregate geometry. Figure 12 depicts that there is a little impact on the concrete compressive for aggregate sizes 10 and 20 in sharp corner geometry, but as soon as aggregate size 30 is used, this increase is significant. On the other hand, while using round corner geometry for aggregates, increase in concrete strength by changing the size of the aggregate from 10 to 20 is evident. Furthermore, this trend has been proven in laboratory results. In addition, it should be mentioned that all the methods applied in this study for prediction of the compressive strength of ordinary concrete are in full agreement.

As it can be seen from Figure 13 as the drying temperature reduces the compressive strength of the concrete increases. Therefore, the compressive strength of concrete dried by a cold wind (10 °C) is much more than that of dried at room temperature. Moreover, the concrete which is dried by a hot wind (30 °C) has a water content lower than usual concrete and it becomes absurd from within because of the water evaporation. It is often found in experiments that it is powdered from the inside and concrete fails even under static load below half of its strength. In other words, the cement in the sample does not have the required strength and it results in fracture of the concrete.

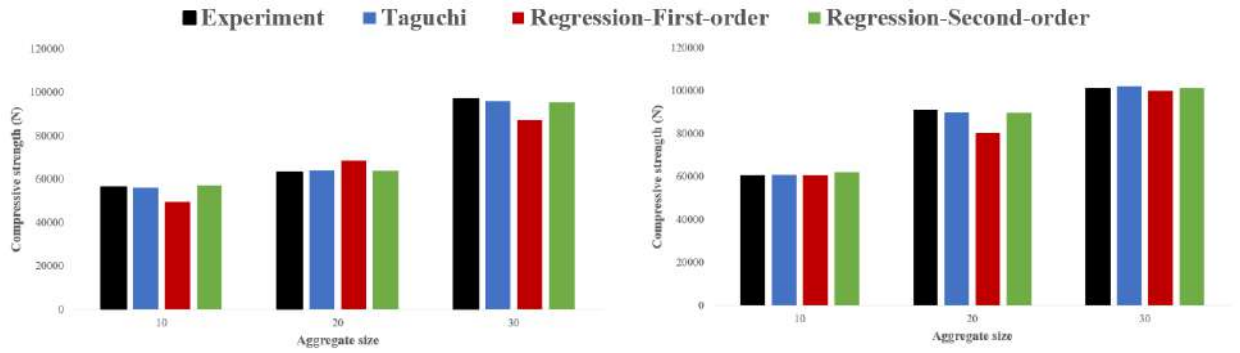

Figure 12. Comparison of estimation of concrete compressive strength in terms of aggregate size with laboratory data for the constant drying temperature of 20 and different aggregate geometries including (A) sharp corners and (B) round corners

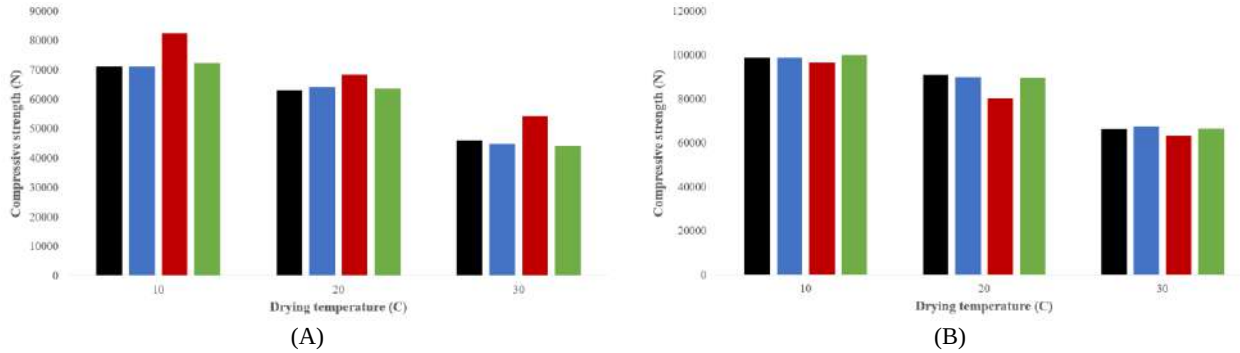

Figure 13. Comparison of estimation of concrete compressive strength in terms of drying temperature with laboratory data for the constant aggregate size of 20 and different aggregate geometries including (A) sharp corners and (B) round corners

Further, the comparison of predicted error percentage using different methods with the experimental data for considering variable aggregate size and drying temperature are reported in Tables 5 and 6, respectively.

The results indicated that the Taguchi method and its prediction algorithm is the best method based on the error level of concrete strength prediction compared to laboratory data. Moreover, it is achieved that when using the first-order equation of MLR, it is not possible to predict the concrete compressive strength with acceptable accuracy. But the results indicated that concrete strength with higher accuracy can be predicted by using the second-order equation of MLR in comparison with the first-order and it is even acceptable compared to the results obtained by Taguchi method.

TABLE 5. Comparison between the predicted error percentage of concrete compressive strength using different methods with laboratory data for drying at room temperature

Aggregate geometry	Aggregate size	Error in comparison with experiment data (%)		
		Taguchi approach	Regression (First-order)	Regression (Second-order)
Sharp	10	0.71003	1.56752	0.088001
	20	1.14999	12.03125	1.517025
	30	0.54123	0.112873	2.362738
Round	10	0.74353	9.651306	1.533491
	20	1.66082	8.501862	1.185668
	30	0.58076	12.45427	1.4309

TABLE 6. Comparison between the predicted error percentage of concrete compressive strength using different methods with laboratory data for the aggregate size of 20

Aggregate geometry	Aggregate size	Error in comparison with experiment data (%)		
		Taguchi approach	Regression (First-order)	Regression (Second-order)
Sharp	10	1.566926	4.504912	0.35858
	20	1.149994	12.03125	1.51702
	30	0.006573	2.196983	1.10754
Round	10	2.263379	18.12662	3.85427
	20	1.660824	8.501862	1.18566
	30	0.009123	15.73784	1.53343

7. CONCLUSION

In this study three different data mining methods including MLR, TA, and DTA were applied to predict the compressive strength of the concrete in terms of different parameters of aggregate geometry, aggregate size, and drying temperature. It is concluded that the most reliable technique is TA model (approximately 1% error compared to experiment results). Moreover, the first-order and the second-order equations were presented based on the MLR that can estimate the ordinary concrete strength by 9 % and 1.5 % error compared to reality. In addition, according to the results achieved by TA and DTA, the most important factor affecting the concrete compressive strength is the aggregate size with impact weight of 47.02 % and 51.38 %, respectively. Among all parameters studied in this research, the aggregate geometry had the least effect on the concrete compressive strength. The results of the analysis indicated that the effect of drying temperature on the concrete strength is several times greater than the effect of the aggregate geometry. The efficiency ratio of drying temperature to aggregate geometry based on the TA and DTA is 2.69 and 2.8, respectively. However, the trend of increasing concrete compressive strength with aggregate size (increasing aggregate size leads to increase strength) is independent of aggregate geometry. Finally, the most important finding of this study is that application of cold wind for drying operation increases the compressive strength by 8.67% and 11.55% for ordinary concrete containing a constant aggregate size of 20 and aggregate geometries of round and sharp corners, respectively.

8. ACKNOWLEDGMENTS

The publication has been prepared with the support of the "RUDN University Program 5-100".

9. REFERENCES

1. Meguid, S. A., Benidir, A., Mahdad, M. H. and Brara, A., "Aggregate size and lateral dimension effects on core compressive strength of concrete", Proceedings IRF2018: 6th International Conference Integrity-Reliability-Failure, (2018).
2. Ogundipe, O. M., Olanike, A. O., Nnochiri, E. S. and Ale, P. O., "Effects of coarse aggregate size on the compressive strength of concrete", ***Civil Engineering Journal***, Vol. 4, No. 4, (2018), 836-842. http://dx.doi.org/10.28991/cej-0309137
3. Kılıç, A., Teymen, A., Özdemir, O. and Atiş, C. D., "Estimation of Compressive Strength of Concrete Using Physico-Mechanical Properties of Aggregate Rock", ***Iranian Journal of Science and Technology - Transactions of Civil Engineering***, Vol. 43, (2019), 171-178. https://doi.org/10.1007/s40996-018-0156-6
4. Li, M., Hao, H., Shi, Y., Hao and Y., "Specimen shape and size effects on the concrete compressive strength under static and

dynamic tests", ***Construction and Building Materials***, Vol. 161, (2018), 84-93.

https://doi.org/10.1016/j.conbuildmat.2017.11.069

5. Nguyen, C. T. and Aniskin, N. A., "Temperature regime during the construction massive concrete with pipe cooling", ***Magazine of Civil Engineering***, Vol. 89, No. 5, (2019), 156-166. DOI: 10.18720/MCE.89.13
6. Kotov, D., "Shrinkage deformations of the concrete modified by chemical and fine mineral additives", ***Magazine of Civil Engineering***, Vol. 7, (2009), 11-21. DOI: 10.18720/MCE.9.5
7. Zinevich, L., "Application of numerical modeling at technology designing of heating and solidification of concrete in monolithic structures", ***Magazine of Civil Engineering***, Vol. 2, (2011), 24-28. DOI: 10.18720/MCE.20.5
8. Darayani, D. H., Tavio, T., Raka I. G. P. and Puryanto, P., "The effect of styrofoam artificial lightweight aggregate (ALWA) on compressive strength of self compacting concrete (SCC)", ***Civil Engineering Journal***, Vol. 4, No. 9, (2018), 211-2123. http://dx.doi.org/10.28991/cej-03091143
9. Buller, A. H., Memon, B. A. and Oad, M., "Effect of 12-hour fire on flexural behavior of recyclable aggregate reinforced concrete beams", ***Civil Engineering Journal***, Vol. 5, No. 7, (2019), 1533–1542. http://dx.doi.org/10.28991/cej-2019-03091350
10. Khademi, F. and Behfarnia, K., "Evaluation of concrete compressive strength using artificial neural network and multiple linear regression models", ***International Journal of Optimization in Civil Engineering***, Vol. 6, No. 3, (2016), 423-432.
11. Nikoo, M., Zarfam, P. and Sayahpour, H., "Determination of compressive strength of concrete using Self Organization Feature Map (SOFM)", ***Engineering with Computers***, Vol. 31, No. 1, (2013), 113-121. https://doi.org/10.1007/s00366-013-0334-x
12. Nikoo, M., Torabian Moghadam, F. and Sadowski, L., "Prediction of concrete compressive strength by evolutionary artificial neural networks", ***Advances in Materials Science and Engineering***, Vol. 2015, (2015), 1-8.

http://dx.doi.org/10.1155/2015/849126

13. Khademi, F., Akbari, M., Jamal, S. M. and Nikoo, M., "Multiple linear regression, artificial neural network, and fuzzy logic prediction of 28 days compressive strength of concrete", ***Frontiers of Structural and Civil Engineering***, Vol. 11, No. 1, (2017), 90–99. https://doi.org/10.1007/s11709-016-0363-9
14. Young, B. A., Hall, A., Pilon, L., Gupta, P. and Sant, G., "Can the compressive strength of concrete be estimated from knowledge of the mixture proportions?: New insights from statistical analysis and machine learning methods", ***Cement and Concrete Research***, Vol. 115, (2019), 379-388. https://doi.org/10.1016/j.cemconres.2018.09.006
15. Rastegarian, S. and Sharifi, A., "An investigation on the correlation of inter-story drift and performance objectives in conventional RC frames", ***Emerging Science Journal***, Vol. 2, No. 3, (2018), 140-147. http://dx.doi.org/10.28991/esj-2018-01137
16. Silva, R. V., De Brito, J. and Dhir, R. K., "The influence of the use of recycled aggregates on the compressive strength of concrete: A review", ***European Journal of Environmental and Civil Engineering***, Vol. 19, No. 7, (2015), 825-849. https://doi.org/10.1080/19648189.2014.974831
17. Deng, F., He, Y., Zhou, S., Yu, Y., Cheng, H. and Wu, X., "Compressive strength prediction of recycled concrete based on deep learning", ***Construction and Building Materials***, Vol. 175, (2018), 562-569. https://doi.org/10.1016/j.conbuildmat.2018.04.169
18. Nour, A. I. and Güneyisi, E. M., "Prediction model on compressive strength of recycled aggregate concrete filled steel tube columns", ***Composites Part B: Engineering***, Vol. 173, (2019), 106938.

https://doi.org/10.1016/j.compositesb.2019.106938

19. Kazemi, M., Madandoust, R. and de. Brito, J., "Compressive strength assessment of recycled aggregate concrete using Schmidt rebound hammer and core testing", ***Construction and Building Materials***, Vol. 224, (2019), 630-638. https://doi.org/10.1016/j.conbuildmat.2019.07.110
20. Mohamed, A. M., "Influence of nano materials on flexural behavior and compressive strength of concrete", ***HBRC Journal***, Vol. 12, No. 2, (2016), 212-225. https://doi.org/10.1016/j.hbrcj.2014.11.006
21. Sorathiya, J., Shah, S. and Kacha, S., "Effect on Addition of Nano "Titanium Dioxide" (TiO2) on Compressive Strength of Cementitious Concrete", ***Kalpa Publications in Civil Engineering***, Vol. 1, (2017), 219-225. https://doi.org/10.29007/sq9d
22. Chithra, S., Kumar, S. R. R. S., Chinnaraju, K. and Alfin Ashmita, F., "A comparative study on the compressive strength prediction models for High Performance Concrete containing nano silica and copper slag using regression analysis and Artificial Neural Networks", ***Construction and Building Materials***, Vol. 114, (2016), 528-535. https://doi.org/10.1016/j.conbuildmat.2016.03.214
23. Bui, D. K., Nguyen, T., Chou, J. S., Nguyen-Xuan, H. and T. D. Ngo, "A modified firefly algorithm-artificial neural network expert system for predicting compressive and tensile strength of high-performance concrete", ***Construction and Building Materials***, Vol. 180, (2018), 320-333. https://doi.org/10.1016/j.conbuildmat.2018.05.201
24. Vakhshouri, B. and Nejadi, S., "Prediction of compressive strength of self-compacting concrete by ANFIS models" ***Neurocomputing***, Vol. 280, (2018), 13-22. https://doi.org/10.1016/j.neucom.2017.09.099
25. ACI-211.1-91, "Standard practice for selecting proportions for normal, heavyweight, and mass concrete", American Concrete Institute, (2002).
26. ISO-1920-3, "Testing of concrete-part 3: Making and curing test specimens", International Standard Organization, (2004).
27. ISO-1920-4, "Testing of concrete-part 4: Strength of hardened concrete", International Standard Organization, (2005).
28. Brown, A., "Reinforced concrete", ***Wilmott***, Vol. 82, (2016), 8-13. https://doi.org/10.1002/wilm.10519
29. Farrahi, G. H., Reza Kashyzadeh, K., Minaei, M., Sharifpour, A. and Riazi, S., "Analysis of resistance spot welding process parameters on the weld quality of three-steel sheets used in automotive industry: Experimental and finite element simulation", ***International Journal of Engineering, IJE TRANSACTION A: Basis***, Vol. 33, No. 1, (2020), 148-157. doi: 10.5829/ije.2020.33.01a.17
30. Omidi-bidgoli, M., Reza-Kashyzadeh, K. and Amiri-Asfarjani, A., "Estimation of critical dimensions for the crack and pitting corrosion defects in the oil storage tank using finite element method", ***International Journal of Solid Materials***, Vol. 1, No.1, (2019), 1-26.
31. Maleki, E. Unal, O. and Kashyzadeh, K. R., "Efficiency analysis of shot peening parameters on variations of hardness, grain size and residual stress via taguchi approach", ***Metals and Materials International***, Vol. 25, No. 6, (2019), 1436-1447. https://doi.org/10.1007/s12540-019-00290-7
32. Mehmed, K. and Hoboken, N., "Data Mining: Concepts, Models, Methods, and Algorithms", ***Technometrics***, Vol. 45, No. 3, (2003), 277–277.
33. Coops, N. C., Waring, R. H., Beier, C., Roy-Jauvin, R. and Wang,

T., "Modeling the occurrence of 15 coniferous tree species throughout the Pacific Northwest of North America using a hybrid approach of a generic process-based growth model and decision tree analysis", ***Applied Vegetation Science***, Vol. 14, No. 3, (2011), 402-414. https://doi.org/10.1111/j.1654-109X.2011.01125.x

34. Ajamu, S. O. and Ige, J. A., "Effect of Coarse Aggregate Size on the Compressive Strength and the Flexural Strength of Concrete Beam", ***Journal of Engineering Research and Applications***, Vol. 5, No. 4, (2015), 2248–2267.
35. Roy, B., Vilane, T. and Sabelo, N., "The Effect of Aggregate Size on the Compressive Strength of Concrete", ***Journal of Agricultural Science and Engineering***, Vol. 2, No. 6, (2016), 66-69.
36. Polat, R., Yadollahi, M. M., Sagsoz, A. E., Arasan, S., "The Correlation between Aggregate Shape and Compressive Strength of Concrete: Digital Image Processing Approach", ***International Journal of Structural and Civil Engineering***, Vol. 2, No. 3, (2013), 62-80.
37. Lie, H. A., Nurhuda, I. and Setiawan, Y., "The Effect of Aggregate Shape and Configuration to the Concrete Behavior", ***Smart Science***, Vol. 2, No. 2, (2014), 85-90. https://doi.org/10.1016/j.jobe.2019.100871
38. Zarehparvar-Shoja, M. and Eskandari-Naddaf, H., "Optimizing compressive strength of Micro- and Nano-silica concrete by statistical method", ***Civil Engineering Journal***, Vol. 3, No. 11, (2017), 1084-1096. http://dx.doi.org/10.28991/cej-030939

Persian Abstract

چکیده

هدف اصلی این مقاله ارزیابی تأثیر هندسه و اندازه‌ی سنگ‌دانه و همچنین فرایند خشک کردن (دمای خشک کردن) بر مقاومت فشاری بتن معمولی است. برای این منظور، دو هندسه‌ی متفاوت سنگ‌دانه شامل تیزگوشه و گردگوشه در سه اندازه‌ی مختلف سنگ‌دانه تهیه شده است. پس از آماده سازی آزمونه‌های بتنی، عملیات خشک کردن در مجاورت دمای اتاق، باد سرد و باد گرم انجام شد. سپس، به منظور دست‌یابی به رابطه‌ای خطی بین استحکام بتن و پارامترهای مطالعاتی از روش رگرسیون خطی چندگانه استفاده شد. در نهایت، میزان اهمیت پارامترها بر استحکام فشاری بتن با تحلیل حساسیت تاگوچی و تحلیل درخت تصمیم‌گیری انجام شد. هر دو تحلیل حساسیت تاگوچی و درخت تصمیم گیری نشان دادند که اندازه ی سنگ دانه و به دنبال آن دمای خشک کردن بیشترین اثر را بر مقاومت فشاری بتن معمولی دارند. همچنین، درصد تاثیر گزارش شده برای هر پارامتر با روش تقریب تاگوچی و روش درخت تصمیم‌گیری مطابقت دارد. نتایج نشان داد که پیش‌بینی استحکام توسط الگوریتم تاگوچی و رگرسیون مرتبه‌ی دوم در مقایسه با داده‌های تجربی تطابق بسیار خوبی دارند. چنین نتیجه می‌شود که تأثیر دمای خشک کردن بر مقاومت بتن چندین برابر بیشتر از اثر هندسه‌ی سنگ‌دانه است. در نهایت، دستاورد اصلی این مقاله پژوهشی مربوط به کاربرد جریان باد سرد در عملیات خشک کردن است که منجر به افزایش مقاومت فشاری به اندازه‌ی ۸.٦۷ ٪ و ۱۱.۵۵ ٪ به ترتیب برای بتن‌های معمولی حاوی اندازه سنگ‌دانه‌ی ۲۰ و هندسه‌های سنگ‌دانه‌ی گردگوشه و تیزگوشه می‌شود.

International Journal of Engineering

Journal Homepage: www.ije.ir

Ballistic Testing and Simulation of Co-continuous Ceramic Composite for Body Armour

A. S. Prasanth*[a], R. Ramesh[b], T. S. Kavinesh Sankaar[a]

[a] *Department of Mechanical Engineering, PSG College of Technology, Coimbatore, India*
[b] *Department of Mechanical Engineering, PSG Institute of Technology and Applied Research, Coimbatore, India*

PAPER INFO

Paper history:
Received 28 March 2020
Received in revised form 13 June 2020
Accepted 04 August 2020

Keywords:
Co-continuous Ceramic Composite
Depth of Penetration
Impact Testing
Numerical Simulation

ABSTRACT

Co-Continuous Ceramic Composites, referred to as C4, have bi-continuous, interconnected and interpenetrating phases of a metal and ceramic. This bestows such composites with a higher strength to weight ratio compared with traditional composites. In this research work, a C4 composite of AA5083/SiC is fabricated for personal body armour, using gravity infiltration technique. A numerical simulation model of the C4 specimen is developed. This finite element model is utilized to simulate the DoP of a subsonic bullet into the C4 and is estimated as 1.47 mm. The C4 specimen is then, subjected to ballistic tests. A medium velocity projectile with a rated velocity of 326 m/s is used to impact the C4 specimen. The ballistic tests validate the numerical simulation with a DoP of 1.5 mm. Visual inspection reveals brittle cracks and interfacial debonding in the impacted C4. The results indicate that, such composites can potentially be utilized as low cost body armour.

***doi**: 10.5829/ije.2020.33.09c.13*

NOMENCLATURE

v	velocity of the bullet (m/s)	m	mass of the bullet (x 10^{-3} kg)
F	Impact force of the bullet (N)	D	distance to be travelled by the bullet for impact (m)
DoP	Depth of Penetration	C4	Co-Continuous Ceramic Composites
IPCs	Interpenetrating Composites	AP	Armour Piercing
FE	Finite Element	ϕ	Diameter

1. INTRODUCTION

Traditional composites typically consist of two constituent phases namely, a continuous matrix phase and a discontinuous reinforcement phase. Composites are used in numerous applications due to their high strength and stiffness combined with low density. In practice, these beneficial properties enable weight reduction without compromising on strength. In contrast to traditional composites, C4 consist of an interpenetrated structure of a soft, ductile metal phase and a hard, brittle ceramic phase [1], both phases being continuous. Such three dimensionally continuous composites provide a variety of desirable properties like high stiffness, low density, high thermal conductivity and high fracture toughness when compared to traditional composites [2]. These properties enable the use of C4 in numerous applications such as ballistic armour, automotive and high speed train braking systems [3, 4]. Due to its light weight [5, 6], aluminium has been widely used in conjunction with ceramics such as silicon carbide (SiC) and alumina (Al_2O_3) for body armour. Among the Al alloys, AA5083 is typically utilized in armour plates, missile components and cryogenics owing to its exceptional corrosion resistance and structural strength properties [7]. Al alloys bonded to ceramic tiles have been assessed for impact performance using 0.50 caliber AP projectiles in the velocity range of 750 to 910 m/s.

*Corresponding Author Email: *asp.mech@psgtech.ac.in* (A. S. Prasanth)

Please cite this article as: A. S. Prasanth, R. Ramesh, T. S. Kavinesh Sankaar, Ballistic Testing and Simulation of Co-continuous Ceramic Composite for Body Armour, International Journal of Engineering (IJE), IJE TRANSACTIONS C: Aspects Vol. 33, No. 9, (September 2020) 1792-1796

The residual DoP in the impacted cylinders measured using X-rays indicated that, the ballistic efficiency of SiC ceramic was higher than boron carbide and alumina [8]. Advanced C4 composites have been created by immersing near net-shape silica preforms into liquid Al. Such composites have been found to possess enhanced toughness and less fragility, properties regarded as beneficial for ballistic armours [3]. Further, numerical simulations on composite armour fabricated with Al_2O_3 or SiC as front ceramic layer and a backing material comprising of high strength steel showed that, SiC ceramics exhibited better ballistic resistance when subjected to ballistic tests with 7.62x54 mm AP projectiles of velocity 850 m/s. It was reported that, the ceramics effectively dissipated the kinetic energy of the impact [9]. Numerical simulation and experimental ballistic studies have been performed on ceramic-aluminium targets using a blunt projectile at a velocity of 700 m/s. The behavior of the ceramic and projectile/target were modeled using the Johnson-Holmquist structural model and Johnson-Cook material model, respectively. The comparison of penetration depth of the projectile, indicated a good agreement between the simulation and experimental investigations with an error of approximately 10 percent [10]. Simulation of impact using tungsten alloy projectiles has been conducted on SiC plates shielded with three metals namely Al alloy, mild steel and Cu alloy at a velocity of 1250 m/s. In the simulation, Johnson-Cook model was adopted for the metals and Johnson-Holmquist model was utilized for the ceramic phase. The residual penetration was estimated using the difference in pre and post penetration weight of the armour. The error in DoP between the simulation and experimental results ranged from 4 to 25 percent for the three shield materials [11]. IPCs have also been produced by pressureless infiltration of an Al-8Mg alloy into Al_2O_3 foams in two configurations namely, 'metal-bonded' and 'ceramic bonded'. The metal-bonded configuration in which Al backing plates were used for the IPC, showed better resistance to penetration when subjected to 7.62 mm AP projectiles [12]. Comparative impact studies have been conducted on interpenetrating 316L/A356 composites and its constituents using an aluminium projectile of mass 10 mg. The shielding performance was evaluated at hypervelocities of 6000 m/s. The study revealed that, the IPC exhibited the least deformation of 0.3 mm and no indication of spalling [13]. Non-linear FE models have been utilized to simulate impact behaviour of reinforced composites. Experimental ballistic tests were performed at velocities of 360 m/s with impact energies of 520 J. The FE simulations of the impact absorption and failures concurred with experimental observations on deformation behaviour with insignificant error [14].

The literature survey reveals that, many researchers have focussed on FE simulation of ballistic impact in reinforced composites or Al/SiC as discrete constituents. In contrast, the present work compares the ballistic performance and numerical simulation results of a C4 consisting of an interpenetrating network of ballistic grade AA5083 in SiC porous foam fabricated using pressureless (gravity) infiltration technique [15].

2. MATERIALS AND METHODS

2. 1. Fabrication of Composite The SiC foam was initially shaped to ϕ 100 mm and thickness, 15 mm in order to be accommodated in the crucible. A crucible containing the weighed, segmented pieces of AA5083 was placed in an induction furnace. The furnace was set to 800º C, above the liquidus temperature of Al alloy. Simultaneously, the ceramic foam was placed inside another furnace for pre-heating. Subsequent to complete melting of alloy, the molten liquid was poured into the ceramic foam and allowed to infiltrate for one hour under gravity [15]. Graphite rod was used to hold the SiC foam in position.

On complete infiltration, the melt was allowed to solidify in furnace atmosphere. During solidification, the Al alloy penetrates into the pores of the SiC foam, forming the C4 as shown in Figure 1. The composite was machined out by a series of parting and milling process.

2. 2. Property assessment of C4 The mechanical properties of the fabricated C4 were obtained through various tests. The testing methods and standards utilized are tabulated in Table 1.

2. 3. Ballistic Testing of C4 Ballistic test was conducted on the fabricated C4 of dimensions ϕ 100 x 15 mm using a projectile from a Walther GSP Expert LR target pistol possessing a 0.22 caliber barrel. The projectile used was a steel core bullet, topped with a lead cap as shown in Figure 2. The projectile was fired from a distance of 10 m. The weight of a bullet was 40 grain with a rated velocity of 1070 fps (326 m/s), categorized as subsonic, medium velocity in ballistic testing.

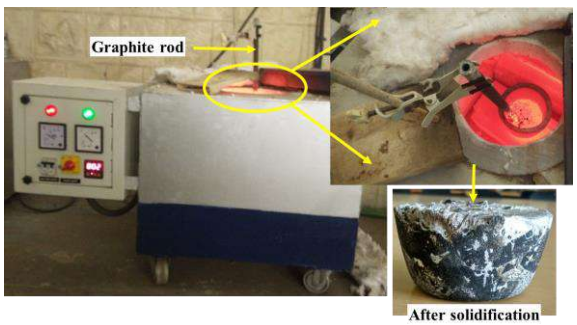

Figure 1. Induction furnace depicting infiltration and solidified composite

TABLE 1. Properties assessed and standards utilized

S.No	Property	Specimen dimension	Testing Method	Standards
1	Volume fraction	-	Water displacement	Archimedes Principle
2	Hardness	1 in^3	Brinell hardness tester	ASTM E10
3	Compression	1 in^3	Universal testing machine	ASTM D695
4	Toughness	55 ×10 × 10 mm^3	Charpy impact test	ASTM A370

Figure 2. The target pistol and projectile

3. RESULTS AND DISCUSSION

3. 1. Numerical Analysis of Ballistic Test The objective of this numerical simulation is to estimate the DoP of the medium velocity projectile into the composite. Towards this, the interpenetrating network of C4 was approximated as a cube and modelled using Autodesk Inventor as shown in Figure 3. This assembled geometry was imported into ANSYS Workbench.

The material properties of the metal/ceramic phases and C4 were appended to the ANSYS library as detailed in Table 2. The results of the assessed properties of the C4 are presented in Table 3. The property assessments are performed based on the testing methods outlined in Table 1.

TABLE 2. Properties of constituent elements

Property	Unit	AA5083	SiC
Density	g/cm^3	2.85	3
Young's Modulus	MPa	73100	2.76
Poisson Ratio	-	0.33	0.14
Bulk Modulus	Pa	7.166E+09	1.277E+09
Shear Modulus	Pa	2.748E+09	1.210E+09
Tensile Yield Strength	MPa	215	14
Tensile Ultimate Strength	MPa	320	240

TABLE 3. Assessed properties of C4

S.No	Property	Result
1	Volume fraction	AA5083=75%, SiC=25%
2	Hardness	91 BHN
3	Compression	588 MPa
4	Toughness	17 J

This numerical model was approximated as a static structure and was meshed with an element size of 1 mm. Fixed supports were modelled on all the faces of the cube except on one face. Since the DoP is directly proportional to the impact kinetic energy [16], the impact force of the medium velocity projectile was modelled on this face, in accordance with Equation (1).

$$F = \frac{Kinetic\ Energy\ of\ bullet}{Distance\ to\ target} = \frac{\frac{1}{2}*m*v^2}{d} \quad (1)$$

where, m and v refer to the mass and velocity of the bullet, respectively. The term 'd' denotes the distance to be travelled by the bullet for impact.

This impact force of the projectile was applied to the numerical model and the analysis revealed that, the maximum DoP of the projectile into the composite was 1.47 mm as shown in Figure 4.

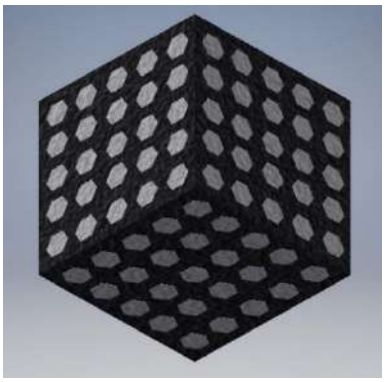

Figure 3. 3D model of interpenetrating C4

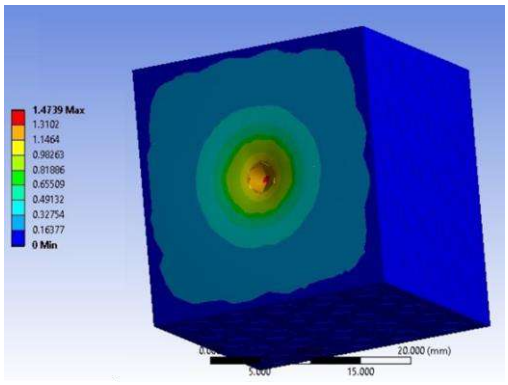

Figure 4. Maximum deformation from ANSYS

3. 2. Inference from Ballistic Test In order to validate the simulation, ballistic tests were performed. Figure 5 shows the C4 composite before and after projectile impact. Though fragmentation of the C4 was not observed, it exhibited brittle fracture with cracks initating at the impact site and progressing radially outward. Further, secondary cracks were detected at the interface of Al/SiC in the vincity of impact site, suggesting the occurrence of debonding at the interface [17]. The maximum DoP and the diameter of the crater produced due to projectile impact were ascertained as 1.5 mm and 9 mm, respectively. This indicates that, the fabricated C4 of AA5083/SiC can be used to defeat medium velocity projectiles with assured conformance.

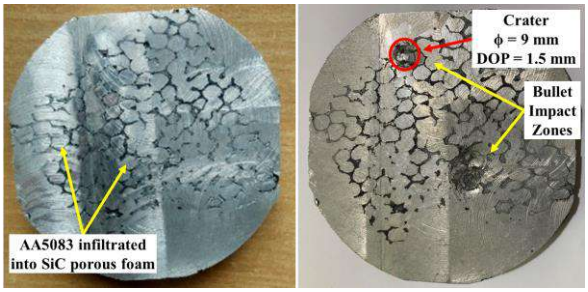

Figure 5. C4 before and after impact

4. CONCLUSION

In this study, a C4 composite was fabricated with AA5083 and SiC as the metal and ceramic phases. Tests to assess its suitability for body armour were performed by means of numerical simulation and practical ballistic tests using a subsonic projectile. The values of DoP of both the tests were proximate to each other. Additionally, brittle fracture and debonding along the interface were observed on the C4. Further tests under high strain rate conditions utilizing AP projectiles at high velocity regimes can be explored in order to assess the suitability of AA5083/SiC C4 composites as affordable alternatives for body armour.

5. ACKNOWLEDGEMENT

The authors would like to express their gratitude to Coimbatore Rifle Club for their support in ballistic testing of the composite.

6. REFERENCES

1. Jiang, L., Jiang, Y. L., Yu, L., Su, N. and Ding, Y. D., "Experimental study and numerical analysis on dry friction and wear performance of co-continuous SiC/Fe-40Cr against SiC/2618 Al alloy composites", ***Transactions of Nonferrous Metals Society of China***, Vol. 22, No. 12, (2012), 2913-2924. DOI: 10.1016/S1003-6326(11)61550-1
2. Wang, Q., Zhang, H., Cai, H., Fan, Q., Li, G. and Mu, X., "Simulation analysis of co-continuous ceramic composite dynamic mechanical performance and optimization design", ***Computational Materials Science***, Vol. 129, (2017), 123-128. DOI: 10.1016/j.commatsci.2016.12.009
3. Daehn, G. S. and Breslin, M. C., "Co-continuous composite materials for friction and braking applications", ***The Journal of The Minerals, Metals and Materials Society***, Vol. 58, No. 11, (2006), 87-91. DOI: 10.1007/s11837-006-0235-1
4. Nong, X. D., Jiang, Y. L., Fang, M., Yu, L. and Liu, C. Y., "Numerical analysis of novel SiC 3D/Al alloy co-continuous composites ventilated brake disc", ***International Journal of Heat and Mass Transfer***, Vol. 108, (2017), 1374-1382. DOI: 10.1016/j.ijheatmasstransfer.2016.11.108
5. Fathya, A., Wagiha, M., Abd El-Hamida, M. and Hassan, A.A., "Effect of Mechanical Milling on the Morphology and Structural Evaluation of Al-Al_2O_3 Nanocomposite Powders", ***International Journal of Engineering, Transactions A: Basics***, Vol. 27, No. 4, (2014), 625-632. DOI:10.5829/idosi.ije.2014.27.04a.14
6. Munasir, N., Triwikantoro, T., Zainuri, M., Bäßler, R. and Darminto, D., "Corrosion Polarization Behavior of Al-SiO_2 Composites in 1M and Related Microstructural Analysis", ***International Journal of Engineering, Transactions A: Basics***, Vol. 32, No. 7, (2019), 982-990. DOI: 10.5829/ije.2019.32.07a.11
7. Gurgen S.,"A Numerical Investigation on Oblique Projectile Impact Behavior of AA5083-H116 Plates", ***Politeknik Dergisi***, Vol. 22, No. 2, (2019), 293-301. DOI: 10.2339/politeknik.403994
8. Kaufmann, C., Cronin, D., Worswick, M., Pageau, G. and Beth, A., "Influence of material properties on the ballistic performance of ceramics for personal body armour", ***Shock and Vibration***, Vol. 10, No. 1, (2003), 51-58. DOI: 10.1155/2003/357637
9. Chabera, P., Boczkowska, A., Morka, A., Kędzierski, P., Niezgoda,T., Oziębło, A. and Witek, A., "Comparison of numerical and experimental study of armour system based on alumina and silicon carbide ceramics", ***Bulletin of the Polish Academy of Sciences***, Vol. 63, No. 2, (2015), 363-367. DOI: 10.1515/bpasts-2015-0040
10. Moslemi Petrudi, A., Vahedi, K., Kamyab, M.H. and Petrudi, M., "Numerical and experimental study of oblique penetration of a blunt projectile into ceramic-aluminum target", ***Modares Mechanical Engineering,*** Vol. 19, No. 5, (2019), 1253-1263.
11. Luo, D., Wang, Y., Wang, F., Cheng, H., Zhang, B. and Zhu, Y., "The influence of metal cover plates on ballistic performance of silicon carbide subjected to large-scale tungsten projectile", ***Materials and Design,*** (2020), 108659. DOI:10.1016/j.matdes.2020.108659
12. Chang, H., Binner, J., Higginson, R., Myers, P., Webb, P. and King, G., "Preparation and characterisation of ceramic-faced metal-ceramic interpenetrating composites for impact applications", ***Journal of Materials Science***, Vol. 46, No. 15, (2011), 5237–5244. DOI:10.1007/s10853-011-5461-4
13. Poole, L.L., Gonzales, M., French, M.R., Yarberry III, W.A., Moustafa, A.R. and Cordero, Z.C., "Hypervelocity impact of PrintCast 316L/A356 composites", ***International Journal of Impact Engineering,*** Vol. 136, (2020), 103407. DOI:10.1016/j.ijimpeng.2019.103407
14. Signetti, S., Bosia, F., Ryu, S. and Pugno, N.M., "A combined experimental/numerical study on the scaling of impact strength and toughness in composite laminates for ballistic applications", ***Composites Part B: Engineering,*** (2020), 108090. DOI:10.1016/j.compositesb.2020.108090

15. Prasanth, A.S. and Ramesh, R., "Investigation of Surface Roughness and Tool Wear in End Milling of Al7075-SiC Co-continuous Composite", in Materials Design and Applications, ***Advanced Structured Materials***, Vol. 65, (2017), 315-327. DOI:10.1007/978-3-319-50784-2_24

16. Basyir, A., Bura, R. O. and Lesmana, D., "Experimental consideration of projectile density and hardness effect on its penetration ability in alumina target", ***Journal of Defense Acquisition and Technology***, Vol. 1, No. 1, (2019), 9-15. DOI:10.33530/jdaat.2019.1.1.9

17. Rollings, L., Mcdonald, S., Roy, M. and Withers, P., "An investigation into the interface behaviour of an aluminium/silicon carbide fibre metal matrix composite", European Conference on Spacecraft Structures, Noordwijk, Netherlands, (2018).

Persian Abstract

چکیده

کامپوزیت های سرامیکی همزمان با هم ، که از آن به C4 یاد می شود ، دارای مراحل دو جداره ، بهم پیوسته و متقابل انتقال فلز و سرامیک هستند. این امر باعث می شود چنین کامپوزیت هایی با نسبت استحکام به وزن نسبت به کامپوزیت های سنتی بیشتر باشند. در این کار تحقیقاتی ، یک کامپوزیت C4 از AA5083 / SiC با استفاده از تکنیک نفوذ گرانش برای زره های بدن شخصی ساخته شده است. یک مدل شبیه سازی عددی از نمونه C4 تهیه شده است. این مدل المان محدود برای شبیه سازی DoP یک گلوله فرعی به C4 استفاده می شود و ۱.٤٧ میلی متر تخمین زده می شود. نمونه C4 سپس در معرض آزمایش های بالستیک قرار می گیرد. یک پرتابه با سرعت متوسط ۳۲٦ متر بر ثانیه برای تأثیرگذاری بر نمونه C4 استفاده می شود. آزمایش های بالستیک شبیه سازی عددی را با DoP 1.5 میلی متر اعتبار می دهد. بازرسی بصری ترک های شکننده و جداسازی سطحی در C4 تحت تأثیر را نشان می دهد. نتایج نشان می دهد که ، چنین کامپوزیت ها به طور بالقوه می توانند به عنوان زره بدن کم هزینه استفاده شوند.

International Journal of Engineering

Journal Homepage: www.ije.ir

Particle Swarm Optimization Based Parameter Identification Applied to a Target Tracker Robot with Flexible Joint

M. H. Sangdani, A. R. Tavakolpour-Saleh*

Department of Mechanical and Aerospace Engineering, Shiraz University of Technology, Shiraz, Iran

PAPER INFO

Paper history:
Received 31 March 2020
Received in revised form 25 April 2020
Accepted 12 June 2020

Keywords:
Flexible Joint
Parameter Identification
Particle Swarm Algorithm
Target Tracker Robot

ABSTRACT

This paper focuses on parameter identification of a target tracker robot possessing flexible joints using particle swarm optimization (PSO) algorithm. Since, belt and pulley mechanisms are known as flexible joints in robotic systems, their elastic behavior affecting a tracker robot is investigated in this work. First, dynamic equations governing the robot behavior are extracted taking into account the effects of considered flexible joints. Thus, a flexible joint is modeled by a non-linear spring and damper system connecting the motor to the link. It is found that the governing dynamic equations include some unknown parameters, which must be identified in order to design the robot system. Consequently, a PSO-based identification scheme is proposed to achieve the unknown variables based on the experimental data of the open-loop system. Lastly, for validating the proposed identification scheme, the obtained results are compared to the experimental measurements as well as the results of another similar work in which the robot is modeled with rigid joints. The consequences reveal that the mathematical model of the robot with flexible joint can describe the elastic behavior of the tracker robot. Thus, a better agreement between the simulation and experimental data are found in comparison with outcomes of the robot model with rigid joints.

***doi**: 10.5829/ije.2020.33.09c.14*

1. INTRODUCTION

One of the most widely used methods for power transmission in the robots is the belt and pulley system called the flexible joint. Flexible joints have several advantages compared to rigid joints such as lower cost, light weight, smaller dimension, and better maneuverability. Considering the flexibility of the joints in the robot model provides a more accurate prediction, which results in a better performance of the robot controller. For an *n*-link robot, 2*n* generalized coordinates are needed to describe the overall dynamic behavior when the joints are considered flexible. Accordingly, modeling a robot with flexible joints is more complex than the rigid joints. Researchers utilized different configuration for modeling the flexible joints. A linear spring is the simplest model that is employed for a flexible joint [1–4]. Chaoui et al. [5] modeled a flexible joint with a spring associated with the friction of motors. Furthermore, the dynamic equations of electric motors can be taken into account in the modeling of robots with flexible joints [6]. To achieve more accurate modeling the flexible joints can be modeled by a pair of spring and damper [7]. Moberg and Hanssen [8] used a model consisting of a pair of spring and damper along with the friction of motor. Indeed, there are various types of dampers. In this regard, Daniel et al. [9] conducted a comprehensive review work on magnetorheological fluid and dampers. Moberg [10] proposed a complete model for a robot with a flexible joint that included the coupling of links and motors. Another issue that has a significant effect on the systems and controllers performance, is the estimated value of parameters versus their real values. Therefore, accurately estimating the value of parameters is an important issue. Wu et al. [11] conducted a review on

*Corresponding Author Institutional Email: *tavakolpour@sutech.ac.ir* (A. R. Tavakolpour-Saleh)

Please cite this article as: M. H. Sangdani, A. R. Tavakolpour-Saleh, Particle Swarm Optimization Based Parameter Identification Applied to a Target Tracker Robot with Flexible Joint, International Journal of Engineering (IJE), IJE TRANSACTIONS C: Aspects Vol. 33, No. 9, (September 2020) 1797-1802

the estimation of the parameters of parallel and series robots. Accordingly, they categorized the identification methods into two parts, i.e. traditional and intelligence methods. The traditional parameters estimation methods include the least-squares method, the maximum probability method, and so on. Because of simplicity in concept and deployment, the least square method is a common method for parameter estimation. In [12–14], the least-square method is used for parameter estimation of a linear system and an electromechanical system with one-degree of freedom. Maximum likelihood is another method for parameter estimation, which is an important method for system identification and has been used in many works [14, 15]. However, in complex nonlinear systems, traditional methods do not provide accurate and effective results. Hence, intelligent algorithms such as particle swarm algorithm, genetic algorithm, ant colony algorithm, and so on are usually used to estimate parameters of complex systems. Particle swarm optimization and genetic algorithm are the most well-known optimization algorithm and many works can be found in which the PSO and GA are compared [16]. Correspondingly, because of the benefits of the PSO, this algorithm is adopted to use in this work. Eberhart and Shi [17] performed a complete study on the particle swarm algorithm and its performance. Particle swarm optimization can be used in different applications such as identifications of magnetorheological fluid dampers [18], chaotic dynamic systems [19], permanent magnet synchronous motors [20], and enhancing the performance of a nonlinear free piston Stirling engine [21]. Another intelligent algorithms like genetic [22–24], gray wolf [25], ant colony [26], and bee colony [27] algorithms can also be employed for identification purpose each of which contains some advantages and drawbacks.

The flexible joints have different behavior compared to the rigid joints, so when a robot is equipped with the flexible joints (e.g. belt and pulley mechanism), it would be better to consider the dynamics of flexible joints in the overall dynamic model of the robotic system. Consequently, this paper is devoted to study a 2-degree-of-freedom target tracker robot equipped with the flexible joints. Thus, an identification scheme based on PSO is applied to an open-loop test rig in order to obtain a more accurate model of the prototype robot. Firstly, the dynamic equation of the target tracker robot with the flexible joint is presented in Section 2. Next, Section 3 describes the parameter identification process of the mathematical model of the robot based on the PSO algorithm. The particle swarm algorithm and the procedure of collecting data are explained in this section respectively. Afterwards, the results of parameter identification and model validation are discussed in Section 4. Finally, the main conclusions of this research work are given in Section 5.

2. ROBOT DYNAMICS

In this section, first, the configuration of a flexible joint is described and the dynamic equations of a flexible joint are extracted. Then, the working principle of the prototype robot is explained and the dynamic equations of the robot with rigid joints are presented. Finally, the section ends up with the extraction of the dynamic equations of the tracker robot with the flexible joint by combining the dynamic equations of the tracker robot with the flexible joint dynamics.

2. 1. Dynamic of Flexible Joint Figure 1 shows the general structure of a simple robot with a flexible joint. The links are considered rigid and the motors are connected to the links elastically. If the flexible joint is considered as a pair of linear spring and damper, the dynamic equations of the robot will be obtained as Equation (1) and (2):

$$I_a\ddot{q}_a + C(q_a,\dot{q}_a)\dot{q}_a + g(q_a) = T_{spring} + T_{damper} \quad (1)$$

$$I_m\ddot{q}_m + B\dot{q}_m + f(\dot{q}_m) + \frac{1}{r}T_{spring} + \frac{1}{r}T_{damper} = T \quad (2)$$

where the link and motor angular positions are indicated as $q_a \epsilon \Re^N$ and $q_m \epsilon \Re^N$, respectively. $I_a \epsilon \Re^{N\times N}$ and $I_m \epsilon \Re^{N\times N}$ are the inertia matrix of the link and the motor. $C(q_a,\dot{q}_a)\epsilon\Re^N$ denotes the Coriolis matrix, $B\ \epsilon\Re^{N\times N}$ is the motor damping matrix and $g(q_a)\epsilon\Re^N$ the gravitational acceleration vector. A vector of friction torques is introduced for this model and is shown by $f(\dot{q}_m)\epsilon\Re^N$. r is the joint reduction ratio and the control input $T\epsilon\Re^N$ used as the torque input at each motor. $T_{spring}\epsilon\Re^N$ and $T_{damper}\epsilon\Re^N$ are also the torque vector of the spring and the damper respectively.

2. 2. Target Tracker Robot Dynamics The target tracker robot consists of a barrel and a base resulting in a 2-DOF dynamic system. The base and the barrel rotations are done in such a way to track a target in the horizontal and vertical directions, respectively. The dynamic equations of the robot without considering the flexibility of joints can be writte as Equations (3)

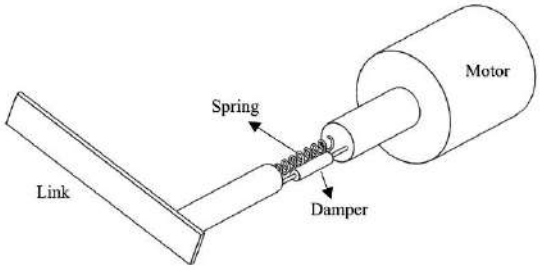

Figure 1. General structure of flexible joint

and (4) ([28]):

$$T_{Base} = (J_\theta + (m+\acute{m})R^2 - (m+2\acute{m}u)R\cos\alpha + J_\alpha \cos^2\alpha)\ddot{\theta} + ((ml+2\acute{m}u)R\dot{\alpha}\sin\alpha - -2J_\alpha\dot{\alpha}\cos\alpha\sin\alpha + b_\theta)\dot{\theta} \quad (3)$$

$$T_{Barrel} = J_\alpha\ddot{\alpha} - \left(\frac{1}{2}(ml+2\acute{m}u)R\sin\alpha - J_\alpha\cos\alpha\sin\alpha\right)\dot{\theta}^2 + b_\alpha\dot{\alpha} + mg\frac{l}{2}\cos\alpha + \acute{m}gu\cos\alpha \quad (4)$$

2. 3. Dynamics of Target Tracker Robot with Flexible Joints The target tracker robot is designed as shown in Figure 2 according to the required performance.

In this prototype robot, the belt and pulley mechanism is used for power transmission from the motors to the base and the barrel. In this study, the belt and pulley system is considered as a flexible joint and is modeled by a pair of nonlinear spring and linear damper.

The nonlinear behavior of the power transmission system (i.e. belt and pulley) can have a great impact on the robot performance. For this reason, the models of springs and friction are considered nonlinear. The following nonlinear equations are chosen as the friction model [9].

$$f_\theta(\dot{\theta}_m) = f_{v\theta}\dot{\theta}_m + f_{c\theta}\,sign(\dot{\theta}_m) \quad (5)$$

$$f_\alpha(\dot{\alpha}_\alpha) = f_{v\alpha}\dot{\theta}_\alpha + f_{c\alpha}\,sign(\dot{\theta}_\alpha) \quad (6)$$

In these equations, f_v is viscous friction and f_c is the Coulomb friction. As mention earlier, the flexible joint is modeled as a nonlinear spring and a linear damper. Therefore, the springs and the dampers connected to the base and the barrel are modeled as:

$$T_{spring-\theta} = K_{\theta1}\left(\frac{\theta_m}{r}-\theta\right) + K_{\theta2}\left(\frac{\theta_m}{r}-\theta\right)^3 \quad (7)$$

$$T_{spring-\alpha} = K_{\alpha1}\left(\frac{\alpha_m}{r}-\alpha\right) + K_{\alpha2}\left(\frac{\alpha_m}{r}-\alpha\right)^3 \quad (8)$$

$$T_{damper-\theta} = C_\theta\left(\frac{\dot{\theta}_m}{r}-\dot{\theta}\right) \quad (9)$$

$$T_{damper-\alpha} = C_\alpha\left(\frac{\dot{\theta}_\alpha}{r}-\dot{\alpha}\right) \quad (10)$$

Figure 2. 3-D solid model of the considered target tracker robot

$$(J_\theta + (m+\acute{m})R^2 - (ml+2\acute{m}u)R\cos\alpha + J_\alpha\cos^2\alpha)\ddot{\theta} + ((ml+2\acute{m}u)R\dot{\alpha}\sin\alpha - 2J_\alpha\dot{\alpha}\cos\alpha\sin\alpha + b_\theta)\dot{\theta} = K_{\theta1}\left(\frac{\theta_m}{r}-\theta\right) + K_{\theta2}\left(\frac{\theta_m}{r}-\theta\right)^3 + C_\theta\left(\frac{\dot{\theta}_m}{r}-\dot{\theta}\right) \quad (11)$$

$$J_{m\theta}\ddot{\theta}_m + B_{m\theta}\dot{\theta}_m + f_{v\theta}\dot{\theta}_m + f_{c\theta}\,sign(\dot{\theta}_m + \frac{1}{r}K_{\theta1}\left(\frac{\theta_m}{r}-\theta\right) + \frac{1}{r}K_{\theta2}\left(\frac{\theta_m}{r}-\theta\right)^3) + \frac{1}{r}C_\theta\left(\frac{\dot{\theta}_m}{r}-\dot{\theta}\right) = T_{Base} \quad (12)$$

$$J_\alpha\ddot{\alpha} - \left(\frac{1}{2}(ml+2\acute{m}u)R\sin\alpha - J_\alpha\cos\alpha\sin\alpha\right)\dot{\theta}^2 + b_\alpha\dot{\alpha} + mg\frac{l}{2}\cos\alpha + \acute{m}gu\cos\alpha = K_{\alpha1}\left(\frac{\alpha_m}{r}-\alpha\right) + K_{\alpha2}\left(\frac{\alpha_m}{r}-\alpha\right)^3 + C_\alpha\left(\frac{\dot{\theta}_\alpha}{r}-\dot{\alpha}\right) \quad (13)$$

$$J_{m\alpha}\ddot{\alpha}_m + B_{m\alpha}\dot{\theta}_m + f_{v\alpha}\dot{\theta}_m + f_{c\alpha}\,sign(\dot{\theta}_m) + \frac{1}{r}K_{\alpha1}\left(\frac{\alpha_m}{r}-\alpha\right) + \frac{1}{r}K_{\alpha2}\left(\frac{\alpha_m}{r}-\alpha\right)^3 + \frac{1}{r}C_\alpha\left(\frac{\dot{\theta}_\alpha}{r}-\dot{\alpha}\right) = T_{Barrel} \quad (14)$$

The dynamic equations of the robot is obtained as Equations (11)-(14) by rewriting Equations (3) and (4) based on Equations (1) and (2) and combining them with Equations (5) - (10). As can be seen, there are some coefficients that there values are unknown. Thus, in the next section, a PSO-based identification scheme is presented for estimating them. At last, it is worth noting that Equations (11) and (12) are for the base and Equations (13) and (14) are for the barrel.

3. PARAMETER IDENTIFICATION SCHEME

The algorithm used for parameter identification in this study is the PSO algorithm. In this part, the parameter identification procedure is described within both experimental and simulation environments. Finally, it is accomplished with the introduction of an appropriate cost function for the PSO algorithm.

The parameter identification is implemented via some open-loop tests on both the mathematical model of the robot and the developed robot (Figure 3) in the laboratory. First, the open-loop test is done on the experimental rig so that the experimental robot is excited by an input signal (see [29]) and the experimental dynamic response (i.e. the output angles of the base and the barrel) of the robotic system is captured. Next, the open-loop test is carried out using the mathematical model of the robot. Therefore, the mathematical model of the robot is simulated in MATLAB/Simulink based on the Equations (11) - (14) and the input voltage is applied to the mathematical model of the robot and the dynamic response of the robot model is captured. Afterward, for the best

matching of the experimental and the simulation results (the output angles of the base and the barrel), the PSO algorithm is utilized for the calculation of the unknown parameters.

According to the designed procedure for parameters identification, the PSO algorithm is used to minimize the error between the angles of the base and the barrel in the experimental and simulation environments. Consequently, the proposed cost function is considered in this paper to meet the demand of this work.

$$J = \sum_{i=1}^{n}(|e_{\theta}^{i}| + |e_{\alpha}^{i}|) \quad (15)$$

where e_{θ}^{i} is the error between simulation and experimental results of *i*-th data for the base, and e_{α}^{i} is the error between simulation and experimental results of *i*-th data for the barrel. *n* represents the number of data used for parameter identification.

4. RESULTS AND DISCUSSION

In this section, the results are presented and the performance of the proposed method is evaluated. For a better assessment, the results are compared to another similar work ([29]) done on the prototype robot with rigid joint. In the beginning, the experimental results for the base and the barrel sections were respectively measured and depicted in Figures 4 and 5.

Figure 3. Experimental model of the target tracker robot

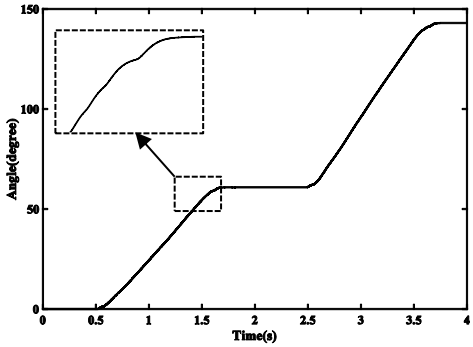

Figure 4. The base angle in experimental test

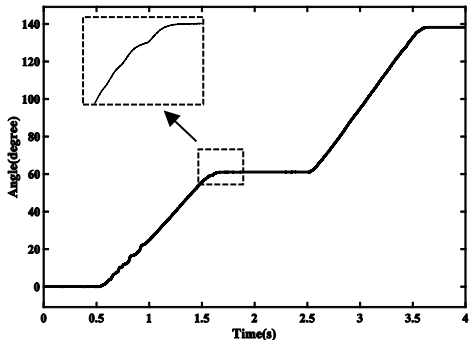

Figure 5. The barrel angle in experimental test

According to the specified area in Figures 4 and 5, an elastic behavior can be observed in the robot. Indeed, this elastic behavior can be attributed to the existence of a flexible joint. That is why the paper has been focused on the flexible joints applied to the target tracker robot.

As discussed earlier, the target tracker robot is modeled by Equations (11) - (14) assuming that the joints are flexible (they modeled by a pair of nonlinear spring and linear damper). According to Equations (11) -(14), there are some unknown coefficients and in the previous section, a procedure was proposed to reach their values. Correspondingly, the unknown parameters are found by using the PSO toolbox in MATLAB, such that the proposed objective function is minimized. At last, the optimal values of considered parameters are acquired and given in Table 1.

TABLE 1. Values of unknown dynamic parameters

Parameter	Value	Parameter	Value	Parameter	Value
J_{θ}	0.095(kg m^2)	$K_{\theta 1}$	91.66(N.m/rad)	$B_{m\theta}$	0.0039(N.m.s/rad)
J_{α}	0.0254(kg m^2)	$K_{\theta 2}$	-261.30(N.m/rad^3)	$B_{m\alpha}$	0.0053(N.m.s/rad)
$J_{m\theta}$	0.0074(kg m^2)	$K_{\alpha 1}$	105.62(N.m/rad)	$f_{v\theta}$	0.1358(N.m.s/rad)
$J_{m\alpha}$	0.0136(kg m^2)	$K_{\alpha 2}$	-183.90(N.m/rad^3)	$f_{c\theta}$	0.1158(N.m)
b_{θ}	0.2598(N.m.s/rad)	C_{θ}	0.0016(N.m.s/rad)	$f_{v\alpha}$	0.1123(N.m.s/rad)
b_{α}	0.01504(N.m.s/rad)	C_{α}	0.0259(N.m.s/rad)	$f_{v\alpha}$	0.0653(N.m)

For validating the results, the dynamic response of the mathematical model of the robot with the flexible joints is compared to the dynamic response of the experimental robot and the dynamic response of the mathematical model of the robot with the rigid joints that done previously in another work. Figures 6 and 7 show this comparison respectively for the base and the barrel.

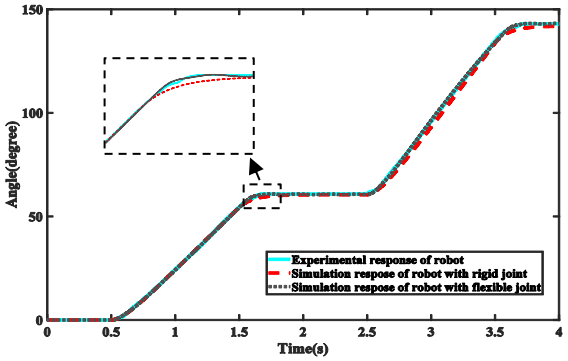

Figure 6. Comparison among simulation response of the robot with rigid and flexible joints and the experimental response (for the base angle)

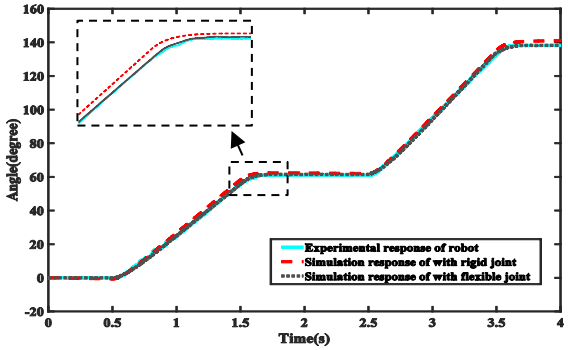

Figure 7. Comparison among simulation response of the robot with rigid and flexible joints and the experimental response (for the barrel angle)

5. CONCLUSION

The paper studied the joints flexibility in a target tracker robot and proposed a procedure for parameter identification of the prototype robot. Based on the experimental test, it was found that the joints had elastic behavior due to the employment of the belt and pulley mechanism as the power transmission system. After obtaining the dynamic equations governing the robot system it was found that some coefficients (inertia and damping coefficients, spring stiffness, viscous friction, Coulomb friction, …) were unknown. Hence, a PSO-based identification scheme is proposed to estimate these parameters. The proposed method contained an open-loop test in both experimental and simulation platforms for collecting data and the particle swarm algorithm was used for obtaining the optimum values of unknown parameters as the first objective of the paper. After achieving the values of unknown parameters, the open-loop simulation results matched well with the experimental data in which the elastic behavior of the robot joint was seen. At the end, validating the obtained results was carried out by comparing the outcomes with the experimental data and the results of another similar work, in which the robot had been modeled with rigid joints. The consequences showed that the mathematical model of the robot with flexible joints possessed a better convergence to the experimental outcomes than that of the robot with rigid joints and thus, the second aim of the paper was fulfilled. Future works will be directed towards the designing of a control system for the prototype robot with the identified dynamic equations in this study to cope with the robot nonlinearities.

6. ACKNOWLEGEMENT

The authors would like to thank the Shiraz University of Technology for providing research facilities and supports.

7. REFERENCES

1. Wang, H., and Xia, X. P. “Simulation of manipulator with flexible joint.” ***Applied Mechanics and Materials***, Vol. 327, (2013), 999–1003. https://doi.org/10.4028/www.scientific.net/AMM.325-326.999
2. Spong, M. W. “Modeling and control of elastic joint robots.” ***Journal of Dynamic Systems, Measurement and Control, Transactions of the ASME***, Vol. 109, No. 4, (1987), 310–319. https://doi.org/10.1115/1.3143860
3. Zhang, D. G., and Angeles, J. “Impact dynamics of flexible-joint robots.” ***Computers and Structures***, Vol. 83, No. 1, (2005), 25–33. https://doi.org/10.1016/j.compstruc.2004.08.006
4. Ettefagh, M. H., Naraghi, M., and Towhidkhah, F. “Position Control of a Flexible Joint via Explicit Model Predictive Control: An Experimental Implementation.” ***Emerging Science Journal***, Vol. 3, No. 3, (2019), 146–156. https://doi.org/10.28991/esj-2019-01177
5. Chaoui, H., Gueaieb, W., Biglarbegian, M., and Yagoub, M. “Computationally Efficient Adaptive Type-2 Fuzzy Control of Flexible-Joint Manipulators.” ***Robotics***, Vol. 2, No. 2, (2013), 66–91. https://doi.org/10.3390/robotics2020066
6. Yoo, S. J., Park, J. B., and Choi, Y. H. “Adaptive dynamic surface control of flexible-joint robots using self-recurrent wavelet neural networks.” ***IEEE Transactions on Systems, Man, and Cybernetics, Part B: Cybernetics***, Vol. 36, No. 6, (2006), 1342–1355. https://doi.org/10.1109/TSMCB.2006.875869
7. Nanos, K., and Papadopoulos, E. G. “On the dynamics and control of flexible joint space manipulators.” ***Control Engineering Practice***, Vol. 45, , (2015), 230–243. https://doi.org/10.1016/j.conengprac.2015.06.009

8. Moberg, S., and Hanssen, S. "Inverse Dynamics of Robot Manipulators Using Extended Flexible Joint Models." In Conference on Multibody Dynamics, Warsaw, Poland. Retrieved from https://www.diva-portal.org/smash/record.jsf?pid=diva2%3A370555&dswid=-6085
9. Cruze, D., G, H., Jebadurai, S. V. S., L, S., D, T., and Christy, S. S. J. E. "A Review on the Magnetorheological Fluid, Damper and Its Applications for Seismic Mitigation." ***Civil Engineering Journal***, Vol. 4, No. 12, (2018), 3074. https://doi.org/10.28991/cej-03091220
10. Moberg, S. Modeling and parameter estimation of robot manipulators using extended flexible joint models, Doctoral thesis, Linköping University Electronic Press, (2010).
11. Wu, J., Wang, J., and You, Z. "An overview of dynamic parameter identification of robots." ***Robotics and Computer-Integrated Manufacturing***. Vol. 26, No.5, (2010), 414-419. https://doi.org/10.1016/j.rcim.2010.03.013
12. Gu, Y., and Ding, R. "A least squares identification algorithm for a state space model with multi-state delays." ***Applied Mathematics Letters***, Vol. 26, No. 7, (2013), 748–753. https://doi.org/10.1016/j.aml.2013.02.005
13. Brunot, M., Janot, A., Carrillo, F., Garnier, H., Vandanjon, P. O., and Gautier, M. "Physical parameter identification of a one-degree-of-freedom electromechanical system operating in closed loop." ***IFAC-PapersOnLine***, Vol. 48, No. 28, (2015), 823–828. https://doi.org/10.1016/j.ifacol.2015.12.231
14. Wang, W., Ding, F., and Dai, J. "Maximum likelihood least squares identification for systems with autoregressive moving average noise." ***Applied Mathematical Modelling***, Vol. 36, No. 5, (2012), 1842–1853. https://doi.org/10.1016/j.apm.2011.07.083
15. El-Kafafy, M., Peeters, B., Guillaume, P., and De Troyer, T. "Constrained maximum likelihood modal parameter identification applied to structural dynamics." ***Mechanical Systems and Signal Processing***, Vol. 72–73, (2016), 567–589. https://doi.org/10.1016/j.ymssp.2015.10.030
16. Hashemi, S. M., and Rahmani, I. "Numerical Comparison of the Performance of Genetic Algorithm and Particle Swarm Optimization in Excavations." ***Civil Engineering Journal***, Vol. 4, No. 9, (2018), 2186. https://doi.org/10.28991/cej-03091149
17. Eberhart, R. C., and Shi, Y. "Particle swarm optimization: Developments, applications and resources." In Proceedings of the IEEE Conference on Evolutionary Computation, ICEC (Vol. 1, pp. 81–86). https://doi.org/10.1109/cec.2001.934374
18. Kwok, N. M., Ha, Q. P., Nguyen, T. H., Li, J., and Samali, B. "A novel hysteretic model for magnetorheological fluid dampers and parameter identification using particle swarm optimization." ***Sensors and Actuators, A: Physical***, Vol. 132, No. 2, (2006), 441–451. https://doi.org/10.1016/j.sna.2006.03.015
19. Modares, H., Alfi, A., and Fateh, M. M. "Parameter identification of chaotic dynamic systems through an improved particle swarm optimization." ***Expert Systems with Applications***, Vol. 37, No. 5, (2010), 3714–3720. https://doi.org/10.1016/j.eswa.2009.11.054
20. Liu, L., Liu, W., and Cartes, D. A. "Particle swarm optimization-based parameter identification applied to permanent magnet synchronous motors." ***Engineering Applications of Artificial Intelligence***, Vol. 21, No. 7, (2008), 1092–1100. https://doi.org/10.1016/j.engappai.2007.10.002
21. Zare, S., and Tavakolpour-Saleh, A. R. "Applying Particle Swarm Optimization to Study the Effect of Dominant Poles Places on Performance of a Free Piston Stirling Engine." ***Arabian Journal for Science and Engineering***, Vol. 44, No. 6, (2019), 5657–5669. https://doi.org/10.1007/s13369-018-3677-1
22. Tavakolpour, A. R., Mat Darus, I. Z., Tokhi, O., and Mailah, M. "Genetic algorithm-based identification of transfer function parameters for a rectangular flexible plate system." ***Engineering Applications of Artificial Intelligence***, Vol. 23, No. 8, (2010), 1388–1397. https://doi.org/10.1016/j.engappai.2010.01.005
23. Zare, S., and Tavakolpour-Saleh, A. R. "Frequency-based design of a free piston Stirling engine using genetic algorithm." ***Energy***, Vol. 109, (2016), 466–480. https://doi.org/10.1016/j.energy.2016.04.119
24. Zare, S., Tavakolpour-Saleh, A. R., and Sangdani, M. H. "Investigating limit cycle in a free piston Stirling engine using describing function technique and genetic algorithm." ***Energy Conversion and Management***, Vol. 210, (2020), 112706. https://doi.org/10.1016/j.enconman.2020.112706
25. Tavakolpour-Saleh, A. R., Zare, S. H., and Badjian, H. "Multi-objective Optimization of Stirling Heat Engine Using Gray Wolf Optimization Algorithm." ***International Journal of Engineering, Transactions C: Aspects*** , Vol. 30, No. 6, (2017), 895–903. https://doi.org/10.5829/ije.2017.30.06c.10
26. Sitarz, P., and Powałka, B. "Modal parameters estimation using ant colony optimisation algorithm." ***Mechanical Systems and Signal Processing***, Vol. 76–77, (2016), 531–554. https://doi.org/10.1016/j.ymssp.2016.01.013
27. Ding, L., Wu, H., Yao, Y., and Yang, Y. "Dynamic Model Identification for 6-DOF Industrial Robots." ***Journal of Robotics***, Vol. 2015, (2015), 1–9. https://doi.org/10.1155/2015/471478
28. Sangdani, M. H., Tavakolpour-Saleh, A. R., and Lotfavar, A. "Genetic algorithm-based optimal computed torque control of a vision-based tracker robot: Simulation and experiment." ***Engineering Applications of Artificial Intelligence***, Vol. 67, (2018), 24–38. https://doi.org/10.1016/j.engappai.2017.09.014
29. Sangdani, M. H., and Tavakolpour-Saleh, A. R. "Robot Using Genetic Algorithm." ***International Journal of Engineering, Transactions C: Aspects***, Vol. 31, No. 3, (2018), 480–486. https://doi.org/10.5829/ije.2018.31.03c.11

Persian Abstract

چکیده

این مقاله به شناسایی پارامترهای یک ربات ردیاب هدف مجهز به اتصالات انعطاف‌پذیر به‌وسیله‌ی الگوریتم گروه ذرات می‌پردازد. با توجه به این که مکانیزم‌های تسمه و پولی در سیستم‌های رباتیکی به عنوان مفاصل انعطاف‌پذیر شناخته می‌شوند، در این مطالعه، تاثیر رفتار کش‌سان این نوع مفاصل بر ربات ردیاب بررسی می‌شود. ابتدا، معادلات دینامیکی ربات با توجه به مفاصل انعطاف‌پذیر استخراج شده‌اند. بدین گونه که یک مفصل منعطف به صورت یک سیستم فنر غیرخطی و دمپر مدل شده است که موتور را به لینک متصل کرده است. بعد از استخراج معادلات دنیامیکی، مشخص شد که تعدادی پارامتر نامشخص وجود دارد که برای طراحی سیستم ربات باید شناسایی شوند. در نتیجه، یک روش برای شناسایی پارامترها برپایه الگوریتم گروه ذرات پیشنهاد شده است. در این روش از داده‌های آزمایشگاهی در تست حلقه‌باز سیستم استفاده می‌شود. در نهایت برای اعتبارسنجی روش پیشنهاد شده، نتایج به دست آمده با نتایج آزمایشگاهی و نتایج یک کار مشابه دیگر که در آن مفاصل صلب در نظر گرفته شده‌اند، مقایسه می‌شوند. نتایج به دست آمده نشان می‌دهند که مدل ریاضی ربات که در آن مفاصل انعطاف‌پذیر در نظر گرفته شده‌اند می‌تواند رفتار کش‌سان ربات ردیاب را توصیف کند. پس، در مقایسه با نتایج به دست آمده از مدل ربات با مفاصل صلب، هم‌گرایی خوبی بین داده‌های شبیه‌سازی و آزمایشگاهی حاصل شده است.

International Journal of Engineering

Journal Homepage: www.ije.ir

Modeling and Optimization of Mechanical Properties of PA6/NBR/Graphene Nanocomposite Using Central Composite Design

M. R. Nakhaei*[a], G. Naderi[b]

[a] *Faculty of Mechanics and Energy, Shahid Beheshti University, Tehran, Iran*
[b] *Iran Polymer and Petrochemical Institute, Tehran, Iran*

PAPER INFO

Paper history:
Received 05 April 2020
Received in revised form 23 April 2020
Accepted 12 June 2020

Keywords:
Central Composite Design
Mechanical Properties
Nanocomposite
PA6/NBR/Graphene
Thermal Properties

ABSTRACT

Thermoplastic elastomer of PA6/NBR reinforced by various nanoparticles have wide application in many industries. The properties of these materials depend on PA6, NBR, and nanoparticle amount and characteristics. In this study, the simultaneous effect of NBR and graphene nanoparticle content on mechanical, thermal properties, and morphology of PA6/NBR/Graphene nanocomposites investigated by Central Composite Design (CCD). Thermal properties and morphology of PA6/NBR/Graphene nanocomposites were investigated by Differential Scanning Calorimetry (DSC), X-Ray Diffraction (XRD), and Scanning Electron Microscopy (SEM). The results indicate that a small percentage of error between predicted values of mechanical properties and experimental values was achieved. An increase in graphene content have a positive impact on the tensile strength but increasing the NBR phase has the opposite effect. A maximum tensile strength of 35.3 MPa for PA6/NBR/Graphene nanocomposites was obtained at the NBR and graphene content of 20 %wt and 1.5 %wt, respectively. The thermal behavior of the PA6/NBR blend improved with addition graphene. With the addition of 1.5 % graphene content to PA6/NBR blend, the crystallization temperature and melting temperature increased from 192.1 to 196.2 °C and 221.1 to 223.4 °C, respectively.

***doi**: 10.5829/ije.2020.33.09c.15*

1. INTRODUCTION

Polyamide 6 (PA6) as one of engineering thermoplastics have wide application in various industries such as automobile, aerospace, and shipbuilding due to its chemical and wear resistance, stiffness, excellent strength properties, low friction and high melting points [1, 2]. The properties of PA6 can be enhanced by mixing with fillers and rubber material such as ethylene-propylene-diene monomer (EPDM), poly (epichlorohydrin -co-ethylene oxide) (ECO) and nitrile butadiene rubber (NBR) [3]. Blending PA6 and NBR leads to thermoplastic elastomer (TPE) material with better toughness. In research conducted by Fagundes et al. [3], the mechanical and morphology of PA6/NBR blend (vulcanize and unvulcanize) as influenced by sulfur content was investigated. They concluded that the mechanical performance of PA6/NBR vulcanizes blends depends on the curing system and morphologies. In addition, the blends of PA6/NBR have good resistance to non-polar solvents. Nakhaei et al. [4] also studied the dynamic crosslinking of PA6/NBR thermoplastic elastomer. The results show that the curing system and dynamic crosslinking in thermoplastic elastomer blends increases the torque which, causes more improvement in mixing. In addition, cured blends have higher tensile strength, elongation, and hardness compared to uncured blends, while cured blends have lower modulus and swelling. The addition of very low content of nanofillers such as nanoclay, carbon nanotube, and graphene enhances mechanical, thermal, and barrier properties dramatically [5, 6]. TPE and TPV nanocomposites are widely consumed in many industries such as automotive, airplane, and ship parts. The effectiveness of nanoparticles such as nanoclay, carbon nanotube, and graphene strongly depends on the uniform dispersion in

*Corresponding Author Institutional Email: *m_nakhaei@sbu.ac.ir* (M. R. Nakhaei)

Please cite this article as: M. R. Nakhaei, G. Naderi, Modeling and Optimization of Mechanical Properties of PA6/NBR/Graphene Nanocomposite Using Central Composite Design, International Journal of Engineering (IJE), IJE TRANSACTIONS C: Aspects Vol. 33, No. 9, (September 2020) 1803-1810

the base material [7]. The rheological and morphological properties of PA6/ECO nanocomposites reinforced by 6 % nanoclay was studied by Taghizadeh et al. [8]. They concluded that the increase in ECO content from 0 to 40 % wt increased the melt yield stress from 500 to 22000 Pa. Paran et al. [9] conducted experiments on the PA6/NBR/HNT nanocomposites. The results show that by adding the NBR phase to the PA6 matrix, the impact strength of both unfilled and HNT filled with these materials increased by 22% and 41%, respectively. The crystallization temperature of base material increased with the addition of HNTs, whereas the increase in NBR content decreased this property.

Graphene nanoparticles (2-10nm) consist of many graphene sheets stacked, which, due to platelet morphology, have high tensile strength (130 ± 10 GPa), high aspect ratio (width-to-thickness) and high young's modulus (~1 TPa). This nanoparticle has much application in conductive rubbers and plastics, thermal polymer composites, and also as a filler to improve tensile strength, abrasion resistance, corrosion resistance, stiffness, and lubricant properties [10]. Reviews of previous literature show that many reports on the TPEs nanocomposites, but no studies regarding the effect of graphene on the microstructure, mechanical and thermal properties on PA6/NBR have been reported. In this study, the mechanical properties of PA6/NBR/Graphene nanocomposites were investigated using Response Surface Methodology (RSM). The central composite design with two factors (NBR and graphene) and five levels was applied for developing a mathematical model that is capable of predicting mechanical properties such as impact strength and tensile strength. Thermal properties and morphology of PA6/NBR/Graphene nanocomposites were investigated by Differential Scanning Calorimetry (DSC), X-Ray Diffraction (XRD), and Scanning Electron Microscopy (SEM). Figure 1 shows the flow chart of the research methodology.

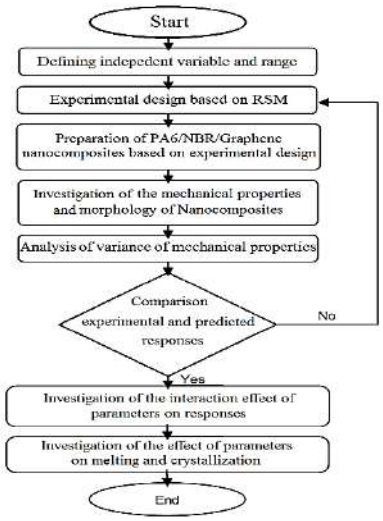

Figure 1. Flow chart of the research methodology

2. MATERIALS AND METHODS

2. 1. Materials The grade name, company, and basic specifications of materials in this study are shown in Table 1.

TABLE 1. List of the materials and their characteristics

Material	Company	Grade name	Characteristics
PA6	Kolon plastics (Korea)	KOPA KN136	Density = 1.14 g/cm3 and MFI at 230°C, 2.16 kg = 3.14 g/10 min
NBR	Kumho polychem (Korea)	35L	Mooney viscosity ML (1+8 min) 100 °C = 41 M Acrylonitrile content 34 wt%, Density = 0.98 g/cm3
Graphene	XG Sciences	xGnP-C750	Thickness: 1 - 20 nm, Oxygen content (%): ~10, Lateral size (mm): 1-50, Specific Surface area (m2/g): 750

2. 2. Preparation The experiments were designed based on a two - factor five levels central composite design (CCD) with three replications. The input variable parameters are NBR and graphene content. Table 2 shows the level of input variables with their ranges and notations. The NBR and graphene content was varied between 10 wt% to 50 wt% and 0.1 wt% to 0.5 wt%, respectively. For the preparation of the PA6/NBR blend and their nanocomposites, PA6 granules and graphene were dried in a vacuum oven for 24 h and 80 °C. For the preparation of nanocomposites, melt-mixing was performed using an internal mixer (Brabender Plasti-Corder, Germany) with the roller blades, chamber volume 55 cm^3, fill factor 0.75, and rotor speed ratio of 2:3. TPO composite with various formulations (according to Table 3) was mixed at 220°C and 80 rpm for 7 min. After melt-mixing the materials, they were dried for about 12 hours at 80 °C in an oven. The suitable samples for mechanical tests and XRD analysis were prepared by the hot press (Collin P 200 E-type) at 230°C for 6 min.

TABLE 2. Parameters, their limits, and levels

Parameters	Notification	Levels				
		-2	-1	0	1	2
NBR (%)	N	10	20	30	40	50
Graphene (%)	G	0	0.5	1	1.5	2

TABLE 3. The formulations of prepared nanocomposites

Code	PA6 (%)	NBR (%)	GPN (%)	Tensile (MPa)	Impact (j/m)
PN0G0	100	0	0	79.0	66
PN30G1	69	30	1	62.5	86
PN40G0.5	59.5	40	0.5	54.2	125
PN50G1	49	50	1	55.1	145
PN30G1	69	30	1	62.4	87
PN30G2	68	30	2	64.0	82
PN30G1	69	30	1	62.7	87
PN30G1	69	30	1	62.4	86
PN30G1	69	30	1	62.6	88
PN30G0	70	30	0	53.3	95
PN20G0.5	79.5	20	0.5	66.1	75
PN40G1.5	58.5	40	1.5	62.3	100
PN10G1	89	10	1	71.0	63
PN20G1.5	78.5	20	1.5	68.5	68

2. 3. Characterization Impact and tensile strength specimens prepared according to ASTM D256 and D638 type I, respectively [11, 12]. Tensile properties of PA6/NBR/Graphene nanocomposites were performed at a cross-head speed of 1mm/min using a Zuker tensile test machine (Zwhck Co., Germany). The impact strength test was performed in a Zwick 4100 machine. At each experimental condition, which is presented in Table 3, three specimens were tested, and the average of three responses is reported in the same table.

The X-ray diffraction (XRD) of graphene and PA6/NBR nanocomposites was evaluated using a diffractometer (Philips X'Pert PRO, Netherlands) at a scan rate of 1◦/min. XRD data were collected using a diffractometer with 50 kV voltage and 40 mA current at room temperature.

The morphology of the specimens was examined using a VEGATESCAN scanning electron microscope. Cryofracture specimens were etched by acetone to extract the NBR phase. The size of the rubber particles was calculated as follows:

$$D_n = \frac{\sum N_i D_i}{\sum N_i} \quad (1)$$

where N_i and D_i are the numbers of particles and their diameters, respectively.

3. RESULTS

3. 1. XRD Analysis X-ray diffraction (XRD) patterns for graphene and the PN30G1 and PN30G2 nanocomposites illustrated in Figure 2. The diffraction patterns of graphene demonstrate a sharp peak at 2θ = 25.8°. According to Bragg's law ($d = \frac{\lambda}{2\sin\theta}$), the interlayer spacing of graphene is 3.45 A. For the PN30G2 and PN30G1 nanocomposite, the peak at 25.8° has shifted to 22.6° (3.93 A) and 18.55° (4.77 A), respectively. The lower angle of PN30G1, and PN30G2 nanocomposite compare to graphene show that the penetration of polymer chain into the graphene layers and better dispersion of graphene in the polymer matrix. For these nanocomposites, it can be seen the significant decrease in peak intensity. The decrease in peak intensity attributed to the exfoliation of graphene layers [12, 13]. This result is consistent with the previous study on PP/EPDM/graphene and elastomer/graphene nanocomposites [10, 13].

3. 2. Analysis of Variance (ANOVA) of Responses The objective of ANOVA is to determine the significance of model and process parameters in the factorial design technique. In RSM methods, Fisher's variance ratio (F-value) is the measure of variation in the data about the mean and estimated by the sum of square data (SS) [14, 15]. The highest F-value reveals a more signicant effect of the parameters on responses. The Design-Expert V7 Software was used to determining the best regression models that fits experimental data. The results of ANOVA tables of three responses (tables 4-6) show that the NBR was the most significant parameter affecting the tensile strength and impact strength of PA6/NBR/graphene nano-composites. According to ANOVA tables, when the P-value for molds is less than 0.05 (for 95% confidence level), it indicates that the parameters or model terms are significant on the response [14]. According to the theory of ANOVA and ANOVA tables for tensile strength and impact strength, it is seen that linear effects of NBR (N) and graphene (G) content and also the interaction effects of NBR and graphene (N×G) are significant for three responses. The quadratic effect of NBR (N^2) is significant on impact strength,

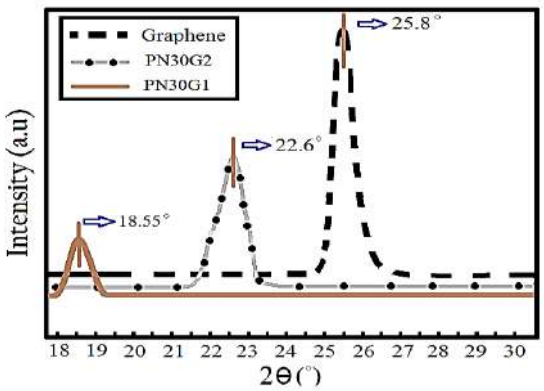

Figure 2. XRD curves of graphene, PN30G2, and PN30G1 nanocomposite

whereas the quadratic effect of graphene (G^2) is significant on tensile strength. In addition, the R^2, adjusted R^2, and predicted R^2 are shown these tables. It can be seen, in all the three responses, that the R^2 values are in reasonable agreement and are close to 1, which is desirable. The high values of adjusted R^2 and predicted R^2 in Tables 4 and 5 shows that the regression models have the great predictive ability.

TABLE 4. ANOVA for the tensile strength

Source	Sum of Squares	df	Mean Square	F-Value	p-value
Model	334.84	5	66.96	121.59	< 0.0001
NBR (N)	212.15	1	212.15	358.89	< 0.0001
Graphene (G)	88.02	1	88.02	159.83	< 0.0001
N×G	7.56	1	7.56	13.73	0.0076
G^2	22.36	1	22.36	40.61	0.0004
N^2	0.43	1	0.43	0.78	0.4060
Residual	3.86	7	0.55		
Lack of Fit	3.79	3	1.26	1.21	0.5703
R^2	0.989		Adj R^2		0.981
Pred R^2	0.913		Adeq Precision		36.37

TABLE 5. ANOVA for the Impact strength

Source	Sum of Squares	df	Mean Square	F-Value	P-value
Model	6416.39	5	1283.28	108.44	< 0.0001
NBR (N)	5808.01	1	5808.01	490.78	0.0018
Graphene (G)	280.33	1	280.33	23.69	< 0.0001
N×G	81.05	1	81.05	6.84	0.0010
G^2	5.83	1	5.83	0.49	0.5055
N^2	242.67	1	242.67	20.51	0.0286
Residual	82.84	7	11.83		
Lack of Fit	81.64	3	27.21	90.71	0.6628
R^2	0.983		Adj R^2		0.978
Pred R^2	0.876		Adeq Precision		37.65

From the discussion above, the final mathematical models to estimate tensile strength and impact strength of nanocomposites are represented in Equations (2) and (3).

In terms of actual factors

$$\textbf{\textit{Tensile strength}} = 45.53 + 5.07\times G - 0.778\times N + 0.275\times G\times N - 3.951\times G^2 \quad (2)$$

$$\textbf{\textit{Impact strength}} = 35.04 + 13.298\times G + 1.147\times N - 0.9\times G\times N + 0.032\times N^2 \quad (3)$$

3. 3. Confirmation Experiments To investigate the validity of the developed models, three confirmation experiments were performed under new test conditions. The experimental condition, the actual values of three responses, the predicted values, and the percentages of error are shown in Table 6. Based on Table 6, data corresponding to the confirmation experiments is in good agreement with experimental values [16].

3. 4. The Interaction Effect of Parameters on Mechanical Properties Figure 3 (a and b) is a perturbation plot that illustrates the main effects plot of NBR (N) and graphene (G) for tensile strength and impact strength of nanocomposites, respectively. With increasing graphene content, the tensile strength

TABLE 6. Comparison of actual and predicted responses

N	G	Tensile strength		Impact strength	
		Actual	70.5	Actual	74.1
20	**1**	Predict	67.1	Predict	70.2
		Error (%)	5.1	Error (%)	5.5
		Actual	63.9	Actual	95.2
30	**0.5**	Predict	59.3	Predict	91.6
		Error (%)	7.7	Error (%)	3.9
		Actual	55.8	Actual	105.5
40	**1**	Predict	58.6	Predict	111.1
		Error (%)	4.7	Error (%)	5.1

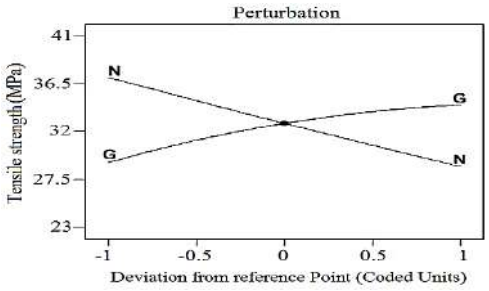

(a)

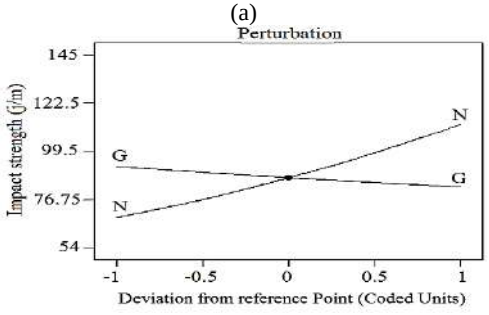

(b)

Figure 3. Perturbation plots showing the effect of all factors on (a) Tensile strength (b) Impact strength

increased while the impact strength of PA6/NBR nanocomposites reduces slightly with increasing the graphene content. The enhancing effect of graphene (G) on the tensile strength of PA6-based nanocomposites was also reported in other papers [17]. From Figure 3, it can also be observed that the tensile strength of nanocomposites decreased with an increase in NBR phase content which is related to the lower tensile strength of neat NBR, whereas increasing the HNT from 20 to 40 wt% leads to an increase in the impact strength from about 65 to 110 j/m. This phenomenon has also been reported in numerous other PP/elastomer nanocomposites and is due to the softening effect of an elastomeric phase like NBR on plastic-based nanocomposites [17, 18].

Figures 4 and 5 show the 3D response surface plots created by the applied software. The interaction effect between NBR and Graphene content on the tensile strength and impact strength are presented in Figures 4 and 5, respectively. Figure 4 (a and b) show that at low NBR content, the maximum tensile strength of the PA6/NBR/Graphene nanocomposites was obtained at the graphene content of 1.5%. This is related to the fact that the higher nanoparticle content in thermoplastic elastomers leads to decreased size of elastomer particles and consequently, an improvement in the mechanical properties. Haghnegahdar et al. [10] concluded that higher contents of nanographene decrease the size of the dispersed phase.

The average size of rubber particles of prepared PA6/NBR/Graphene nanocomposites was reported in Table 7. Figure 6 shows the cryofractured surfaces of PN30G0, and PN30G2 samples, and the dark holes represent the NBR phase by selectively etching in acetone. Comparing the two samples shows that very small rubber particles are obtained when using 2 %wt of graphene nanoparticle. According to Equation (1) and Figure 6, the size of the NBR phase was decreased from 3.24 to 0.85 µm with the addition of 2 %wt of graphene. Paran et al. [9] concluded that higher contents of halloysite nanotube decrease the size of the NBR phase in the PA6 matrix. They stated that this might be because the viscosity difference between matrix and rubber decreases by adding HNTs to PA6/NBR. The results of research by Haghnegahdar et al. [19] show that another possible effect may be the hindering role of graphene on the coalescence of rubber particles.

The best impact strength of the PA6/NBR/Graphene nanocomposite (122.25 j/m) is achieved at 40 wt% of NBR content and 0.5 wt% of graphene content, according to Figure 5. According to Figure 5, at the minimum amount of loading of NBR, the effect of graphene content on impact strength was not much. With the addition of nanoparticles to PA6/NBR, the size of elastomer decreased, which this behavior increases impact strength. On the other hand, nanoparticles act as stress concentration which leads to decreases impact strength. Previous results by some other researchers shows that the different effect of nanoparticles on the microstructure of thermoplastic elastomer is the reason for not changing the value of impact strength at a low level of NBR content [9, 11].

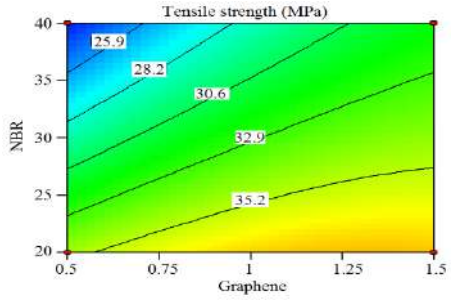

(a)

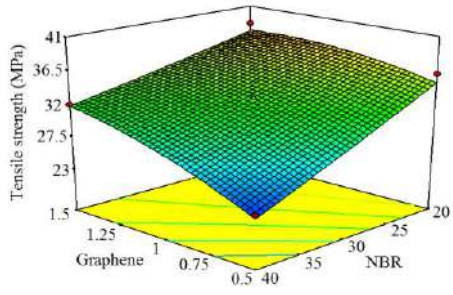

(b)

Figure 4. (a) Contours plots and (b) response surface diagram showing the effect of N and G on tensile strength

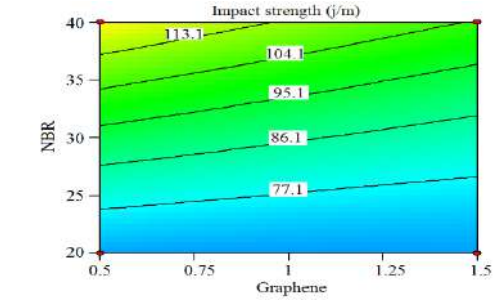

(a)

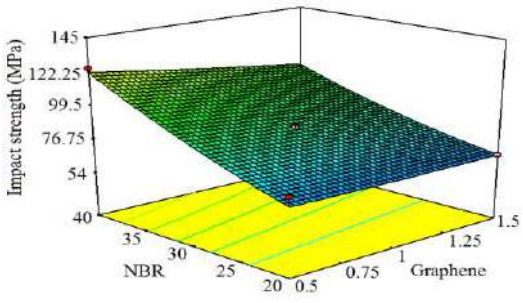

(b)

Figure 5. (a) Contours plots and (b) response surface diagram showing the effect of N and G on impact strength

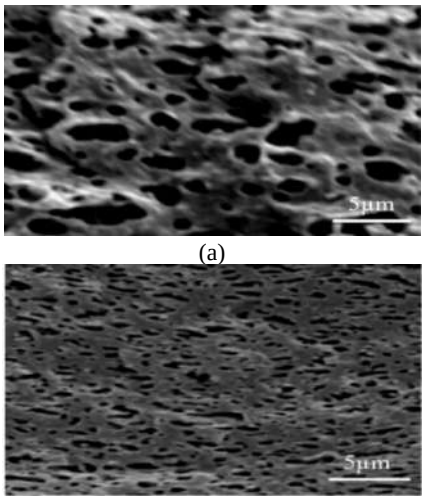

(a)

(b)

Figure 6. SEM micrograph of PA6/NBR/Graphene blend with (a) 0% (b) 2% Graphene content

TABLE 7. Rubber particle sizes of PA6/NBR nanocomposites prepared with graphene

	PN30G1	PN40G0.5	PN50G1	PN30G2
Rubber size (µm)	2.12	4.35	4.93	0.85
	PN30G0	PN20G0.5	PN40G1.5	PN20G1.5
	3.24	1.98	2.87	1.03

At the high level of NBR content, impact strength decreased with an increase in graphene content at 0.5 to 1.5 wt%. This behavior could be related to the weak compatibility and adhesion between NBR as the dispersed phase and PA6 as the continuous phase, especially at the high content of NBR [19].

The best impact strength of the PA6/NBR/Graphene nanocomposite (122.25 j/m) is achieved at 40 wt% of NBR content and 0.5 wt% of graphene content, according to Figure 5. At the minimum amount of loading of NBR, effect of graphene content on impact strength was not much. The different effect of nanoparticles on the microstructure of thermoplastic elastomer is the reason for not changing the value of impact strength at a low level of NBR content [20].

At the high level of NBR content, impact strength decreased with an increase in graphene content at 0.5 to 1.5 wt%. This behavior could be related to the weak compatibility and adhesion between NBR as the dispersed phase and PA6 as the continuous phase, especially at the high content of NBR [18].

3. 5. Effect of Parameters on Crystallization

Table 8 shows the melting and crystallization properties of PA6/NBR/Graphene nanocomposites. Delta H (ΔH) was obtained by DSC thermograms and the area under the peak. The crystallinity percent (χ) of these materials was calculated from Equation (4):

$$\chi\,(\%) = \frac{\Delta H}{\Delta H_m} \times 100 \quad (4)$$

TABLE 8. Melting and crystallization temperatures of PA6/NBR/Graphene nanocomposites

Code	ΔH_m (J/g)	X_c (%)	T_c (°C)	T_m (°C)
PN30G1	44.9	20.1	197.2	222.4
PN40G0.5	46.5	20.2	194.1	221.9
PN50G1	44.8	18.9	194.1	222.0
PN30G2	43.1	19.4	198.7	222.8
PN30G0	47.7	21.4	195.1	221.5
PN20G0.5	47.1	21.1	197.2	222.3
PN40G1.5	43.5	19.1	196.1	222.2
PN10G1	46.4	20.4	199.8	223.0
PN20G1.5	44.6	20.1	199.2	222.8

According to the results in Table 8, comparing ΔH, crystallinity percent, crystallization temperature and melting temperature of the samples PN30G0 and PN30G2 shows that the addition of graphene nanoparticle to the PA6/NBR blend led to decrease ΔH and crystallinity percent. At the same time, it increases the crystallization temperature and melting temperature. With addition of 2 wt% graphene content to PA6/NBR blend, the crystallization temperature, and melting temperature increased from 195.1 to 198.7 °C and 221.5 to 222.9 °C, respectively. This behavior attributed to the fact that graphene nanoparticles act as a nucleating agent and increase crystallization temperature [10]. The addition of graphene and rubber particles decreased size and increased the number of spherulites of PA6, which this behavior led to decreasing the percentage of crystallinity. According to Table 8, comparing the PN30G0 and PN30G2 and also PN10G1 and PN50G1 shows that the addition of 2% of graphene and 40% rubber content to PA6/NBR blends decreases the percentage of crystallinity from 21.4 to 19.4% and 20.4 to 18.9 %, respectively. These results were attributed to the effect of nanoparticle and rubber on the size of the spherulites of the PA6 matrix that these results consistent with the results of other researchers [19, 20].

4. CONCLUSION

In this study, the response surface methodology was used to examine the effects of NBR and graphene content on responses such as tensile strength and impact strength. Experiments were designed based on central composite design. The most important results are as follows:

1. The interlayer spacing of graphene in the nanocomposite with 1 wt% graphene compare to graphene was increased from 3.45 to 4.77A that this show the better dispersion of graphene in the polymer matrix.
2. The rubber particle size decreased from 3.24 to 0.85 µm when graphene content increased from 0 to 2 wt%.
3. At the high level of NBR content, impact strength decreased from 122.5 j/m to 98.3 j/m with an increase in graphene content at 0.5 to 1.5 wt%, while the tensile strength increased from 23.1 MPa to 32.2 MPa.
4. At low NBR content, the maximum tensile strength (36.5 MPa) and impact strength (76.8 j/m) of the PA6/NBR/Graphene nanocomposites was obtained at the graphene content of 1.5%.
5. The addition of graphene nanoparticle to the PA6/NBR blend led to decrease the crystallinity percent and Delta H.
6. With addition of 2% graphene content to PA6/NBR blend, the crystallization temperature, and melting temperature increased from 195.1 to 198.7 °C and 221.5 to 222.9 °C, respectively.

5. REFERENCES

1. Azdast, T., and Hasanzadeh, R. "Tensile and Morphological Properties of Microcellular Polymeric Nanocomposite Foams Reinforced with Multi-walled Carbon Nanotubes." ***International Journal of Engineering, Transactions C: Aspects***, Vol. 31, No. 3, (2018), 504–510. https://doi.org/10.5829/ije.2018.31.03c.14
2. Adejuyigbe, I. B., Chiadighikaobi, P. C., and Okpara, D. A. "Sustainability Comparison for Steel and Basalt Fiber Reinforcement, Landfills, Leachate Reservoirs and Multi-Functional Structure." ***Civil Engineering Journal***, Vol. 5, No. 1, (2019), 180. https://doi.org/10.28991/cej-2019-03091235
3. Fagundes, E. C. M., and Jacobi, M. A. M. "TPVs PA/NBR: Sistema de reticulação e propriedades." ***Polimeros***, Vol. 22, No. 2, (2012), 206–212. https://doi.org/10.1590/S0104-14282012005000021
4. Nakhaei, M. R., Mostafapour, A., and Naderi, G. "Optimization of mechanical properties of PP/EPDM/ clay nanocomposite fabricated by friction stir processing with response surface methodology and neural networks." ***Polymer Composites***, Vol. 38, (2017), E421–E432. https://doi.org/10.1002/pc.23942
5. Nakhaei, M. R., Mostafapour, A., Dubois, C., Naderi, G., and Reza Ghoreishy, M. H. "Study of morphology and mechanical properties of PP/EPDM/clay nanocomposites prepared using twin-screw extruder and friction stir process." ***Polymer Composites***, Vol. 40, No. 8, (2019), 3306–3314. https://doi.org/10.1002/pc.25188
6. Mosalman, S., Rashahmadi, S., and Hasanzadeh, R. "The Effect of TiO2 Nanoparticles on Mechanical Properties of Poly Methyl Methacrylate Nanocomposites." ***International Journal of Engineering, Transactions B: Applications***, Vol. 30, No. 5, (2017), 807–813. https://doi.org/10.5829/idosi.ije.2017.30.05b.22
7. Mostafapour, A., Naderi, G., and Nakhaei, M. R. "Effect of process parameters on fracture toughness of PP/EPDM/nanoclay nanocomposite fabricated by novel method of heat assisted Friction stir processing." ***Polymer Composites***, Vol. 39, No. 7, (2018), 2336–2346. https://doi.org/10.1002/pc.24214
8. Taghizadeh, E., Naderi, G., and Razavi-Nouri, M. "Effects of organoclay on the mechanical properties and microstructure of PA6/ECO blend." ***Polymer Testing***, Vol. 30, No. 3, (2011), 327–334. https://doi.org/10.1016/j.polymertesting.2011.01.007
9. Paran, S. M. R., Naderi, G., and Ghoreishy, M. H. R. "Microstructure and mechanical properties of thermoplastic elastomer nanocomposites based on PA6/NBR/HNT." ***Polymer Composites***, Vol. 38, (2017), E451–E461. https://doi.org/10.1002/pc.23936
10. Haghnegahdar, M., Naderi, G., and Ghoreishy, M. H. R. "Fracture toughness and deformation mechanism of un-vulcanized and dynamically vulcanized polypropylene/ethylene propylene diene monomer/graphene nanocomposites." ***Composites Science and Technology***, Vol. 141, (2017), 83–98. https://doi.org/10.1016/j.compscitech.2017.01.015
11. Nakhaei, M., Bani Mostafa Arab, N., and Rezaei, G. "Investigation on Tensile Strength of Friction Stir Welded Joints in PP/EPDM/Clay Nanocomposites." ***International Journal of Engineering, Transactions C: Aspects***, Vol. 28, No. 9, (2015), 1383–1391. https://doi.org/10.5829/idosi.ije.2015.28.09c.17
12. Bakhtiari, A., Ashenai Ghasemi, F., Naderi, G., and Nakhaei, M. R. "An approach to the optimization of mechanical properties of polypropylene/nitrile butadiene rubber/halloysite nanotube/polypropylene- <scp> *g* </scp> -maleic anhydride nanocomposites using response surface methodology." ***Polymer Composites***, Vol. 41, No. 6, (2020), 2330–2343. https://doi.org/10.1002/pc.25541
13. Berki, P., László, K., Tung, N. T., and Karger-Kocsis, J. "Natural rubber/graphene oxide nanocomposites via melt and latex compounding: Comparison at very low graphene oxide content." ***Journal of Reinforced Plastics and Composites***, Vol. 36, No. 11, (2017), 808–817. https://doi.org/10.1177/0731684417690929
14. Feng, X., Tufail, R. F., and Zahid, M. "Experimental Investigation and Statistical Modeling of FRP Confined RuC Using Response Surface Methodology." ***Civil Engineering Journal***, Vol. 5, No. 2, (2019), 268. https://doi.org/10.28991/cej-2019-03091243
15. Moradi, H. M., Zinatizadeh, A. A., and Zinadini, S. "Influence of Operating Variables on Performance of Nanofiltration Membrane for Dye Removal from Synthetic Wastewater Using Response Surface Methodology." ***International Journal of Engineering, Transactions C: Aspects***, Vol. 29, No. 12, (2016), 1650–1658. https://doi.org/10.5829/idosi.ije.2016.29.12c.03
16. Mostafapour, A., Akbari, A., and Nakhaei, M. R. "Application of response surface methodology for optimization of pulsating blank holder parameters in deep drawing process of Al 1050 rectangular parts." ***International Journal of Advanced Manufacturing Technology***, Vol. 91, No. 1–4, (2017), 731–737. https://doi.org/10.1007/s00170-016-9781-z
17. Tarawneh, M. A., Yu, L.-J., Al-Tarawni, M. A., and Ahmad, S. "High performance thermoplastic elastomer (TPE) nanocomposite based on graphene nanoplates (GNPs)." ***World Journal of Engineering***, Vol. 12, No. 5, (2015), 437–442. https://doi.org/10.1260/1708-5284.12.5.437
18. Asgarzadeh, Z., and Naderi, G. "Morphology and properties of unvulcanized and dynamically vulcanized PVC/NBR blend reinforced by graphene nanoplatelets." ***International Polymer Processing***, Vol. 33, No. 4, (2018), 497–505. https://doi.org/10.3139/217.3515
19. Haghnegahdar, M., Naderi, G., and Ghoreishy, M. H. R. "Microstructure and mechanical properties of nanocomposite based on polypropylene/ethylene propylene diene monomer/graphene." ***International Polymer Processing***, Vol. 32, No. 1, (2017), 72–83. https://doi.org/10.3139/217.3286
20. Hajibaba, A., Naderi, G., Esmizadeh, E., and Ghoreishy, M. H. R. "Morphology and dynamic-mechanical properties of PVC/NBR blends reinforced with two types of nanoparticles." ***Journal of Composite Materials***, Vol. 48, No. 2, (2014), 131–141. https://doi.org/10.1177/0021998312469242

Persian Abstract

چکیده

پلاستیک گرمانرم الاستومرهای تفویت شده با نانوذرات مختلف به صورت گسترده در صنایع مختلف کاربرد دارد. در این تحقیق، تاثیر هم‌زمان مقدار گسترده‌ای NBR و درصد نانوذرات بر روی خواص مکانیکی، حرارتی و ریزساختار نانوکامپوزیت‌های PA6/NBR/Graphene با طراحی مرکزی مرکب بررسی شده است. خواص حرارتی و ریز ساختار نانو کامپوزیت ها با استفاده از آزمون گرماسنجی تفاضلی روبشی (DSC)، پراش اشعه ایکس (XRD) و میکروسکوپ الکترونی روبشی (SEM) مورد بررسی قرار گرفت. نتایج نشان می دهد که درصد خطای کوچکی بین نتایج پیش بینی و نتایج تجربی به دست آمده است. افزایش مقدار گرافن تاثیر مثبت بر روی استحکام کششی دارد اما افزایش NBR تاثیر منفی دارد. ماکزیمم استحکام کششی ۳۵/۵ MPa برای PA6/NBR/Graphene هنگامی بدست خواهد آمد که مقدار NBR و گرافن به ترتیب ٪۲۰ و ۱/۵٪ است. رفتار حرارتی کامپوزیت PA6/NBR با افزودن گرافن بهبود خواهد یافت. با افزودن ۱/۵ ٪ گرافن به ترکیب PA6/NBR، دمای بلورینگی و دمای ذوب به ترتیب از ۱۹۲/۱ به ۱۹٦/۲ °C و از ۲۲۱/۱ به ۲۲۳/٤ °C درجه سانتی گراد افزایش یافت

International Journal of Engineering

Journal Homepage: www.ije.ir

Effect of Heat Input on Microstructural and Mechanical Properties of AISI 304 Welded Joint Via MIG Welding

S. A. Rizvi*

University Polytechnic, Jamia Millia Islamia,New Delhi, India

P A P E R I N F O

Paper history:
Received 29 April 2020
Received in revised form 02 August 2020
Accepted 05 August 2020

Keywords:
AISI 304
Fracture Mode
Heat Input
Microhardness
Microstructure
MIG Welding
SEM

A B S T R A C T

In this experimental work, AISI 304 was welded via metal inert gas (MIG) welding process with Argon (Ar) as shielding gas. In the present study, AISI 304 was subjected to different heat input using a standard 308L electrode. Weld quality i.e. ultimate tensile strength, toughness, microhardness, and microstructure of AISI 304 were examined. Microstructures of welded joints were studied using scanning electron microscopy (SEM), linked to the SEM was used to determine the chemical composition of phases formed at the joint interface and from the result, it was revealed that at low heat input ultimate tensile strength is higher than those at medium and low heat input. From the result, it was also observed that grain coarsening extent in the HAZ increases with an increase in the heat input. It was also found that the fractures of toughness samples were brittle in nature which shows the low ductility and brittle fracture. Weld zone microstructure exhibited skeletal δ-ferrite in austenite matrix with various ferrite contents. Microhardness of weld bead was found to decrease with increases in the heat input. It was also observed that at medium heat input there was an improvement in tensile strength, elongation, and hardness due to finer grain structure and smaller inter-dendritic spacing.

***doi**: 10.5829/ije.2020.33.09c.16*

NOMENCLATURE

HI	Heat input	ASS	Austenatic stainless steel
MIG	Metal inert gas	UTS	Ultimate tensile strength
V	Arc voltage	HAZ	Heat effected zone
I	Welding current	SEM	Scaning electron miroscope
S	Welding speed	TIG	Tungsten inert gas
AISI	Aremican Iron and steel institute	ASS	Austenatic stainless steel

1. INTRODUCTION

Manufacturing industries including automotive, railway, aerospace, shipbuilding, and petrochemical develop products ranging from simple to big in complex shapes. Conventionally, stainless steels are joined by metal inert gas welding, tungsten inert gas welding, friction stir welding etc. In MIG welding, the common variations of power supplies, shielding gases, and copper coated wire have significant effects resulting in a number of different and important process parameters [1]. MIG welding frequently accepted globally due to high productivity rate and spatter free quality [2]. AISI 304 is frequently used in structural industries for fabrication purpose as it is more economical and anti corrosion-resisting steels as compared to other steels. Stainless-steel sheets are increasingly used for boiler, vessels, pharmactical, aerospace, thermal power plant, kitchen, building, transportation, etc., because of their high corrosion resistivity, beautiful appearance, superior strength, toughness and low temperature toughness [3-5]. AISI 304 can be welded with several welding process such as MIG, TIG, friction, laser beam welding etc. Extensive stidies were carried out on the effect of heat input [6, 7] on the microstructure and mechanical properties of AISI 304 (Austenitic stainless steel). Hsieh et al. [8] reported that shielding gas using for welding

*Corresponding Author Email: *saritbhu@gmail.com* (S. A. Rizvi)

Please cite this article as: S. A. Rizvi, Effect of Heat Input on Microstructural and Mechanical Properties of AISI 304 Welded Joint Via MIG Welding, International Journal of Engineering (IJE), IJE TRANSACTIONS C: Aspects Vol. 33, No. 9, (September 2020) 1811-1816

purpose significantly promote the depth/width ratio of welded joint of SS204H by TIG welding whereas silicon and phosphorus have a least significant effect on the depth/width ratio. Saluja and Moeed [9] studied the effect of pulse-GMA welding process parameters on the hardness of AISI 304 steel and they reported in their result that cooling rate and alloying elements significantly vary micro-hardness. Heat input also play an important role in grain size of a weldment and grain size of the weldments increases with the increasing in the heat input [10]. Moradi et al. [11] developed a mathematical model to study the parameter dependencies in laser hybrid arc welding of high strength steel by design-of-experiment (DOE) and mass balance. Moradi et al. [12] studied the numerical and experimental geometrical dimensions on laser-TIG hybrid welding of stainless steel 1.4418. Khorram et al. [13] investigated the effect of linear haet input on bead geometery, microstructure and mechanical properties of Ti-6Al-4V sheet welded by CO_2 laser welding and it was observed from result that on increasing the linear heat input caused to change the martensistic phase from an acicular ferrite. The novelty of this research work is to investigate the effect of heat input on microstructure and mechanical properties of AISI 304 ASS on different heat input i.e. on six different values of heat input. it is also observed from previous studies that six different values of heat input were not considered.

2. EXPERIMENTAL DETAILS

2. 1. Work Piece Material AISI 304 is one of the most commonly used materials in manufacturing industries because it has better corrosion resistance and good weldability [14]. The parent metal used in this study was AISI 304 (ASS) in the plate form of 150x60x6 mm^3 size and welded by Metal inert gas (MIG) welding, with polarity of direct current electrode negative (DCEN) with ER308 electrode. Chemical composition of base metal, filler wire, mechanical properties, and MIG welding parameters of AISI 304 (ASS) are provided in Tables 1, 2 and 3, respectively. The actual welding set used in this process is shown in Figure 1.

For shielding purpose pure Agron (Ar) gas was used. Butt joints were successfully prepared in this study using selected welding process parameters and tensile test samples and toughness test samples were prepared as per ASTM. All essential care was considered during the welding process to avoid joints distortion by using proper clamping arrangement. Six weld coupons of various heat input with nealry equal interavls were sellected for investigation purpose. Welding parameters and samples designation are listed in Table 4.

TABLE 1. Chemical composition of parent metal and filler wire

Material	% of C	% of Cr	% of Ni	% of S	% of Mn	% of P	% of Si	Fe
Type AISI 304	0.065	18-20	8-10.5	0.015	1.25	0.025	0.48	Rest
Filler wire ER 308	0.035	18.5	8.5	0.04	1.55	0.02	---	

TABLE 2. Mechanical properties of base metal

Material	YS (MPa)	UTS (MPa)	% Elongation	Toughness (J)	Hardness (HV)
AISI 304	315	650	50	105	90

TABLE 3. Parameters used for MIG welding process to obtain various heat input condition

Welding current (A)	Arc Voltage (V)	Shielding gas flow rate (l/min)	Wire feed speed (IPM)
200	20	10	250

Figure 1. Actual set up for MIG welding

TABLE 4. Parameters used for MIG welding process to obtain various heat input condition

Sample No	Welding current (A)	Arc voltage (V)	Welding speed (mm/s)	Heat input (Kj/mm)
G2	160	20	1.464	2.18
G4	170	21	2.86	1.25
G10	175	22	1.411	2.73
G12	180	23	1.39	2.97
G15	188	24	1.38	3.27
G16	195	25	1.38	3.52

Welding heat input (HI) is defined as the product of arc voltage (V) and welding current (I) divided by welding speed (S) and methamatically is expressed as follows:

$$Q_{arc} = 60 \; X \; V \; X \; I/(S) \quad (1)$$

where V is the arc voltage (V), I is the arc current (A) and S is the welding speed in mm/min.

3. RESULT AND DISCUSSION

3. 1. Mechanical Properties For weld quality purpose, mechanical properties like ultimate tensile test, toughness test, and microhardness test were carried out. Tensile strength of a welded joint is too much influence in grain size of weldment [15]. Figure 2 shows the geometrical sketch of a tensile test sample used in this study and tensile test sample and toughness samples were fabricated as per ASTM. Effect of welding heat input on tensile strength and toughness of welded joints were investigated at different heat input and for each condition of heat input, three samples were conducted for tensile test and toughness test and the average value was recorded and presented in Figure 3. From Figure 3 it is very clear that at only 1.25 kJ/mm (low heat input) UTS and toughness increases while on increasing the heat input tensile strength (UTS) and toughness of weldment decreases [16]. It is only due to increasing the arc voltage and formation of δ-ferrite grains in the weld region.

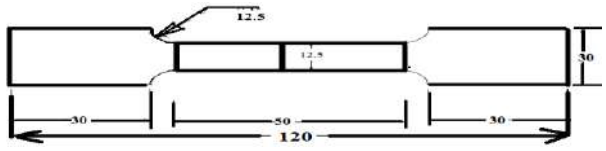

Figure 2. Geometrical sketch of a tensile test sample

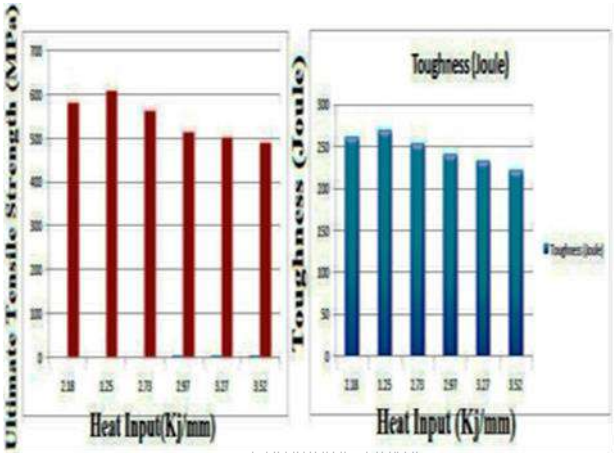

Figure 3. Effect of Parameters on Mechanical properties

3. 2. Microhardness Microhardness (HV) of various zones of weldments was measured by VHN testing machine. Figure 4 presents the microhardness of weldments at different heat input at different zones i.e. base metal zone (BM), heat affected zone (HAZ), and weld zone (WZ) or fusion zone measured in the longitudinal direction and the trends of curves are like "M" world which is very common and heat input influence the hardness of welded joint. It can be seen that the hardness distribution of weldments were similar, so taking heat input 2.73kJ/mm as an example to exhibit the microhardness variation in above-said each zone of weldments. From Figure 4 it is very clear that the hardness of weld zone is lower than HAZ, and parent metal zone (PM) [17]. Increasing in hardness is only due to the larger contents of δ-ferrite in the weld zone and finer grain size in the HAZ by increasing heat input [18]. From the previous research it is very clear that the presence of δ-ferrite in the weldment enhance the mechanical properties [19]. Hardness in HAZ is still higher than the parent metal (PM), this is only due to rapid cooling of weldment leads to refinement of the grains. On increasing the heat input overall value of hardness of weldment decreases; this is only due to lower the δ–ferrite contents lead to lowering the hardness value [20].

3. 3. Fractrography SEM fractogrph of toughness test samples at different heat inputs of various zone i.e. parent metal zone, HAZ, and weld zone (WZ) are shown in Figure 5. Figure 5 (a) shows the ductile fracture mode with several numbers of voids. It is due to different cooling rate. Brittle fracture is formed in fusion zone with dimple formed on the tearing ridges. High heat input requires more time to solidification hence responsible to produce the coarse or large dimple [21] as shown in Figure 5(c).

3. 4. Microstracture Microstructure examination of welded joints under different heat inputs values has been carried out by optical microscope and fartrography of toughness samples were studied by SEM. Weld zone

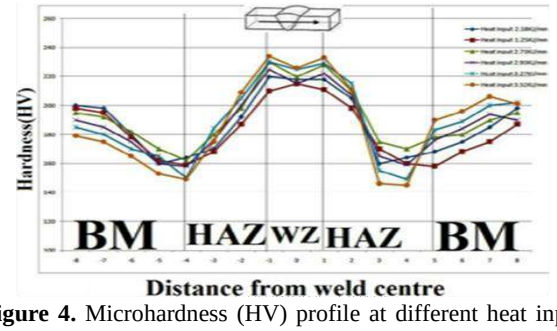

Figure 4. Microhardness (HV) profile at different heat input indicating hardness on weldment at various zones

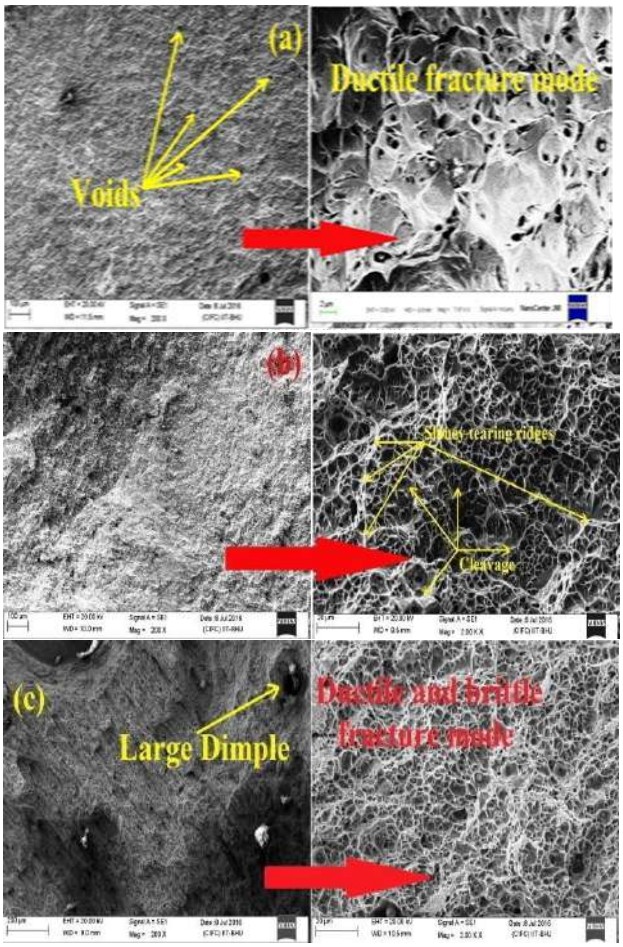

Figure 5. Macro image and SEM fracture of Toughness fracture surface of Base metal, HAZ, and Weld zone

attained the maximum temperature, which is just below the solidus temperature. Microstructures of welded joints are given below at different heat input. From Figure 6 it was observed that microstrucute of AISI 304 welments containing two micro-constituents, namely δ-ferrite (dark) and austenite (light). Figure 6 shows the variation of δ-ferrite morphology in the different zone and it is also observed from Figure 5 that three different kinds of δ-ferrite i.e. δ-ferrite, lathy, and skeletal ferrite (in weld zone has a wider spacing) are formed in the austenite matrix [22]. Figure 6 (b) G4 samples at low heat input leads to formation of finer dendrite size it is due to slow cooling [23, 24]. Figure 6 (d) sample G12 shows the fusion zone and fusion area increased with increase in heat input. Microstructure of weldments is significantly influence by heat input as voltage is a function of heat input [25]. From literature reviews it is very clear that heat input having major effect on microstructure of AISI
304 weldment [26, 27].

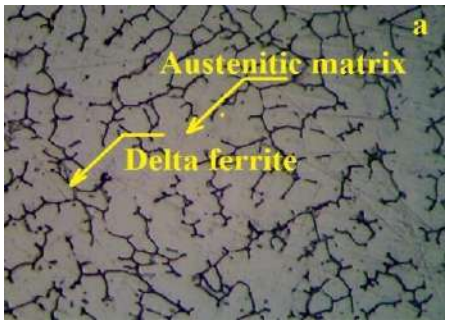

G2

G10

G4

G15

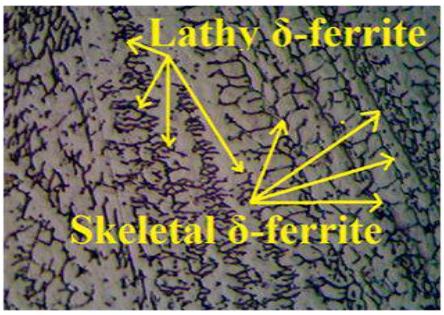

G12

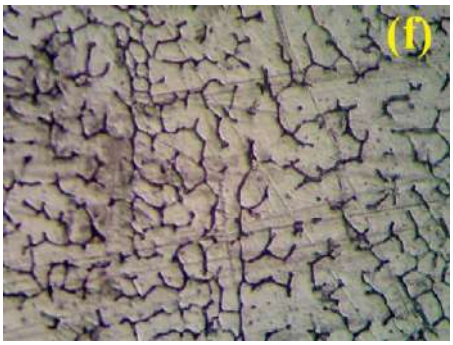

G16

Figure 6. Optical microstructures of the welded samples under pure Ar shielding with different heat input: weld metal structure welded at (a) 2.18 kJ/mm, (b) 1.25 kJ/mm, (c) 2.73 kJ/mm, (d) 2.97 kJ/mm, (e) 3.27 kJ/mm, and (f) 3.52 kJ/mm

4. CONCLUSSION

The following conclusion have been drawn from the present study:

- AISI 304 austenatic stainless steel (ASS) was successfully welded at different heat input by GMA welding without any observing any spatter proble.
- Heat input influence the mechanical and microstructural properties of weldments. At medium heat input weld was found best of quality.
- On increasing the heat input there is decrement in the UTS. It is due to the faster cooling rate
- Microstructure structure of AISI 304 weldment consisting of austenite matrix with little amount of δ-ferrite.
- Microhardness of weld bead decrease with increasing in the heat input.
- It was also observed that at medium heat input there is improvement in tensile strength, elongation, and hardness due to finer grain structure and smaller inter-dendritic spacing.
- In SEM fractrograph of welded joint ductile and brittle fracture mode was observed in toughness test samples with large dimples.
- Hardness of weld zone (WZ) is higher than the parent metal (PM) zone due to faster cooling and rapid heating.

5. REFERENCES

1. Handbook, W., "Fundamentals of welding", ***American Welding Society, Miami***, Vol. 1, (1976), 9-11.
2. Rizvi, S.A., "Advanced welding technology", Katson publishers, New Delhi, India, (2007), 48-49.
3. Takuda, H., Mori, K., Masachika, T., Yamazaki, E. and Watanabe, Y., "Finite element analysis of the formability of an austenitic stainless steel sheet in warm deep drawing", ***Journal of Materials Processing Technology***, Vol. 143, (2003), 242-248. DOI.10.1016/S0924-0136(03)00348-0
4. Viswanathan, R. and Bakker, W., "Materials for ultrasupercritical coal power plants—boiler materials: Part 1", ***Journal of Materials Engineering and Performance***, Vol. 10, No. 1, (2001), 81-95. https://doi.org/10.1361/105994901770345394
5. Lakshminarayanan, A., Shanmugam, K. and Balasubramanian, V., "Effect of autogenous arc welding processes on tensile and impact properties of ferritic stainless steel joints", ***Journal of Iron and Steel Research International***, Vol. 16, No. 1, (2009), 62-68. https://doi.org/10.1016/S1006-706X(09)60012-1
6. Abioye, T., "The effect of heat input on the mechanical and corrosion properties of aisi 304 electric arc weldments", ***Current Journal of Applied Science and Technology***, Vol. 20, No. 5, (2017), 1-10. DOI: 10.9734/BJAST/2017/32846
7. Saha, S., Mukherjee, M. and Pal, T.K., "Microstructure, texture, and mechanical property analysis of gas metal arc welded aisi 304 austenitic stainless steel", ***Journal of Materials Engineering and Performance***, Vol. 24, No. 3, (2015), 1125-1139. DOI:10.1007/s11665-014-1374-0
8. Hsieh, R.-I., Pan, Y.-T. and Liou, H.-Y., "The study of minor elements and shielding gas on penetration in tig welding of type 304 stainless steel", ***Journal of Materials Engineering and Performance***, Vol. 8, No. 1, (1999), 68-74. DOI:10.1361/105994999770347188
9. Saluja, R. And Moeed, K., "Effects of process parameters and alloying elements on micro-hardness distribution in pulse arc 304l austenitic stainless steel welded plates", ***Journal of Engineering Science and Technology***, Vol. 14, No. 4, (2019), 2271-2291.
10. Kurt, H.İ. and Samur, R., "Study on microstructure, tensile test and hardness 304 stainless steel jointed by tig welding", ***International Journal of Science and Technology***, Vol. 2, No. 2, (2013), 163-168.
11. Moradi, M., Salimi, N., Ghoreishi, M., Abdollahi, H., Shamsborhan, M., Frostevarg, J., Ilar, T. and Kaplan, A.F., "Parameter dependencies in laser hybrid arc welding by design of experiments and by a mass balance", ***Journal of Laser Applications***, Vol. 26, No. 2, (2014), 022004. http://dx.doi.org/10.2351/1.4866675
12. Moradi, M., Ghoreishi, M. and Rahmani, A., "Numerical and experimental study of geometrical dimensions on laser-tig hybrid welding of stainless steel 1.4418", ***Journal of Modern Processes in Manufacturing and Production***, Vol. 5, No. 2, (2016), 21-31.
13. Khorram, A., Jafari, A. and Moradi, M., "Effect of linear heat input on the morphology and mechanical properties of ti-6al-4v welded using a com 2 laser", ***Lasers in Engineering (Old City Publishing)***, Vol. 40, (2018).
14. Çaligülü, U., Dikbaş, H. And Taşkin, M., "Microstructural characteristic of dissimilar welded components (aisi 430 ferritic-aisi 304 austenitic stainless steels) by CO_2 laser beam welding (lbw)", ***Gazi University Journal of Science***, Vol. 25, No. 1, (2012), 35-51.
15. 15. Rizvi, S. A., Tewari, S. P.,, "Effect of different welding parameters on the mechanical and microstructural properties of stainless steel 304h welded joints", ***International Journal of Engineering*, *Transactions A: Basics,*** Vol. 30, No. 10, (2017), 1592-1598. doi: 10.5829/ije.2017.30.10a.21
16. Gupta ,S.K., Raja, A.R., Vashista, M. and Yusufzai, M.Z.K., "Effect of heat input on microstructure and mechanical properties in gas metal arc welding of ferritic stainless steel", ***Materials Research Express***, Vol. 6, No. 3, (2018), 036516.
17. Paulraj, P. and Garg, R., "Effect of welding parameters on mechanical properties of gtaw of uns s31803 and uns s32750

weldments", ***Manufacturing Review***, Vol. 2, No. 29, (2015), DOI:10.1051/mfreview/2015032.

18. Gharibshahiyan, E., Raouf, A.H., Parvin, N. and Rahimian, M., "The effect of microstructure on hardness and toughness of low carbon welded steel using inert gas welding", ***Materials and Design***, Vol. 32, No. 4, (2011), 2042-2048. https://doi.org/10.1016/j.matdes.2010.11.056
19. Hsieh, C.-C., Lin, D.-Y., Chen, M.-C. and Wu, W., "Microstructure, recrystallization, and mechanical property evolutions in the heat-affected and fusion zones of the dissimilar stainless steels", ***Materials Transactions***, Vol. 48, No. 11, (2007), 2898-2902. doi:10.2320/matertrans.MRA2007162
20. Ogundimu, E., Akinlabi, E. and Erinosho, M., "Effect of welding current on mechanical properties and microstructure of tig welding of type-304 austenite stainless steel", in Journal of Physics: Conference Series, IOP Publishing. Vol. 1378, No. 3, 032022.
21. Moi, S.C., Pal, P.K., Bandyopadhyay, A. and Rudrapati, R., "Effect of heat input on the mechanical and metallurgical characteristics of tig welded joints", ***Journal of Mechanical Engineering*** Vol. 16, No. 2, (2019), 29-40.
22. Li, J.-Y., Sugiyama, S. and Yanagimoto, J., "Microstructural evolution and flow stress of semi-solid type 304 stainless steel ," ***Journal of Materials Processing Technology***, Vol. 161, No. 3, (2005), 396-406. DOI: 10.1016/j.jmatprotec.2004.07.063
23. Unnikrishnan, R., Idury, K.S., Ismail, T., Bhadauria, A., Shekhawat, S., Khatirkar, R.K. and Sapate, S.G., "Effect of heat input on the microstructure, residual stresses and corrosion resistance of 304l austenitic stainless steel weldments", ***Materials Characterization***, Vol. 93, (2014), 10-23.
24. Taiwade, R.V., Patil, A.P., Ghugal, R.D., Patre, S.J. and Dayal, R.K., "Effect of welding passes on heat affected zone and tensile properties of aisi 304 stainless steel and chrome-manganese austenitic stainless steel", ***ISIJ International***, Vol. 53, No. 1, (2013), 102-109. http://dx.doi.org/10.1016/j.matchar.2014.03.013
25. Kumar, S. and Shahi, A., "Effect of heat input on the microstructure and mechanical properties of gas tungsten arc welded aisi 304 stainless steel joints", ***Materials and Design***, Vol. 32, No. 6, (2011), 3617-3623. DOI: 10.1016/j.matdes.2011.02.017
26. Mosa, E., Morsy, M. and Atlam, A., "Effect of heat input and shielding gas on microstructure and mechanical properties of austenitic stainless steel 304l", ***International Research Journal of Engineering and Technology***, Vol. 4, No. 12, (2017), 370-377.
27. Tabish, T., Abbas, T., Farhan, M., Atiq, S. and Butt, T., "Effect of heat input on microstructure and mechanical properties of the tig welded joints of aisi 304 stainless steel", ***International Journal of Scientific and Engineering Research***, Vol. 5, No. 7, (2014), 1532-1541.

Persian Abstract

چکیده

در این کار تحقیقاتی ، AISI 304 از طریق فرآیند جوشکاری گاز بی اثر فلزی (MIGبا آرگون (Ar) به عنوان گاز محافظ جوش داده شد. در مطالعه حاضر، AISI 304 با استفاده از الکترود استاندارد L۳۰۸ در معرض ورودی به گرمای مختلف قرار گرفت. کیفیت جوش یعنی مقاومت کششی نهایی، چقرمگی، ریز مقاومت و ریزساختار AISI 304 مورد بررسی قرار گرفت. ریزساختارهای اتصالات جوش داده شده با استفاده از میکروسکوپ الکترونی روبشی (SEMمورد بررسی قرار گرفت ، به SEM متصل شد برای تعیین ترکیب شیمیایی فازهای تشکیل شده در رابط مشترک و از نتایج ، مشخص شد که در ورودی کم حرارت مقاومت کششی نهایی بالاتر است. نسبت به آنهایی که در گرمای متوسط و کم قرار دارند. از نتایج ، همچنین مشاهده شد که میزان درشت دانه در HAZ با افزایش ورودی گرما افزایش می یابد. همچنین مشخص شد که شکستگی نمونه های چقرمگی از نظر طبیعی شکننده بوده و نشانگر انعطاف پذیری کم و شکستگی شکننده است. ریزساختار منطقه جوش، -δفریت اسکلتی را در ماتریس آستنیت با محتویات مختلف فریت به نمایش گذاشته است. میکرو سختی مهره جوش با افزایش در ورودی حرارت کاهش می یابد. همچنین مشاهده شد که در ورودی گرمای متوسط، استحکام کششی، کشیدگی و سختی به دلیل ساختار دانه ریزتر و فاصله بین دندریتیک کوچکتر بهبود یافته است.

AIMS AND SCOPE

The objective of the International Journal of Engineering is to provide a forum for communication of information among the world's scientific and technological community and Iranian scientists and engineers. This journal intends to be of interest and utility to researchers and practitioners in the academic, industrial and governmental sectors. All original research contributions of significant value focused on basics, applications and aspects areas of engineering discipline are welcome.

This journal is published in three quarterly transactions: Transactions A (Basics) deal with the engineering fundamentals, Transactions B (Applications) are concerned with the application of the engineering knowledge in the daily life of the human being and Transactions C (Aspects) - starting from January 2012 - emphasize on the main engineering aspects whose elaboration can yield knowledge and expertise that can equally serve all branches of engineering discipline.

This journal will publish authoritative papers on theoretical and experimental researches and advanced applications embodying the results of extensive field, plant, laboratory or theoretical investigation or new interpretations of existing problems. It may also feature - when appropriate - research notes, technical notes, state-of-the-art survey type papers, short communications, letters to the editor, meeting schedules and conference announcements. The language of publication is English. Each paper should contain an abstract both in English and in Persian. However, for the authors who are not familiar with Persian, the publisher will prepare the latter. The abstracts should not exceed 250 words.

All manuscripts will be peer-reviewed by qualified reviewers. The material should be presented clearly and concisely:

- *Full papers* must be based on completed original works of significant novelty. The papers are not strictly limited in length. However, lengthy contributions may be delayed due to limited space. It is advised to keep papers limited to 7500 words.
- *Research* notes are considered as short items that include theoretical or experimental results of immediate current interest.
- *Technical notes* are also considered as short items of enough technical acceptability with more rapid publication appeal. The length of a research or technical note is recommended not to exceed 2500 words or 4 journal pages (including figures and tables).

Review papers are only considered from highly qualified well-known authors generally assigned by the editorial board or editor in chief. Short communications and letters to the editor should contain a text of about 1000 words and whatever figures and tables that may be required to support the text. They include discussion of full papers and short items and should contribute to the original article by providing confirmation or additional interpretation. Discussion of papers will be referred to author(s) for reply and will concurrently be published with reply of author(s).

INSTRUCTIONS FOR AUTHORS

Submission of a manuscript represents that it has neither been published nor submitted for publication elsewhere and is result of research carried out by author(s). Presentation in a conference and appearance in a symposium proceeding is not considered prior publication.

Authors are required to include a list describing all the symbols and abbreviations in the paper. Use of the international system of measurement units is mandatory.

- On-line submission of manuscripts results in faster publication process and is recommended. Instructions are given in the IJE web sites: www.ije.ir-www.ijeir.info
- Hardcopy submissions must include MS Word and jpg files.
- Manuscripts should be typewritten on one side of A4 paper, double-spaced, with adequate margins.
- References should be numbered in brackets and appear in sequence through the text. List of references should be given at the end of the paper.
- Figure captions are to be indicated under the illustrations. They should sufficiently explain the figures.
- Illustrations should appear in their appropriate places in the text.
- Tables and diagrams should be submitted in a form suitable for reproduction.
- Photographs should be of high quality saved as jpg files.
- Tables, Illustrations, Figures and Diagrams will be normally printed in single column width (8cm). Exceptionally large ones may be printed across two columns (17cm).

PAGE CHARGES AND REPRINTS

The papers are strictly limited in length, maximum 6 journal pages (including figures and tables). For the additional to 6 journal pages, there will be page charges. It is advised to keep papers limited to 3500 words.

Page Charges for Papers More Than 6 Pages (Including Abstract)	
For International Author ***	**$55 / per page**
For Local Author	**100,000 Toman / per page**

AUTHOR CHECKLIST

- Author(s), bio-data including affiliation(s) and mail and e-mail addresses).
- Manuscript including abstracts, key words, illustrations, tables, figures with figure captions and list of references.
- MS Word files of the paper.

International **J**ournal of **E**ngineering, P.O. Box 13145-1659, Tehran, I.R. Iran
Materials and Energy Research Center, 5 Ahuramazda St., Alvand Ave., Argentina Sq., Tehran, Islamic Republic of Iran
www.merc.ac.ir - www.emerc.ac.ir

THOMSON REUTERS

WEB OF SCIENCE

Scopus®

CAS®
A DIVISION OF THE
AMERICAN CHEMICAL SOCIETY

Google
Scholar